Turbulência

Atila P. Silva Freire
Programa de Engenharia Mecânica
COPPE/UFRJ

Anderson Ilha
Divisão de Metrologia Científica
Inmetro

Robert Breidenthal
Department of Aeronautics and Astronautics
University of Washington

Editores

ABCM – Associação Brasileira de Ciências e Engenharia Mecânica
COPPE/UFRJ – Instituto Alberto Luiz Coimbra de
Pós-Graduação e Pesquisa de Engenharia
IME – Instituto Militar de Engenharia

Coleção Cadernos de Turbulência
Turbulência, Volume 5, Tomo 2.

5^a Escola de Primavera em Transição e Turbulência
Instituto Militar de Engenharia, Rio de Janeiro
25 a 29 de setembro de 2006

Editores

Atila P. Silva Freire, *Programa de Engenharia Mecânica*, COPPE/UFRJ
Anderson Ilha, *Divisão de Metrologia Científica*, Inmetro
Robert Breidenthal, *Department of Aeronautics and Astronautics*,
University of Washington

Ficha catalográfica preparada pela Seção de Processos Técnicos da
Biblioteca do Centro de Tecnologia da Universidade Federal do Rio de Janeiro

Escola de Primavera em Transição e Turbulência (5.:2006: Rio de Janeiro, RJ)
Turbulência: Anais da V Escola de Primavera em Transição e Turbulência,
Rio de Janeiro, 25 a 29 de setembro de 2006 /editores Atila P. Silva Freire,
Anderson Ilha e Robert Breidenthal. Rio de Janeiro: ABCM, 2006.
XII, 253 p.; 23,5 cm – (Coleção Cadernos de Turbulência. Turbulência, V. 5, Tomo 2)
Inclui bibliografias
1. Turbulência. 2. Mecânica dos fluidos. 3. Fenômenos de transporte.
I. Freire, Atila P. Silva II. II. V EPTT (5.:2006: Rio de Janeiro, RJ).
III. Associação Brasileira de Ciências e Engenharia Mecânica. IV. Título. II.
Série
629.1332
E74t
ISBN (10 dígitos): 85-85769-25-4
ISBN (13 dígitos): 978-85-85769-25-4

Copyright 2006, Associação Brasileira de Ciências e Engenharia Mecânica, ABCM.
A ABCM não autoriza a reprodução de qualquer parte desta publicação para sua distribuição em geral, para promoções, para a criação de novas publicações ou para a venda.
Apenas através de prévia solicitação, por escrito, e em casos.
Documento preparado pelos Editores em LaTeX.
Impresso no Brasil pela Gráfica Graffito.

Contents

Prefácio

O ato quase solene de escrever o Prefácio de um livro necessariamente provoca em seu escritor momentos de profunda reflexão. Afinal, o objeto de tanta dedicação intelectual se mostra por completo, desnudo, em suas virtudes e defeitos.

Em sua forma definitiva, que não pode ser modificada, o livro deveria não apenas transmitir aos seus leitores a letra fria do rigor de suas construções teóricas, mas, principalmente, o espírito de toda a sofisticação intelectual que se pretende alcançar.

O presente texto pertence a uma já extensa e exitosa família. A série de escolas dedicadas exclusivamente à investigação da turbulência de fluidos deu origem a outros textos que marcaram época. A manutenção da alta estirpe, pois, poderia causar sérios embaraços a novas contribuições.

A Turbulência é uma matéria com sabidas dificuldades conceituais, que exige de seus militantes especializações múltiplas e sofisticadas. Esse texto, sem dúvida, preencherá lacunas importantes no arcabouço de métodos e técnicas que se pretendem disponíveis para um ataque consistente às dificuldades de natureza teóricas e práticas impostas pela Turbulência àqueles que a ambicionam assaltar. Temas do mais alto grau de complexidade e importância são dissecados em dois tomos que formam uma obra com doze capítulos. Um julgamento honesto dos Editores classifica a presente contribuição como da maior relevância tanto para iniciantes como para pesquisadores experientes no assunto.

A dedicação dos autores e seu compromisso com o resultado final dessa jornada foram da maior sensibilidade. Os Editores, sinceramente, esperam que os leitores reconheçam as muitas horas de trabalho abnegado que permitiram a existência desta obra.

Finalmente, talvez devêssemos agora nos inquirir sobre o propósito de tudo isso. Por que trabalhar com tamanho afinco para a existência dessa obra? A resposta é simples e singela: para a construção de uma sociedade melhor. Um objetivo que nos tem sido caro e que nos possibilitou encontrar aliados importantes na ABCM, na FAPERJ e no CNPq. Este projeto é, sobretudo, uma iniciativa feliz da ABCM e do Pronex "Núcleo de Excelência em Turbulência" um projeto apoiado pela FAPERJ e pelo CNPq (Processo No E-26/171.198/2003).

Os Editores

Acknowledgments

Author Listing

Chapter 1 **page 1**

B. C. Khoo
Dept. of Mechanical Engineering
National University of Singapore
Kent Ridge
Singapore 119260

Y. T. Chew
Singapore-MIT Alliance (SMA)
4 Engineering Drive 3
Singapore 117576

Chapter 2 **page 115**

Dana Dabiri
Dept. of Aeronautics & Astronautics
University of Washington
Seattle, WA 98195
USA

Chapter 3 **page 205**

Robert Breidenthal
Dept. of Aeronautics & Astronautics
University of Washington
Seattle, WA 98195-2400
USA

Chapter 4 **page 223**

Aline Cotel
Dept. of Civil and Environmental Engineering
University of Michigan
Ann Arbor, MI 48109-2125
USA

Chapter 1

Dynamic response of the near-wall hot-wire/hot-film system and near-wall velocity measurements

1.1 Introduction

Despite the recent progress made in the technique of PIV (Particle Image Velocimetry) for use in velocity measurements and the availability of LDA (Laser Doppler Anemometer) as another alternative since the 1970's, hot-wire anemometry remains the preferred choice for many researchers in turbulence measurements. The smallness in size of the active hot-wire element measuring in microns not only enables good spatial resolution of the velocity field, the correspondingly low thermal inertia of the said wire promises fast response, thus permitting the high frequency fluctuations of a turbulent flow to be followed faithfully.

Earlier, Perry & Morrison (1971) had shown that both their hot-wire and DANTEC-made system yielded a frequency response of at least over 5 kHz when subjected to direct velocity perturbation in a wall remote flow. The velocity perturbation test was carried out using the Karman vortex shed from one side of the cylinder; the frequency response being obtained from the shedding frequency of the vortex expressed in Strouhal number as a known function of flow Reynolds number, Re_d (based on freestream velocity and diameter of cylinder), while the amplitude response was deduced from comparisons of the intensity of streamwise velocity fluctuations across the wakes of cylinders with different sizes at corresponding downstream positions for a given $\mathrm{Re}_d = 140$. Such a fast response for the conventional hot-wire, as measured in terms of frequency without any amplitude attenuation, is of prime consideration for many workers in turbulence research,

where accurate time resolution of the flow field is of utmost importance.

Researchers, however, are only too aware that the performance of the same hot-wire changes as it approaches the wall. The hot-wire, when operating under wall remote conditions, is principally only subjected to convective heat loss whence the latter can be made related to the prevailing convective velocity via the calibration curve. In the presence of a nearby wall, there is additional heat loss from the wire to the wall substrate. Of equal importance is the accentuation of the aerodynamic interference effect due to the presence of the hot-wire prongs, which may alter the flow field thereby resulting in larger convective heat loss.

The subject of increased aerodynamic interference effects in near-wall hot-wire operations is discussed in Comte Bellot *et al.* (1971), Azad (1983) and in the recent work of Chew *et al.* (1998a). Chew *et al.* (1998a) also systematically investigated the other effects of wall substrate with different thermal conductivity, wire length to diameter (L/d) ratio and the overheat ratio imposed. On the other hand, the hot-wire having been calibrated under the usual free stream conditions must be subjected to some form of wall corrections for near-wall applications (*e.g.* see Bhatia *et al.*, 1982). Alternatively, the hot-wire may be calibrated directly in a known flow near to the wall with the wall effect being calibrated away. Khoo *et al.* (1996) suggested two methods to account for the wall effect on near-wall hot-wire measurements such that an accurate time-resolved streamwise velocity measurement is still feasible.

Despite the recent spate of works in near-wall hot-wire operations, including investigations of the effects of l^+ (wire length in wall units) on turbulence measurements in the viscous sub-layer (Khoo *et al.*, 1997), and other numerous earlier studies as found in Polyakov & Shindin (1978, 1979) and Zemskaya *et al.* (1979), to name a few, there is still a dearth in the literature on the dynamic response of a hot-wire operating in the vicinity of the wall. This is, to a very large extent, due to the difficulties in implementing a suitable mode of generating a known fluctuating flow field at a relatively high frequency near the wall. The hot wire, in the presence of a nearby wall, may present itself as a system with a vastly different thermal capacity and dynamic response, as compared to a wall-remote situation.

Khoo *et al.* (1995), in their attempt to determine the dynamic response of a marginally-elevated hot-wire anemometer probe for near-wall velocity and wall shear stress measurements, have for the first time, developed a viable means of generating a known high frequency fluctuating velocity field for purposes of quantifying both the frequency and amplitude response of the said hot-wire anemometer. Khoo *et al.* (1995) found that a 5 μm diameter wire mounted at 50 μm above the thermally less conducting epoxy-based wall substrate responded fully to imposed fluctuations of up to 1600 Hz without any amplitude attenuation, so was observed for another similar-sized wire but mounted at 12μm above the wall substrate. Their attempts to impose an increasingly higher fluctuation so as to determine the dynamic response in terms of the so-called "upper frequency limit" (henceforth termed f_D), when amplitude attenuation of imposed velocity change begins or when the said wire cannot respond fast enough to the imposed frequency, whichever occurs first, was thwarted by limitations due to excessive vibration ex-

perienced in their the experimental setup. That being so, Khoo *et al.* were unable to ascertain if there was any difference in the dynamic response of the hot-wire mounted at different heights from the wall, and it may be noted too that their successful tests of up to 1600 Hz were still way below the dynamic response of a wall-remote hot-wire of at least O(5 kHz) as recorded by Perry & Morrison (1971). The work of Khoo *et al.*, however, has definitely indicated the feasibility of imposing a known fluctuating flow very near to the wall for quantification of the near-wall hot-wire response.

In a similar way, despite the importance of quantifying the dynamic response of a hot element mounted very close or flushed with the wall as a wall shear stress gauge for suitability in the study of turbulent wall shear stress fluctuations, no attempt has been made thus far. Already, the hot-element wall shear stress gauge is preferred over the traditional force balance surface gauge with its complex mechanical linkages partly because of the perceived faster response characteristics of the former to reflect faithfully the changing quantities expected in a turbulent flow field although there is hardly any quantitative evidence to substantiate it. Still if interest is primarily confined to measuring the mean quantity in a stationary turbulent flow, the response characteristics of the wall shear stress probe may not be a major issue unless the turbulence statistics of the wall shear stress fluctuations are required or measurements are being made in a non-stationary turbulence field where the mean value is a function of time.

There are, however, only some fairly *qualitative* works carried out in the investigation of the response characteristic of a flush-mounted hot-element wall shear stress gauge. Cook & Giddings (1988) found that the buried flush-wire and Platinum-film gauges placed in a laminar oscillating flow produced on a flat plate by a freestream velocity comprising a mean component and a superimposed sinusoidal variation indicate a wall shear stress variation that lags the true (numerically obtained) variation even in the relatively low frequency range of between 3 to 20 Hz used in their experiments. They attributed the observed lag to "unsteady heat conduction effects in the gauge substrate". Since no attempt was made to calibrate the gauges for determination of the mean and oscillating components of the wall shear stress, there is no comparison concerning the magnitude of wall shear stress to ascertain the possibility of amplitude attenuation. In a subsequent follow up work, Cook (1994) subjected different types of hot-element wall shear stress gauges to unsteady turbulent flow; one of which a step-like flow was generated by rapidly opening the valve between the evacuated vacuum tank and the test facility hence producing a steady downstream velocity. What is most interesting was the observation of a wall remote hot-wire probe requiring only O(0.1) seconds to attain the steady freestream velocity value whereas it took about O(0.3) seconds for the cavity gauge to reach the steady wall shear stress quantity and up to O(40) seconds for the quartz substrate and glue-on gauges to assume the steady state value of the wall shear stress.

The results have two important implications. Firstly, even if the imposed perturbation is not a true step-like flow, the output from the hot-wire in the freestream would have indicated the nature of the flow and its response is clearly a

few factors faster than the hot-element cavity gauge mounted on the wall. Secondly and even more significant is the response indicated by the hot-element quartz substrate gauge or the glue-on gauge coming close to two orders of magnitude slower relative to the cavity gauge. Comparison among the hot-element gauges suggests that the type of thermally conducting/insulating material on which the hot element is mounted on may have far reaching consequences on its response. Other works like Houdeville *et al.* (1984) have also carried out limited testing of the various gauges and their results seem to support the use of the cavity gauge (where the surface level hot element presides above a small cavity beneath presumably to reduce substrate heat transfer) with better response characteristics as compared to other substrate-type gauges. Despite all these efforts carried out to determine a responsive wall shear stress gauge, no study, analytical or experimental, has been made to provide the quantitative information pertaining to the associated response characteristics.

The desire to fill the void in the literature on the quantification of the dynamic response of a marginally-elevated hot-wire as a velocity probe and flush-mounted hot-element wall shear stress gauge provides the motivation for the series of present work. Comparisons are made between the dynamic response frequency and the cut-off frequency according to the usual electronic perturbation test. Consequent to the establishing of a viable near-wall hot-wire velocity probe, near-wall measurements in the turbulent shear flow for both the channel and boundary layer flows are then carried out to elucidate the flow physics.

1.2 Experimental set for determination of the dynamic response (f_D) of hot-wire

1.2.1 Rotating disk

The basic design and construction of the rotating disk apparatus for the generation of a known velocity near to a surface is given previously in great detail in Khoo *et al.* (1995). Here, only the salient features are described with the improvements made such that a much higher frequency of imposed fluctuations is possible without excessive vibration which plagued the original set-up. The improved experimental rig is shown systematically in Fig.(1.1).

A heavy flywheel is placed concentrically over the top rotating disk of 150 mm radius and the said disk is made to rotate via a spring loaded central shaft enclosed within an external housing linked by a timer belt to a heavy duty DC motor mounted firmly on a structural column for purpose of rigidity. The timer belt and spring loaded shaft seek to minimize vibration from the motor, and the latter, with its larger lateral extent, as compared to the previous setup which used a relatively much smaller diameter shaft, also serve the function of reducing possible inaccuracy when mounted perpendicularly to the flywheel. The top rotating disk attached to the flywheel can be changed; in the first instance, a flat top disk was set with different gap sizes (δ) in the range from below 200μm to over 400 μm

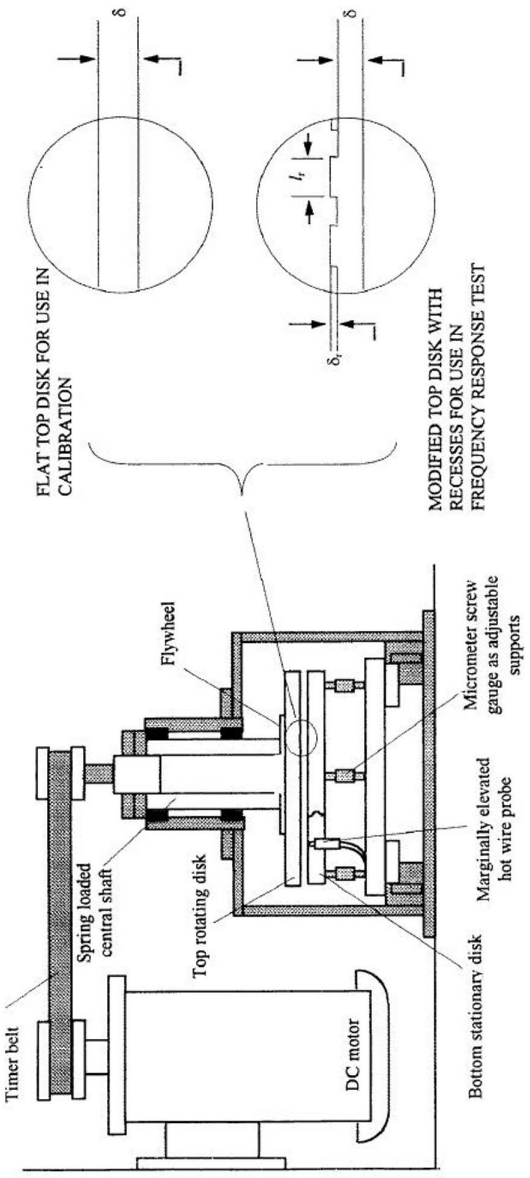

Figure 1.1: Layout of the apparatus for the generation of a known flow field between disks.

for purpose of calibrating the hot-wire. According to Stewartson (1953), the flow generated is given as

$$v = \omega r \left[\varepsilon - (\mathrm{Re}_s^2/6300)(8\varepsilon + 35\varepsilon^4 - 63\varepsilon^5 + 20\varepsilon^7) + O(\mathrm{Re}_s^4)\right] , \quad (1.1)$$

$$u = -\omega r(\mathrm{Re}_s^2/60)(4\varepsilon - 9\varepsilon^2 + 5\varepsilon^4) + O(\mathrm{Re}_s^3) , \quad (1.2)$$

where ω is the angular velocity of the top rotating disk, $\mathrm{Re}_s \equiv \omega\delta^2/\nu$ is the Reynolds number based on the gap size δ. u and v are the radial and azimuthal velocity components, respectively, and $\varepsilon \equiv z/\delta$ is the non-dimensional vertical coordinate with r as the radial coordinate.

During calibration, with the hot-wire mounted at a fixed height above the bottom stationary disk, a known Couette-like flow in the azimuthal direction is present since Re_s was made very small ($\mathrm{Re}_s << 1$) as deduced from Eq.(1.1). In order to generate a known fluctuating flow, the top disk is replaced by a similar sized modified perspex disk whose surface has 100 recesses of 45μm (δ_r) depth machined radially from the outer edge to half the disk radius (see Figure 1.1), similar to that carried out in Khoo *et al.* (1995).

The rectangular shaped recesses are distributed evenly on the disk. As discussed in Khoo *et al.*, the placement of the hot wire at r_m= 115 mm where the local azimuthal extent of each recess l_r (at $\mathrm{r} = \mathrm{r}_m$) is 3.6 mm, hence giving a ratio of $l_r/\delta_r = 80$, coupled with previous known works of flow over a backward facing step which indicates flow separation at the step with reattachment occurring within 10 step heights thereafter (see Isomoto & Honami, 1989 and Shu *et al.*, 1994), strongly suggest the presence of two different Couette-like flows imposed by the modified top disk with two effective surfaces separated by distances of δ and $(\delta + \delta_r)$ from the bottom stationary disk. It is reckoned that the disturbances caused by the sudden change in gap size is largely contained within the reattachment region; this scenario is further supported by the hot-wire output which shows fairly clear 'square-wave' like signals (see Figure 1.4) (Some discussions on the generation of near Couette-like flow can also be found in Khoo *et al.*, 1995). In this work, the hot-wire is also mounted at r_s = 95 mm and r_l = 130 mm, equivalent to l_r/δ_r of 53 and 102, respectively. In this way, the period of the fluctuating waveform as deduced from the hot-wire output can be compared to the imposed fluctuation, and the magnitude of the hot wire signal interpreted as velocity via the calibration curve can be compared quantitatively to the amplitude of the fluctuating velocity field. The presence of any amplitude attenuation of imposed velocity change or the detection of the inability of the hot-wire to follow the imposed fluctuations, whichever comes first, can be construed as the dynamic response frequency (f_D) of the hot-wire system.

To provide for a known fluctuating wall shear stress as dictated by the corresponding fluctuating flow field, the top flat disk is replaced by a modified disk with 100 evenly distributed recesses of 45 μm (δ_r) depth machined on its surface stretching from the disk edge at r = 150 mm to half the disk radius at r = 75 mm. At the respective radial position of $\mathrm{r}_i = \mathrm{r}_s$ (95 mm), r_m (115 mm) and r_l (140 mm) where the hot-element wall shear stress gauge is mounted, the presence of

two Couette-like flows imposed by the modified top disk rotating at a tangential velocity of $\omega \mathrm{r}_i$ separated by two effective gaps of δ and $(\delta + \delta_r)$ necessarily implies the presence of two associated tangential wall shear stresses given as

$$\tau = \mu \frac{\omega r_i}{\delta} \,, \tag{1.3}$$

and

$$\tau = \mu \frac{\omega r_i}{(\delta + \delta_r)} \,. \tag{1.4}$$

In this way, the frequency of imposed fluctuation (f_{imp}) and the magnitude of the imposed wall shear stresses can be used for comparison to the measured output of the wall shear stress gauge mounted at r_i. With 100 recesses on the modified top disk, the imposed frequency is

$$f_{imp} = \frac{\omega}{2\pi} \times 100\,\mathrm{Hz} \,. \tag{1.5}$$

The detection of the onset of amplitude attenuation of the imposed wall shear stress change or the inability of the gauge to follow the imposed frequency fluctuation, whichever occurs first, shall be considered as the dynamic response frequency (f_D) of the said gauge.

1.2.2 Marginally elevated hot-wire as a velocity probe

The construction of the hot-wire probe follows closely to that of Chew *et al.* (1994) and Khoo *et al.* (1995), albeit some modifications incorporating a micrometer screw gauge for adjusting the height of the wire from the wall and the use of different wall substrate materials. The probe consists of a KANOMAX-0251 single hot-wire mounted within a cylindrical hollow plug with two small holes at the top section for the protrusion of the said hot-wire prongs above the wall (see Figure 1.2).

Several identical plugs of different thermal conductivities were manufactured such that the placement of the 5 μm diameter DANTEC-made platinum-plated tungsten wire on the tip of the prongs enabled the wire to be exposed to the plugs' top wall substrate made of the respective materials. Because the top section of the plug which measures 7 mm in diameter is considerably bigger in extent compared to the wire length of $\mathrm{l} = 1.2$ mm mounted at the center of the plug (hence giving a wire length to diameter ratio of at least 200 to ensure negligible heat loss through the prongs (see Ligrani & Bradshaw, 1987; Chew *et al.*, 1998a), it is reckoned that the overall active wire element will be subjected to the immediate influence of the particular wall substrate beneath. The whole plug was in turn mounted flush with the wall of the bottom stationary disk during the experiments.

At the other end of the hot-wire probe, a micrometer screw gauge was attached to enable adjustments of the required wire height above the wall. The respective probe was then connected to a DISA 56C01 CTA unit. The CTA unit was linked via the Keithley made DAS-20 data acquisition system to a microcomputer. Data

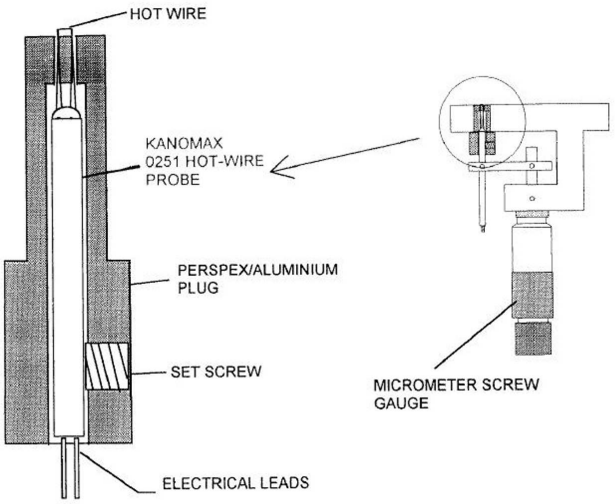

Figure 1.2: Schematic diagram of the marginally elevated hot-wire anemometer.

acquisition was effected at rates between 5 to over 50 kHz, with the higher rates of acquisition used for higher rates of imposed velocity fluctuation via the modified top disk.

1.2.3 Flushed-mounted hot-wire and hot film as wall shear stress probe

Two different types of hot-element wall shear stress gauges are used in the present study. The first type is the commercially available DANTEC-made 55R45 and 55R46 flush-mounted hot-film shear stress probes whose active nickel-based element, deposited on a quartz substrate, measures 0.2 mm by 0.75 mm. For the 55R45 gauge, a 0.5 μm thick quartz coating covers the active element as opposed to a 2 μm thick quartz coating for the 55R46 gauge. The second type is the flush-mounted hot-wire where the 5 μm diameter DANTEC-made platinum plated tungsten wire is placed in contact with the perspex wall substrate. The construction of the latter is similar to that described in Section 1.2.2.

The required hot-wire is soldered onto the prongs and fine adjustment of the wire height above the top surface of the perspex plug till it touches the wall is achieved by means of a micrometer screw gauge which is attached to the probe. A schematic of the probe is given in Fig.(1.3) for ease of reference. The respective wall shear stress gauge was then connected to the DISA 56C01 CTA unit, which in turn was linked to a micrometer via the Keithley-made DAS-20 data acquisition system.

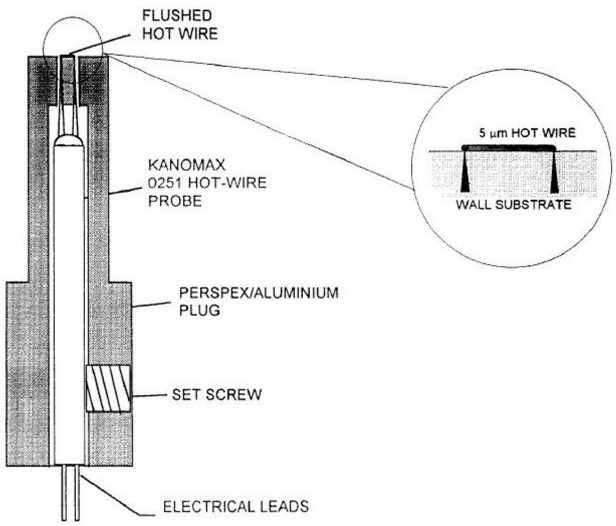

Figure 1.3: Schematic diagram of the flush-mounted hot-wire wall shear stress gauge.

1.3 The dynamic response of the hot-wire anemometer

1.3.1 Near-wall hot-wire for velocity measurement

1.3.1(a) Calibration of the hot-wire probe

Calibration of the marginally-elevated hot-wire probe was carried out in the same manner as in Khoo *et al.* (1995) with the flat rotating disk set at a fixed distance of δ from the bottom stationary disk. By keeping $\mathrm{Re}_s << 1$, for a range of angular speeds, the imposed azimuthal velocity (v) given by Eq.(1.1) at the wire's location (z = h) can be correlated against the output voltage (E) of the hot-wire via King's law

$$E^2 = A + Bv^n \,, \tag{1.6}$$

where A, B and n are calibration constants. As noted in Chew *et al.* (1994) and Khoo *et al.* (1996), calibration of the hot-wire in this manner effectively ensured that the wall influence was accounted for or calibrated away.

To ensure consistency of results, calibration utilizing the flat top disk was carried out before and after each series of experiments. If there was any drift of the calibration constants by more than 2%, the results were discarded. Monitoring of the air temperature was done simultaneously and the data was accepted only when the temperature variation was less than $\pm 0.2^{\circ}$C.

1.3.1(b) The frequency limit (f_D) of a hot-wire mounted at 50 μm above perspex wall

With the modified top disk set at $\delta = 300$ μm from the stationary bottom disk, typical voltage-time series for selected rotational speeds are shown in Fig.(1.4) for a hot-wire mounted at $r_m = 115$ mm and h = 50 μm above the perspex wall substrate. For each rotational speed of Ω rpm, the imposed fluctuation frequency (f_{imp}) associated with 100 recesses of the modified top disk is evaluated as

$$f_{imp} = 100\Omega/60\,\mathrm{Hz} \tag{1.7}$$

and duly reflected on the same figure.

The typical voltage signals taken w.r.t. time indicate a fairly well-defined and regular "square-wave" series with relatively flat top and trough sections; the respective series yields an average period which coincides with the imposed frequency, hence implying that the hot-wire is responding faithfully to the frequency of the externally imposed fluctuating flow field. As discussed at length in Khoo *et al.* (1995), the presence of the flat top and trough voltage traces provides the possibility that the probe can also respond to the full amplitude change in the imposed velocity fluctuation. Shown in each of the voltage-time traces are the *calculated* maximum and minimum voltages associated with the velocities at the wire's location (via the calibration curve) subjected to near-Couette flows with the top moving surface mounted at δ and $(\delta + \delta_r)$, respectively, from the stationary bottom surface. The top surface is moving at the local tangential velocity given by $\Omega r_m \pi/30$ mm/s.

Figure 1.4 clearly depicts that, with the exception of case (a), the hot wire is able to respond fully to the frequency and amplitude of the imposed fluctuating flow field. For case (a), although the evaluated frequency coincides with f_{imp} at 3000 Hz, there is obvious amplitude attenuation. There is a marked absence of the flat top and trough sections of the periodic waveform and the resulting peak and trough voltages cannot match the *calculated* voltages. This may suggest that amplitude attenuation is the limiting factor in the determination of the dynamic response of the hot-wire rather than just the consideration of the frequency per se. In this respect, the results of Fig.(1.4) are replotted in Figure 1.5(a) with other data showing the maximum and minimum velocities associated with the "saturated" voltage *measured* corresponding to the relatively flat top and trough portions of the voltage-time trace, respectively, via the calibration curve.

As argued in Khoo *et al.* (1995), the fairly sharp rise and fall of the voltage-time trace with small disturbances of higher frequency accompanying the saturated voltage readout are associated with the flow attachment effect following the movement of a recess past the hot-wire. Discounting the rise and fall of the voltage-time trace from the flat top and trough sections, only the voltage readouts in the center half portion of each flat section are evaluated as velocities for computation of the average maximum and minimum velocities. Also shown in Figure 1.5(a) are the *calculated* velocities at the wire's position obtained from Eq.(1.1) corresponding

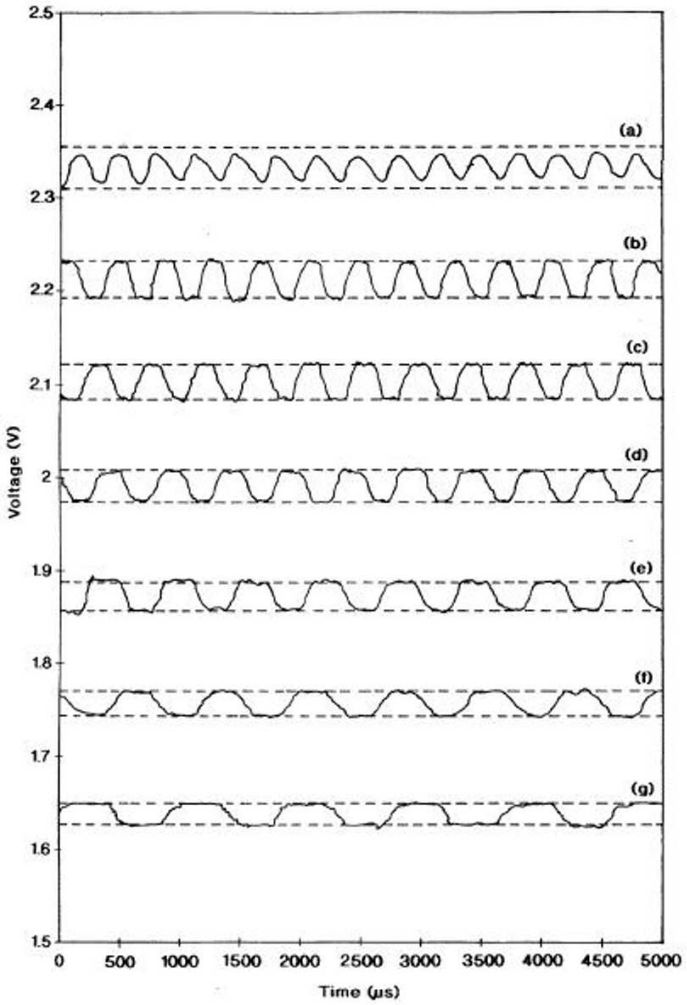

Figure 1.4: The voltage-time trace of the hot-wire mounted at 50 μm above the Perspex wall substrate for different imposed rates of rotation: (a) 3000 Hz, (b) 2490 Hz, (c) 2262 Hz, (d) 1993 Hz, (e) 1625 Hz, (f) 1335 Hz, (g) 1078 Hz. Calculated maximum and minimum voltages for each imposed frequency are shown as broken lines.

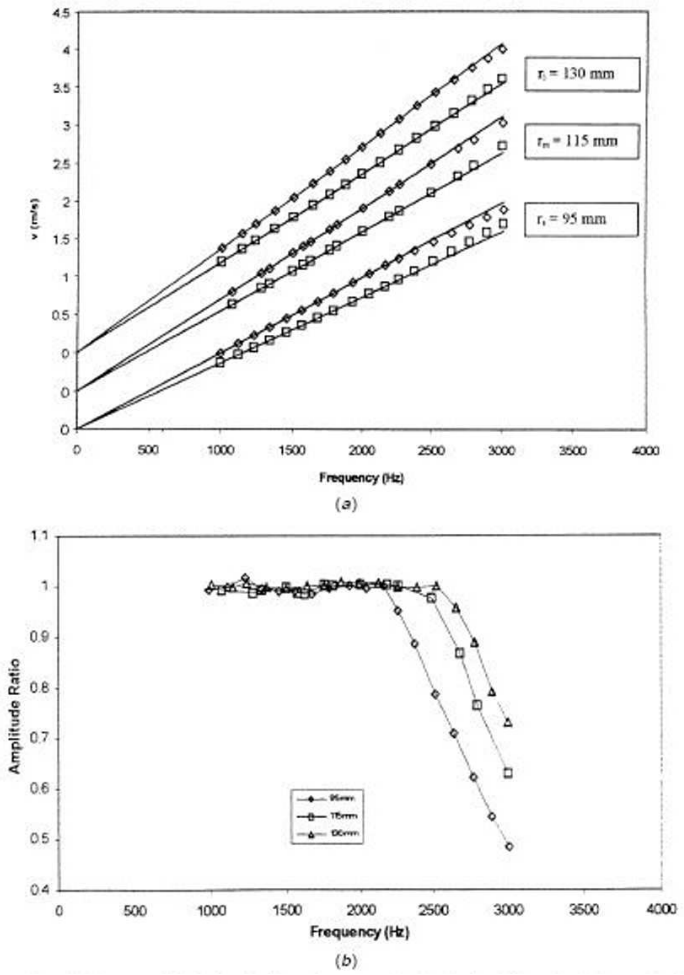

Figure 1.5: Comparison between calculated velocity and measured velocity for different rotation rates obtained from the hot-wire anemometer mounted 50 μm above the Perspex wall substrate at $r_s = 95$ mm, $r_m = 115$ mm and $r_l = 130$ mm. Calculated velocities are represented as full lines according to equation (1.1). ($\Diamond$) and ($\Box$) represent the maximum and minimum of mean velocity fluctuation respectively. *(b)* Amplitude ratio, defined as a_{mea}/a_{imp}, for the hot-wire anemometer mounted 50 μm above the Perspex wall substrate at $r_s = 95$ mm, $r_m = 115$ mm and $r_l = 130$ mm for different imposed frequencies.

to gap sizes of δ and $(\delta + \delta_r)$ which are presented as solid lines passing through the origin.

Figure 1.5(a) shows that the hot-wire mounted at h = 50μm from the perspex wall substrate can respond fully to a fluctuating flow field without any amplitude attenuation up to $f_{imp} \approx 2500$ Hz. Beyond 2500 Hz, the probe shows obvious amplitude attenuation and the measured velocities depart increasingly from the calculated velocities as f_{imp} becomes even larger. Figure 1.5(b) shows the amplitude ratio, defined as a_{mea}/a_{imp} (*i.e.* ratio of the *measured* amplitude of velocity fluctuation to the amplitude of the imposed velocity fluctuation), versus the imposed frequency. The dynamic response (f_D) is defined as the upper frequency limit where the onset of amplitude attenuation of the imposed velocity change occurs, the threshold of which is set at $a_{mea}/a_{imp} = 0.9$ (which is in line with the experimental uncertainty of about 10% for evaluated a_{mea}/a_{imp}), or when the said wire is no longer able to respond fast enough to the imposed frequency, whichever occurs first. Hence, from Figure 1.5(b), we may conclude that the dynamic response of the said hot-wire mounted at $r_m = 115$ mm and a height of 50 μm above the perspex wall substrate is given as $f_D \approx 2625$ Hz corresponding to a mean imposed convective velocity v_D of 2.94 m/s. It is reasonable to infer that for the same $v_D = 2.94$ m/s, at an imposed frequency of less than $f_D = 2625$ Hz, the hot-wire will not have encountered any amplitude attenuation or at the very most limited to a damping value less than 10%.

Figures 1.5(a) and 1.5(b) also show the results of the *same* hot-wire placed at radial positions $r_s = 95$ mm and $r_l = 130$ mm. The voltage-time traces (not shown) bear similar features to those depicted in Figure 1.4 for $r_m = 115$ mm; at lower imposed frequencies, distinct flat top and trough sections are discernible whilst at much higher imposed frequencies, the resulting periodic peak and trough voltages are not able to match the calculated voltages even though the evaluated frequencies are identical to the respective imposed frequencies. From Figure 1.5(b), it is observed that for h = 50 μm at $r_s = 95$ mm, f_D is found to be 2345 Hz corresponding to a mean imposed convective velocity v_D of 2.17 m/s. On the other hand, the hot-wire placed at r_l indicates a higher f_D of 2750 Hz and the corresponding mean velocity is $v_D = 3.48$ m/s.

It can thus be seen that a hot-wire mounted at a fixed height of 50 μm above the perspex wall substrate exhibits a distinct trend of increasing dynamic response (f_D) as the convective velocity increases. As the streamwise convective velocity is closely related to the forced convective heat transfer from the wire, it may thus be suggested that the dynamic response of a hot-wire system is also positively correlated with larger convective heat loss from the wire-element.

The placement of the modified top disk at $\delta = 300$ μm in the experiments, together with a fixed $\delta_r = 45$ μm, necessarily implied an amplitude of velocity change ($\Delta v/v$) of 13% for the above dynamic response tests. In the present study, we maintained a constant ($\Delta v/v$) of 13% throughout.

1.3.1(c) Wall effect on the dynamic response of a marginally-elevated hot-wire

Further tests were carried out to investigate the influence of wall effect on f_D for a marginally-elevated hot-wire. To discount the influence of convective velocity, it is imperative that the convective velocity at the wire's location be kept constant. However, in the determination of f_D using the present experimental rig, the convecting velocity at the wire's location cannot be preset independently, as both f_D and the corresponding v_D are obtained simultaneously. In this regard, several tests at different r and h were carried out with the aim of achieving similar values of v_D. Shown in Figs.(1.6a) and (b) are the results for wires mounted at h = 65 μm and r_s = 95 mm, for which f_D = 2390 Hz and v_D = 2.9 m/s; for the wire at h = 40 μm and r_l = 130 mm, f_D = 2690 Hz and v_D = 2.7 m/s.

Also plotted on the same figure for comparison is the result previously presented for h = 50 μm at r_m = 115 mm, where f_D = 2625 Hz and v_D = 2.9 m/s. It is evident that with the same nominal convective velocity at the wire's location, hence implying a similar convective heat transfer from the wire, the placement of the wire closer to the wall from h = 65 μm to h = 50 μm and finally down to h = 40 μm has resulted in a monotonically increasing f_D.

Conventionally, the closer the hot-wire is to the wall, the greater is the wall influence. It is therefore appropriate to suggest that the increase in wall effect has led to an improvement in f_D of the said wire. It is also important to mention that the wall effect is closely associated with greater heat transfer from the wire due to the physical presence of the wall. This can be mainly attributed to direct radiation heat transfer to the surrounding wall substrate or to the localized aerodynamic interference of the flow around the wire w.r.t. the nearby wall, thus resulting in an increase in convective heat transfer from the wire to the flow and the surrounding wall substrate.

1.3.1(d) Summary of results of f_D in semi-dimensionless plot

The findings from previous Sections 1.3.1(b) and 1.3.1(c) have shown that an increase in heat transfer from the hot-wire, whether due to convective heat transfer or to increasing wall effect, results in an improvement in f_D. These results obtained for the perspex wall substrate are reiterated in the semi-dimensionless plot of f_D versus h^+ (*i.e.* height of wire expressed in wall units $\nu/\overline{U_\tau}$) in Fig.(1.7). Besides the data for fixed heights of h = 25 μm and 50 μm, as well as for $v_D \approx 2.9$ m/s as demarcated by the respective loci, other results obtained are also plotted together with the "interpolated" loci indicating possible behaviour of the hot-wire mounted at r_l, r_m and r_s.

Several interesting features can be observed from Fig.(1.7). The hot-wire registers f_D as 2690 Hz with v_D = 2.7 m/s when positioned at r_l = 130 mm and h = 40 μm (equivalent to $h^+ = 2.6$). At about the same value of h^+, corresponding to h = 50 μm and r_s = 95 mm, the hot-wire exhibits f_D as 2345 Hz with a correspondingly smaller v_D of 2.17 m/s. Since a similar value of h^+ implies equivalent influence of

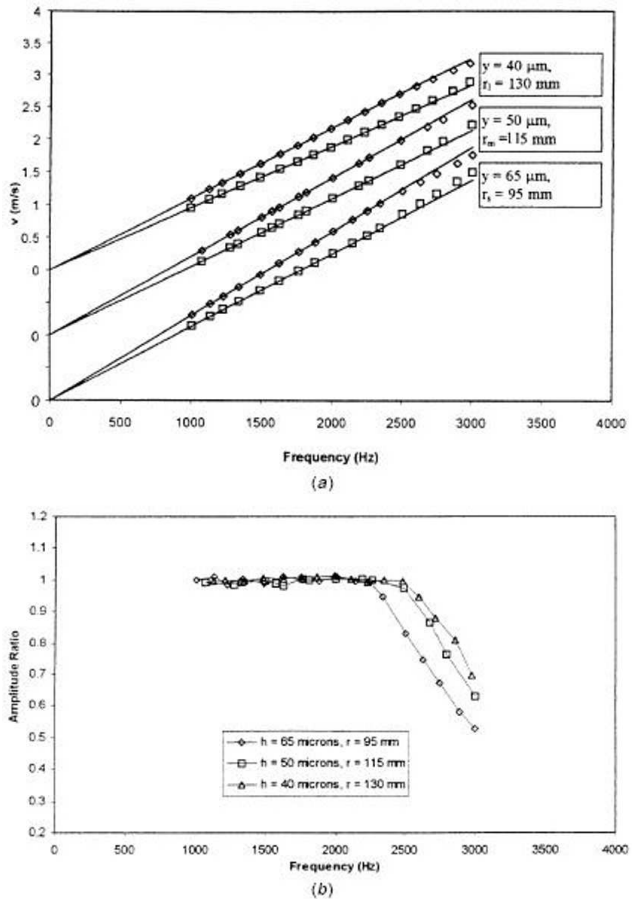

Figure 1.6: Comparison between calculated velocity and measured velocity for different rotation rates obtained from the hot-wire anemometer mounted 65 μm, 50 μm and 40 μm above the Perspex wall substrate at $r_s = 95$ mm, $r_m = 115$ mm and $r_l = 130$ mm respectively. Calculated velocities are represented as full lines according to equation (1.1). ($\Diamond$) and ($\Box$) represent the maximum and minimum of mean velocity fluctuation respectively. *(b)* Amplitude ratio, defined as a_{mea}/a_{imp}, for the hot-wire anemometer mounted 65 μm, 50 μm and 40 μm above the Perspex wall substrate at $r_s = 95$ mm, $r_m = 115$ mm and $r_l = 130$ mm for different imposed frequencies.

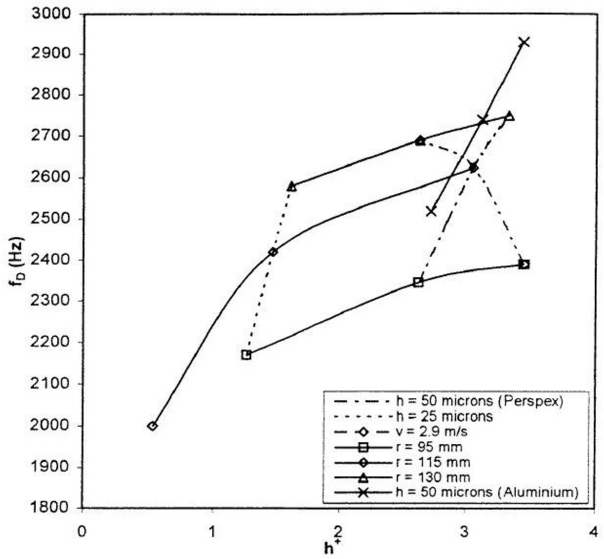

Figure 1.7: Semi-dimensionless plot of f_D for different values of h^+ for marginally elevated hot-wires placed above the Perspex and aluminium wall substrates.

wall effect on the hot-wire, it becomes apparent that an increase in the convective velocity on the wire with resulting greater convective heat transfer gives rise to an increase in f_D. Another feature, already discussed in Section 1.3.1(c), which is worth reiterating is that, for the same convective velocity of $v_D \approx 2.9$ m/s, the hot-wire shows the trend of increasing f_D with decreasing h^+, the latter being directly related to decreasing h. Since a smaller h^+ implies larger wall influence on the performance of a hot-wire with accompanying larger heat transfer from the wire, this suggests that a larger wall influence has actually a positive effect on f_D. The above two features clearly support the notion of f_D for a marginally-elevated hot wire increasing with enhanced heat transfer.

Finally, the results obtained for fixed heights of h = 25 μm and 50 μm show that as v_D increases, f_D increases. It is interesting to note that at a fixed elevation, an increase in h^+ is caused by an increase in v_D. As already discussed, a larger h^+ implies smaller wall influence with the tendency to cause a drop in f_D. Therefore, an increase in v_D, with consequential increase in the convective heat transfer from the wire, must have been sufficiently large to offset the effects of decreasing wall influence (corresponding to increasing h^+) such that the overall heat transfer is still larger, as manifested by the corresponding rise in f_D. The converse, *i.e.* the dominance of decreasing v_D on the convective heat transfer from the wire over the effect of increasing wall influence hence resulting in an overall decrease in f_D, is also true.

1.3.1(e) Effect of wall substrate material on f_D

The findings from Sections 1.3.1(c) and 1.3.1(d) have suggested that an increase in heat transfer from the wire due to increasing influence of wall effect has actually resulted in an increase in f_D. In their investigation of the near-wall corrections for single hot-wire measurements, Chew *et al.* (1995) found that a thermally more conducting wall substrate brings about an overall larger wall effect on the hot-wire resulting in larger heat loss to the wall, thereby necessitating a greater magnitude of wall corrections. In this regard, it is deemed appropriate to perform another series of tests to determine f_D for a wall substrate of different thermal conductivity to evaluate and further substantiate the effect of wall influence on the behaviour of f_D. A thermally more conducting Aluminium wall substrate, as compared to the perspex wall substrate used previously, was selected for this purpose. The hot-wire was mounted at a fixed height of h = 50 μm above the wall of the Aluminium plug, which was in turn mounted at r_s = 95 mm, r_m = 115 mm and r_l = 130 mm on the bottom stationary disk for the determination of the respective f_D.

Figure 1.8 shows the results for the measured maximum and minimum velocities versus imposed frequency for the hot-wire at r_s, r_m and r_l for comparison with the *calculated* velocities which are presented as straight lines passing through the origin. The results of Fig.(1.5) and Fig.(1.8) can then be compared to investigate the effects of wall substrate thermal conductivity on f_D for wires sharing same values of h and r.

For the case of the wire mounted at r_m, with the modified top disc rotating at 1575 rpm (equivalent to an imposed frequency of 2625 Hz), the wire above the perspex wall shows signs of amplitude attenuation first, and f_D is subsequently found to be 2625 Hz (see Figure 1.5). On the other hand, under the same operating conditions, the wire above the Aluminium wall did not show any indication of amplitude attenuation at 2625 Hz; it was only at a higher rotating speed of the top disc (at f_D = 2740 Hz) did the said wire show signs of amplitude attenuation (see Figure 1.8). It is therefore logical to conclude that *relatively*, a wire at a particular height above a perspex wall exhibits a poorer dynamic response (as characterized by f_D) compared to a wire mounted at the same height above a Aluminium wall.

The same behaviour can also be observed for hot wires mounted at r_s and r_l for the two different perspex and Aluminium wall substrates (c.f. Figure 1.5 and 1.8), thereby lending further support to the conclusion that an increase in wall influence on hot-wire performance has correspondingly given rise to an improvement in f_D.

Results for the hot-wire placed next to an Aluminium wall at h = 50 μm are also plotted in a semi-dimensionless form and shown in Fig.(1.7) for further comparison to results for the hot-wire above a perspex wall. A locus is also drawn through the former data points which supposedly should characterize the dynamic response of the said wire at the same height but subjected to different imposed convective velocities. The same argument holds for the locus passing through the data points of the hot-wire mounted at h = 50 μm above the perspex wall. At any

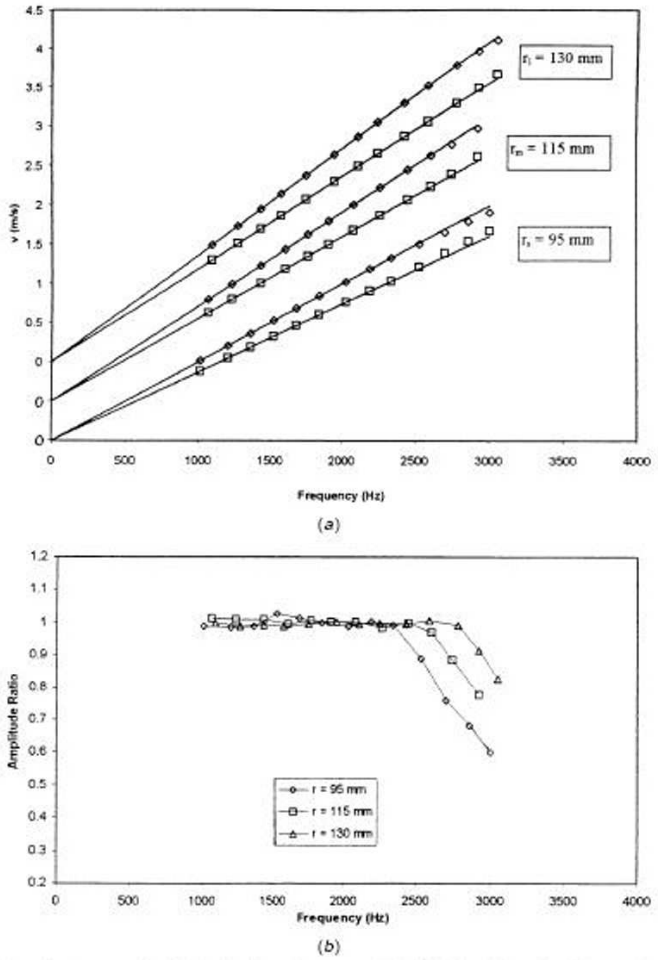

Figure 1.8: Comparison between calculated velocity and measured velocity for different rotation rates obtained from the hot-wire anemometer mounted 50 μm above the aluminium wall substrate at r_s = 95 mm, r_m = 115 mm and r_l = 130 mm. Calculated velocities are represented as full lines according to equation (1.1). ($\Diamond$) and ($\Box$) represent the maximum and minimum of mean velocity fluctuation respectively. *(b)* Amplitude ratio, defined as a_{mea}/a_{imp}, for the hot-wire anemometer mounted 50 μm above the aluminium wall substrate at r_s = 95 mm, r_m = 115 mm and r_l = 130 mm for different imposed frequencies.

given value of h^+, the value of f_D on the interpolated locus of the Aluminium wall substrate is almost always larger than the corresponding f_D lying on the locus for the perspex wall.

Previous works have shown experimentally (Khoo *et al.*, 1996 and Chew *et al.*, 1998a) and numerically (Chew *et al.*, 1995) that a wire of the same diameter at the same h^+ exhibits a larger heat loss for the case of a thermally more conducting wall as opposed to one with lower thermal conductivity. In other words, at the same h^+, the wall effect due to the Aluminium wall substrate is invariably greater than the perspex wall substrate. It is therefore evident that the presence of a thermally more conducting wall with larger wall effects has resulted in a larger f_D which is in accord with the conclusions arrived at in the earlier sections.

1.3.1(f) Concluding remarks for Section 1.3.1

Experiments were carried out using a specially designed apparatus consisting of a modified top rotating disk with recesses cut on its surface and a bottom stationary disk to generate a known near-wall fluctuating flow field for purpose of quantifying the dynamic response of marginally-elevated hot-wire probes. Results have shown that while the hot-wire may be able to respond to the imposed frequency, it is the amplitude of velocity change ($\Delta v/v$) which serves as the limiting factor for the hot-wire to follow fully which leads to amplitude attenuation. For a hot-wire mounted at height $h = 50$ μm from the perspex wall substrate , the dynamic response frequency increases monotonically from 2345 Hz to 2750 Hz as the nominal convective velocity (v_D) changes from 2.17 m/s to 3.48 m/s. The same hot-wire mounted at $h = 25$ μm exhibits a similar behaviour for f_D, which improves from 2170 Hz to 2580 Hz, with v_D increasing from 1.00 m/s to 1.63 m/s. These findings suggest that an increase in the convective velocity, which is synonymous with a larger convective heat transfer from the wire, results in an increase in f_D.

When the hot-wire is subjected to a constant convective velocity of $v_D \approx 2.9$ m/s at different heights of 65 μm, 50 μm and 40 μm above the perspex wall, f_D shows an increasing trend with corresponding values of 2390 Hz, 2625 Hz and 2690 Hz, respectively. The decreasing heights, when expressed in wall units, indicate a decreasing h^+ with increasing effect of wall influence. This suggests that f_D improves with larger wall effects. The influence of greater wall effects also invariably implies more heat transfer from the wire due to localized aerodynamic influence of the flow around the wire w.r.t. the nearby wall (Chew *et al.*, 1995). This, together with the above findings, suggest that the dynamic response frequency of a marginally-elevated hot-wire increases with larger heat loss from the said wire irrespective of whether the greater heat loss is due to forced convection or due to wall effects.

Further experiments were also performed on a hot-wire mounted at the same height $h = 50$ μm above a thermally more conducting Aluminium wall substrate. It was found to exhibit a relatively better response characteristic compared to its counterpart above a perspex wall substrate under identical operating condi-

tions. At the same h^+, the hot-wire above the Aluminium wall indicates a consistently higher f_D than that above the perspex wall. As the wall influence on a marginally-elevated hot wire increases for a thermally more conducting wall, the results support the general conclusion that f_D increases with greater heat loss from the wire, in particular the influence of larger wall effect. More importantly, a wall possessing higher thermal conductivity ensures better response characteristics for marginally-elevated hot wires utilized for near-wall velocity measurements.

Further discourse on this Section 1.3.1 can be found in Khoo *et al.* (1998a).

1.3.2 Flushed-mounted hot-wire and hot-film for wall shear stress measurement

1.3.2(a) Calibration of the hot-element wall shear stress probe

The calibration of the respective hot-element wall shear stress probe was carried out with the flat rotating disk set at a distance δ from the bottom stationary disk. With $Re_s << 1$, the tangential wall shear stress (τ) according to Eq.(1.3) is correlated against the output voltage (E) via the equivalent King's law relationship,

$$E^2 = A + B\tau^n \,, \tag{1.8}$$

where A, B and n are calibration constants, for different rotation rates ω and gap sizes δ. The methodology described is similar to that used in Chew *et al.* (1994). It may be noted too that Shah & Antonia (1987) used an identical equation (1.8) for their calibration except they carried out their calibration in a known turbulent channel flow and both the voltage (E) and shear stress (τ) were interpreted as mean quantities. In our experiments, calibration was carried out before and after the tests with the modified top disk. If there was any significant drift of the calibration constants by more than 2%, the results were discarded and repeated. The air temperature was monitored during the experiments to ensure a variation of less than $\pm 0.2°C$.

1.3.2(b) The dynamic response (f_D) of a flush-mounted hot-wire wall shear stress gauge

The hot-wire was mounted physically in contact with the perspex wall substrate as a wall shear stress gauge. The modified top disk was placed at a height of $\delta = 300$ μm from the bottom stationary disk where the gauge was mounted throughout the experiments. This implies an amplitude of imposed wall shear stress fluctuations ($\Delta\tau/\tau$) of 13%, similar to the work in Section 1.3.1.

Figure 1.9 shows the various voltage-time traces of the said hot-wire positioned at r_m and subjected to the rotating movement of the modified top disk. At the lower imposed frequency $f_{imp} \leqslant 1250$ Hz (*i.e.* case (f) - (h)), the typical voltage signal shows a fairly well defined regular series with relatively flat top and trough

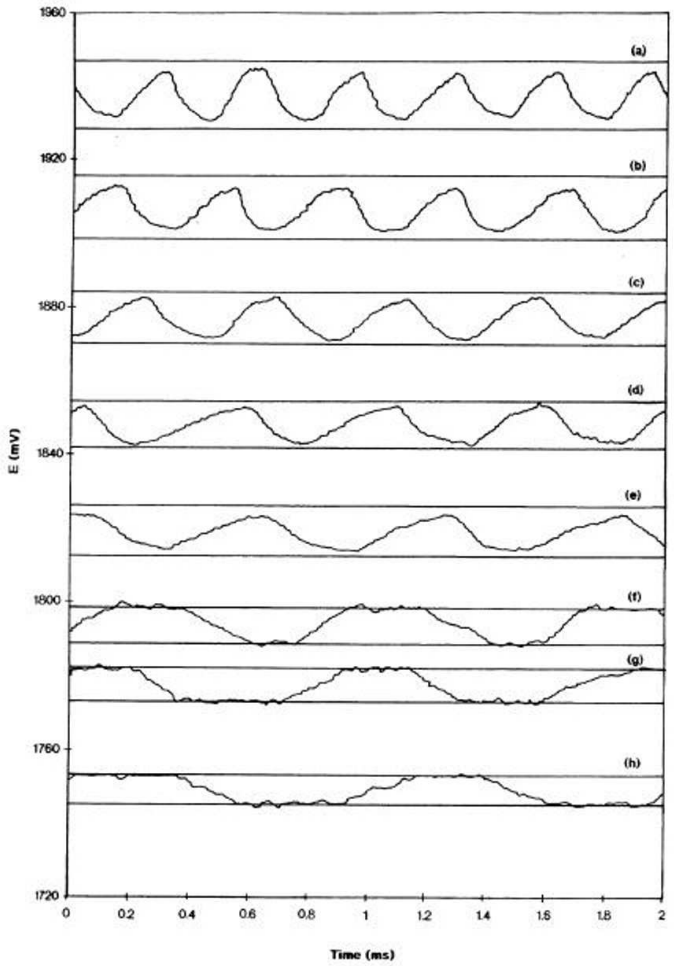

Figure 1.9: The voltage-time trace of the flush-mounted hot-wire wall shear stress gauge for different imposed rates of rotation: (a) 3033 Hz, (b) 2613 Hz, (c) 2250 Hz, (d) 1948 Hz, (e) 1678 Hz, (f) 1250 Hz, (g) 1107 Hz and (h) 925 Hz. *Calculated* maximum and minimum voltages for each imposed frequency are shown as full lines.

sections whose average period coincides with the imposed frequency. As similarly carried out in Section 1.3.1, on each voltage-time trace are the *calculated* maximum and minimum voltages associated with the wall shear stress (via the calibration curve) subjected to near-Couette flows with the top surface mounted at δ and $(\delta + \delta_r)$, respectively, from the bottom stationary surface and moving at a local tangential velocity of $\omega \mathrm{r}_m$. The concurrence of the flat top and trough sections of the voltage-time traces with the *calculated* maximum and minimum voltages for case (f) - (h) therefore indicates that the hot-wire can respond fully to the frequency and the amplitude of the imposed fluctuating wall shear stress.

The next higher imposed frequency shown for f_{imp} =1678 Hz (case (e)) shows a marked absence of the flat top and trough sections of the voltage-time trace and whose resulting peak and trough voltages are unable to match the *calculated* voltages, although the average period of the waveform agrees well with the period of the imposed fluctuations. There is clear amplitude attenuation for the above case (e), and the same can be said for the other higher imposed frequencies depicted in Fig.(1.9) from cases (a) to (d). Figure 1.9 therefore suggests that the upper frequency limit whereby the hot-wire can respond fully to the imposed fluctuations is essentially constrained by the occurrence of amplitude attenuation.

Results of Fig.(1.9) are replotted in Fig.(1.10) in terms of the *calculated* and *measured* maximum and minimum wall shear stresses at each imposed frequency. The *measured* maximum and minimum wall shear stresses correspond via the calibration curve to the relatively flat top and trough portions of the voltage-time traces for the lower frequencies in cases (f) - (g), and the peak and trough voltages for the higher frequencies in cases (a) - (e), and others. These measured mean values are ensemble-averaged over many cycles. In the same Figure 1.10(a) are the *calculated* wall shear stress quantities as obtained from Eqns. (1.3) and (1.4) corresponding to the near-Couette flows with gap sizes of δ and $(\delta + \delta_r)$, respectively, and the top surface moving at a velocity of $\omega \mathrm{r}_m$. These are represented as solid lines which pass through the origin.

Shown in Figure 1.10(b) is the amplitude ratio of measured wall shear stress change (a_{mea}) to the imposed wall shear stress change (a_{imp}) for the determination of the dynamic response frequency (f_D), which corresponds to the onset of amplitude attenuation set at $\mathrm{a}_{mea}/\mathrm{a}_{imp} = 0.9$. This is similar to that used in Section 1.3.1 and in line with the experimental uncertainty of about 10% for $\mathrm{a}_{mea}/\mathrm{a}_{imp}$. It is apparent that for the flush-mounted hot-wire, f_D is 1545 Hz and the corresponding mean shear stress value (τ_D) is 0.64 N/m^2. It is logical to infer that at the same τ_D = 0.64 N/m^2, the flush-mounted hot-wire when subjected to a fluctuating wall shear stress with an imposed frequency of less than f_D = 1545 Hz will not exhibit any amplitude attenuation or at most limited to a damping value less than 10%.

Figure 1.10 also shows the respective results for the flush-mounted wire positioned at r_s and r_l (the voltage-time traces are not presented). The said figure clearly shows that f_D attains a value of 1240 Hz and a corresponding τ_D of 0.42 N/m^2 for the wire placed at the smaller radial position of r_s. At the larger radial position r_l, the wire registers a higher f_D of 1760 Hz, with a corresponding τ_D

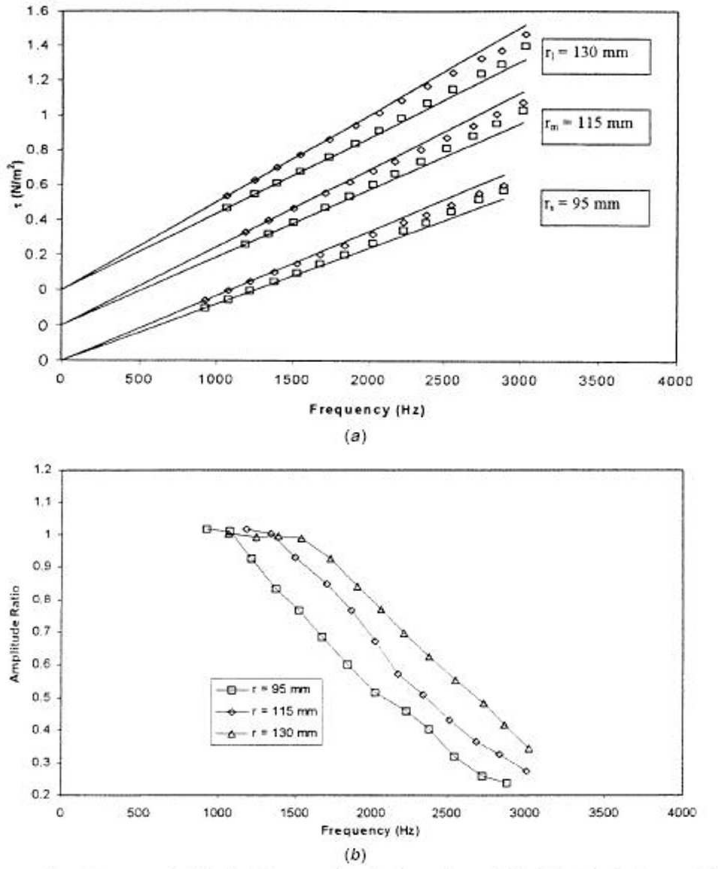

Figure 1.10: Comparison between calculated and measured wall shear stress obtained for the flush-mounted hot-wire gauge mounted at $r_s = 95$ mm, $r_m = 115$ mm and $r_l = 130$ mm for different rotation rates and $\delta = 300$ μm. Calculations are represented as full lines according to equation (1.4) with effective gaps given as δ and $(\delta + \delta_r)$. Experimental data: ($\Diamond$), ($\Box$) represent the maximum and minimum of wall shear stress fluctuations respectively. *(b)* Amplitude ratio, defined as a_{mea}/a_{imp}, for the flush-mounted hot-wire shear stress probe at $r_s = 95$ mm, $r_m = 115$ mm and $r_l = 130$ mm for different imposed frequencies.

of 0.82 N/m^2. The above results therefore suggest a trend of increasing f_D with greater imposed wall shear stress. Since a larger wall shear stress (and hence a larger velocity gradient) necessarily implies greater convective heat transfer from the hot-wire, the findings suggest a positive correlation between enhanced heat loss from the flush-mounted hot-wire and $f_{D,}$ which is a trend similarly observed for the dynamic response of an elevated hot-wire as discussed at length in Section 1.3.1.

1.3.2(c) The dynamic response (f_D) of the DANTEC-made 55R45 and 55R46

In reality, the above "flush-mounted" hot wires touching the perspex wall substrate are offset by 2.5 μm from the wire center to the wall and it is conceivable that (forced) convection remains the dominant mode of heat transfer as compared to conduction heat loss, since the region of contact with the wall substrate is rather limited. On the other hand, it would be interesting to determine the dynamic response of a flush-mounted hot film with the active element completely buried flush with the surrounding wall substrate. For the latter, it can be reckoned that conduction heat transfer is the dominant mode with secondary contribution from convective heat loss at the surface. In this respect, the commercially available DANTEC-made 55R45 and 55R46 wall shear stress gauges are selected; the former has a 0.5 μm quartz coating as opposed to the latter with a 2.0 μm quartz coating over the identical active hot element.

In the preliminary runs using the modified top disk with 100 recesses mounted at $\delta = 300\mu$m and rotating at only O(10) rpm, the 55R45 and 55R46 wall shear stress gauges placed at r_m exhibited great difficulties in following the amplitude of imposed wall shear stress fluctuations. In direct comparison to the experiments using the flush-mounted hot-wire under similar operating conditions where the hot-wire did not encounter any difficulty pertaining to amplitude attenuation until a much higher imposed frequency of 1545 Hz, it can be suggested that *relatively*, the hot-wire possesses better response characteristics than either the 55R45 or 55R46 shear stress probes. Because the apparatus is not designed for very low rotation rates, another modified top disk with only one recess of $\delta_r = 45$ μm was manufactured and employed to characterize the responsiveness of the hot-film wall shear stress gauge. The same gap size of $\delta = 300$ μm was maintained throughout. The imposed frequency is given as

$$f_{imp} = \frac{\omega}{2\pi}\,\mathrm{Hz}\,, \tag{1.9}$$

where ω is the angular velocity of the top disk in rad/s. With the 55R46 gauge mounted at r_m, the typical output voltage-time traces at different imposed frequencies show similar behaviour and salient features as those depicted for the flush-mounted hot-wire in Fig.(1.9) (except the timescale for the abscissa is several orders greater), and are thus not presented here. The results are expressed in terms of τ versus f_{imp} in Figure 1.11(a). Figure 1.11(b) shows the corresponding ratio of a_{mea} to a_{imp}, and it can be deduced that f_D assumes the value of 0.46 Hz

with $\tau_D = 0.02$ N/m^2. The results obtained for the same gauge mounted at radial positions r_s and r_l are also shown in the same figure. At the larger radial position of r_l, the 55R46 gauge exhibits a better response characteristic of $f_D = 0.59$ Hz, occurring at $\tau_D = 0.028$ N/m^2. On the other hand, the said gauge indicates $f_D = 0.41$ Hz at $\tau_D = 0.014$ N/m^2 when mounted at the smaller radial position r_s. From the above, the trend of f_D increasing with larger τ_D is discernibly similar to that found for the flush-mounted hot-wire. In other words, an increase in the convective heat transfer at the surface of the wall results in an improvement in the response characteristics of the flush-mounted 55R46 hot-film gauge.

The next series of tests is carried out for the 55R45 wall shear stress gauge mounted at r_s, r_m and r_l, and the corresponding results are plotted in Fig.(1.12). Figure 1.12(b) shows that f_D takes on the values of 0.63 Hz, 0.86 Hz and 1.15 Hz corresponding to τ_D of 0.022 N/m^2, 0.036 N/m^2 and 0.054 N/m^2, respectively. In general, the trend of increasing f_D with increasing τ_D is apparent for the 55R45 gauge, which bears resemblance in behaviour to the flush-mounted hot-wire and 55R46 gauges. It may be noted that under the same operating conditions for both the 55R45 and 55R46 gauges mounted at the same radial position, say r_m, when the imposed frequency is increased, the 55R46 gauge experiences amplitude attenuation first with $f_D = 0.46$ Hz, while the 55R45 gauge does not indicate any attenuation until a distinctly higher frequency, where $f_D = 0.86$ Hz. This observation, coupled with similar behaviour for the two gauges positioned at r_s and r_l, strongly suggests that the 55R45 gauge responds *relatively* better than the 55R46 gauge.

For purposes of further comparison, results for the dynamic response frequency of the three gauges are summarized and plotted in Fig.(1.13), where f_D is plotted against τ_D. The respective loci are traced through the data points corresponding to each gauge to indicate the trend of f_D with varying τ_D. The locus pertaining to the 55R45 gauge is always above that for the 55R46 gauge within the common range of τ shared by the 2 gauges, where the ratio of f_D for the 55R46 gauge to the 55R45 gauge averages out to be approximately 0.55. This implies that at the *same* τ, f_D for the 55R45 gauge is clearly superior to the 55R46 gauge. It may also be noted that for the same τ, the flow conditions above the two said gauges are identical. Because the 55R45 gauge has a thinner quartz substrate coating of only 0.5 μm, as compared to the 55R46 gauge which has a 2.0 μm quartz coating over the hot element of similar size, it can be construed that there is a correspondingly larger heat loss through the quartz coating to the flow for the 55R45 gauge, which resulted in a better response as characterized by f_D. This can be further explained in terms of the thermal resistance; the lower the thermal resistance of the wall substrate as for the case of the 55R45 gauge which has a thinner quartz coating, the better is the resultant response characteristic. This deduction about a more responsive flush-mounted hot film as a wall shear stress gauge resulting from larger heat loss from the active element is very similar to the conclusion arrived at in Section 1.3.1 for the marginally-elevated hot-wire as a probe for velocity measurements (where the response increases with increasing heat transfer irrespective of the origin).

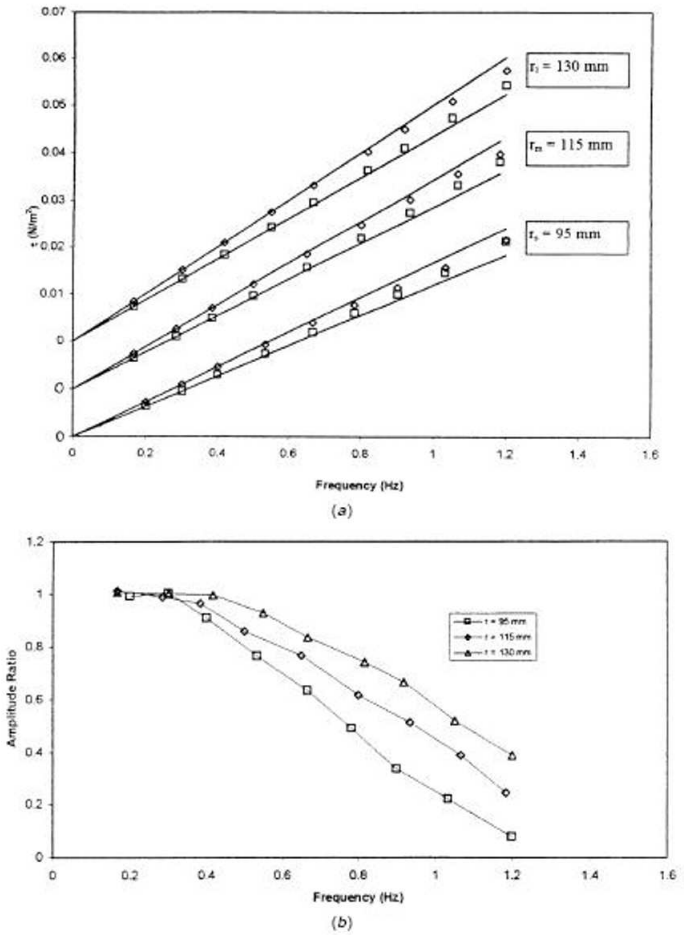

Figure 1.11: Comparison between calculated and measured wall shear stress obtained for the DANTEC 55R46 gauge mounted at r_s = 95 mm, r_m = 115 mm and r_l = 130 mm for different rotation rates and δ = 300 μm. Calculations are represented as full lines according to equation (1.4) with effective gaps given as δ and $(\delta + \delta_r)$. Experimental data: ($\Diamond$), ($\Box$) represent the maximum and minimum of wall shear stress fluctuations respectively. *(b)* Amplitude ratio, defined as a_{mea}/a_{imp}, for the DANTEC 55R46 gauge at r_s = 95 mm, r_m = 115 mm and r_l = 130 mm for different imposed frequencies.

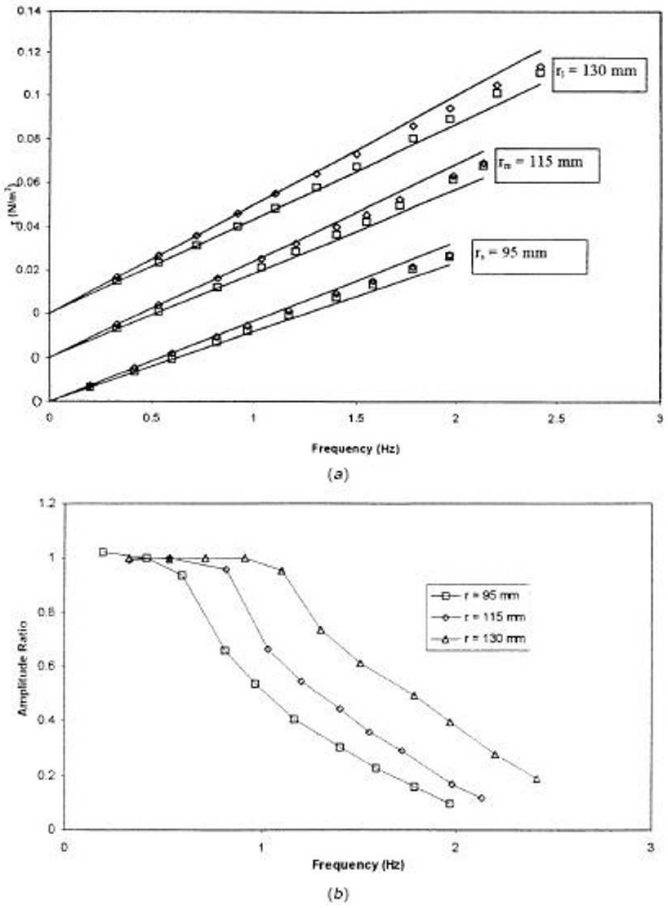

Figure 1.12: Comparison between calculated and measured wall shear stress obtained for the DANTEC 55R45 gauge mounted at r_s = 95 mm, r_m = 115 mm and r_l = 130 mm for different rotation rates and δ = 300 μm. Calculations are represented as full lines according to equation (1.4) with effective gaps given as δ and $(\delta + \delta_r)$. Experimental data: ($\Diamond$), ($\Box$) represent the maximum and minimum of wall shear stress fluctuations respectively. *(b)* Amplitude ratio, defined as a_{mea}/a_{imp}, for the DANTEC 55R45 gauge at r_s = 95 mm, r_m = 115 mm and r_l = 130 mm for different imposed frequencies.

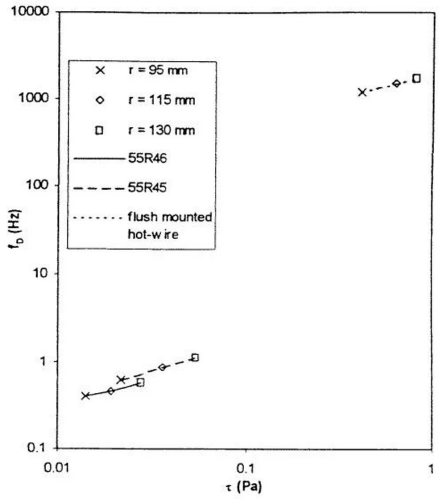

Figure 1.13: Dynamic response frequencies versus wall shear stress at onset of amplitude attenuation for the flush-mounted hot-wire wall shear stress gauge and the DANTEC 55R45 and 55R46 wall shear stress probes mounted at $r_s = 95$ mm, $r_m = 115$ mm and $r_l = 130$ mm.

If one is allowed to extrapolate the results for the flush-mounted hot-wire into the lower range of τ, common to the 55R45/55R46 gauges, it may be suggested that the performance of the former is still about two orders better than the latter two gauges at the same τ. Intuitively, it is conceivable that since the flush-mounted hot-wire is positioned almost in full contact with the convecting fluid, any changes in the flow velocity or velocity gradient at the wall will be felt almost instantaneously by the wire, with appropriate response from the CTA unit. For a flush-mounted hot film (like the 55R45 and 55R46 gauges) "buried" within the wall substrate, or even a hot-wire "buried" beneath the wall substrate, any variation in the flow conditions would probably be manifested only as a change in the boundary conditions on the top surface of the wall substrate for unsteady heat conduction to occur from the hot element linked to the CTA unit. For the latter, the thermal inertia of the wall substrate surrounding (and in full contact) with the active element would probably be featured prominently in the response characteristics of the flush-mounted hot film.

With conduction heat loss as the primary mode of heat transfer, the thermal conductivity of the surrounding substrate would also exact an influence on the response as observed for the 55R45 gauge vis-à-vis the 55R46 gauge which is diagnosed above. It can thus be postulated that the response of the said hot-film gauges would not be as fast as the flush-mounted hot-wire, where the dominant mode of heat loss is via direct (forced) convection. Indirect evidence is provided in

the work of Cook *et al.* (1988) where they found both the "buried" flush-wire and hot-film gauges exhibiting responses which lagged behind the imposed oscillating wall shear stress variations even at relatively low frequencies between 3 and 20 Hz. In fact, Cook *et al.* commented that the "buried" flush wire tended to yield a marginally larger magnitude of phase lag than the platinum film gauges. We may suggest that as the hot-wire is "buried" within the substrate, the dominant mode of heat loss becomes conduction, thus resulting in a behaviour which is very similar to that of a flush-mounted hot film. A full discourse of this subject can only be satisfactorily resolved with further work like a direct numerical simulation of an unsteady flow to examine the heat transfer from a hot element placed separately above and beneath the wall substrate and its relation to the ensuing response characteristics.

1.3.2(d) Further comparison of the responsiveness of the flush-mounted hot-wire wall shear stress gauge and DANTEC 55R45 and 55R46 wall shear stress gauges

Because of the inordinately vast difference in the dynamic response of the hot-wire and the hot-film (55R45 and 55R46) wall shear stress gauges, a further series of experiments were carried out to confirm qualitatively the difference in the response characteristics. The hot-wire was mounted at $r_m = 115$ mm on the bottom disk and diametrically opposite, the 55R46 was mounted at the same radial position. The top flat disk was placed at $\delta = 300\mu$m and made to rotate at 100 rpm for a period of time until the voltage outputs from both gauges indicated steady state condition (V_{ss}). The top disk was made to stop by turning off the power supply to the DC motor; due to the back emf induced in the motor, the disk stopped within about O(1) second. The respective non-dimensional voltage-time traces evaluated as

$$\bar{V}(t) = \frac{V(t) - V_o}{V_{ss} - V_o} \tag{1.10}$$

(where V_o is the voltage corresponding to the null state) from the Yokogawa-made (DL1540) digital oscilloscope are plotted in Fig.(1.14). Noting that the viscous action of the fluid medium (*i.e.* air) would require about $\delta^2/\nu \sim$ O(0.01 sec) for the flow within the gap to come to a halt, therefore the time lag of the flow field following the rotating disk motion is effectively immediate. From Fig.(1.14), the time required for $\bar{V}(t)$ to reach null state for the hot-wire wall shear stress gauge is about 1 second, hence implying a very fast response characteristic. More importantly, the comparison with the 55R46 gauge requiring up to about 160 seconds to reach the null state strongly suggests a qualitative time ratio of about two orders of magnitude, which is in broad agreement to that obtained by comparing the dynamic response frequencies.

Further tests were carried out under the same conditions but with the 55R46 gauge replaced by the 55R45 gauge. Since the voltage-time trace of the hot wire output is fairly repeatable, the later result is plotted staggered with the former result on Fig.(1.14) for comparison. It is apparent that the 55R45 gauge takes a shorter time of about 90 seconds to reach the null state after the rotating top disk

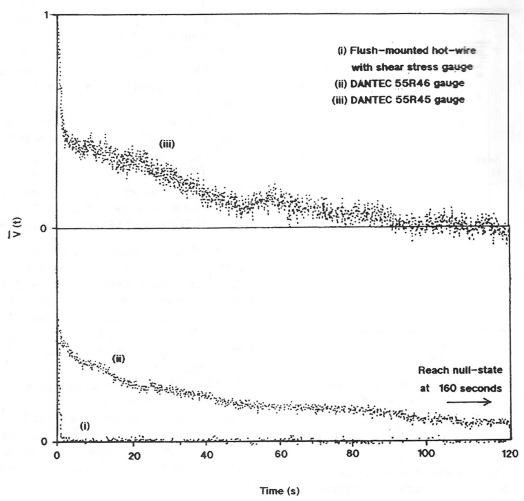

Figure 1.14: Dimensionless voltage-time trace for the flush-mounted hot-wire wall shear stress gauge and DANTEC 55R46 and DANTEC 55R45 gauges subjected to a sudden stoppage of the flat top disk rotating at 100 rpm.

comes to a halt, as compared to the 55R46 gauge. The ratio of the time interval required to reach null state for the 55R45 gauge, compared to the 55R46 gauge works out to be 0.56, which is in fair agreement with the ratio of the respective dynamic response frequencies of about 0.55. This test seeks to provide a qualitative yet independent check on the results obtained in the earlier sections on the dynamic response frequencies of the various wall shear stress gauges.

1.3.2(e) Concluding remarks for Section 1.3.2

Experiments were performed using a modified top rotating disk above a stationary bottom disk where different flush-mounted hot-element wall shear stress gauges were mounted, with the objective of determining the respective dynamic response frequency (f_D). It is found that the flush-mounted hot wire in contact with the wall substrate has a much higher frequency response of up to two orders of magnitude compared to the DANTEC-made 55R45 and 55R46 flush-mounted hot-film gauges. Despite its better performance, the f_D of the flush-mounted hot-wire is still discernibly lower than the marginally-elevated hot-wire used in near-wall velocity measurements as reported in Section 1.3.1. The perceived deterioration in the f_D for the flush-mounted hot-element wall shear stress gauge may have accounted for the relatively lower values of turbulence intensity and other higher order moments of wall shear stress fluctuations as observed by Cook (1994) for his three gauges compared to the equivalent near-wall velocity turbulence statistics extrapolated to the wall, as reported in Alfredsson *et al.* (1988).

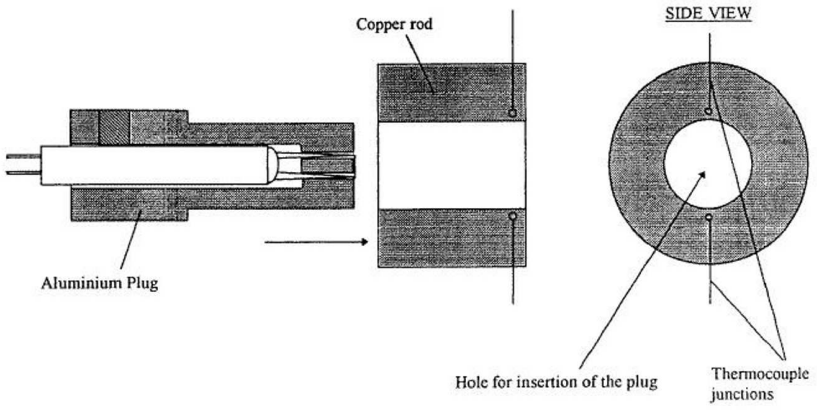

Figure 1.15: A schematic diagram of the plug and the copper sheath used in the square-wave test.

Further discourse on this Section 1.3.2 can be found in Chew *et al.* (1998b).

1.4 The dynamic response (f_D) vis-à-vis electronic perturbation test

The square-wave voltage perturbation test has been and may continue to be the preferred means from which the response of a hot-wire system can be determined in terms of the cut-off frequency. This can be partly attributed to the ease by which such a test can be carried out with any commercial CTA unit and abetted in no small way by the experimental difficulties encountered in carrying out a dynamic test. The latter invariably requires the imposition of a fluctuating velocity of sufficiently high known frequency and amplitude *directly* on the hot-wire so as to obtain the frequency response of the system.

One of the practical direct means incorporates the use of a high-frequency vibrating table with controllable frequency to which the hot-wire was attached. The latter, however, suffers from response problems associated with the vibration of the hot-wire relative to the prongs and the technique was quickly abandoned (Bellhouse & Rasmussen, 1968). Comte-Bellot (1977) employed radiative heating of the hot-wire or hot-film sensor using a sinusoidally amplitude- modulated laser beam from an Argon laser to quantify the frequency response of the sensor. Although the use of laser enables heating frequencies as high as 100 kHz, quantification of the amount of heating based on the output voltage of the anemometer is not so straightforward. The quantification of the amount of heating required is deemed necessary in determining whether the sensor has suffered from any (heat) amplitude attenuation. Another factor which has to be considered is that perturbations

in the heating of the sensor may not be strictly synonymous to perturbations in the flow velocity, and it is the latter which is of relevance in quantifying the dynamic response of a velocity-measuring probe.

It is the intention of this Section 1.4 to compare systematically the dynamic response of a near-wall hot-wire system as obtained from direct velocity perturbation with that shown by the usual voltage perturbation test, and to ascertain experimentally if these are similar in magnitude and trend. There are two main types of voltage perturbation tests, namely the square wave perturbation and the sine-wave perturbation; these will be studied in Sections 1.4.1 and 1.4.2, respectively.

1.4.1 Square wave perturbation test (f_S)

1.4.1(a) Square wave perturbation test (f_S) for the hot-wire and hot film: Some preliminaries

Initial trials were performed to determine if the placement of the marginally elevated hot-wire probe above the wall in various geometrical configurations, whether in the vertical, horizontal or upside down positions, will affect the frequency response as deduced from the square-wave test (f_S). It was found that there was no noticeable difference in the value of f_S which suggests that the effects of buoyancy and natural convection surrounding the active element are fairly negligible. In this respect, all subsequent tests were carried out with the hot element mounted above a horizontal wall.

The test configuration to study the effects of different wall temperature and imposed overheat ratio on f_S incorporates the use of the Aluminium plug. The plug was inserted into a through-hole previously drilled on a copper plate with two thermocouple junctions soldered to the inner radius of the copper annulus. The construction is illustrated in Fig.(1.15). Here the overheat ratio is defined conventionally as T_W/T_A, where T_W and T_A are the temperatures of the hot-wire and the surrounding ambient air, respectively. A heater with pre-adjusted temperature was brought into contact with the copper annulus and the steady state temperature registered by the thermocouple was taken to be the temperature of the Aluminium wall substrate to which the hot-wire was exposed. In the same way, by changing the wire temperature, different overheat ratios can be imposed to determine its influence on f_S for a given wall substrate temperature.

For measurements under mean flow conditions, the hot-wire was placed in the gap formed between a flat bottom stationary disk and a flat top disk rotating at an angular velocity ω. According to the analysis by Stewartson (1953), the flow

field in the gap is previously given in Section 1.2.1 and is repeated here as

$$\frac{v_\theta}{\omega r} = \left[\varepsilon - \left(\frac{\mathrm{Re}_\delta^2}{6300}\right)\left(8\varepsilon + 35\varepsilon^4 - 63\varepsilon^5 + 20\varepsilon^7\right) + O\left(\mathrm{Re}_\delta^4\right)\right], \tag{1.11}$$

$$\frac{v_r}{\omega r} = -\left[\left(\frac{\mathrm{Re}_\delta}{60}\right)\left(4\varepsilon + 9\varepsilon^2 + 5\varepsilon^4\right) + O\left(\mathrm{Re}_\delta^3\right)\right], \tag{1.12}$$

$$\frac{v_z}{\omega r} = 2\frac{\delta}{r}\left[\left(\frac{\mathrm{Re}_\delta}{60}\right)\left(2\varepsilon^2 - 3\varepsilon^3 + \varepsilon^5\right) + O\left(\mathrm{Re}_\delta^3\right)\right], \tag{1.13}$$

where (v_r, v_θ, v_z) are the velocities in the cylindrical (r, θ, z) coordinate system, ε ($\equiv z/\delta$) is the non-dimensional vertical coordinate normalised using the gap spacing (δ) between the two disks and measured from the stationary bottom disk, and Re_δ ($\equiv \omega\delta^2/\nu$) is the flow Reynolds number. By keeping Re_δ small ($\mathrm{Re}_\delta << 1$), the flow approaches a Couette-like flow in the azimuthal direction. This feature was further substantiated by Khoo *et al.* (1998b) using DNS (direct numerical simulation) and used in the previous experimental works of Khoo *et al.* (1995), Chew *et al.* (1994) and Brown & Davey (1971) for purpose of near-wall hot-wire calibration. In our application, the hot-wire is subjected to different imposed mean velocities by rotating the top disk at different angular velocities. For all the runs, the hot-wire was connected to a DANTEC 56C01 CTA unit. The output from the latter was fed into a YOKOGAWA model DL1540 digital oscilloscope for monitoring and recording the response of the hot-wire subjected to a square-wave voltage perturbation input. The same CTA unit was used in Section 1.3.1. Adjustment was made to the CTA unit until a "marginally flat low-frequency response as well as the highest cut-off frequency" (Freymuth, 1977) as depicted in Fig.(1.16) was obtained. Here, τ_S is the optimum (minimum) time interval for the pulse (with some 13-15% undershoot w.r.t. the maximum) to decay to 3% of the maximum value as advocated by Freymuth (1977). Freymuth suggested that the frequency response (f_S) of the optimised hot-wire system (-3 dB point) is given by

$$f_S = \frac{1}{1.3\,\tau_S}\,. \tag{1.14}$$

The expression was used by Freymuth & Fingerson (1977) in their evaluation of the overall hot-wire response subjected to different free-stream convective velocities for eventual comparison to cylindrical hot-film probes. It may also be noted that DANTEC suggested a rather similar procedure for tuning and optimising the CTA unit w.r.t. the hot-wire probe although no mention was made about the evaluation of the associated frequency response.

For operation of the flush-mounted hot-film used as wall shear stress probe, (specifically the DANTEC-made 55R45 and 55R46), the manufacturer recommended a lower overheat ratio compared to the hot-wire. In this case it was set at 1.4, similar to that used in the velocity/flow perturbation experiments of Section 1.3.2. The hot- film probe was mounted in the rotating disk apparatus where the presence of a Couette flow in the azimuthal direction necessarily prescribed the associated velocity gradient and hence the imposed wall shear stress. The hot-film

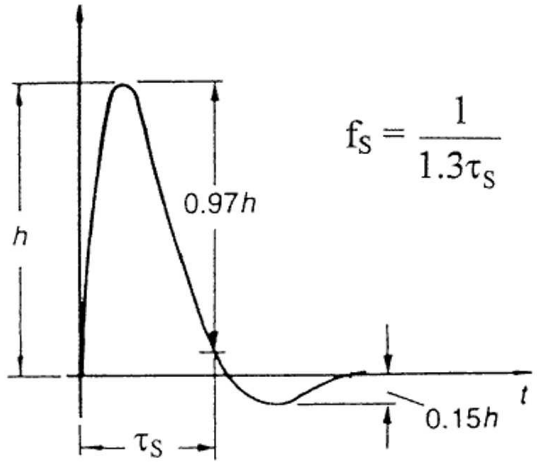

Figure 1.16: The square-wave-test frequency-response estimate for hot-wire sensors; from Brunn (1995).

probe was then connected to the same 56C01 CTA unit used in Section 1.3.2 and subjected to a square-wave voltage perturbation test. The output from the CTA was viewed using the YOKOGAWA made digital oscilloscope. When properly adjusted for optimum operation, the typical voltage-time trace is shown in Fig.(1.17) where f_S (the response frequency using the -3 dB point criteria) is nominally given as

$$f_S \approx \frac{1}{\tau_S}\,, \tag{1.15}$$

which is obtained empirically by Freymuth & Fingerson and subsequently substantiated by Freymuth (1981) (see also Bruun, 1995). Here, τ_S corresponds to the time interval at the voltage level "midway between the minimum and maximum of the resonance" after the initial peak as reckoned by Freymuth (1981); in Moen & Schneider (1993, 1994), τ_S is evaluated as the time interval from the voltage rise till the first minimum and the difference is not expected to be very significant and limited to about 10% variation. Huang *et al.* (1995) used the same definition for τ_S as Moen & Schneider, but instead modified the expression for the cut-off frequency to $f_S = 1/(1.5\tau_S)$.

One feature worth noting is the presence of the "tail" in the voltage-time trace after the resonance which is effectively absent in the typical optimised hot-wire response. This has been attributed to unsteady conduction heat loss to the wall substrate (*e.g.* see Davis, 1970) although, as seen above in Moen & Schneider and Huang *et al.* and many others like Kreplin & Eckelmann (1979), its effect is routinely disregarded by researchers in the evaluation of f_S without any explanation. Cook & Giddings (1988) have also commented that "indeed, time-

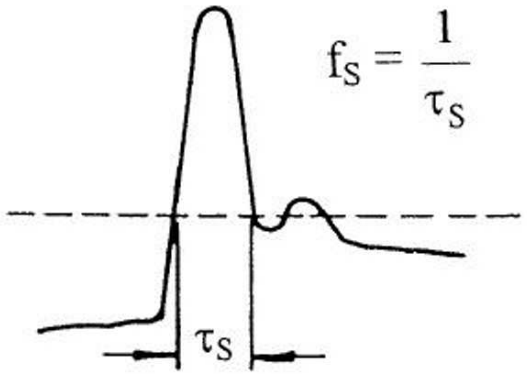

Figure 1.17: The square-wave-test frequency-response estimate for hot-film sensors; from Brunn (1995). See also Freymuth and Fingerson (1977).

dependent heat conduction in the substrate appears to be an important factor in gauge response" in their study of the response of hot-element wall shear stress gauges in laminar oscillating flow. In this Section 1.4.1, we shall primarily adopt this widely accepted practice of evaluating f_S (*i.e.* Fig.(1.17) and Eq.(1.15)) since it also provides an avenue for comparison to published works. However, for purpose of further qualitative comparison, we shall also evaluate $(f_S)_{withtail}$ taking into account the tail end response of the hot film. Because of the large experimental uncertainty incurred in determining the exact time taken for the output voltage to reach the null state due to the nature of the asymptotic decay, it is suggested that the time interval $(\tau_S)_{withtail}$ corresponding to the state when the output voltage has decreased to 10% of the maximum value be used for evaluation of $(f_S)_{withtail}$ in conjunction with Eq.(1.15). It may be noted in Moen & Schneider (1994) where the square-wave tests were carried out for their flush-mounted hot-film sensors, it was mentioned that the characteristic "tail" in the output voltage is due to "high-order behaviour observed in the system; the voltage did return before the beginning of the next square-wave however".

1.4.1(b) f_S for the near-wall hot-wire at different heights

Under conditions of forced convection where a known mean velocity (V) is imposed on the marginally-elevated hot-wire, the frequency response to a square-wave perturbation is obtained for different V and wire elevations. (The overheat ratio was set at 1.8 throughout, similar to the velocity perturbation experiments of Section 1.3.1.) The results are shown in Figure 1.18(a) with the wire height expressed non-dimensionally in wall units (h^+) for the abscissa.

For any given wire's physical height above the Perspex wall substrate, it is apparent that as V increases, f_S increases monotonically. This implies that as

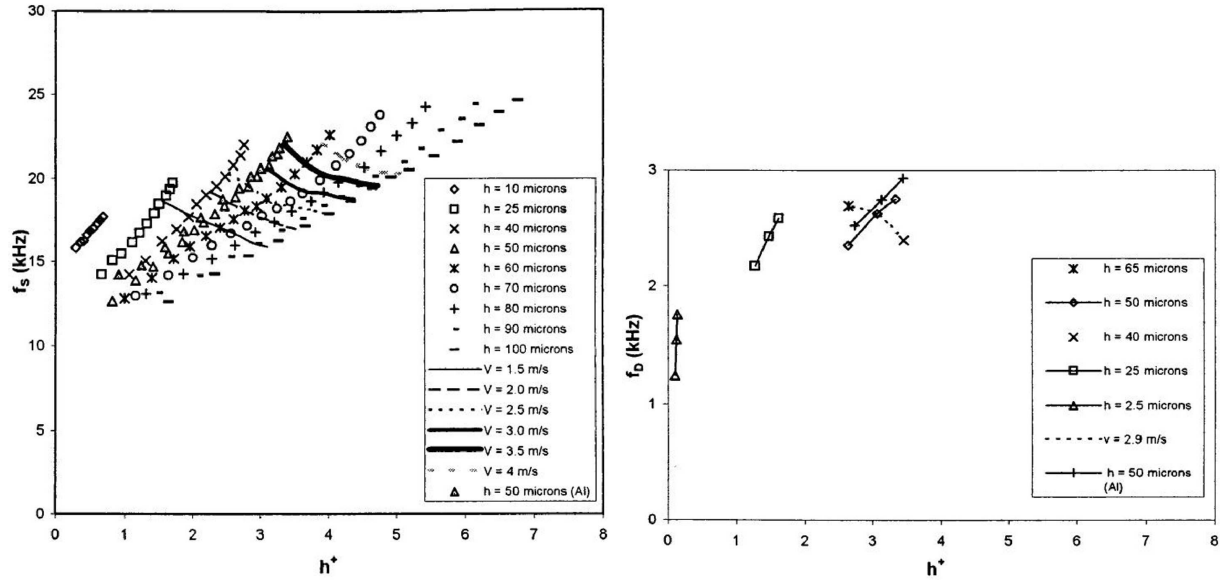

(a) (b)

Figure 1.18: The square-wave frequency response f_S of a hot-wire mounted at various heights h above Perspex and aluminium wall substrates subjected to a tangetial convective velocity V plotted against dimensionless wall units h^+. The overheating ratio of the hot-wire is 1.8 and the nominal wall temperature is 24°C. *(b)* A semi-dimensionless plot of the dynamic frequency response f_D for various values of h^+ for marginally elevated hot-wires placed above Perspex and aluminium wall substrates.

the (forced) convective heat transfer from the wire becomes larger, the response characteristics in terms of f_S becomes better. This trend is consistent with the results provided by Freymuth and Fingerson (1977) for their hot-wire placed under free stream conditions where an increase in velocity from 0 to 9.1 m/s (30 ft/s) to 91.4 m/s (300 ft/s) is accompanied by a continuous improvement in f_S. Although Moen & Schneider (1994) only obtained f_S for their hot-film sensors in stagnant air, their final remark that "the steady flow that exists prior to the perturbation is likely to offset the results in a significant manner" attest to the importance of forced convection. Conventionally, the effect of wall influence on hot-wire operation is indicated by the dimensionless variable h^+ as can be deduced from works on wall proximity correction for hot-wire measurements (see Bhatia *et al.*, 1982; Hebbar, 1980 and Khoo *et al.*, 1996). These works show that the wall influence on near-wall hot-wire operation increases with smaller h^+, hence requiring a large correction factor. By keeping h^+ fixed, (*i.e.* similar wall effect on the wires), the increase in f_S with increasing V in Figure 1.18(a) necessarily implies that an enhanced forced convection leads to an improvement in f_S, all other factors being equal.

When some of the results in Figure 1.18(a) are presented in Table 1.1 for a given typical mean flow velocity of 3.0 m/s with wire's height decreasing from 100 μm to 50 μm (equivalent to a change of h^+ from 4.37 to 3.09), f_S shows a discernible and continuous increase from 18.76 kHz to 20.63 kHz. Using the argument that the nominal heat transfer from the hot wire due to forced convection is directly related to the mean convective velocity which is kept constant, it is reasonable to suggest that the increase in f_S with decreasing h^+ can be attributed directly to the increase in wall effect with accompanying greater heat loss from the wire to its surroundings (see also Chew *et al.*, 1995, for a discourse on the effect of wall influence on h^+ behaviour and its relation to additional heat loss to the flow and nearby wall substrate.) Shown correspondingly in Figure 1.18(a) is the locus of constant convective velocity at 3.0 m/s. Other loci of constant velocity ranging from 1.5 m/s to 4 m/s are also provided which clearly indicate the distinctive trend of increasing f_S with decreasing h^+ hence further attesting to the above suggestion. In Figure 1.18(a), the results for a hot-wire mounted at h = 50 μm above an Aluminium wall substrate are provided for further comparison to its counterpart mounted above a Perspex wall substrate at the same wire height. At the same h^+, the effect of wall influence pertaining to the Aluminium substrate on hot-wire operation is greater than the thermally less conducting Perspex substrate. This has effectively resulted in a higher f_S for the former in full accord with the above suggestion.

It is equally interesting to note from Figure 1.18(a) that an increase in V for a wire of fixed height, which translates directly into increasing h^+, has a trend of increasing f_S as noted earlier. This characteristic is irrespective of the adjacent wall substrate material. It can therefore be further argued that the effect of an increase in V with larger convective heat transfer must be sufficiently overwhelming to shadow the effect of decreasing wall effect (or increasing h^+) with the consequential result of increasing f_S. As noted earlier, decreasing wall effect or heat loss to the wall leads to a decrease in f_S. A discussion of the results displayed in Figure

Table 1.1: A comparison of the square-wave-test frequency-response f_S for hot-wires mounted at various heights from a Perspex wall substrate with the same imposed mean flow velocity of 3 m s^{-1}.

Physical height of the hot-wire from wall substrate h (μm)	Height of hot-wire in terms of dimensionless wall units h^+	Square-wave frequency response (kHz) $f_S = 1/(1.3\tau_S)$
50	3.09	20.63
60	3.39	19.76
70	3.66	19.24
80	3.91	19.14
90	4.15	18.87
100	4.37	18.76

1.18(b) will be deferred till Section 1.4.1(d).

The main conclusion drawn is that f_S increases with greater heat transfer from the hot-wire, and this is irrespective of whether it is due to forced/natural convection or effects of wall influence. It may be mentioned that in a given flow, the placement of a hot-wire closer to the wall will necessarily see its response (f_S) decrease due to a decrease in the convective velocity in the near-wall region. This effect will be mitigated to some extent by the increase in heat transfer from the wire due to increasing wall effect.

1.4.1(c) f_D for flush-mounted hot-wire and hot-film wall shear stress probes

The typical response of a hot-wire after optimization is shown in Fig.(1.16). As the hot-wire is lowered until contact is made with the Perspex wall substrate, the optimized response output as depicted in Fig.(1.19) still bears close resemblance to Fig.(1.16) and hence f_S is still evaluated according to Eq.(1.14).

The response characteristics of the "flush-mounted" hot-wire subjected to different flow conditions as indicated by the variation in the imposed wall shear stress (τ) at the wall is shown in Figure 1.20(a). (Whereas for an elevated hot-wire, the amount of forced convection and its influence on f_S is measured by the convecting velocity, in this case an equivalent indicator is the wall shear stress.) Again, the overheat ratio was maintained at 1.8, similar to the direct flow perturbation experiments in Section 1.3.2. Figure 1.20(a) shows explicitly that as τ increases, f_S increases monotonically. This is perhaps not surprising in view that a larger f_S associated with increasing convective heat loss from the flush-mounted hot-wire as τ increases is consistent with our results for the elevated hot-wire. The range of f_S experienced by our flush-mounted hot-wire is in the same order of magnitude as that estimated by Shah & Antonia (1987), who reported a frequency response of 25 kHz for their 5 μm Wollaston wire mounted in contact with a Perspex wall.

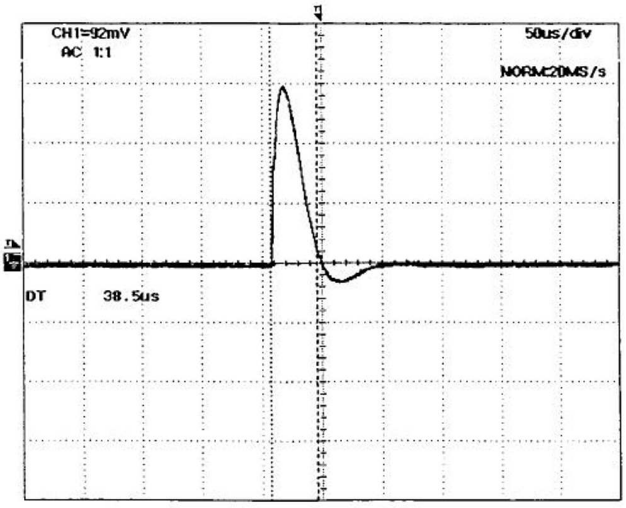

Figure 1.19: The output waveform for a flush-mounted hot-wire wall shear-stress probe subjected to a square-wave voltage-pertubation test at an imposed wall shear stress of 1.34 N m^{-2}.

It was not reported, however, whether Shah & Antonia had used the factor of 1.3 in the evaluation of f_S nor was it mentioned whether the test was carried out with the hot wire subjected to a mean flow. The observed differences can also be attributed directly to the instrumentation employed, *i.e.* the use of different types of hot-wire and CTA units.

Unlike the output waveform for an optimised hot-wire where the decay to null state is fairly rapid, the typical response for an optimised hot-film wall shear stress probe (DANTEC 55R45 and 55R46) is shown in Fig.(1.21) for stagnant air.

Evaluating τ_S according to the definition depicted in Fig.(1.17) and Equation (1.15) gives f_S = 595 kHz and 538 kHz for 55R45 and 55R46, respectively. If one, however, measures the time constant associated with the "tail" of the output voltage (see Section 1.4.1(a)), the 55R45 probe takes a relatively longer time of about 0.14 ms ($\pm$10%) while the 55R46 probe requires an even larger period of about 0.26 ms ($\pm$5%). These are equivalent to $(f_S)_{withtail} \approx$ 7.1 kHz and 3.8 kHz, respectively, assuming the validity of Eq.(1.15). The latter calculations should only be viewed as a broad indicator incorporating the "tail" of the output voltage-time trace which has often been associated with continual heat loss to the surrounding wall substrate (see Davis, 1970) or other "higher order behaviour observed in the system" (Moen & Schneider, 1994). Shown in Figure 1.20(a) is the variation of f_S (with and without "tail") against the imposed wall shear stress (τ) for the wall shear stress probes. Within the range of τ investigated, it is apparent that both f_S and $(f_S)_{withtail}$ are rather independent of the prevailing wall shear stress. A similar

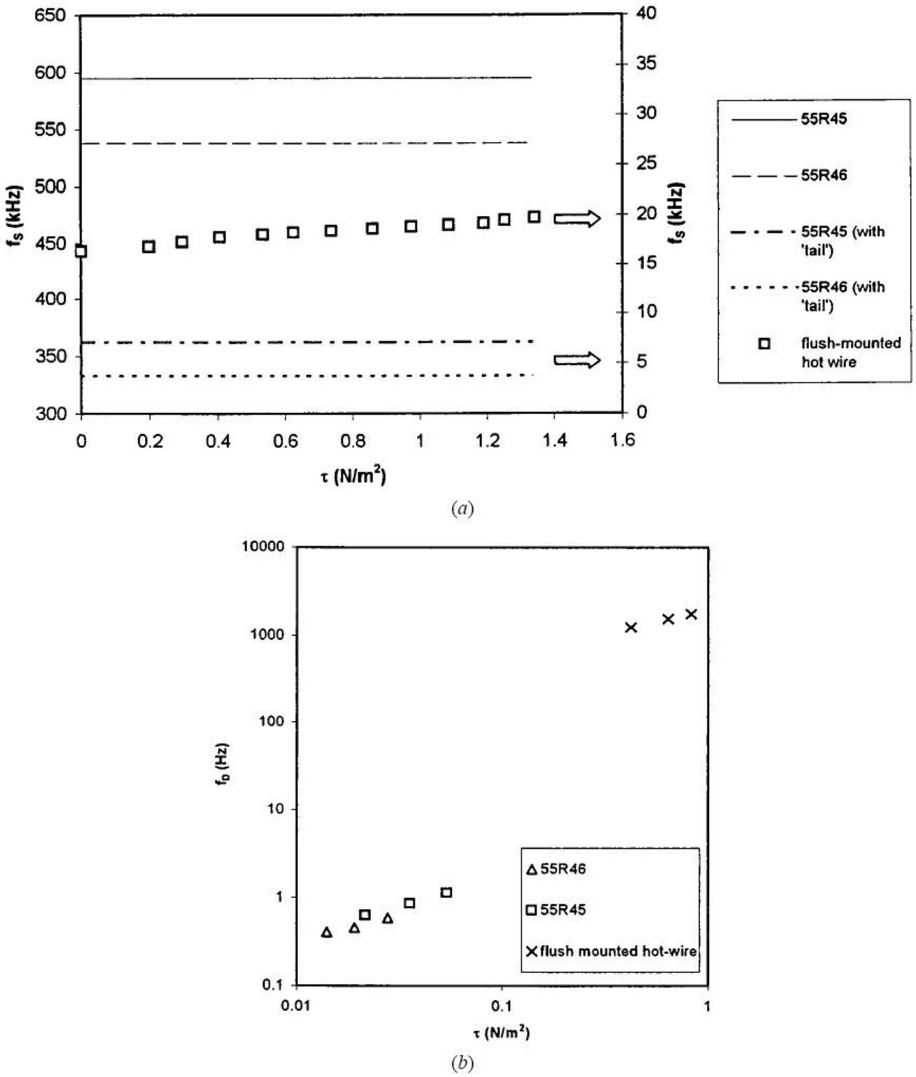

Figure 1.20: The square-wave frequency response f_S for a flush-mounted hot-wire wall shear-stress gauge and for commercially available DANTEC 55R45 and 55R46 hot-film wall shear-stress gauges subjected to various values of the wall shear stress τ. *(b)* The dynamic frequency response f_D for a flush-mounted hot-wire wall shear-stress gauge and for DANTEC 55R45 and 55R46 wall shear-stress probes subjected to various values of the wall shear stress τ.

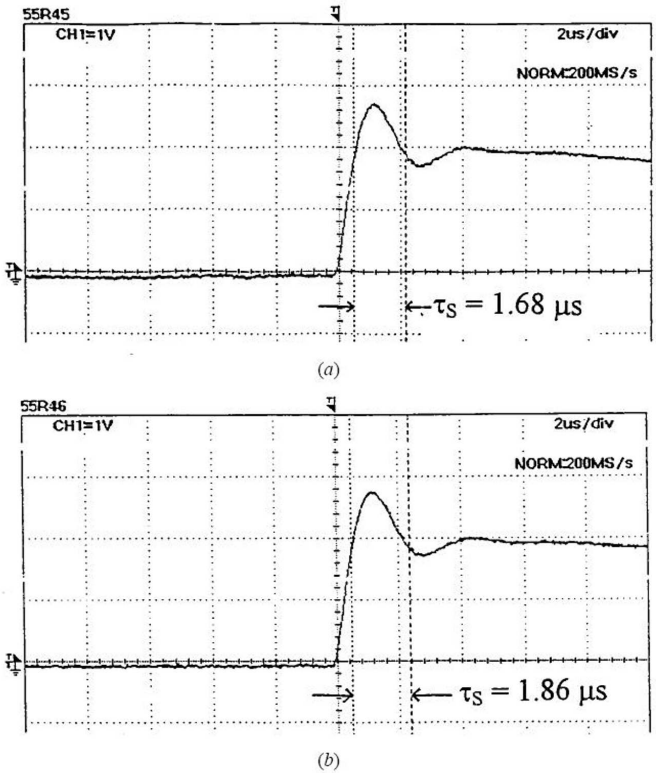

Figure 1.21: The output waveform of the DANTEC 55R45 hot-film wall shear-stress probe subjected to a square-wave voltage-pertubation test in stagnant air. *(b)* The output waveform of the Dantec 55R46 hot-film wall shear-stress probe subjected to a square-wave voltage-pertubation test in stagnant air.

observation was reported by Kreplin & Eckelmann (1979), who noted that their quartz-coated DISA 55A93 flush-mounted hot-film wall shear stress gauge (predecessor to the 55R45 probe) exhibited a square-wave frequency response which remained constant with or without a flow. Regardless of the criterion used to establish f_S, the 55R45 model indicates a better response than the 55R46 counterpart. Since the 55R45 gauge has a thinner top surface quartz coating compared to the 55R46 gauge, it can be construed that the former whose active element is in the midst of a thermally more conducting surroundings, hence experiencing a relatively larger overall heat transfer has given rise to the observed behaviour. This trend is consistent with the findings reported by Huang *et al.* (1995) and Moen & Schneider (1993) that the respective hot-film element mounted on a thermally more conducting substrate material has exhibited better response characteristics in terms of f_S.

1.4.1(d) Comparison of f_S and f_D

(i) Marginally elevated hot-wire velocity probe

Results of the velocity perturbation tests in Section 1.3.1 are reproduced in Figure 1.18(b) as f_D versus h^+. For purpose of completeness, some of the salient features are discussed below. At the same wire height of h = 25 μm or 50 μm above the Perspex wall substrate, an increase in the convective velocity (with an accompanying increase in h^+) results in a continual rise in f_D. This trend bears close resemblance to that observed for the square-wave voltage perturbation test. In Section 1.3.1, it was suggested that the increase in convective heat transfer for the elevated hot-wire has given rise to an improvement in f_D which is identical to the suggestion put forth for the behaviour in f_S (see Section 1.4.1(b)). From Figure 1.18(b), it can be further observed that for the hot-wire set at different heights above the wall substrate, but exposed to the same convective velocity of V = 2.9 m/s (thereby implying similar nominal convective heat loss), the wire mounted at 40 μm exhibits a higher f_D compared to that at 50 μm, followed by the lowest value of f_D registered at h = 65 μm. The wire's height in terms of wall units indicates that f_D increases with decreasing h^+. This suggests that an increase in wall effect with greater heat transfer from the wire due to localised aerodynamic interference of the flow around the wire w.r.t. the nearby wall has resulted in better response characteristics of the hot-wire expressed in terms of f_D.

The results of square-wave voltage perturbation test have also indicated a remarkably similar behaviour for f_S (see Table 1.1 and Section 1.4.1(b)). At the same $h^+ = 2.6$ (Figure 1.18(b)), which can be constructed as having similar level of wall influence for the wires mounted at h = 40 μm and 50 μm above the Perspex wall substrate, the wire at the lower height with higher prevailing convective velocity has seen an improvement in f_D. The said f_D increases from 2345 Hz to about 2750 Hz. Similar behaviour for f_S is apparent from Figure 1.18(a). The increase in convective heat transfer from the wire at the same h^+ (with similar wall effect) has therefore enabled an improvement in the response characteristics of the hot-wire whether evaluated in terms of f_S or f_D.

Generally, the results from the velocity perturbation test which gives rise to f_D have indicated very similar behaviour to f_S in terms of trends. An increase in heat transfer from the wire, whether due to convective heat loss or to increasing wall influence, results in an improvement in both f_S and f_D. The effect of wall influence is further exemplified from the results of the hot-wire placed at h = 50 μm above the Aluminium wall substrate for comparison to its counterpart above the Perspex wall substrate. Both the trends of f_S and f_D indicate better performance at the same h^+ for which the wall effect pertaining to the Aluminium wall substrate is obviously higher.

The finding of similar trend in the behaviour of f_S and f_D may lull us into the possible belief that the square-wave voltage perturbation and velocity perturbation

tests are equivalent. Therefore, it is timely and important to make a quantitative comparison too. Presented in Tables 1.2 and 1.3 are the respective values of f_S and f_D obtained under identical parametric conditions. Because the hot-wire used in conjunction with the CTA unit is the same, possible contributory factors such as equipment employed which may account for the differences in the results of f_S and f_D can be effectively ruled out.

Table 1.2 shows the comparison for the cases of a hot-wire mounted at different heights of h = 25 μm and 50 μm above both the Perspex and the Aluminium wall substrates with varying convective velocities, and Table 1.3 presents the results for different values of h with the convective velocity kept fixed at 2.9 m/s. Although Tables 1.2 and 1.3 depict similar trends for f_S and f_D, there is a great difference in the absolute magnitude for the corresponding cases. The ratio of f_S to f_D for the respective cases is generally in the region of an order of magnitude. There must be some fundamental differences between the square-wave voltage perturbation and the velocity perturbation tests. Further discussion on the possible causes is deferred to Section 1.4.1(e).

(ii) Flush-mounted hot-wire as wall shear stress probe

By lowering the height of the hot-wire until contact was made with the Perspex wall substrate, the flush-mounted hot-wire was used as a wall shear stress probe. The modified rotating disk apparatus of Section 1.3.1 was employed to generate two known quantities of fluctuating wall shear stress for the purpose of obtaining the associated dynamic response frequency (f_D) in Section 1.3.2. The results are reproduced in Figure 1.20(b). With the imposed wall shear stress increasing from 0.42 N/m^2 to 0.82 N/m^2, f_D assumes a continuous and perceptible improvement from 1.2 kHz to 1.8 kHz. This behaviour has the same trend as that discerned for f_S (see Figure 1.20(a)).

Despite the similarities between the observed trend for f_D and f_S, it is equally important to compare the absolute magnitude of frequency. Results of the frequency are tabulated in Table 1.4 for similar parametric conditions of imposed τ. It is clear that f_S is much larger than f_D with a ratio of at least an order of magnitude for the corresponding cases. The large difference in magnitude observed justifiably raises the issue of the equivalence between f_S and f_D, of which further discussion on the subject is deferred to Section 1.4.1(e).

(iii) Hot-film wall shear stress probes: DANTEC 55R45 and 55R46

Results of the dynamic response frequency (f_D) as in Section 1.3.2 for DANTEC 55R45 and 55R46 are shown in Figure 1.20(b). The feature of better frequency response for the 55R45 gauge as compared to the 55R46 gauge when measured in terms of f_S is replicated for the f_D characteristic. Upon comparing the magnitudes of f_S and f_D, Table 1.4 shows that f_S is at least up to 5 orders of magnitude greater than f_D. (The ratio of $(f_S)_{withtail}$ to f_D is still 3 orders of magnitude or more.) It is thus timely to examine carefully the implications of the frequency responses f_S

Table 1.2: A comparison of the dynamic frequency-response (f_D) and the square-wave frequency response (f_S) for hot-wires mounted at the same height above the wall substrate.

Material	Physical height of the hot-wire above wall substrate h (μm)	Dimensionless height h^+	Dynamic frequency response f_D (kHz)	Square-wave frequency response (kHz) $f_S = 1/(1.3\tau_S)$	Velocity (m s^{-1})
Perspex	25	1.26	2.17	15.66	1.00
	25	1.47	2.42	17.45	1.36
	25	1.61	2.58	19.14	1.63
	50	2.63	2.35	18.92	2.17
	50	3.06	2.63	20.52	2.94
	50	3.33	2.75	21.97	3.48
Aluminium	50	2.73	2.52	18.4	2.33
	50	3.13	2.74	20.89	3.07
	50	3.44	2.93	24.25	3.71

Table 1.3: A comparison of the dynamic frequency response (f_D) and the square-wave frequency response (f_S) for hot-wires mounted at various heights above the Perspex wall substrate subjected to the same convective velocity of 2.9 m s^{-1}.

Physical height of the hot-wire above wall substrate h (μm)	Dimensionless height h^+	Dynamic frequency response f_D (kHz)	Square-wave frequency response $f_S = 1/(1.3\tau_S)$ (kHz)
40	2.72	2.69	21.57
50	3.04	2.63	20.45
65	3.47	2.39	19.91

Table 1.4: A comparison of the dynamic frequency-response (f_D) and the square-wave frequency response (f_S) for the flush-mounted hot-wire wall shear-stress probe and the DANTEC 55R45 and 55R46 hot-film wall shear-stress probes.

Probe	Dynamic frequency response f_D (kHz)	Square-wave frequency response f_S (kHz)	Shear stress (N m^{-2})
Flush-mounted hot-wire	1.24	17.78	0.42
	1.545	18.28	0.64
	1.760	18.56	0.82
55R45	0.000 63	595	0.022
	0.000 83	595	0.036
	0.001 15	595	0.054
55R46	0,000 41	538	0.014
	0,000 46	538	0.019
	0,000 59	538	0.028

and f_D, which constitutes the subject of discussion in the following section.

1.4.1(e) Plausible inherent differences between f_S and f_D

Freymuth (1977) carried out an analysis of the constant temperature hot-wire anemometer in an effort to study the frequency response and associated electronic testing. After linearizing the governing equations, and assuming that there are only small deviations of u (output voltage), r (resistance of hot-wire) and v (forced convection velocity at the wire's location) from the steady state operating conditions of U, R and V, respectively, the dynamic (response) equation becomes

$$\frac{MM"}{G}\frac{d^3u}{dt^3} + M_y\frac{d^2u}{dt^2} + M_x\frac{du}{dt} + u = Sv + M_z\left(\frac{\gamma U_t}{c/H} + \frac{dU_t}{dt}\right). \tag{1.16}$$

Here M"is a constant pertaining to the amplifier, G is the amplifier gain, γ is a function of the resistance in the bridge, c is the thermal inertia of the wire, H(V) is a heat transfer function dependent on the flow velocity which accounts for convective heat loss from the wire to the surroundings, and (M, M_x, M_y, and M_z) are further functions of the electrical resistances, G, M"and H(V). S is the sensitivity of the anemometer and simplifies to

$$S \approx \frac{U_0}{2}\frac{1}{H}\frac{dH(V)}{dV}, \tag{1.17}$$

where U_0 is dependent on the resistances in the anemometer, the temperature coefficient of resistance of the wire α and the heat transfer function H(V). The first source term on the RHS of Eq.(1.16) represents the (small) velocity v perturbation effect while the second term accounts for the input electronic test signal U_t. It is interesting to note from Eq.(1.16) that for purely electronic testing utilising square-wave voltage perturbations as input (*i.e.* setting v = 0), the cut-off frequency (f_S) is as much a function of the prevailing convective velocity as verified by the results in Section 1.4.1(b). In the present application of the hot-wire mounted close to the wall, H(V) is also likely to be dependent on the nearby wall substrate thermal conductivity. It is thus not surprising that the findings in Section 1.4.1(b) show that f_S is indeed influenced by the wall substrate material. (In this analysis, we have assumed Eq.(1.16) as derived by Freymuth for a wall remote hot-wire in a freestream to be equally valid for near-wall applications by interpreting H(V) as the overall heat transfer function responsible for heat loss from the wire to the surroundings. In this respect, the said equation may still be used to elucidate the main physics for a flush-mounted hot-wire.) Therefore, it is important to realise that f_S does not just measure the response of the electronic system per se without consideration of the actual hot-wire operation.

A careful examination of Eq.(1.16) reveals that both the velocity and electronic perturbation tests routinely introduced to determine the response characteristic of the system, can be considered as separate source terms which appear on the RHS of the equation. The respective source terms are quite different in form

and composition with S encompassing the derivative of H(V) w.r.t. V and which governs the velocity perturbation test unique to the first term. In the different perturbation tests, one can be considered to be solving for u to obtain the overall time characteristic with the appropriate source term. If Eq.(1.16) is assumed to be linear with the coefficients on the LHS independent of u and the coefficients of v and U_t on the RHS independent of time, classical control theory (*e.g.* Ogata, 1990) reveals that the frequency response of the system depends only on the coefficients on the LHS This in turn affects the location of the poles in the transfer functions relating u to v and U_t. Freymuth (1977) considered the two source terms on the RHS of Eq.(1.16) separately, and obtained two dimensionless equations governing the anemometer's response to velocity and electronic testing, respectively. As the coefficients on the LHS are exactly the same, it is thus not surprising that the cut-off frequency deduced from both perturbation tests are identical, although Freymuth did not explicitly state the equivalence of the two tests. If, on the other hand, the coefficients of v (*i.e.* S) and U_t, which are functions of H(V) are somehow dependent on the imposed frequency of velocity perturbations (see also Guo & Hyung 1997), then the respective source terms on the RHS of Eq.(1.16) must be solved separately together with the LHS to obtain the associated response of the overall system. Furthermore, since S is uniquely dependent on dH/dV, it is very unlikely that the introduction of additional poles and zeros into the transfer function relating u and v will be identical to the overall transfer function relating u and U_t. As a consequence, both perturbation tests will yield entirely different cut-off frequencies.

Freymuth (1978) carried out a similar analysis of the cylindrical hot-film sensor for use under free stream conditions. The equivalent response equation is given as

$$u\left[1+M_x\omega_c\left(\frac{p}{\omega_c}\right)^{1/2}+M_y\omega_c^2\left(\frac{p}{\omega_c}\right)^{3/2}+\frac{MM"}{G}\omega_c^3\left(\frac{p}{\omega_c}\right)^{5/2}\right] = Sv+M_zU_t\left[\frac{\gamma}{c/H}+\omega_c\left(\frac{p}{\omega_c}\right)^{1/2}\right], \tag{1.18}$$

which is a $2\frac{1}{2}$ order system. Here all the shared symbols are identical to that pertaining to Eq.(1.16), ω_c is the critical frequency introduced by Weidman & Browand (1975), and $u = \hat{u}e^{pt}$, with p characterising the frequency of input variables v or U_t. H(V) is still taken to be the heat transfer function of the film exposed to the effective (convective) velocity in a free stream. The output voltage waveform subjected to an electrical step input for the cylindrical hot-film sensor (see Fig.(1.17) or Freymuth & Fingerson, 1977) and flush-mounted hot-film sensor (Section 1.4.1(c) and Fig.(1.19)) take on a similar form. This suggests that the primary feature and characteristic of the latter are essentially captured by Eq.(1.18). Previous studies by Moen & Schneider (1994) and Huang *et al.* (1995) have also reported similar output waveforms for their respective flush-mounted hot-film wall shear stress sensors. It is also conceivable that for an electronic step input, the $2\frac{1}{2}$-order system of Eq.(1.18) which gives rise to the transient response reflected

in Fig.(1.17) for a hot-film sensor is different from Fig.(1.16) for a hot-wire sensor with a 3rd-order system equation as put forth by Freymuth (1981). Following the same argument as for the hot-wire sensor, due to the possible dependence of H(V) on frequency, and the uniqueness of the term dH/dV in S, the introduction of additional poles and zeros into the transfer function linking u to v is unlikely to be similar to the poles and zeros of the overall transfer function relating u to U_t. To a hot-film user, the direct test which yields f_D is a far better indicator and more direct reflection of the probe's responsiveness to imposed wall shear stress fluctuations.

1.4.1(f) Concluding remarks for Section 1.4.1

Experiments using the electronic square-wave voltage perturbation test were systematically performed for the first time to evaluate the response frequency (f_S) of near-wall hot wires. In addition, two commercially available flush-mounted wall shear stress gauges were tested. A fixed wire height above the wall substrate, an increase in the convective velocity leads to an increase in f_S. For a hot-wire exposed to a constant convective velocity, f_S increases with decreasing heights from the wall substrate. This is also equivalent to a decreasing h^+ with increasing effect of wall influence, hence suggesting that f_S improves with greater wall effects. A hot-wire mounted at the same height h = 50 μm above a thermally more conducting Aluminium wall substrate exhibits a higher value of f_S compared to its counterpart above a Perspex wall substrate under similar operating conditions. These findings strongly suggest that f_S increases with increasing heat transfer from the wire, regardless of whether it is due to forced/natural convection or effects of wall influence. For a flush-mounted hot-wire, an increase in the imposed wall shear stress yields a corresponding increase in f_S. The value of f_S (with and without "tail") for the DANTEC 55R45 wall shear stress gauge is consistently higher than that for the 55R46 gauge, hence indicating the better frequency response of the 55R45 gauge.

Results of the frequency response according to square-wave voltage perturbation tests (f_S) were then compared to those obtained using velocity perturbation tests (f_D) in Section 1.3.1 and Section 1.3.2. Although f_S and f_D show similar trends for the near-wall hot-wire and hot-film probes, f_S is consistently greater than f_D. The magnitudes of f_S and $f_D$are vastly different, being an order of magnitude for the marginally-elevated and flush-mounted hot wires. For the hot-film wall shear stress probes, this (ratio) difference is up to five orders of magnitude (without "tail") and three orders of magnitude (with "tail"). From a user's point of view, however, the dynamic frequency response (f_D) should serve as a more accurate indicator of the overall frequency response of the hot-wire/film system, since f_D signifies the onset of amplitude attenuation when the hot-wire/film is subjected to *direct* velocity or shear stress perturbations.

The large differences in magnitude between f_S and f_D show that the square-wave voltage perturbation test may not be all-sufficient in establishing the response frequency of a near-wall hot-wire or flush-mounted hot-film shear stress

probes. Plausible inherent differences between f_S and f_D may be explained using the response equation for a hot-wire anemometer (Freymuth, 1977) and a hot-film anemometer (Freymuth, 1978). The sensitivity of the anemometer S depends on the heat transfer function (H) and the derivative of H with respect to the velocity V (dH/dV), which are likely to be frequency dependent. As a result, S may introduce additional poles and zeros into the transfer function which relates the output voltage to the perturbation velocity, thus rendering this transfer function to be different from that which relates the output voltage to the perturbation voltage. This is physically manifested as a difference in cut-off frequencies deduced from both types of perturbation tests.

Further discourse on this Section 1.4.1 can be found in Khoo *et al.* (1999).

1.4.2 Sine-wave perturbation test (f_{sine})

Although the square-wave test serves as a convenient means of quantifying some frequency response of a wall-remote hot-element system, one must exercise extreme caution in interpreting and associating it with the dynamic response especially in near-wall application. Freymuth (1979) noted that a constant temperature hot-wire anemometer has essentially *two* or *two* groups of attenuation frequencies when subjected to velocity, voltage or temperature perturbations. The first attenuation which occurs at low frequencies is due to end conduction heat loss for hot wires of low aspect ratios, which results in an attenuation in heat transfer fluctuations. One of the first thorough investigations on this issue was performed by Bremhorst & Gilmore (1978). A similar low-frequency attenuation has also been observed by Bellhouse & Schultz (1967), Bellhouse & Rasmussen (1968) and Comte-Bellot (1977) for non-cylindrical hot-film probes and have been termed as "side loss" effects.

The heat transfer from a hot-element sensor essentially consists of two main components. The first and desirable component is the heat flux that is convected *directly* from the heated sensor into the surrounding fluid. The second component is the heat flux that is first conducted to the prongs or wire-supports for the case of hot wires and to the surrounding wall substrate for the case of hot film sensors, and this heat flux is subsequently convected into the surrounding fluid. Alternatively, one may generally view the second component as the additional heat loss to the wall substrate or due to the presence of the wall such that the occurrence would be absent for wall-remote applications. As the frequency increases from steady-state, the conduction fluctuations are first attenuated due to the attenuation of heat waves along the wire or substrate. This continues until a sufficiently high frequency when only the first desirable component of the heat flux associated with convective heat transfer remains. This first attenuation due to the so-called "end/side loss" occurs at low frequencies, after which the attenuated response extends to high frequencies before the second and final attenuation. The latter is attributed to the finite frequency response of the electronic feedback control components in

the anemometer. It is imperative to note that the second attenuation bears no reference or relevance to the first attenuation and they are completely separate effects (Freymuth & Fingerson 1977 and Freymuth 1979).

From the above discussion, it is perhaps reasonable to suggest some possible association between the *lower* magnitude dynamic response frequency (f_D) obtained in Sections 1.3.1 and 1.3.2 and the range of frequencies at which the first attenuation occurs. On the other hand, the frequency corresponding to the second attenuation is reflected by the square-wave test results (f_S) which yield the much higher magnitude cutoff frequency of the anemometer. For the marginally-elevated or flush-mounted hot-wire probes used in Sections 1.3.1 and 1.3.2, the wire length to diameter ratio was consistently greater than the conventionally accepted value of 200 so as to reduce end conduction losses through the prongs (Ligrani & Bradshaw 1987 and Chew *et al.*, 1998a). It is thus suggested that the amplitude attenuation corresponding to f_D is attributed to the effect of additional heat loss to or due to the presence of the wall.

In this Section, an extensive series of sine-wave tests will be carried out systematically for the marginally-elevated hot-wire and wall shear stress sensors investigated previously. The sine-wave test results are analyzed over the entire frequency range of interest to detect/seek the (causality) presence of any attenuation occurring below the high cutoff frequency which may correspond to f_D in the dynamic velocity or wall shear stress perturbation tests. The high cutoff frequency which is obtained from the sine-wave test (f_{sine}) can also be compared to that obtained using the conventional square-wave test (f_S) to investigate the equivalence or consistency of the two electronic perturbation tests for near-wall hot-element probes.

1.4.2(a) Sine wave perturbation test (f_{sine}) for the hot-wire and hot film: Some preliminaries

In the square-wave voltage perturbation test, the output response of the anemometer subjected to an *instantaneous* rise (or fall) in the input test signal is used to determine a characteristic time which quantifies the frequency response of the hot-element system. However, it is not possible to merely employ a *single* characteristic time (or frequency) to study or assess the relative response of a system over a *range* of frequencies. In contrast, for the sine-wave voltage perturbation test, an entire range of frequencies of sine-wave voltage perturbation is used to investigate the response or flatness of the system over the whole frequency range. This is similar to dynamic perturbation testing, where varying frequencies of dynamic perturbations are employed to obtain the dynamic frequency response of the system.

In order to perform a sine-wave test, a sinusoidal test signal output E_t from a Kenwood model FG-273 function generator was fed into the bridge, as shown in Fig.(1.22). The frequency of the sinusoidal test signal E_t was varied over a wide range of frequencies, while its amplitude was kept constant. Corresponding to each input frequency, the sinusoidal output response E of the anemometer was displayed on the digital oscilloscope and the amplitude (e) of the output was

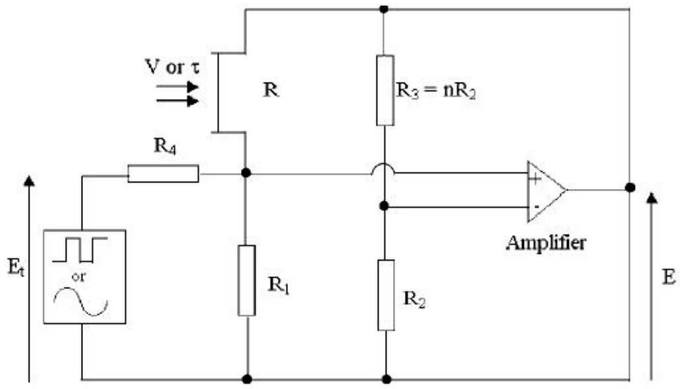

Figure 1.22: The circuit of the constant temperature anemometer.

noted. The amplitude of the sinusoidal output e was subsequently plotted against the corresponding frequency f in logarithmic scales to obtain the test response of the hot-wire or hot-film system (see Figure 1.23(a)).

For a wall-remote hot-wire sensor, the upward positive sloping region of the sine-wave response curve should have a slope of unity. This upward sloping line should extend to infinity ideally if the gain of the amplifier is infinite and there are no reactances in the amplifier or bridge. However, the reactances which are present limit the response to a finite frequency and the actual sine-wave response curve exhibits a decaying trend at high frequencies. The cutoff frequency of the anemometer can then be determined from the value of the frequency at which the actual sine-wave response curve drops 3 dB below the ideal response curve, as depicted in Figure 1.23(a). This cutoff frequency obtained from the sine-wave test (f_{sine}) should correspond to the square-wave frequency response (f_S), as validated by the wall-remote hot-wire model proposed by Freymuth (1977). (In the present work, it was carried out for near-wall hot-wire and flush-mounted hot-film probes.) Moreover, Freymuth & Fingerson (1977) commented that a 3 dB drop in the actual sine-wave response curve below the ideal one would correspond to the *same* drop for sinusoidal velocity fluctuations. Figure 1.23(b) illustrates the presence of low-frequency bulging effect obtained by Freymuth & Fingerson from the sine-wave tests conducted on a conical film sensor.

1.4.2(b) Comparison for (high) cutoff frequency obtained from sine-wave (f_{sine}) and (f_S)

(i) DANTEC-made 55R45/55R46 flush-mounted hot-film wall shear stress probes

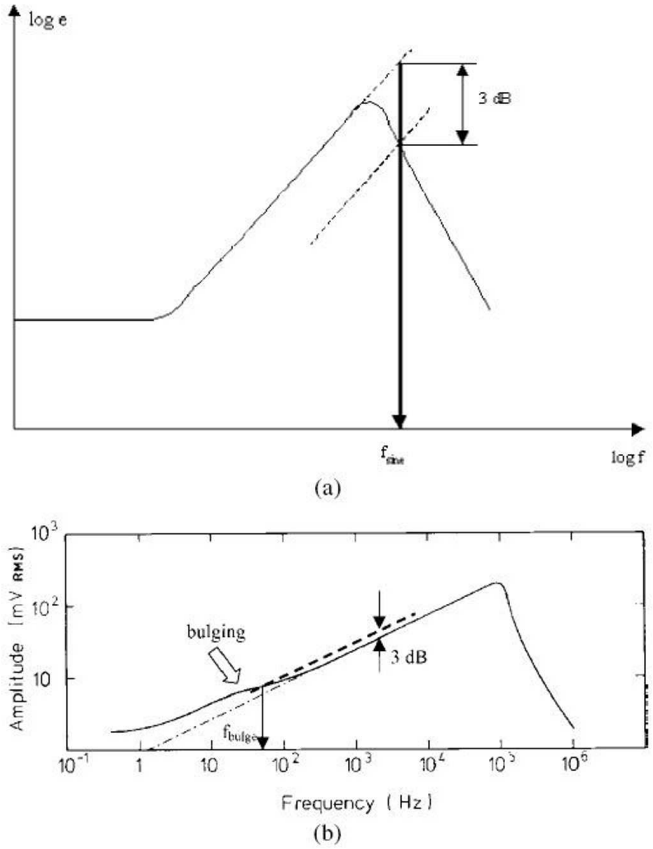

Figure 1.23: The cut-off frequency (f_{sine}) obtained from the sine-wave test response of a hot-wire anemometer. *(b)* The bulging effect observed with sine-wave testing for non-cylindrical hot-film sensors (the experimental results were obtained from Freymuth (1980) with a cone sensor.

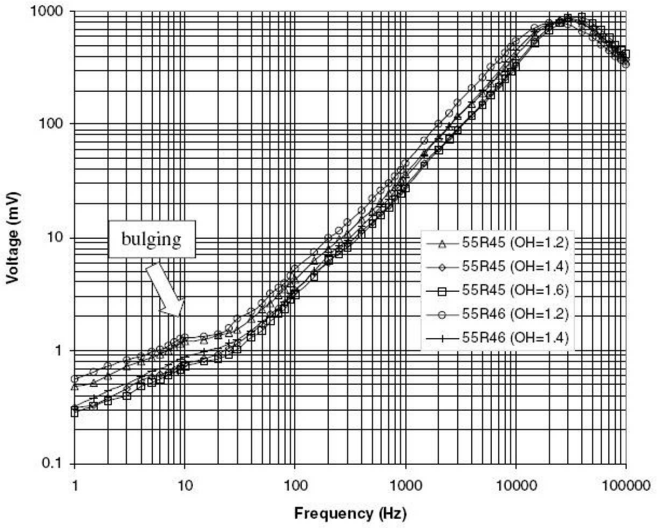

Figure 1.24: Sine-wave test responses of DANTEC 55R45 and 55R46 flush-mounted hot-film wall shear stress probes subjected to various overheating ratios.

Figure 1.24 shows the sine-wave test results for the 55R45 and 55R46 flush-mounted hot-film wall shear stress probes obtained in the absence of a flow. For the 55R45 probe, overheat ratios between 1.2 and 1.6 were used, whereas for the 55R46 probe, the overheat ratio had to be kept below an upper limit of 1.4 according to the manufacturer. For each probe, when the overheat ratio was held constant, the sine-wave test response was relatively independent of the magnitude of the prevailing wall shear stress over the entire range of frequencies investigated (not shown). The imposed wall shear stress (τ) ranged from 0 to 1.0 Pa in the tests. This implies that the cutoff frequency (f_{sine}) does not have a strong dependence on τ. When the square-wave test was performed at a fixed overheat ratio, the output waveform and hence the square-wave frequency response (f_S) was also found to be invariant when τ was varied. The independence of f_S with τ has also been noted by Kreplin & Eckelmann (1979), who reported that their quartz-coated DISA 55A95 gauge (a precursor of the 55R45 probe) operating at an overheat ratio of 1.02 displayed a square-wave frequency response which remained constant with or without a mean flow.

Presented in Table 1.5 are the values of the cutoff frequencies evaluated using the sine-wave and square-wave tests subjected to different overheat ratios. For each probe, both f_{sine} and f_S increase monotonically with the overheat ratio. Moen & Schneider (1994) have reported a similar trend of f_S increasing with the overheat ratio for their flush-mounted hot-film sensors operated in stagnant air. Table 1.5

also shows that the 55R45 gauge possesses a higher cutoff frequency than the 55R46 gauge, regardless of the type of voltage perturbation test used. The 55R45 gauge, which possesses a thinner top surface quartz coating than the 55R46 gauge, has its active element in the midst of surroundings with lower thermal resistance. It can thus be construed that the higher cutoff frequency of the 55R45 gauge is due to the enhanced overall heat transfer to the surroundings. This is also supported by the earlier observation that the cutoff frequency increases with increasing overheat ratio resulting in enhanced overall heat transfer to the surroundings.

It is evident that for each overheat ratio, f_{sine} and f_S bear the same order of magnitude, with f_S assuming a consistently higher value than f_{sine} by 10 to 20%. This difference might be due to the current CTA unit employing an in-built amplifier with a shaped gain which renders the square-wave test output for the hot-film gauges to resemble that of a wall-remote hot-wire probe. It should be noted that Freymuth's (1977) derivation of Eq.(1.14) for evaluation of f_S has not taken into account the variation of the amplifier gain with frequency, thus the factor of 1.3 may not be strictly applicable in this case. From Table 1.5, it is apparent that the difference between the cutoff frequencies yielded by both types of voltage perturbation tests reduces dramatically if a factor of 1.5 is used, and f_S is evaluated as

$$f_S = \frac{1}{1.5\,\tau_S}\,. \tag{1.19}$$

A similar factor of 1.5 has been just used by Huang *et al.* (1996) in evaluating the square-wave frequency response (f_S) of their micro-electro-mechanical system (MEMS) based thermal shear stress sensors without any explanation. (It may be noted in Berger *et al.* (1963) that if the anemometer system is adjusted to a second order response, the factor of 1.5 applies.)

(ii) Flush-mounted hot-wire wall shear stress probe

The sine-wave test response of a flush-mounted hot-wire with and without an imposed τ is shown in Fig.(1.25). The presence of τ at 0.56 Pa compared to null value results in a rightward and downward shift of the output response curve. The cutoff frequency (f_{sine}) increases correspondingly from 42.5 kHz to 44 kHz. In contrast to the commercial hot-film wall shear stress probes, the increased τ has improved the frequency response of the flush-mounted hot-wire probe slightly. Similar to the trends depicted by the sine-wave test, an imposed $\tau = 0.56$ Pa was found to improve the square-wave cutoff frequency f_S (evaluated using (1)) from 47.4 kHz (at $\tau = 0$) to 50.2 kHz. Such a trend is consistent with Freymuth's (1977) model for a *wall-remote* wire where f_S increased monotonically with velocity (*i.e.* corresponding to an increase in heat transfer H from the wire). For the flush-mounted hot-wire probe, H is interpreted as the overall heat transfer to the surroundings which increases with τ. For the said hot-wire, it is again evident that Eq.(1.14) results in values of f_S which are higher than f_{sine}. Application of Eq.(1.19) culminates in values of f_S which compare more favourably with those of f_{sine}.

Table 1.5: A comparison of cutoff frequencies obtained using the sine-wave test (f_{sine}) and the square-wave (f_S) for the DANTEC 55R45 and 55R46 hot-film wall shear-stress probes.

Probe	Sine-wave test response f_{sine} (kHz)	Square-wave test response f_S evaluated using equation (1.14) (kHz)	Square-wave test response f_S evaluated using equation (1.19) (kHz)	Overheating ratio
55R45	29.5	35.0	30.3	1.2
	34.5	40.9	35.4	1.4
	40.0	44.2	38.3	1.6
55R46	21.0	25.0	21.7	1.2
	28.0	33.7	29.2	1.4

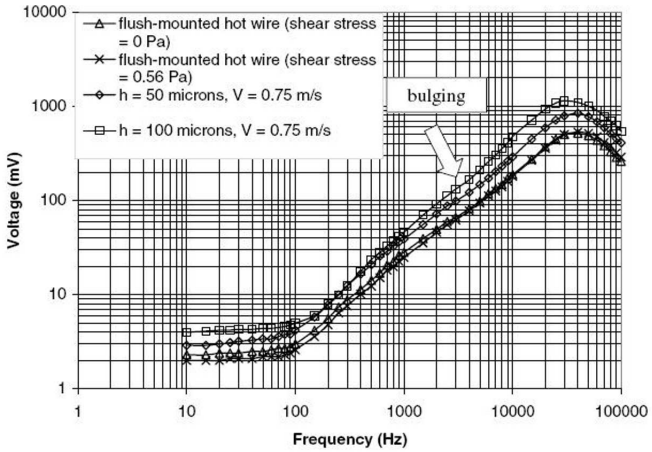

Figure 1.25: Sine-wave responses of flush-mounted and marginally elevated hot-wire.

(iii) Marginally-elevated hot-wire velocity probe

Presented in Fig.(1.26 are the sine-wave test response curves of a hot-wire placed at an elevation (y) of 50 μm above a Perspex wall substrate and exposed to varying magnitudes of convective velocity (V). The overheat ratio of the wire was held constant at 1.6. Values of f_{sine} obtained are summarized in Table 1.6. For y = 50 μm, an increase in V from 0 to 1.5 m/s leads to a corresponding increase in f_{sine} from 33 kHz to 39 kHz. (Although the elevation of the hot-wire is kept constant, the effects of wall influence experienced by the wire, as quantified by the height of the wire in wall units y^+ ($\equiv yu_\tau/\nu$) varies.) To assess the effects of V and y^+ on f_{sine}, the sine-wave test response of a hot-wire mounted at an elevation y = 100 μm and exposed to V = 0.75 m/s was obtained and plotted on Fig.(1.25), and the value for f_{sine} tabulated in Table 1.6. For the same y^+ (signifying equivalent effects of wall influence), an increase in V results in a corresponding increase in f_{sine}. On the other hand, a decrease in y^+ (which implies more significant wall effects) leads to an increase in f_{sine} when V is kept constant. These observations are consistent with those obtained for f_S, where enhanced heat loss from the wire either brought about by an increase in V or a decrease in y^+ results in higher values for f_S.

Similar to the flush-mounted hot-wire, f_S evaluated using Eq.(1.14) was found to be higher than f_{sine} for each corresponding parametric condition (see Table 1.6). Once again, Eq.(1.19) leads to values of f_S which are in better agreement with f_{sine}.

Table 1.6: A comparison of cutoff frequencies obtained using the sine-wave test (f_{sine}) and the square-wave test (f_S) for marginally elevated hot-wires mounted above a Perspex wall substrate. NA = not applicable.

Physical height of hot-wire above wall substrate y (μm)	Dimensionless height y^+	Sine-wave test response f_{sine} (kHz)	Square-wave test response f_S evaluated using equation (1.14) (kHz)	Square-wave test response f_S evaluated using equation (1.19) (kHz)	Velocity (m s^{-1})
50	NA	33.0	36.3	31.5	0
50	1.68	37.5	42.1	36.5	0.75
50	2.37	39.0	43.8	38.0	1.5
100	2.37	34.5	39.0	33.8	0.75

1.4.2(c) The low frequency attenuation from the sine-wave test (f_{bulge})

(i) DANTEC-made 55R45/55R46 flush-mounted hot-film wall shear stress probes

Although the square-wave test can be performed easily, the sine-wave test is able to yield more precise information pertaining to the flatness of the frequency response over the entire range of frequencies tested. Figure 1.24 shows the sine-wave frequency response of the DANTEC 55R45 and 55R46 probes subjected to different overheat ratios. At frequencies below approximately 100 Hz, a distinctive bulging effect appears in the test response curve for all overheat ratios investigated. This bulging effect, corresponding to the first amplitude attenuation at low frequencies, was observed by Freymuth & Fingerson (1977) for non-cylindrical cone and wedge-shaped sensors used for velocity measurements.

It would be useful to identify where this low-frequency attenuation of the thermal waves (which appears as a bulge in sine-wave tests) occurs. However, there appears to be some uncertainty in locating the *exact* frequencies at which this attenuation begins and ends. We have thus adopted the following methodology for obtaining a characteristic frequency representing the range over which the flush-mounted hot-film sensor suffers from this low-frequency amplitude attenuation. As shown in Fig.(1.23b), the said frequency (f_{bulge}) at which the amplitude response to sine-wave testing has risen by 3 dB above the straight line rising portion of the amplitude response curve (as the frequency is decreased) is used in the characterization. (In essence, this procedure follows that of Freymuth (1977, 1981a) and other workers in characterizing the (high) cutoff frequency of a hot-wire or hot-film anemometer by utilizing the value of the frequency at which the amplitude response to sine-wave electronic testing has dropped 3 dB *below* the region of flat response which corresponds to the ideal straight line rising portion of the amplitude response curve.) The results of f_{bulge} for the 55R45 and 55R46 probes at different overheat ratios are presented in Table 1.7. It can be seen that f_{bulge} is range-bound between 16 and 22 Hz, with no seemingly clear trend within limits of experimental accuracy. This suggests that the bulging effect is fairly independent of both the overheat ratio and the thickness of the quartz coating above the active heated element. As mentioned in Section 1.4.2(b), corresponding to the same probe operated at the same overheat ratio, the sine-wave response is independent of the magnitude of τ. Therefore it can be concluded that f_{bulge} is not affected by the prevailing flow conditions.

In Section 1.3.2, it was already established that the dynamic frequency response (f_D) of the hot film wall shear stress probes is of the order of 1 Hz. If we further assume an average value of 20 Hz for f_{bulge}, it is possible to relate f_{bulge} and f_D by a causal relationship given by

$$f_{bulge} \sim 20\, f_D\,. \tag{1.20}$$

This broad relationship would be invaluable to users who have no access to dynamic

Table 1.7: The frequencies (f_{bulge}) characterizing the bulging effect observed in the sine-wave test response curve and the dynamic frequency response (f_D) for the DANTEC 55R45 and 55R46 hot-film wall shear stress probes. NB: the wall shear stress τ was varied between 0 and 1.0 Pa and was found to have no influence on the values of f_{bulge} for the same probe operating at the same overheating ratio.

Probe	Frequency characterizing bulging effect f_{bulge} (Hz)	Dynamic frequency response f_D (Hz)	Overheating ratio
55R45	20	0.75	1.2
	16	0.8	1.4
	17	0.73	1.6
55R46	17	0.43	1.2
	22	0.45	1.4

testing facilities, but have the means to perform sine-wave electronic testing. We wish to emphasize that from a user's point of view, it is the dynamic response, *i.e.* the response of the sensor to *actual* wall shear stress perturbations that is of prime concern when the probe is employed for turbulent wall shear stress measurements. Therefore, in view of the complexities in conducting a separate dynamic perturbation test, the sine-wave electronic test can serve as an invaluable proxy or indicator to estimate f_D by invoking the above causal relationship.

Although f_S and f_{sine} are comparable in magnitude and consistent, both are approximately 5 orders of magnitude greater than f_D. Users of non-cylindrical hot-film thermal sensors who persist, whether knowingly or otherwise, in relying solely on the square-wave test to substantiate the use of such probes for high frequency turbulence measurements are likely to obtain erroneous results. This is exemplified by the work of Alfredsson *et al.* (1988) who employed near-wall hot-wire/film probes to obtain near-wall turbulence statistics in a turbulent air boundary layer flow at a Reynolds number (based on boundary layer thickness and free stream velocity) of 28,000. The same DANTEC 55R45 probe yielded a value of 0.095 for the intensity of streamwise wall shear stress fluctuations ($\tau'/\bar{\tau}$), whereas a marginally-elevated hot-wire probe gave a value of 0.39. Here $\bar{\tau}$ and τ' denote the mean and RMS value of the wall shear stress fluctuations respectively. Alfredsson *et al.* further reported a f_S quantity of more than 10 kHz for both the 55R45 hot-film and marginally-elevated hot-wire probes, although Section 1.3.2 has shown clearly that f_D is about 2 kHz for the latter compared to the extremely low values of O(1) Hz for the former. Alfredsson *et al.* did not report any sine-wave testing. Instead, they discussed about the frequency response by comparing the streamwise wall shear stress power spectra obtained from the 55R45 probe and their marginally-elevated hot-wire sensor. It was found that the power spectrum yielded by the 55R45 probe grossly underestimated the latter. Corresponding to

a frequency of 10 Hz, the power spectrum obtained from the 55R45 probe was up to 90% lower. In contrast to the square-wave test which only emphasizes the high cut-off frequencies, the sine-wave test is further able to reveal the effects of low-frequency thermal wave attenuation effects for non-cylindrical hot-film sensors. From the causality condition proposed above, f_{bulge} is still a closer and better approximation to f_D as compared to f_S or f_{sine}.

It is appropriate to mention a word of caution in the use of the sine-wave test. Huang *et al.* (1996) did evaluate the frequency response of their micro-electro-mechanical system (MEMS) based thermal shear stress sensors using both the sine-wave and square-wave voltage perturbation tests. The cutoff-frequencies (9 kHz for their sensor with a cavity and 130 kHz for their sensor without a cavity) yielded by both tests were found to be consistent, similar to our observation for the near-wall hot-wire/film sensors. However, a close examination of their sine-wave test response revealed that it has been plotted on a linear-log plot rather than a classical log-log plot. Such a procedure is not sufficiently sensitive to reveal the bulging effect due to the attenuation of thermal waves at low frequencies.

(ii) Flush-mounted hot-wire wall shear stress probe and marginally-elevated hot-wire velocity probe

Sine-wave tests were first performed on a wall-remote hot-wire subjected in turn to a stationary fluid and a uniform flow at 12 m/s, so that detailed comparisons can be subsequently made w.r.t. the results for a near-wall hot wire at y = 50 μm (see Figure 1.26). In Fig.(1.26), the response of a wall-remote hot-wire bears close resemblance to the corresponding results of Freymuth & Fingerson (1977). In particular, the flatness is vindicated by the positive sloping region of the response curves bearing a gradient close to unity. Although the near-wall hot-wire still exhibits a continuously upward increasing trend for frequencies ranging between 100 Hz and tens of kHz, differences exist between the observed response and its wall-remote counterpart. The response curve of the near-wall hot-wire shows a bulging effect similar to that observed for the flush-mounted hot-film wall shear stress gauges. However, the observed bulging effect for the near-wall hot wire is very much weaker than that for the flush-mounted hot-film gauges. The location of the bulging effect also occurs over a much higher and wider frequency range of 0.8 to 4 kHz for the near-wall hot-wire, as contrasted to O(20 Hz) for the flush-mounted hot-film gauges.

Extensive dynamic velocity perturbation tests performed in Section 1.3.1 have indicated that the dynamic frequency response f_D of near-wall hot-wire probes is O(2 kHz). Square-wave tests conducted on the said probes yielded values of f_S which are approximately one order of magnitude higher than f_D (see Table 1.6) or Section 1.4.1).

From the above sine-wave test results, the frequency range where the bulging effect is observed corresponds much more closely to f_D. It may be suggested that the low frequency amplitude attenuation effect observed (f_D) is also due to the attenuation of the heat waves from the heated wire to the surrounding wall

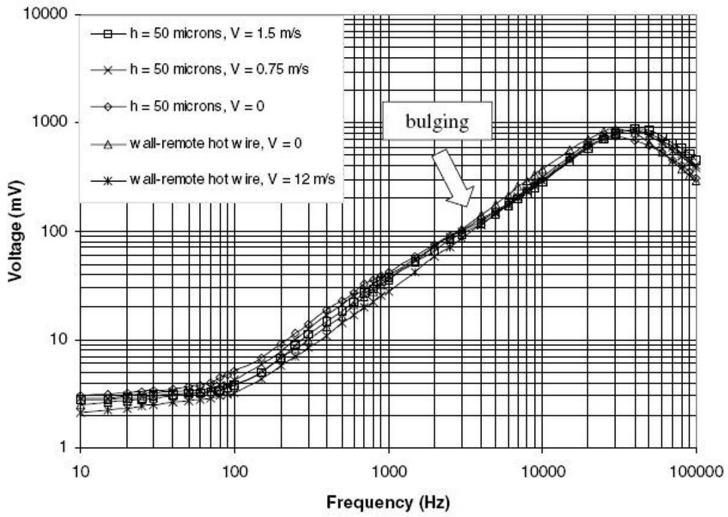

Figure 1.26: Sine-wave responses of marginally elevated and wall-remote hot-wire probes.

substrate. However, in contrast to the flush-mounted hot-film gauges, where the active elements are completely embedded in the surrounding quartz substrate, the near-wall hot-wire is also exposed to the surrounding ambient air. This attenuation of heat waves to the surrounding wall substrate is thus deemed to be less severe for the near-wall hot-wire than the flush-mounted hot-film sensors, which serves to explain the qualitatively weaker bulging effect for the near-wall hot-wire. When the hot-wire is placed at a higher elevation of 100 μm and subjected to V = 0.75 m/s (Figure 1.25), the bulging effect is still barely discernable near the 0.8 to 4 kHz range. Also displayed in Fig.(1.25) are the response curves of a flush-mounted hot-wire wall shear stress probe exposed to varying wall shear stress. The bulging effect occurring in the 0.8 to 4 kHz range seems qualitatively stronger. Overall, for the marginally-elevated and flush-mounted hot-wire probes, it is thus possible to relate f_{bulge} and f_D by a causal relationship given by

$$f_{bulge} \sim f_D \sim O(2\,\mathrm{kHz})\,. \tag{1.21}$$

1.4.2(d) Concluding remarks for Section 1.4.2

Experiments using the electronic sine-wave voltage perturbation test were systematically performed for the first time on marginally-elevated and flush-mounted hot-wire probes. Two commercial flush-mounted hot-film wall shear stress gauges were also tested. For both the hot-film and hot-wire sensors, the cutoff frequency

of the anemometer yielded by the sine-wave test (f_{sine}) was found to be in fair agreement and to exhibit the same trends as results obtained using the traditional electronic square-wave voltage perturbation test (f_S). For the hot-film gauges, f_{sine} obtained for the DANTEC 55R45 gauge was consistently higher that those for its 55R46 counterpart under identical conditions of overheat ratio and wall shear stress (τ). For both gauges, an increase in overheat ratio resulted in a rise in f_{sine}, whereas variations in τ for the same overheat ratio did not seem to have cast any effect. For the marginally-elevated hot-wire probes, an increase in the convective velocity (V) leads to an increase in f_{sine} when the wire is either kept at a fixed physical distance or at the same y^+ above the wall substrate. When V is held constant, a decrease in y^+ signifying increased wall influence culminates in larger values of f_{sine}. These results suggest that f_{sine} increases with increasing heat transfer from the wire, regardless of whether it is due to forced convection or effects of wall influence. For the flush-mounted hot-wire wall shear stress sensor, an increase in the imposed τ results in a corresponding increase in f_{sine}.

Apart from yielding the cutoff frequency of the anemometer, the sine-wave test is also capable of indicating the flatness of the frequency response over a limited frequency range and detect the presence of any amplitude attenuation which arises as a result of the attenuation of heat waves to the surrounding wall substrate at high frequencies. A significant bulging effect appears in the sine-wave test response curves for the hot-film wall shear stress probes. A causality relationship $f_{bulge} \approx 20 f_D$ was observed for the hot-film gauges, where f_{bulge} and f_D denote the frequency characterizing the bulging effect and the dynamic frequency response respectively. Compared to f_S (and f_{sine}) which is five orders of magnitude greater than f_D, f_{bulge} provides a much better indicator or proxy for predicting f_D. It is to be realized that in the application of the hot-film wall shear stress gauges to measure fluctuating shear stress in a turbulent flow, it is the lower dynamic response frequency f_D which sets an upper limit to the overall responsiveness of the gauge.

For the flush-mounted and marginally-elevated hot-wire sensors, a very slight bulging effect was also observed in the 0.8 to 4 kHz range, which corresponds much more closely to the values of f_D. This is contrasted to f_S, which is typically one order of magnitude larger than f_D. The frequencies f_{bulge} and f_D can be related by the causality relationship $f_{bulge} \sim f_D$ for the near-wall hot-wire probes. It must be noted that the lower magnitude f_D is the critical frequency ultimately determining the responsiveness of the near-wall hot-wire probe to fluctuating velocities expected in a turbulent flow. Therefore, it is suggested that instead of relying solely on the square-wave test, users of near-wall hot-wire or hot-film anemometers who do not have access to dynamic perturbation testing facilities should perform a sine-wave test to detect the presence of any amplitude attenuation for frequencies (f_{bulge}) below the cutoff frequency.

Further discourse on this Section 1.4.2 can be found in Teo *et al.* (2001).

1.5 A model for the frequency response of a near-wall hot-wire

In Section 1.4.2, we have proposed a causality relationship between the bulging frequency (f_{bulge}) and f_D, both of which occur at the lower frequency range below that indicated by either f_s or f_{sine}. This has one very important implication: simply by employing the sine-wave voltage perturbation test, one may be able to deduce the dynamic response frequency of the near-wall hot-wire system. After all, from the user's point of view, it is the response of the sensor to the actual flow fluctuation /perturbation that is of prime concern when the probe is employed for turbulent flow measurements in near-wall configurations.

In this Section, we seek to present a simplified 1-D model capable of predicting the behavioral trend of a hot-wire operating close to the wall under different parametric/operating conditions. The computed results of f_D and f_{bulge} are compared to the experiments under the conditions of varying wire height (in terms of wall units) and different magnitudes of convection velocity. It is important to note that compared to a full scale 3-D numerical simulation where it is much more time consuming and compute-intensive, the model can accord a very timely discourse on the changes to the response characteristic of the near-wall hot-wire as a velocity probe operating under different conditions.

1.5.1 A simplified 1-D model for the hot-wire probe

In the analysis of the 1-D model for the flushed-mounted hot-film wall shear stress probe, Freymuth (1980) greatly simplified the complicated 3-D heat transfer across the substrate into areas adjacent to the film by 1-D heat transfer from the planar film surface across the substrate to another planar surface below the substrate at temperature T(z=-h). The active planar film at temperature T(z=0), which is exposed to the convection heat loss at the top section, is assumed to be of negligible thickness compared to the thickness h of the substrate. The length and breadth of the film are l and L, respectively (see Figure 1.27). The model hot film is placed on one arm of the Wheatstone bridge and a circuit analysis is carried out with input sine-wave voltage or imposed fluctuating wall shear stress on the hot film.

In a move similar to Freymuth (1980) and Teo *et al.*, applying an energy balance to the near-wall hot-wire which is placed on one arm of the Wheatstone bridge yields

$$\frac{E^2 R}{(R+R_1)^2} - H(V)(T_w - T_0) = lLK \left.\frac{\partial T}{\partial z}\right|_{z=0} + \frac{c}{\beta}\frac{dR}{dt}\,, \tag{1.22}$$

where c is the thermal inertia of the wire, H(V) represents the heat transfer function from the wire to the flow, K is the thermal conductivity of the substrate, β denotes the temperature coefficient of the wire resistance R, and T_w and T_o are temperature on the hot-wire and ambient, respectively. The electrical circuitry of the Wheatstone bridge of the CTA is provided in Fig.(1.22). Here R_1 is another

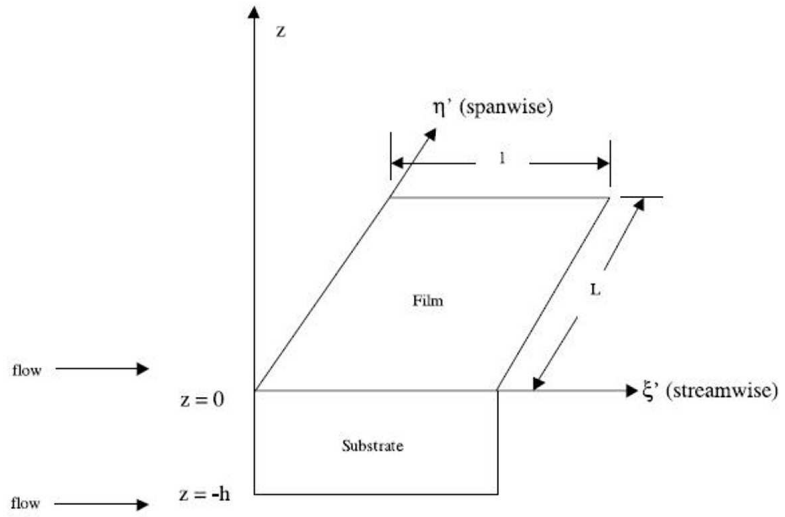

Figure 1.27: Model of a non-cylindrical hot-film according to the Bellhouse-Schultz model.

bridge arm in series with R, whereas R_2 and R_3 (=nR_2), which constitute the remaining 2 arms of the bridge, are resistances connected in parallel to R_1 and R, respectively. The electronic test signal E_t is fed into the bridge via resistance R_4 ($>> R_1$) and E is the voltage over the bridge. R_0 is the wire resistance at ambient reference temperature. A schematic of the near-wall hot-wire is given in Fig.(1.28).

Equation (1.22) is almost identical to the equation by Freymuth (1980) describing the energy balance of the non-cylindrical hot film, except for the additional second term on the RHS of Eq.(1.22) which takes into consideration the hot-wire's change in internal energy with time. It may be noted that the heat transfer to the substrate is modelled as one-dimensional and represented by the first term on the RHS of Eq.(1.22). As in Freymuth, the boundary condition at the lower, not electrically heated, surface reads

$$H'(V)\{T(z=-h)-T_0\} = lLK \left.\frac{\partial T}{\partial z}\right|_{(z=-h)} . \tag{1.23}$$

Here H'(V) is the heat transfer function from the lower surface of the substrate to the surrounding fluids. Equation (1.22) can be re-written as

$$\frac{E^2 R}{(R+R_1)^2} = H(V)(T_w - T_0) + \frac{H'(V)}{x'+1}(T|_{z=0} - T_0) + \frac{c}{\beta}\frac{dR}{dt} , \tag{1.24}$$

where the Biot number $x' = hH'(V)/(lLK)$. Further simplification can be made if we assume since the hot-wire is placed very close to the wall within the viscous

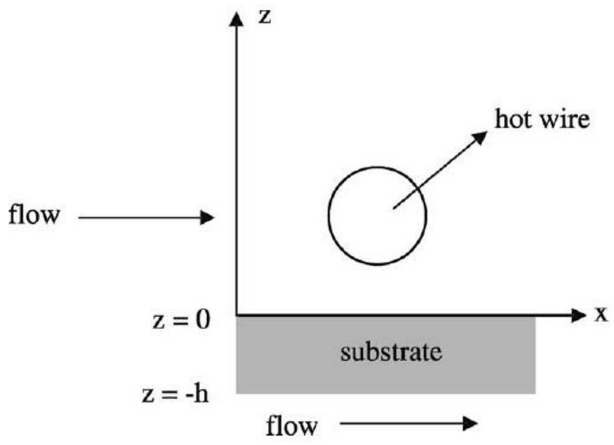

Figure 1.28: Model of a near-wall hot-wire.

sublayer such that $T_{z=0} \sim T_w$ and $H' \sim H$ for a given V. (In similar 1-D analysis as carried out in Bellhouse & Schultz (1967) and Freymuth (1980) for a non-cylindrical hot film probe subjected to convection velocity, we have here largely assumed that the heat transfer of the near-wall hot-wire under convection velocity V has the same order of magnitude as that for a surface subjected to the same V. On the other hand, a general but more complex model of relating H to H' by a factor or even set independent of each other will invariably introduce further unknowns that have to be calibrated against experiments and cannot be used on its own for prediction or comparison.) This is also in line with the intent of a simplified 1-D model able to predict to predict the behavioral trend of the near-wall hot-wire as opposed to convey numerical quantity per se. Equation (1.24) becomes

$$\frac{E^2 R}{(R+R_1)^2} = H(V)(T_w - T_0)\left(\frac{2+x}{1+x}\right) + \frac{c}{\beta}\frac{dR}{dt}\,, \tag{1.25}$$

where $x = hH(V)/(lLK)$. As such, the first term on the R.H.S. can be interpreted as the sum of the heat loss directly from the hot-wire to the flow (*i.e.* H(V)$(T_w - T_0)$) and the heat loss from the wire to the wall substrate (*i.e.* $H(V)(T_w - T_0)\left(\frac{1}{1+x}\right)$). After linearizing the boundary conditions and taking into account the bridge-amplifier combination, we obtain the final governing response equation for the anemometer output e subjected to sinusoidal voltage, velocity and ambient temperature fluctuating perturbations (denoted by E_t, v and T_0',

respectively)

$$e = \frac{n+1}{2}\frac{R}{R-R_o}\frac{R_1}{R_4}\frac{1+x}{2+x}E_t\left(\gamma' + a'\frac{b'-c'}{b'+c'} + \frac{i\Omega Dc}{h^2 H}\right) - \frac{E}{2}\frac{1+x}{2+x}\frac{\alpha}{R-R_o}T_o'\left(1+\frac{2a'}{b'+c'}\right) + \frac{E}{2}\frac{1+x}{2+x}\frac{1}{H}\frac{dH}{dV}v\left(1+\frac{1}{1+x}\frac{2a'}{b'+c'}\right), \tag{1.26}$$

where

$$a' = (i\Omega)^{1/2}/x\,,$$
$$b' = \exp\left[(i\Omega)^{1/2}\right]\left\{\left[(i\Omega)^{1/2}/x\right]+1\right\},$$
$$c' = \exp\left[(i\Omega)^{1/2}\right]\left\{\left[(i\Omega)^{1/2}/x\right]-1\right\},$$
$$\gamma' = 1+\left(\frac{R-R_1}{R+R_1}\right)\left(\frac{R-R_o}{R}\right)\frac{2+x}{1+x}$$

and $\Omega = (2\pi f)h^2/D$ is the dimensionless frequency. Here f and D denote the frequency and the thermal diffusivity of the substrate, respectively.

The normalized amplitude response of the anemometer subjected to dynamic velocity perturbations is given by

$$|R_v| = 1 + \frac{(1+x)[2a'/(b'+c')]-1}{2+2x+x^2}\,. \tag{1.27}$$

For the near-wall hot-wire probe subjected to electronic sine-wave perturbations (*i.e.* $T_0' = v = 0$), the fluctuating output is proportional to

$$e' = \frac{\alpha}{1-1/\alpha}\left(\frac{1+x}{2+x}\right)\left[1-(1-\alpha)\left(\frac{1-n}{1+n}\right)\frac{2+x}{1+x} + a'\frac{b'-c'}{b'+c'} + i\Omega m\right], \tag{1.28}$$

where the overheating ratio $\alpha = R/R_0$ and $m = Dc/(h^2H)$.

1.5.2 Results and discussions on the 1D model

1.5.2(a) Probe subjected to different magnitudes of convection velocity (V)

Previous DNS by Chew *et al.* (1995), Lange *et al.* (1999) and Li *et al.* (2006) simulating the heat loss from a hot-wire operating in close proximity to the wall have revealed that the amount of heat loss by the wire to the wall, when evaluated as a fraction of the total amount of heat loss or dissipated by the wire, remains fairly constant for the same value of y^+, as long as the thermal conductivity of the wall substrate material is unchanged. From Eq.(1.25), since this fraction is

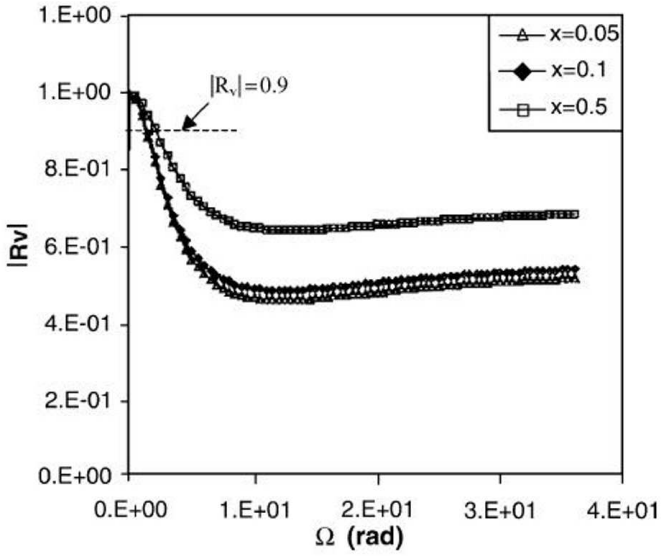

Figure 1.29: Normalized amplitude response of near-wall hot-wire anemometer subjected to dynamic velocity pertubations for various values of Biot numer x.

only a function of the Biot number x, it can be deduced that for the same value of y^+, x can be assumed to be a constant. To study the effect of V on the frequency response of the near-wall hot-wire while keeping y^+ constant, it is necessary to vary H. It may be noted that, for a given wall substrate, keeping y^+ constant (and x fixed) is equivalent to constant wall influence on the operation of the near-wall hot-wire. However, since $x \equiv hH/(lLK)$ depends on the heat transfer function H, the value of the substrate thickness h has to be varied in order that x remains unaltered.

We shall first discuss how the model predicts the dynamic response of a near-wall hot-wire subjected to velocity perturbations. The distributions of $|R_v|$ against Ω are depicted in Fig.(1.29) for various values of x ranging between 0.05 and 0.5. Each curve shows the variation of $|R_v|$ with Ω for the same y^+.

Consider two near-wall hot wires with identical effects of wall influence and exposed to V_1 (wire 1) and V_2 (wire 2) such that $V_2 > V_1$. Since H(V) for the second wire is higher than that for the first wire, $h_2 < h_1$ in order to keep x unchanged. For the same x, $\Omega_D$corresponding to the point when $|R_v|$ has decayed or attenuated to 0.9 remains fixed. (In the experiments in Section 1.3.1, the onset of amplitude attenuation was taken to be the frequency of the imposed fluctuation when the ratio of the measured amplitude to the imposed amplitude (a_{mea}/a_{imp}) equals 0.9.) Since for the two wires $(\Omega_D)_1 = (\Omega_D)_2$ and $\Omega_D = (2\pi f_D)h^2/D$, the presence of $h_2 < h_1$ necessarily implies that $(f_D)_2 > (f_D)_1$. That is wire 2 which

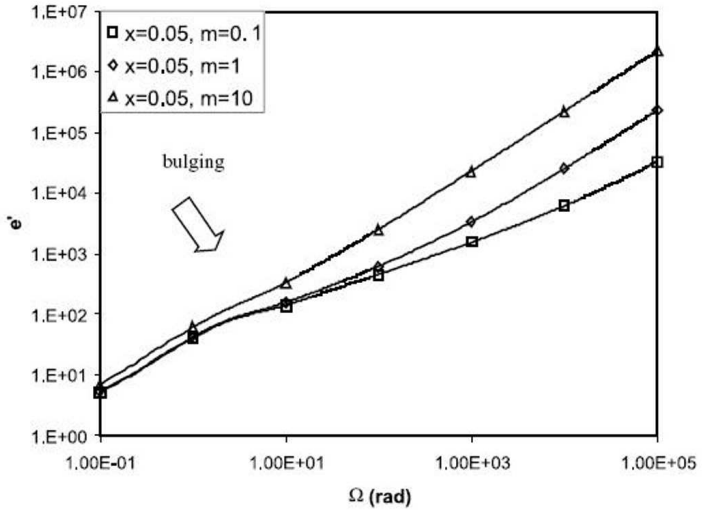

Figure 1.30: Sine-wave test response of a near-wall hot-wire anemometer subjected to different magnitudes of convecting velocity.

is exposed to a larger V possesses a higher dynamic frequency response than wire 1. This concurs with the experimental observations in Section 1.3.1, where it was found that an increase in V at the same y^+ has resulted in a concomitant improvement in f_D for the near-wall hot-wire.

In the experiments, a hot-wire mounted at height y = 40 μm above the perspex wall substrate and exposed to V = 2.7 m/s has a dynamic frequency of f_D = 2690 Hz. This value is larger than the corresponding quantity of f_D = 2345 Hz when the same hot-wire was exposed to a smaller V = 2.17 m/s. For the latter, the wire was set at y = 50 μm such that the same $y^+ = 2.6$ prevailed.

From the model it is clear that a higher convection velocity on near-wall hot-wire with similar influence of wall effect exhibits a better dynamic response frequency. Next, it would also be interesting to investigate how the model predicts the frequency response of a near-wall hot-wire subjected to sine-wave voltage perturbation testing. Again, for a given y^+ (and hence x), the product of h and H remains invariant. The response given by Eq.(1.28) shows that e' is only dependent on the value of $m \equiv Dc/(h^2H)$. If $H_2 > H_1$ as with $V_2 > V_1$ (*i.e.* larger convection velocity), a constant value of x implies that $h_2 < h_1$ and hence $m_2 > m_1$. Equation (1.28) is plotted on Fig.(1.30) for various values of m ranging from 0.1 to 10 for x = 0.05, say, and $\alpha = 1.6$ and a resistance ratio n = 1/20.

Smaller values of m are observed to result in a more significant and distinct "bulging" effect. As the value of m increases to 10, the "bulging" effect becomes less distinct. Two interpretation of results can be suggested. At smaller values of m where the "bulging" effect is more distinct, the dimensionless frequency Ω cor-

responding to the location of the "bulge" (Ω_{bulge}) remains somewhat unchanged. (The bulging effect occurs over a range of frequency; see also Section 1.4.2.) This implies that dimensional $(f_{bulge})_2 > (f_{bulge})_1$, which is similar to that observed for the above-mentioned f_D. The diminishing "bulging" effect as m becomes larger can be construed as the decreasing importance of the lower magnitude dimensional f_{bulge} in deference to the higher magnitude cut-off frequency f_{sine}. Overall, it may be suggested that for a near-wall hot wire subjected to equal effects of wall influence, a larger convection velocity will improve the frequency response and may cause the "bulging" effect to be diminished.

Another salient feature which can be observed from Fig.(1.30) is that the slopes of the predicted sine-wave test response curves asymptote to a limiting value of unity for large values of the dimensionless frequency Ω. This is comparable to the results obtained for the sine-wave tests (prior to the cutoff frequency) performed on near-wall hot-wire probes, as shown in the experiments discussed in Section 1.4.2. Moreover, the range of values of Ω corresponding to the "bulging" effect predicted by the model in Fig.(1.30) bears the same order of magnitude as Ω_D (Figure 1.29). This is consistent with the experimental observations in Section 1.4.2 where it was found that $f_{bulge} \sim f_D \sim O(2\text{kHz})$ for the 5 μm diameter near-wall hot-wire probe. The experiments in Section 1.4.2 had led to the proposal of the causality relation

$$f_{bulge} \sim f_D \tag{1.29}$$

for ease of obtaining the dynamic response frequency of the hot-wire in near-wall operations.

1.5.2(b) Probe subjected to different values of y^+ (V constant)

In this section, we wish to analyze how the proposed model predicts the effect of y^+ on the frequency response subjected to the *same* V. As mentioned in Section 1.5.2(a), the amount of heat loss from the hot-wire to the wall, evaluated as a fraction of the total amount of heat dissipated by the wire, depends on the value of y^+ for a particular wall substrate material. The numerical works of Chew *et al.* (1995) and Lang *et al.* (1999) indicate that this fraction is weakly dependent on the friction velocity u_τ and it increases as the value of y^+ decreases. From Eq.(1.25), this fraction works out to be 1/(2+x). A smaller value of y^+ (associated with greater wall influence and a subsequent larger fraction of heat loss to the wall) thus implies a smaller value for x. In other words, x can be broadly construed as an indicator of the wall influence and is inversely proportional to it.

Referring to Fig.(1.29), Ω_D decreases as the value of x decreases. For a probe subjected to the same V, the heat transfer function H should remain approximately constant. Consider two hot wires 1 and 2 having Biot numbers $x_1 = 0.1$ and $x_2 = 0.05$, respectively. Since $x_2 < x_1$, it is obvious that $y_2^+ < y_1^+$. As H remains invariant since V is held constant, $x_2/x_1 = h_2/h_1 = 0.5$. From Fig.(1.29), it can be seen that $(\Omega_D)_2/(\Omega_D)_1 \approx 1$. This implies that $(f_{D2}h_2^2)/(f_{D1}h_1^2) \approx 1$ and hence $f_{D2}/f_{D1} \approx 4$, *i.e.* $f_{D2} > f_{D1}$. It can thus be inferred that wire 2 which loses a

larger fraction of heat to the wall substrate due to its lower value of y^+, has a better dynamic frequency response.

To illustrate further, consider wires 1 and 3 possessing $x_1 = 0.1$ and $x_3 = 0.5$, respectively. For the same V, $x_3/x_1 = h_3/h_1 = 5$. Similarly, from Fig.(1.29), it can be deduced that $(\Omega_D)_3/(\Omega_D)_1 \approx 1.5$ and hence $f_{D3}/f_{D1} \approx 0.06$ (note that although $(\Omega_D)_3 > (\Omega_D)_1$, $f_{D3} < f_{D1}$). An increase in x, corresponding to a smaller fraction of heat loss to the wall and larger values of y^+, has culminated in a poorer f_D. In the experiments of Section 1.3.1, f_D for the near-wall hot-wire was found to increase from 2390 Hz (y = 65 μm, $y^+ = 3.44$) to 2625 Hz (y = 50 μm, $y^+ = 3.05$) to 2690 Hz (y = 40 μm, $y^+ = 2.63$) at the similar convection velocity of V = 2.9 m/s. It should be noted that with V fixed, the convection heat loss remains unchanged. A larger fraction of heat loss to the wall substrate as observed above such that there is an overall greater heat loss from the hot-wire has led to a larger value of f_D. This, together with the results in Section 1.5.2(a), suggests that the dynamic response frequency of a near-wall hot-wire increases with larger heat loss from the wire, which is irrespective of whether the loss is due to forced convection or to the effect of wall influence.

The output response curves of a near-wall hot-wire subjected to sine-wave voltage perturbation testing are presented in Fig.(1.31) for various values of x. With a fixed V, and $\alpha = 1.6$ and n = 1/20, a rise in x corresponds to an increase in h and hence decreasing wall influence (*i.e.* y^+ increases).

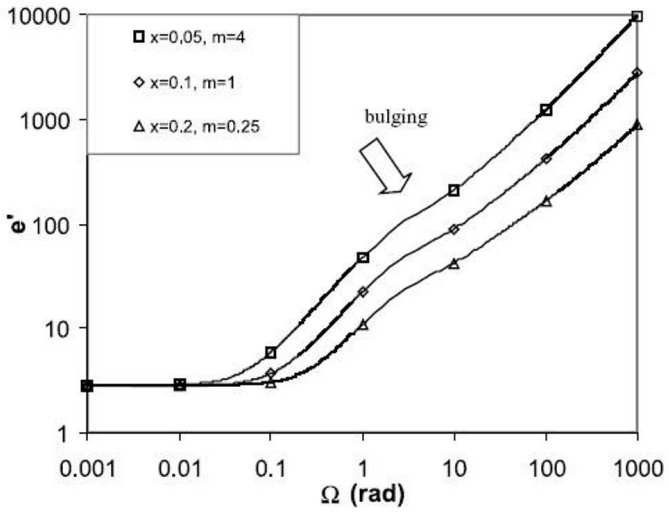

Figure 1.31: Sine-wave test response of near-wall hot-wire subjected to different effects of wall influence (y^+). (For a fixed V, an increasing wall influence of decreasing y^+ is equivalent to decreasing Biot number x with greater proportion of heat loss to the wall substrate.)

Figure 1.31 shows that the location of the bulge or Ω_{bulge} remains relatively unaffected, and there is a mildly perceptible diminishing bulging effect for the lower magnitude range of m. As in Section 1.5.2(a), we can suggest two interpretations. For the range of higher m which indicates invariant Ω_{bulge}, this corresponds to f_{bulge} decreasing with increasing x which is similar to that observed for f_D above. The diminishing effect of bulging as x becomes even larger (and m becomes much smaller) is associated with ever increasing y^+ such that the wall effect becomes increasingly insignificant. In experiments, a hot-wire operating under increasing free-stream conditions will experience increasingly better f_D, the presence of only the f_{sine} feature in the electronic sine-wave testing, and the absence of f_{bulge}. It can be construed that the "bulging" effect is caused by heat loss to the substrate and is thus related to the first attenuation. As the proportion of heat loss to the wall decreases greatly with large y^+ (towards outside the viscous sublayer), we thus observed the bulging effect becoming less conspicuous in the sine-wave response curve. This concurs with the experiments observations of Section 1.4.2.

1.5.2(c) Consideration of other effects

In Section 1.3.1, it was found that f_D for the hot-wire mounted at 50 μm above the aluminum wall substrate is always higher than the corresponding hot-wire at the same height above the perspex wall substrate. The results obtained can be expressed in terms of dimensionless wire height in wall units such that for a given y^+ both wires are exposed to the same convection velocity, and any difference in heat transfer characteristic of the wire is solely attributed to the different additional heat loss to the wall substrate. For the aluminum wall substrate, there is greater heat transfer from the wire (Khoo *et al.*, 1996 and Chew *et al.*, 1998b) which is in accord with the conclusion reached in Section 1.5.2(b) on the link between heat transfer and f_D. It would be interesting to analyze the prediction based on the model.

At the same V, we have

$$x_{perspex}(\equiv hH/lLK_{perspex}) > x_{aluminum}(\equiv hH/lLK_{aluminum})\,,$$

to account for greater effect of the aluminum wall influence on the near-wall hot-wire operation. From Fig.(1.29), it is clear that

$$(\Omega_D)_{perspex} > (\Omega_D)_{aluminum}\,,$$

which apparently may imply that the model has given the incorrect trend. On closer examination, since $\Omega_D = 2\pi h^2 f_D/D$, even if $(\Omega_D)_{perspex} > (\Omega_D)_{aluminum}$, it is *not* so straightforward that $(f_D)_{perspex} > (f_D)_{aluminum}$ since the thermal diffusivity of aluminum is much greater than perspex by a factor of at least two orders of magnitude. That is $D_{aluminum}/D_{perspex} \sim O(10^2)$. Therefore any change in Ω_D in response to the change in x due to the different thermal conductivity of wall substrate will be mitigated or even overwhelmed by the change in D such that f_D may take on different direction of change from Ω_D. (It may

just be noted too from Fig.(1.29) that corresponding to a change of one order of magnitude of x, Ω_D changes by a much smaller factor.) In essence, the model suggests that a change of wall substrate of different thermal conductivity will only give rise to a limited change in f_D. From the experiments in Section 1.3.1 with $K_{aluminum}/K_{perspex} \sim O(10^2)$, we observed that f_D of a hot-wire placed above an aluminum substrate improves by only about 10-15% over the corresponding perspex substrate.

It is worth mentioning that the effect of a change in wire diameter (d) on the dynamic response of a near-wall hot-wire can be deduced from the model. As d is decreased, l will be corresponding smaller. From the heat transfer relationship by McAdams (1954) correlating the Nusselt number (Nu) of a cylinder in a submerged flow,

$$(Hd/\nu)Pr^{-0.3} = 0.35 + 0.56(\rho V d/\mu)^{0.52}\,, \tag{1.30}$$

we can infer that H is broadly related inversely to d such that H increases with decreasing d while keeping V constant. From the definition of x, the effect of a smaller d which entails smaller l gives rise to larger value of x. Therefore, from Fig.(1.29), the model suggests that we can possibly obtain better f_D simply by reducing the wire diameter.

Although there are no experiments for verification, this is perhaps not very surprising since logically a smaller wire diameter has lower thermal inertia and a possibility exists that it should be more responsive to changing external flow conditions. One word of caution, though, the thermal inertia of the wire is not related explicitly to f_D as seen in Eq.(1.27) for the model.

Applying the idea of a smaller d to the model for sine-wave test while keeping V constant, the effect of a corresponding increase in x can be inferred and interpreted from Fig.(1.31). As d decreases, the thermal inertia of the wire also decreases and together with a larger H lead to a much smaller m. Figure 1.31 therefore suggests a resultant output response curve which has a diminishing bulging effect. As discussed in Section 1.5.2(b), the decrease in bulging effect can be construed as an improvement in the frequency response of system such that the effect of first amplitude attenuation at low frequencies (due primarily to influence of wall effect) becomes unimportant. Only the second and final attenuation due to the finite frequency response of the electronic feedback in the anemometer remains.

Although the results in Sections 1.5.2(a) and 1.5.2(b) have indicated similar trend behavior of f_D and f_{bulge}, and the experimental findings in Section 1.4.2 suggested a functional relationship between them, it should be noted that according to the model there is one marked difference. That is, f_{bulge} is dependent on the additional parameter m which also clearly indicates the explicit dependence on the wire thermal inertia c. There is no such dependence on m for f_D.

It may be added, however, that the material used in the fabrication of the hot-wire has been predisposed towards tungsten or platinum after many years since the beginning of hot-wire anemometry and having taken into consideration many other features like ductility for ease of manufacturing, strength ... etc. The use of different material solely to affect a change in c is not deemed likely to be considered

as an alternative by an end user to change the hot-wire response characteristic, and hence may not pose a critical issue in the continual use of f_{bulge} as an effective proxy to obtain f_D via the functional relationship given in Eq.(1.29). However, the model serves as a reminder that the various types of perturbation tests, in particular the sine-wave test which gives rise to the bulging effect for a near-wall hot-wire and the velocity perturbation test, are not exactly equivalent even though they share several important characteristic traits.

1.5.2(d) Concluding remarks for Section 1.5

In this work, a model for the response characteristic of the near-wall hot wire subjected to sine-wave voltage perturbation and velocity perturbation tests is developed. It is found that the computed response frequency f_{bulge} (according to sine-wave perturbation test) and f_D (according to velocity perturbation test), which correspond to the first of the two groups of attenuation frequencies, concur very well with the experiments discussed in Sections 1.3.1 and 1.4.2. The first attenuation which occurs at low frequencies is attributed to the influence of wall effect whereas the second and final attenuation is associated with the finite frequency response of the CTA system. Both f_D and f_{bulge} indicate a similar trend of increasing with the convection velocity and increasing effect of wall influence (*i.e.* y^+ decreases) or both, and support the causality relationship of $f_D \sim f_{bulge}$ as suggested in Section 1.4.2.

It is further shown from the model that the response frequency of the near-wall hot-wire can be made to increase by decreasing the wire diameter and the effect of different wall substrate material as measured by the property of thermal conductivity is very much limited. In experiments, it was found that a change of the wall substrate from perspex to aluminum has only resulted in about 10-15% improvement for f_D even though the ratio of the respective thermal conductivity is at least two orders of magnitude. The model, however, indicates that there are differences between f_D and f_{bulge}. It is an important and timely reminder that such perturbation tests are not identical in all aspects as f_D measures the response to heat lost from the wire or gauge by velocity perturbation while f_{bulge} measures the frequency response to the total heat lost from the wire or gauge.

Overall, although the model developed is a very simplified one-dimension, it is able to provide insight into the behavioral trends of the response frequency of the near-wall hot-wire without the complexities of a full 3D numerical simulation with the associated requirement of extensive computing resources. It can also serve as a predictive tool for the end-user who may want to change or ensure sufficient responsiveness of the near-wall hot-wire probe operating under different conditions.

1.6 On near-wall hot-wire velocity measurements

During the past decade, the quest for drag reduction has prompted several researchers to propose various schemes which seek to alter the flow structures and velocity profile very close to the wall, in view of the fact that skin friction drag constitutes the major component of drag for streamlined bodies. Examples of such schemes include the employment of riblets (Walsh, 1992), the use of large eddy break-up (LEBU) devices (Savill & Mumford, 1988), the application of compliant surface (Lee *et al.*, 1993) and the addition of polymers (Koskie & Tiederman, 1993). In assessing the merits of these passive drag reduction schemes, it is imperative to attain a thorough comprehension of the flow characteristics very close to the wall, so that detailed comparison can be made with respect to the unmanipulated flow in order that the physics and mechanism responsible for the said reduction in drag can be brought to light.

It is well known that all the commonly available velocity measuring instruments are plagued by problems very close to the wall, although the cause of limitation differs from one instrument to another. The rapid development of PIV and the accessibility of LDV have not culminated in the extinction of the hot-wire anemometer, especially for near-wall measurements. Both the LDV and PIV require seeding of the flow and measurements significantly depend on the passage of the said particles through the respective control volumes, hence yielding a non-continuous output. This issue is accentuated in the near-wall region where the particle count diminishes considerably, resulting in an appreciably lower and variable data rate. Moreover, the relatively large measuring volume of the LDA raises doubts pertaining to the spatial averaging of the particle velocity, especially in the near wall region where the velocity gradient is normally large. For instance, in the LDV measurements of Karlsson & Johansson (1988) made in the viscous sublayer of a low-speed water boundary-layer flow, the extent of the measurement volume in the direction normal to the wall was $O(0.5\nu/u_\tau)$, where ν/u_τ is the viscous length unit. Durst *et al.* (1995) made LDA measurements in the near-wall region of a turbulent pipe flow and their axial velocity component was measured in the vertical plane with a spatial resolution of $0.7\nu/u_\tau$ at the lowest Reynolds number (the spatial resolution must necessarily be larger than $0.7\nu/u_\tau$ for their results at higher Reynolds numbers). In contrast, the hot-wire whose diameter is merely microns enables an extremely fine spatial resolution and yields a continuous signal, hence ensuring a non-biased statistical account of the turbulent flow field characteristics.

The ability of the hot-wire to yield a continuous output does not necessarily imply that it possesses an infinitely high frequency response for accurate time resolution of the flow field. In Section 1.3.1, we found that the dynamic response of a near-wall hot-wire was typically better than 2 kHz, which should be adequate for the accurate time resolution of most commonly encountered wall-bounded turbulent shear flows. Spalart (1988), who performed a direct numerical simulation (DNS) for a turbulent boundary layer on a flat plate with zero pressure gradient, commented that a typical timescale of turbulence near the wall is about 15 wall

time units (*i.e.* $15\nu/u_\tau^2$, where ν and u_τ are the kinematic viscosity and the mean friction velocity, respectively), which further implies that the dynamic frequency response of the hot-wire probe must be greater than $u_\tau^2/15\nu$ in order for the most rapid turbulence generating events to be accurately resolved by the probe.

Having ascertained the sufficiently high frequency response of a hot-wire operating in close proximity to the wall, near-wall hot-wire sensors can next be applied to investigate the physics of the flow in the very near-wall region of various wall bounded turbulent shear flows. Despite a dynamic frequency response of more than O(2 kHz) for a near-wall hot-wire, in the near-wall turbulence measurements of Fernholz & Warnack (1998), the sampling frequency for their near-wall hot wires was limited to a relatively low value of 250 Hz (thus giving an even lower cutoff frequency of 125 Hz), which may not be sufficiently high to elucidate the correct physics that characterize the high frequency components (or the dissipating range) of the turbulent flow field. Fernholtz & Warnack employed the traditional square-wave test to justify the frequency response of their near-wall hot wires. Although they obtained a square-wave frequency response "in excess of 20 kHz", their sampling frequency was limited to 250 Hz without any explanation.

In Section 1.4.1, we have cautioned against the over-reliance on the square-wave test, since it overestimates the dynamic frequency response of a marginally-elevated hot-wire by close to one order of magnitude. In this Section 1.6, higher sampling frequencies will be used for measurement of the wall shear stress and streamwise velocity fluctuations in the viscous sublayer.

The establishment of a viable calibration procedure for near-wall hot-wire probes, coupled with the above-mentioned investigations pertaining to the ability of near-wall hot-wire probes to accurately resolve all the length and time scales of turbulence in the viscous sublayer, have strongly boosted our confidence in the application of the said probes to actual turbulence measurements in the viscous sublayer of different types of flow. As described previously, the motivation of near-wall velocity measurements stems from the importance of measuring the flow field very near the wall accurately in order to elucidate the physics and mechanisms of near-wall turbulence events in both unmanipulated and manipulated wall-bounded flows using passive drag or skin friction reduction schemes.

A further motivation of the present work arises from its application to near-wall turbulence modelling. Statistical descriptions of turbulence based on the Reynolds-averaged Navier-Stokes equations suffer from the problem of closure in that the Reynolds stresses and the extra terms which appear in the scalar transport equations as a consequence of time averaging are unknown and thus require modelling. The two-equation k-ε model which attempts to model most of the constituent terms in the transport equations for k (turbulence kinetic energy) and ε (dissipation rate of the turbulence kinetic energy), has been and may continue to be a turbulence model extensively used by many computational fluid dynamists. At high Reynolds numbers, the standard k-ε model (Launder & Spalding 1974) avoids the need to integrate the model equations right down to the wall by making use of the universal behaviour of near wall flows. Different modifications to the k-ε model to enable it to cope with low Reynolds number flows are reviewed in

Patel *et al.* (1985). At low Reynolds numbers, wall damping functions are invariably applied to ensure that the viscous stresses take over from the Reynolds stresses in the viscous sublayer adjacent to the wall. However, the damping functions introduced to model the different terms in the ε-equation are rather ad-hoc and a critical assessment of the models is by no means possible because the accurate measurement of ε in the near-wall region poses insurmountable difficulties. Our near-wall hot-wire measurements can help in assessing the validity of the wall damping function.

1.6.1 Calibration of near-wall hot-wire probe for spanwise intensity measurement

Calibration of the hot-wire for the streamwise velocity follows that described in Section 1.3.1(a). On the other hand, the use of a single hot-wire probe inclined at different angles to the mean flow direction for time-averaged two-component velocity measurements has been documented in detail by Bruun (1995). During calibration of the inclined hot-wire probe, the output E of the probe is normally determined in terms of the magnitude of the flow velocity V and the yaw angle α (where the yaw angle α is defined as the angle between the direction of the velocity vector and the normal to the axis of the hot-wire), *i.e.*

$$E = E(V, \alpha)\,, \tag{1.31}$$

with E being correlated with the effective velocity V_e using King's Law; that is

$$E^2 = A + BV_e^n\,. \tag{1.32}$$

V_e can be expressed as

$$V_e = Vf(\alpha)\,, \tag{1.33}$$

where f(α) is the yaw function. Several expressions have been proposed for f(α), the most popular being

$$f(\alpha) = (\cos^2\alpha + k_T^2 \sin^2\alpha)^{1/2}, \tag{1.34}$$

where k_T is the tangential cooling coefficient, which was first proposed by Hinze (1959). Another extensively-used expression for f(α), first introduced by Bradshaw (1971), is

$$f(\alpha) = \cos(\alpha_{eff}), \tag{1.35}$$

where α_{eff} is the effective angle which has to be determined from a yaw calibration. The probe is calibrated by first setting $\bar{\alpha}$ to be 45° or -45° in order to determine the calibration constants A, B and n in (1.32). This is followed by rotating the probe in the x-z plane through small variations $\theta = \alpha - \bar{\alpha}$, in the yaw angle as the flow velocity is kept constant, and noting the output voltage E_α of the CTA for each value of α (or θ). The values of θ used were 0°, ±5°, ±10° and ±15°.

Following the procedure recommended by Bradshaw, a graph of (cos θ - E_θ) is plotted against sin θ, where E_θ is defined as

$$E_\theta = \left[\frac{E_\alpha^2 - A}{E_{\bar{\alpha}}^2 - A}\right]^{1/n} . \tag{1.36}$$

The effective angle α_{eff} for a particular velocity can then be determined from the slope of the best-fit line, m, with m = $\tan(\alpha_{eff})$.

For each different height h of the hot-wire above the wall substrate, the near-wall hot-wire probe is first calibrated in the laminar flow calibration rig at α = 0°, 45° and -45° and the effective angles α_{eff} are obtained over a range of flow velocities. In order to determine the spanwise turbulence intensity in the viscous sublayer of the channel and flat-plate boundary layer flows, the plug housing the near-wall hot-wire probe is rotated with the axis of rotation being normal to the wall (*i.e.* in the x-z plane) and the output voltages E_0, E_1 and E_2, corresponding to $\alpha = 0°$, 45° and -45° respectively, are sampled digitally. The effective velocities V_{e0}, V_{e1} and V_{e2} can then be deduced from E_0, E_1 and E_2 respectively via equation (1.33). The Reynolds stresses are then evaluated using the following expressions:

$$\overline{w^2} = \frac{\overline{V_{e1}^2} + \overline{V_{e2}^2} - 2\,\overline{V_{e0}^2}\,\cos^2\alpha_{eff}}{2\,\sin^2\alpha_{eff}} \tag{1.37}$$

and

$$\overline{uw} = \frac{\overline{V_{e2}^2} - \overline{V_{e1}^2}}{2\,\sin 2\alpha_{eff}} , \tag{1.38}$$

For the channel and flat-plate boundary layer flows, $\overline{uw}$ was found to be negligibly small within the viscous sublayer.

1.6.2 Mean velocity profile

The mean velocity profile normalized by the centreline velocity for the channel flow at h^+ = 390 is presented in Fig.(1.32). The mean wall shear stress $\bar{\tau}$ and hence the mean friction velocity $\overline{u_\tau}$ were determined from streamwise pressure gradient measurements.

Also shown in Fig.(1.32) are the DNS results of Antonia *et al.* (1992) for a channel flow at h^+ = 395. It is evident that the experimental results bear close resemblance to the simulation results. Figure 1.32 also shows the mean velocity profiles normalized using the free-stream velocity for the flat plate boundary layer flow at Re_θ (based on the momentum thickness and the free stream velocity) of 2900, 3400 and 4100. It is apparent that an increase in Re_θ enhances the "bulging" of the boundary layer profile (*i.e.* the velocity profile becomes fuller). Although not displayed in Fig.(1.32), the near-wall velocity profile of the channel flow at h^+ = 180 compares well to Kim *et al.*'s (1987) DNS results of a channel flow at the same h^+.

Figure 1.33 depicts the mean velocity profiles for the channel and boundary layer flows scaled using inner variables. There is excellent agreement between

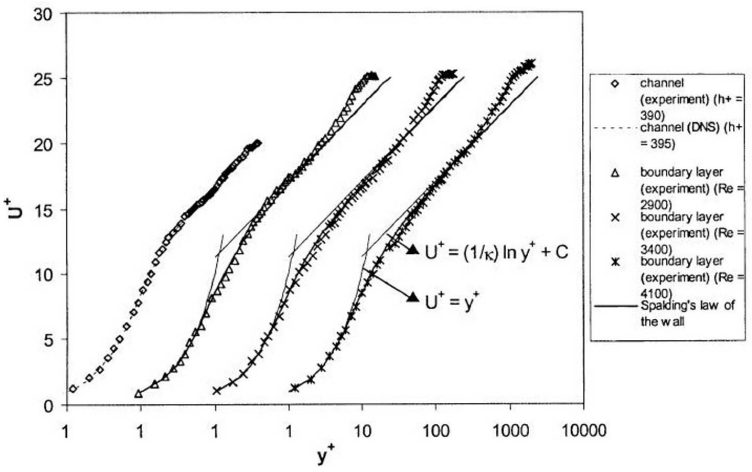

Figure 1.32: Mean streamwise velocity profile normalized using inner variables.

the experimental and computational results for the channel flow. The wall shear stress values (τ_w) for the boundary layer flow at different values of Re_θ were obtained using the Clauser Chart technique. The evaluated skin friction coefficient C_f ($\equiv \tau_w/(0.5\rho U_\infty^2)$) compares very favourably to those obtained by previous investigators using the Preston tube method, which are compiled in Fernholz & Finley (1996). It can be noted that, away from the wall, starting from $y^+ \approx 30$, the profiles closely follow the logarithmic law of the wall

$$U^+_{log} = (1/\kappa)\ln y^+ + C\,, \tag{1.39}$$

with universal constants $\kappa = 0.4$ and $C = 5.5$. At distances further from the wall, Coles (1962) described the development of a low Reynolds number boundary layer using "the strength of the wake" $\Delta\mathrm{U}^+$, defined as the maximum value of (U^+ - U^+_{log}), which is the largest deviation of the outer layer velocity profile from the log law. This quantity assumes a asymptotically constant value of 2.75 for $\mathrm{Re}_\theta < 6000$ when the defect law is satisfied and drops gradually to zero when $Re_\theta \approx 500$. The values of $\Delta\mathrm{U}^+$ (using the above-mentioned values for the constants in the log law) work out to be 2.35, 2.26 and 2.39 for Re_θ of 2900, 3400 and 4100, respectively. These results are in fair comparison to the experimental results of $\Delta\mathrm{U}^+$ for a wide range of Re_θ values compiled by Coles (1962) and more recently by Fernholz & Finley (1996).

In the immediate vicinity of the wall, the near-wall hot-wire probe accurately predicts the velocity profile

$$U^+ = y^+\,, \tag{1.40}$$

valid in the viscous sublayer of the channel and boundary layer flows for $y^+ \leqslant 5$, which is the conventionally accepted extent of the viscous sublayer. (See Schlicht-

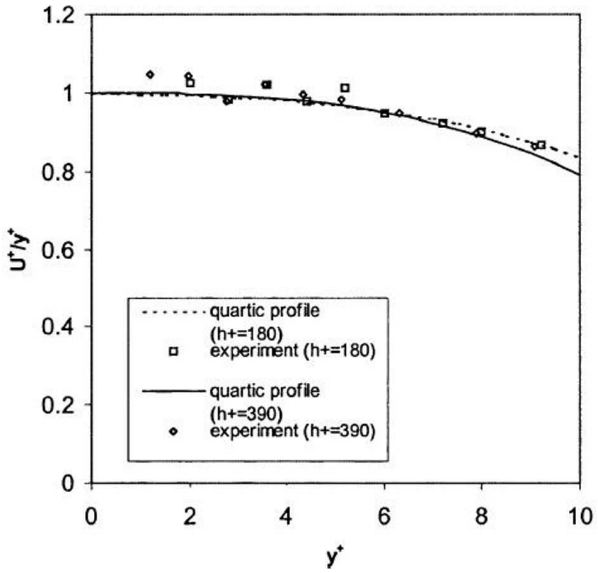

Figure 1.33: Dimensionless streamwise mean velocity U^+ divided by y^+ as a function of y^+ in viscous sublayer of channel flow.

ing, 1979. See also the simulation results of Kim *et al.*, 1987 and Antonia *et al.*, 1992, for a channel flow and Spalart, 1988, for a boundary layer flow.) This clearly demonstrates the viability of the near-wall hot-wire to directly measure the velocity distribution very near the wall accurately (without the need for any wall correction), when the effects of wall influence are calibrated away using the laminar flow calibration rig as described in Section 1.3.1(a).

Spalding (1961), in an attempt to describe fully the mean streamwise velocity distribution next to the wall, proposed the law of the wall given by

$$y^+ = u^+ + e^{-\kappa C}\left[e^{\kappa u^+} - 1 - \kappa u^+ - \frac{(\kappa u^+)^2}{2} - \frac{(\kappa u^+)^3}{6}\right], \qquad (1.41)$$

with $\kappa = 0.4$ and $C = 5.5$. In Fig.(1.32), there is reasonable agreement of experimental data with Spalding's (1961) law of the wall for both the channel and boundary layer flows; for the latter, concurrence is valid up to $y^+ \approx 400$. Very recently, based on theory and analysis of DNS results, Cenedese *et al.* (1998) have suggested the use of a quartic profile to represent the mean velocity in the region $y^+ < 10$. This profile is given as $u^+ = y^+ - (1/2h^+)y^{+2} + ey^{+4}$, where $e \approx -10^{-5}(h^+)^{0.5}$. This quartic profile is evaluated for a channel flow at $h^+ = 180$ and 390 and the profiles are plotted alongside the experimental results in Fig.(1.33). It can be inferred that the experimental values are fairly well described by the quartic profile for $y^+ < 10$. Attention should also be drawn to

Fig.(9) of Cenedese *et al.*, which shows the quartic profile and their very near-wall hot-wire results obtained for $h^+ = 1670$. For $y^+ < 4$, the hot-wire results expressed as U^+/y^+ do not exhibit a fairly constant value tending towards unity as expected. Instead, it displays a clear monotonic increasing trend as the wall is approached, with U^+/y^+ rising to 1.2 when $y^+ \approx 2.5$. This is not surprising in view of the fact that wall effects have not been accounted for nor calibrated away for their near-wall hot-wire results, thus culminating in the spurious rise in value of U^+/y^+ with decreasing y^+. This rise in U^+/y^+ is also a manifestation of increasing wall influence. In contrast, the experimental results in Fig.(1.33) do not bear such a trend as the wall is approached, hence further verifying the validity of our calibration techniques.

1.6.3 Turbulence flow intensities

1.6.3(a) Streamwise velocity component

The root-mean-square (rms) values of the fluctuating streamwise velocities, normalized using the mean friction velocity is presented in Fig.(1.34).

The experimental results for the channel flow at $h^+ = 390$ agree well with the DNS results of Antonia *et al.* (1992) for a channel flow at $h^+ = 395$. The experimental results for the boundary layer suggests a barely discernible trend of increasing u'^+ with Re_θ at a given y^+ valid for $y^+ \geqslant 30$. This trend can also be observed from the extensively compiled boundary layer data in the review article by Fernholz and Finley (1996) and the experimental results for a channel flow at different Reynolds numbers reported in Antonia *et al.* (1992). The DNS results of Spalart (1988) and Antonia *et al.* (1992) confirm the tendency for u'^+ to increase with Reynolds number. Furthermore, it may be noted from Fig.(1.34) that the maximum value of u'^+ is approximately 2.75 and occurs at $y^+ \approx 15$ for both the boundary layer and the channel flows, which compares reasonably well with the values provided by other researchers. For example, Ligrani & Bradshaw (1987b) employed wires of different length to diameter ratios in a turbulent boundary layer at $Re_\theta = 2620$ and found that the results for the value of u'^+ at $y^+ = 17 \pm 0.5$ (where the value of u'^+ reaches a maximum) collapsed onto a single curve when plotted against the wire length in wall units. Their results indicate that the maximum value of u'^+ assumes a value of approximately 2.8 at $y^+ \approx 17$. Kim *et al.* (1987) obtained a maximum value of about 2.7 at $y^+ \approx 12$ for their DNS of a channel flow at $h^+ = 180$. Spalart (1988) found a systematic increase in the maximum value of u'^+ with Re_θ for his DNS of a boundary layer flow, the value increasing from 2.5 to 2.7 corresponding to a Re_θ increase from 300 to 1410. However, within the limits of experimental accuracy, it is not possible to discern any systematic dependence of this maximum value on Re_θ for our boundary layer measurements. On the other hand, Mochizuki & Nieuwstadt (1996) made a survey on 47 independent experimental and numerical studies for zero pressure gradient boundary layer and fully developed internal flows (including pipes and channels)

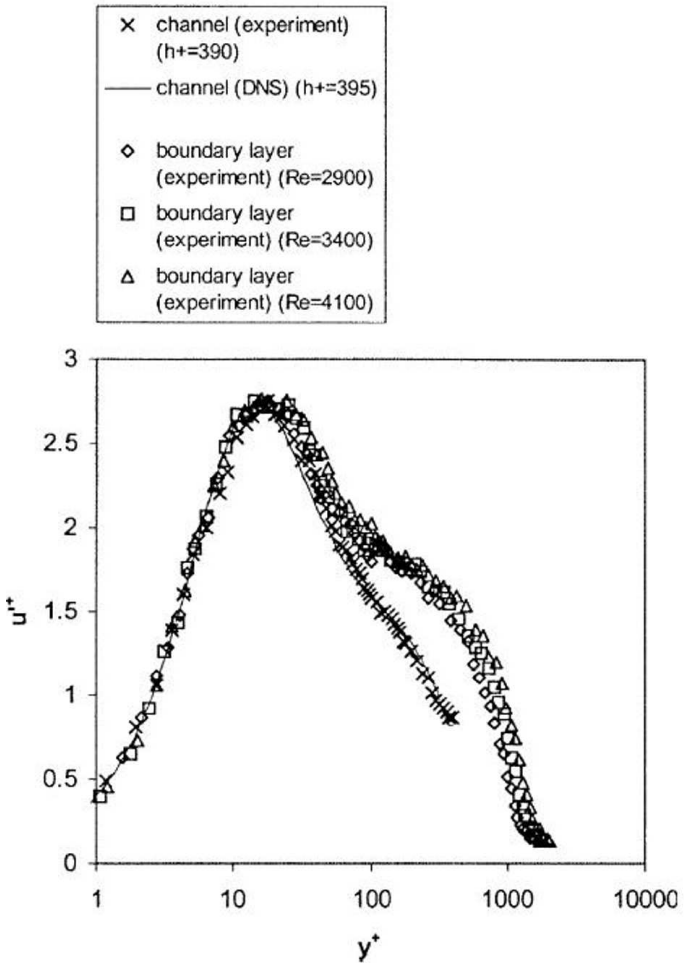

Figure 1.34: Distribution of rms streamwise velocity fluctuations normalized using inner variables.

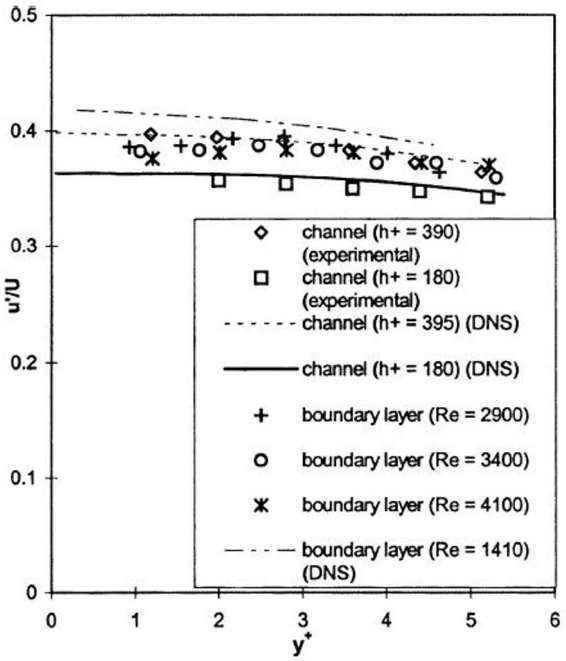

Figure 1.35: Streamwise turbulence intensity distribution in the viscous sublayer.

over an extensive range of Reynolds numbers and found the peak value of u'$^+$ to be independent of the Reynolds number within limits of statistical error. Their survey reveals that this parameter assumes a value of 2.71 $\pm$ 0.14 (occurring at an average y$^+$ of 14.4) and 2.70 $\pm$ 0.09 (occurring at an average y$^+$ of 14.6) for boundary layer and internal flows, respectively. Marusic *et al.* (1997) speculated the peak value of u'$^+$ occurring at $y^+ \approx 15$ to be associated with "the early formation process of the attached eddies" and further lamented that "very little is understood about this region".

Experimental results in the near-wall viscous sublayer region is shown in Figure 1.35, where the local rms value of the streamwise velocity fluctuations are normalized using the local mean velocity.

The results for the channel flow at h$^+$ = 180 and 390 compare favourably with the simulation results of Kim *et al.* (1987) and Antonia *et al.* (1992) respectively, thus suggesting the calibrated near-wall hot-wire probe's capability in time-resolved velocity measurements and the validity of the calibration technique employed. The general rise in the distribution for the streamwise turbulence intensity corresponding to an increase with h$^+$ is consistent with the trend revealed by the DNS results. This has been attributed by Spalart (1988) and Antonia *et al.* (1992) and Antonia and Kim (1994) to an "inactive motion", first proposed by

Townsend (1961) and Bradshaw (1967), which intensifies as the Reynolds number increases. This inactive motion which consists of the large-scale vorticity field and the pressure fluctuations of the large eddies in the outer layer is nominally irrotational. Such motions have very large wavelengths (of order δ) and time-scales in comparison to the viscous (inner) layer scales. As the wall is approached, the normal (v) component (to the wall) of the inactive motion has to be brought to rest due to the impermeability condition imposed by the wall, thus releasing their normal component of the energy into the other two orthogonal tangential components u and w. This "splat effect" motion's influence on the shear stress is small, thus producing very little effect on the log law of the wall for the mean velocity. As the Reynolds number increases, this inactive motion contributes appreciably to the low wavenumber components of the u and w spectra, thus causing the magnitudes of u'$^+$ (and hence $u'/\overline{U}$) and w'$^+$ to increase with Reynolds number.

The turbulence intensity of the streamwise velocity fluctuations at a given y$^+$ for the boundary layer flow does not reveal any significant variance or increase with increasing Re$_\theta$, which may be attributed to the narrow range of Re$_\theta$ investigated in this present study. Furthermore, it can be observed from Fig.(1.35) that the distribution of $u'/\overline{U}$ for the boundary layer flow for the range of Re$_\theta$ investigated bears close resemblance to that obtained for the channel flow measurements at $h^+ = 390$. The value of $u'/\overline{U}$ assumes a marginally increasing trend as y$^+$ decreases towards a constant value of approximately 0.38, which compares favourably with the results of other researchers available in the literature. Alfredsson *et al.* (1988) obtained a slightly higher constant value of $u'/\overline{U} \approx 0.4$ within the viscous sublayer for their marginally-elevated hot-film probes in an oil channel flow at Re$_c$ (based on centerline velocity and channel half-width) of 3800, which concurs well with our findings, within a variation of about 5%.

Unlike (our) near-wall hot-wire operation in air which is strongly affected by wall effects which have to be calibrated away, Alfredsson *et al.*'s hot-film operation in oil is not influenced by such effects as the ratio of the direct heat loss to oil is about one order of magnitude greater than that in air. In fact, when Alfredsson *et al.* utilized a hot-wire probe (whose wall effects have not been calibrated away) in an air boundary layer, they found that u'$/\overline{U}$ attained a maximum of 0.39 at y$^+$ = 5 and decreased considerably towards the wall and attained a value of 0.16 at y$^+$ = 0.6. One important consideration for near-wall hot-wire anemometry is the length of the hot-wire l$^+$ (in wall units). Ligrani & Bradshaw (1987b) indicated that the streamwise turbulence intensity is independent of l$^+$ in the buffer region and beyond provided $l^+ < 20{-}25$. Khoo *et al.* (1997) demonstrated that the streamwise turbulence intensity at a particular value of y$^+$ in the viscous sublayer attenuates in magnitude as l$^+$ increases and would incur an error of at most 5-10% if $l^+ \approx 20$.

Karlsson & Johansson (1988) employed a two-colour counter-based Argon-Ion LDV system to obtain velocity measurements in a turbulent boundary layer of a water channel, with Re$_\theta$ = 2420. They also obtained a u'$/\overline{U}$ distribution which displayed an approximately constant value of between 0.37 to 0.39 for $y^+ \leqslant 5$, which serves as a significant and independent comparison, as the measurements are

not based on hot-wire anemometry where wall effects influence the convective heat transfer characteristics of the wire. Recently, other near-wall LDV measurements have also been reported. Durst *et al.* (1995) made measurements using a two-component He-Ne LDV system in a pipe flow at Re_B (based on pipe diameter and bulk velocity) of 7442 and obtained an asymptotic value for $u'/\overline{U}$ of 0.37 as the wall was approached. Their results further indicated a slight increase in this asymptotic value as Re_B was increased.

Fontaine & Deutsch (1995) performed three-component, coincident, time resolved LDV measurements in the near-wall region of a pipe flow at a relatively much lower $Re_\theta \approx 720$ and obtained $u'/\overline{U}$ values in the viscous sublayer which compared favourably to those reported by Karlsson & Johansson (1988). However, it may be noted that near-wall LDV users have to contend and account for the drop in data rate as the wall is approached. This can be attributed to a decrease in particles close to the wall. Karlsson & Johansson reported that the substantial drop in data rate very near the wall compelled them to use a lower sampling frequency.

Another problem encountered in the use of LDV for near-wall velocity measurements is the relatively large control volume straddling a region of large velocity gradient. Measurements of near-wall turbulence thus require corrections to be applied to the gradient-broadening effects and the application of such corrections requires caution. As mentioned in Durst *et al.* (1995), "in the literature, no unique correction procedure exists to take this influence into account". If the gradient broadening effects are not accounted for or ad hoc correction methods are applied, the accuracy of near-wall turbulence measurements will greatly suffer. Niederschulte *et al.* (1990) performed two-component LDV measurements in a channel flow at $\mathrm{h}^+ = 178.6$ and 158.5 in an attempt to verify the accuracy of the DNS results of Kim *et al.* (1987). Niederschulte *et al.* did not report any attempt to correct for the gradient broadening effects and obtained a streamwise turbulence intensity $(u'/\overline{U})$ of approximately 0.4 for y^+ between 2.5 and 5. This is about 10% larger than the value of 0.36 obtained from the simulation results of Kim et al. For $y^+ < 2.5$, Niederschulte *et al.* found that the value of $u'/\overline{U}$ increases drastically, registering a maximum value of 0.54 at $y^+ = 1$, and attributed this disparity to the lack of accuracy in Kim *et al.*'s computation due to the use of insufficient nodes or an excessively small computational domain.

It is interesting to note that Niederschulte et al's observation of a rising trend in $u'/\overline{U}$ as the wall is approached for $y^+ < 2.5$ is remarkably similar to Durst *et al.*'s (1995) results which have *not* been corrected for gradient broadening effects. After correcting for the gradient broadening effects, however, Durst *et al.* were able to obtain a $u'/\overline{U}$ distribution for $y^+ < 2.5$ which conformed closely to the simulation results of Kim *et al.*. This is a testament illustrating the importance of implementing appropriate and valid correction techniques for gradient broadening effects encountered in near-wall LDV turbulence measurements.

It should be further mentioned that all the near-wall LDV measurements available in the literature are limited to relatively low Reynolds numbers, as severe spatial resolution problems are imposed by the finite width of the laser beam at high

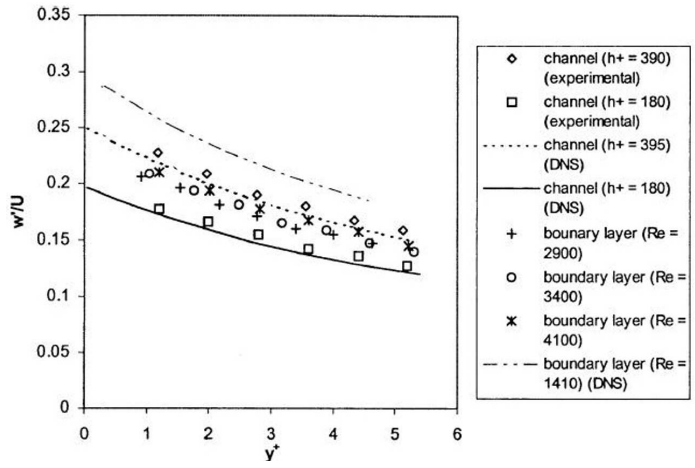

Figure 1.36: Spanwise turbulence intensity in the viscous sublayer.

Reynolds number. This is in addition to temporal resolution problems which can and usually arise due to the extremely low particle count very near the wall. On the other hand, it is always possible to extend the use of the near-wall hot-wire probe to high Reynolds numbers, as exemplified by the measurements we have made in the boundary layer flow at $\mathrm{Re}_\theta = 4100$, which is already higher than the Reynolds numbers of the flow reported by most of the near-wall LDA researchers available in the literature.

1.6.3(b) Spanwise velocity component

The local rms value of the spanwise velocity fluctuations normalized using the local mean velocity is shown in Fig.(1.36).

It is evident that the experimental results for the channel flow at $\mathrm{h}^+ = 180$ and 390 lie close to the respective DNS results of Kim *et al.* (1987) and Antonia *et al.* (1992), hence further attesting to the accuracy of the time-resolved velocity measurements by the near-wall hot-wire system. Similar to the streamwise turbulence intensity, the spanwise turbulence intensity distribution also shows an increasing trend for larger values of h^+, which is in line with the trend manifested by the simulation results. This may be again attributed to an 'inactive motion' which causes both the magnitudes of $\mathrm{u'}^+$ and $\mathrm{w'}^+$ to increase with Reynolds number, as previously discussed. Moreover, it seems plausible to suggest that an increase in Reynolds number causes an increase in vortex stretching in the inner region, thus resulting in a concomitant increase in the vorticity of the hairpin or quasi-streamwise vortices near the wall, which is subsequently accompanied by an increase in both $\mathrm{w'}^+$ and $\mathrm{v'}^+$ (not measured). At $h^+ = 180$, $w'/\overline{U}$ assumes a value of 0.18 at $y^+ \approx 1$. This value rises to 0.23 at the same y^+ for $h^+ = 390$. On the other

hand, the spanwise turbulence intensity at a given y^+ for the boundary layer flow only reveals a barely discernibly weak dependence on increasing Re_θ; this may be attributed to the relatively narrow range of Re_θ investigated in this present study. Overall, the spanwise intensity for the boundary layer flow exhibits a distribution closer to that for the channel flow at $h^+ = 390$. Unlike the streamwise turbulence intensity distribution depicted in Fig.(1.35), which shows that $u'/\overline{U}$ at a particular h^+ (or Re_θ) is approximately constant within the viscous sublayer, or at best only increasing very gradually as y^+ decreases, the spanwise intensity distribution presented in Fig.(1.36) shows that $w'/\overline{U}$ increases much more rapidly with decreasing y^+.

Spanwise turbulence intensity measurements in the viscous sublayer undertaken by other researchers utilizing hot-wire anemometry and LDV have also been reported in the literature, and it would be of interest to compare the present findings with available results. As previously discussed, Kreplin & Eckelmann (1979) made measurements in an oil channel using an in-house V hot-film probe. Their measurements indicated that $w'/\overline{U}$ registered a maximum value of 0.195 at $y^+ \approx 3.5$ and subsequently dropped to 0.065 at the wall. Similar to the trend borne by the streamwise turbulence intensity, the abrupt drop in the spanwise turbulence intensity as the wall was approached can be attributed to wall effects which had not been accounted for nor calibrated away. Our near-wall hot-wire measurements show the correct trend of $w'/\overline{U}$ rising as the wall is approached. Based on the comparison of their $u'/\overline{U}$ results in the viscous sublayer with those of Kreplin & Eckelmann, Alfredsson *et al.* (1988) suggested that the spanwise wall shear stress turbulence intensity (*i.e.* applicable at $y^+ = 0$) should be approximately equal to the maximum value of $w'/\overline{U}$ in the viscous sublayer obtained by Kreplin & Eckelmann, which was found to be approximately 0.2. Our spanwise turbulence intensity results, which range about 0.2 next to the wall, thus affirms the suggestion put forth by Alfredsson *et al.*. Near-wall spanwise turbulence intensity measurements have also been attempted by several researchers of late.

Karlsson (1993) employed a two-component Argon-Ion LDV system for measurements in a turbulent boundary layer at $Re_\theta = 2400$ and obtained a $w'/\overline{U}$ distribution which increased from approximately 0.12 to 0.18 as y^+ decreased from 5 to 1.5. This distribution is of similar trend but lower magnitude compared to the present boundary layer measurements obtained at higher Re_θ. Near-wall turbulence measurements using a two-component He-Ne LDV system were performed by Durst *et al.* (1995) in a pipe flow at Re_B (based on pipe diameter and bulk velocity) of 7442, yielding an asymptotic value for $w'/\overline{U}$ of 0.21 as the wall was approached. Fontaine & Deutsch (1995) conducted three-component, coincident, time resolved LDV measurements in the near-wall region of a pipe flow at $Re_\theta \approx 720$ and obtained $w'/\overline{U}$ values in the viscous sublayer which compared favourably to the DNS results of Antonia *et al.* (1992) and hence with our experimental results.

1.6.4 Turbulence kinetic energy in the viscous sublayer

Having obtained the streamwise (u') and spanwise (w') components of the velocity fluctuations in the viscous sublayer, it would be interesting to investigate the behavior of the turbulence kinetic energy (k), where

$$k = 0.5(u'^2 + v'^2 + w'^2) \tag{1.42}$$

and v' is the normal (to the wall) component of the fluctuating velocity. Neglecting the v' component in the viscous sublayer has very little effect on the evaluation of the turbulence kinetic energy k, as v' is likely to be negligible compared to u' and w' in the viscous sublayer. For example, Finnicum & Hanratty (1985) deduced the limiting value of v' in the immediate vicinity of the wall to be $v'^+ = 0.005y^{+2}$, while Kim et al (1987) deduced a correlation of $v'^+ = 0.009y^{+2}$ from their DNS results of a channel flow at $h^+ = 180$, with v' being merely 7% of u' at $y^+ \approx 5$, v' decreases very rapidly with decreasing y^+. Gunther *et al.* (1998) obtained a rather similar expression $v'^+ = 0.012y^{+2}$ as $y^+ \to 0$ for their DNS of a channel flow at $h^+ = 300$, with v' being 8% of u' at $y^+ \approx 5$. It may be noted that our use of the very near-wall hot-wire probe to measure the streamwise and spanwise turbulence intensities has inherently assumed that $v' << u'$ and $v' << w'$ in the viscous sublayer. The fact that our near-wall hot-wire results compare favorably to those of other researchers obtained using LDV and DNS provides evidence that this assumption is reasonable and valid in the viscous sublayer.

The distributions of the turbulence kinetic energy normalized using inner variables, k^+ ($\equiv u'^{+2} + v'^{+2} + w'^{+2}$) in the viscous sublayer for the channel and boundary layer flow, neglecting v', are depicted in Fig.(1.37). The experimental results for the channel flow at $h^+ = 180$ and 390 are observed to be reasonably compatible with the simulation results of Kim *et al.* (1987) and Antonia *et al.* (1992). This reaffirms that the neglect of v'^+ has little effect in the evaluation of k^+ in the viscous sublayer, especially for $y^+ \leqslant 4$. Moreover, the rise in k^+ at the same y^+ when h^+ is more than doubled is in line with the trend exhibited by the numerical results. This is not surprising, in view of the rise in u'^+ and w'^+ for the same y^+ when h^+ is increased, which may be attributed to an inactive motion or increased stretching of the vortices in the wall region, as previously discussed. Once again, the k^+ distribution for the boundary layer flow displays greater invariance corresponding to a rise in Re_θ, bearing closer similarity to the results for the channel flow at $h^+ = 390$.

From Fig.(1.37), it is further suggested that, with the exception of the results for the channel flow at $h^+ = 180$, the values of k^+ in the viscous sublayer ($y^+ \leqslant 5$) for the boundary layer flow at $2900 \leqslant Re_\theta \leqslant 4100$ and $h^+ = 390$ for a channel flow can be correlated well by

$$k^+ = -0.0059y^{+3} + 0.1081y^{+2}\,. \tag{1.43}$$

This correlation should be invaluable to users of the k-ε model in modeling the behavior of k in the viscous sublayer. Previously, Karlsson (1993) has also provided

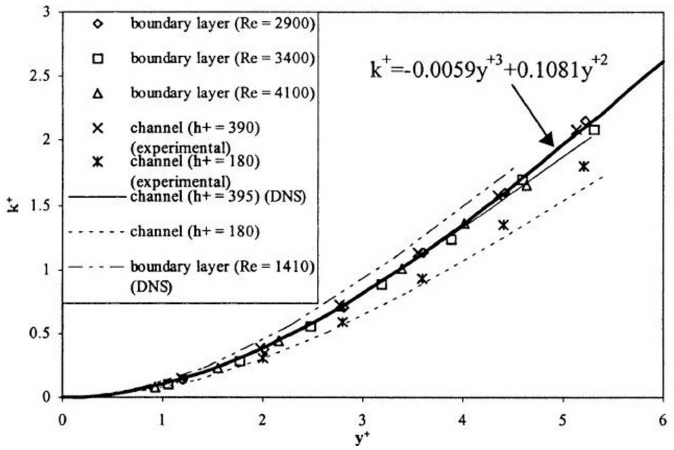

Figure 1.37: Distribution of normalized turbulence kinetic energy k^+ in the viscous sublayer.

a correlation equation of the form $k^+ = -0.0064y^{+3} + 0.096y^{+2}$ valid for $y^+ \leqslant 5$ for their near-wall LDV measurements in a turbulent boundary layer based solely on a *single* flow condition of $\mathrm{Re}_\theta = 2400$. This relation shows strong resemblance in characteristics to the equation proposed above except for the coefficients. Similarly, Kim *et al.*'s (1987) DNS of a channel flow computed at a single $h^+ = 180$ yields a correlation of $k^+ = -0.0066y^{+3} + 0.0829y^{+2}$ in the viscous sublayer; the difference lying only in the coefficients. At a higher h^+ of 300, Gunther *et al.*'s (1998) DNS results indicate a correlation of $k^+ \approx 0.1076y^{+2}$ in the viscous sublayer, the coefficient of y^{+2} in rather close agreement with ours. Correlations of this form are vital as they provide an avenue for assessing the ability/validity of two-equation and second-order near-wall turbulence closures in predicting near-wall turbulence statistics. Because of the existence of many proposed correlations, based on experiments or otherwise, it is imperative that accurate data be used as a basis of comparison *ab initio*. For example, Patel *et al.* (1985) used the correlation $k^+ = 0.05y^{+2}$ based on experimental data available then (these are near-wall hot-element measurements by Kreplin & Eckelmann, 1979 and others) to assess the behavior of various previously proposed two-equation turbulence closures. However, this correlation clearly yields k^+ values which are substantially lower than presently available DNS and experimental values (see Alfredsson *et al.*, 1988), and this can lead to incorrect assessment of turbulence models.

1.6.5 The dissipation rate

The full expression for the dissipation rate ε is given by

$$\varepsilon = \nu \overline{u_{i,j}(u_{i,j} + u_{j,i})}\,, \tag{1.44}$$

where $u_{i,j}$ represents the velocity derivative $\partial u_i/\partial x_j$. However, it should be noted that it is virtually impossible to measure all the 12 terms which appear on the right hand side of Eq.(1.44), especially in the near-wall region where wall influence increasingly dominates generally for all velocity-measuring instruments, including the hot-wire. The physical presence of the wall also causes problems in maneuvering the instrument to obtain a fine distribution across the usually thin viscous sublayer. By assuming the dissipating range of eddy sizes to be statistically isotropic, the dissipation rate ε_{iso} can be substantially simplified to

$$\varepsilon_{iso} = 15\nu\overline{(\frac{\partial u}{\partial x})^2}\,. \tag{1.45}$$

By further assuming the validity of Taylor's hypothesis, equation (1.45) becomes

$$\varepsilon_{iso} = 15\frac{\nu}{U_c^2}\overline{(\frac{\partial u}{\partial t})^2}\,, \tag{1.46}$$

where U_c is the local convection velocity, which is usually assumed to be equal to the mean velocity $\overline{U}$ at the point of measurement. Furthermore, if $E_u(k_1)$ is the spectral density of longitudinal velocity fluctuations, where the wavenumber $k_1 = 2\pi f/U_c$,

$$\varepsilon_{iso} = 15\nu\int_0^\infty k_1^2\, E_u(k_1)\, dk_1\,. \tag{1.47}$$

Equations (1.46) and (1.47) are two commonly used methods for estimating ε.

Azad & Kassab (1989) employed hot wires of different lengths and diameters in a boundary layer flow at $\mathrm{Re}_\theta \approx 4200$, $y/\delta = 0.1$ and obtained ε_{iso} using equations (1.46) and (1.47). For wires with the same length and diameter, Azad & Kassab found that the spectra (*i.e.* Eq.(1.47)) yielded results of ε_{iso} that were consistently higher than those obtained using $\overline{(\partial u/\partial t)^2}$ (*i.e.* Eq.(1.46)) by about 30%. They attributed the discrepancies to inadequacies in the "calibration of $\partial u/\partial$t, and other deterministic errors owing to the experimental set-up and the experimenter". Their measurements were made in the wall-remote region of $y^+ \geqslant 50$. However, in a separate study conducted by Elsner *et al.* (1993) in a turbulent channel flow, both methods were found to yield almost identical values for ε_{iso}, thus contradicting Azad & Kassab's contention that ε_{iso} yielded by spectra are consistently 30% higher.

To reconcile this apparent controversy of whether the spectra would yield larger values of ε_{iso}, both methods of evaluating ε_{iso} were applied to the present study of boundary layer flow at $\mathrm{Re}_\theta = 3400$ for the wall-remote region (as carried out in Azad & Kassab) and the near-wall region. The spectral density $\mathrm{E_u(k_1)}$ of longitudinal velocity fluctuations was obtained using a Fast Fourier Transform (FFT) algorithm, and the convective velocity U_c was also assumed to be the mean velocity $\overline{U}$ at the point of measurement. The distributions of ε_{iso}^+ employing these two methods are plotted on Fig.(1.38). As can be seen from the figure, both methods of evaluating ε_{iso} yield almost identical results throughout the entire

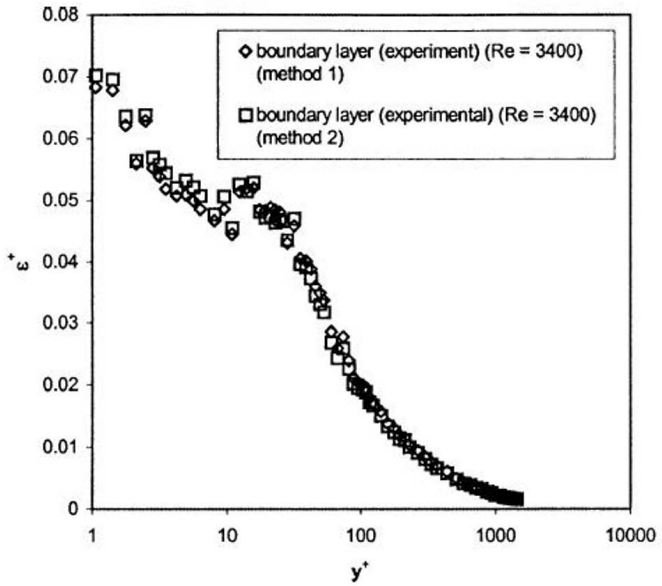

Figure 1.38: Distribution of normalized isotropic dissipation rate ε^+_{iso} dstribution in a boundary layer flow at $\mathrm{Re}_\theta = 3400$ using method 1: $\varepsilon_{iso} = 15\nu \int_0^\infty k_1 E_1(k_1) dk_1$ and method 2: $\varepsilon_{iso} = 15\nu \overline{(\partial u/\partial t)^2}/U_c^2$, with $U_c = \overline{U}$.

channel flow, even in the very near-wall viscous sublayer and buffer region. In particular, in the wall-remote region, the concurrence is almost exact.

Similar observations were also obtained for the channel flow at $\mathrm{h}^+ = 180$ and 390 as well as the boundary layer flow at other Re_θ (not shown), thus substantiating Elsner *et al.*'s argument that both methods should yield essentially identical values of ε_{iso}. It is conjectured that the persistently higher values of ε_{iso} obtained by Azad & Kassab using the spectra method might be attributed to an excessively low sampling frequency used and which have inordinate influence on the evaluation, thus rendering $\overline{(\partial u/\partial t)^2}$ to be grossly underestimated. However, this cannot be ascertained, as Azad & Kassab did not explicitly state the sampling frequency at which they have acquired their hot-wire data.

It would be of further interest to investigate the effects of using different expressions for the convective velocity U_c. Denoting $(\varepsilon_{iso})_1$ as the value of ε_{iso} evaluated by assuming the convective velocity U_c in equation (18) to be the mean velocity at the point of measurement, $\overline{U}$ (an approach widely adopted in the literature), the experimental values of $(\varepsilon^+_{iso})_1$ obtained for the channel flow at $h^+ = 390$ are plotted in Fig.(1.39) together with the true values for ε^+ corresponding to the DNS results of Antonia *et al.* (1992) for $h^+ = 395$. It is evident that the experimental

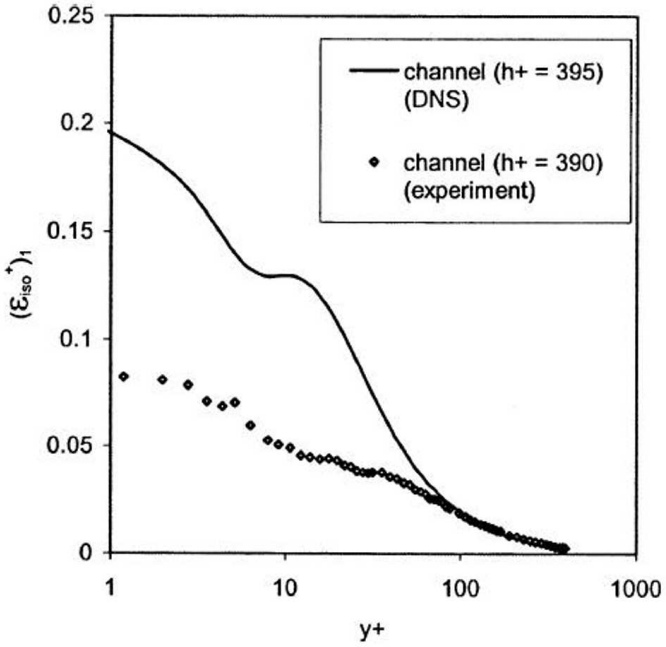

Figure 1.39: Experimental distribution of $(\varepsilon^+_{iso})_2$ and DNS results of ε^+ for a channel flow.

and computational results agree well only when

$$(y^+)_{1,critical} \geqslant 80\,. \tag{1.48}$$

This suggests the validity of assuming U_c to be equal to $\overline{U}$ *and* local isotropy in the evaluation of ε for large values of y^+, which is consistent with the widely accepted notion of local isotropy in a turbulent flow far from the wall (see Hinze, 1975). For low values of y^+, since the assumptions of local isotropy and Taylor's hypothesis are unlikely to be valid due to flow anisotropy in the strong shear flow region (where the strain rate is large), increasing discrepancies are observed between the computational and experimental results.

Strictly, the assumption that the convective velocity U_c is equal to the mean velocity $\overline{U}$ at the point of measurement when Taylor's hypothesis is invoked requires that the streamwise turbulence intensity be less than about 10% (see Saddoughi & Veeravalli, 1994, for example), which is clearly violated in the buffer region and especially in the viscous sublayer, where the streamwise turbulence intensity registers values as high as 40% (see Section 1.6.3(a)). Johansson *et al.* (1991) analyzed the DNS results of Kim *et al.* (1987) for a channel flow at $h^+ = 180$ using a VISA technique (the spatial counterpart of the VITA technique) and deduced that the propagation velocity of the near-wall shear layers was $10.6\mathrm{u}_\tau \pm 61.0u_\tau$.

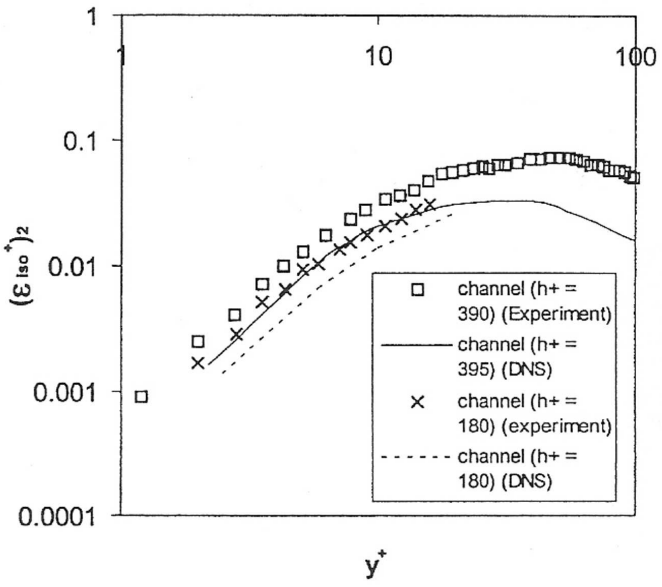

Figure 1.40: Experimental distribution of $(\varepsilon_{iso}^+)_1$ and DNS results for ε_{iso}^+ for a channel flow at different values of h^+.

Following the methodology of Kim *et al.*, Xu *et al.* (1996) conducted a DNS of a channel flow at $h^+ = 172$ to analyze the origin of high kurtosis levels of the normal velocity fluctuations in the viscous sublayer. Xu *et al.* observed that the high values of the kurtosis were due to extremely rare spatial and temporal events characterized by spikes in the time series with extremely negative values. These spikes only appeared in the very near-wall region and were propagated at a velocity of $10.6u_\tau \pm 0.8u_\tau$, which is strikingly close to the value deduced by Johansson *et al.*. It is interesting to note that the propagation velocity of shear layers, pressure fluctuations and spikes in the viscous sublayer ($\sim 10.6u_\tau$) is larger than the local mean velocity; this difference increases as the wall is approached. Denoting $(\varepsilon_{iso})_2$ as the value of ε_{iso} evaluated by assuming the convective velocity U_c in Eq.(1.47) to be $10.6u_\tau$, the distributions of $(\varepsilon_{iso}^+)_2$ $[\equiv (\varepsilon_{iso})_2\nu/u_\tau^4)]$ for the channel flows at $h^+ = 180$ and 390 are plotted in Fig.(1.40) together with the DNS results of Kim *et al.* (1987) for $h^+ = 180$ and Antonia *et al.* (1992) for $h^+ = 395$; the DNS results for ε_{iso} are obtained without invoking Taylor's hypothesis.

It can be seen that for both values of h^+, within the viscous sublayer and the inner portion of the buffer region, agreement between the experimental values of $(\varepsilon_{iso}^+)_2$ and the DNS results is fair. However, the experimental results are consistently greater than the DNS results, this difference increasing as y^+ increases, which is anticipated as the convective velocity is unlikely to remain constant at $10.6u_\tau$ further away from the wall. The experimental distribution for $(\varepsilon_{iso}^+)_2$ bears

the same trend as the DNS results for

$$(y^+)_{2,critical} \geqslant 15\,, \tag{1.49}$$

where the local turbulence intensity $u'/\overline{U}$ exceeds 25%. This suggests the reasonable assumption made above that $U_c = 10.6u_\tau$ in the flow region with $u'/\overline{U} > 0.1$ where it is no longer valid to accept the conventionally used relationship of $U_c = \overline{U}$. As h^+ increases from 180 to 390, the experimental value of $(\varepsilon^+_{iso})_2$ at the same y^+ increases, thus reflecting the presence of low Reynolds number effects. It should also be noted that the convective velocity of $10.6u_\tau$ in the very near-wall region deduced from DNS results is strictly valid and obtained for $h^+ \approx 180$, and it is not generally known if this value will change as h^+ increases. Experimental methods of determining the convective velocity have yielded results with marginally greater magnitudes. Johansson *et al.* (1987) used the VITA technique and obtained a value of $13u_\tau$ for the propagation velocity of near-wall shear layers, while Schewe (1983) experimentally obtained the propagation velocity of high-amplitude wall-pressure fluctuations to be approximately $12u_\tau$ in a boundary layer flow at Re_θ of 1400. It may be pointed out that if the convective velocity U_c is assumed to be $13u_\tau$ rather than $10.6u_\tau$, even closer agreement is obtained between the experimental and DNS results (not shown).

It may be of interest to examine how the experimentally obtained $(\varepsilon^+_{iso})_1$ and $(\varepsilon^+_{iso})_2$ compare with the true values of ε^+ obtained from DNS results. The ratios of $(\varepsilon^+_{iso})_1/\varepsilon^+$ and $(\varepsilon^+_{iso})_2/\varepsilon^+$ for the channel flow at $h^+ = 180$ and 390 are presented in Fig.(1.41). Also depicted in Fig.(1.41) are the DNS results for $(\varepsilon^+_{iso})/\varepsilon^+$, denoted by $(\varepsilon^+_{iso})_{DNS}/\varepsilon^+$ which is obtained without invoking Taylor's hypothesis.

It is evident that within the viscous sublayer and lower portion of the buffer region, agreement between $(\varepsilon^+_{iso})_2/\varepsilon^+$ and $(\varepsilon^+_{iso})_{DNS}/\varepsilon^+$ is much better than that between $(\varepsilon^+_{iso})_1/\varepsilon^+$ and $(\varepsilon^+_{iso})_{DNS}/\varepsilon^+$. This reiterates the finding from Fig.(1.40) that $10.6u_\tau$ is a better representation for the convective velocity U_c in the very near-wall region, as compared to $\overline{U}$. In the viscous sublayer, $(\varepsilon^+_{iso})_1/\varepsilon^+$ ranges from 0.3 to 0.4, this ratio bearing a slight but discernible increasing trend as h^+ increases for the same value of y^+. However, the ratios $(\varepsilon^+_{iso})_2/\varepsilon^+$ and $(\varepsilon^+_{iso})_{DNS}/\varepsilon^+$ are much less than 1 in the very near-wall region. For $h^+ = 395$, the DNS results reveal that $(\varepsilon^+_{iso})_{DNS}/\varepsilon^+$ decreases very rapidly from approximately 0.1 at $y^+ = 6$ to less than 0.01 at $y^+ = 2$. Similarly, the experimental results for $h^+ = 390$ depict a rapidly declining trend as y^+ decreases, with $(\varepsilon^+_{iso})_2/\varepsilon^+$ decreasing from 0.09 at $y^+ = 5.1$ to 0.005 at $y^+ = 1.2$. It is thus reasonable to suggest that although the assumption of local isotropy per se results in a severe underestimation of the actual value of ε, the additional assumption of Taylor's hypothesis with U_c assumed to be $\overline{U}$ has fortuitously served to reduce significantly the vast difference between the experimentally determined value and the actual value of ε. This is further exemplified by the results of ε obtained by Ligrani & Bradshaw (1987b) in a turbulent boundary layer at $y^+ = 17$. Taking the near-wall DNS results of Antonia *et al.* (1991) at $h^+ = 395$ to be equally applicable to a boundary layer flow, the DNS results reveal that at $y^+ = 17$, the value of $(\varepsilon^+_{iso})_{DNS}/\varepsilon^+$ is approximately 0.3. However, the experimental value of $(\varepsilon^+_{iso})_2/\varepsilon^+$ obtained by

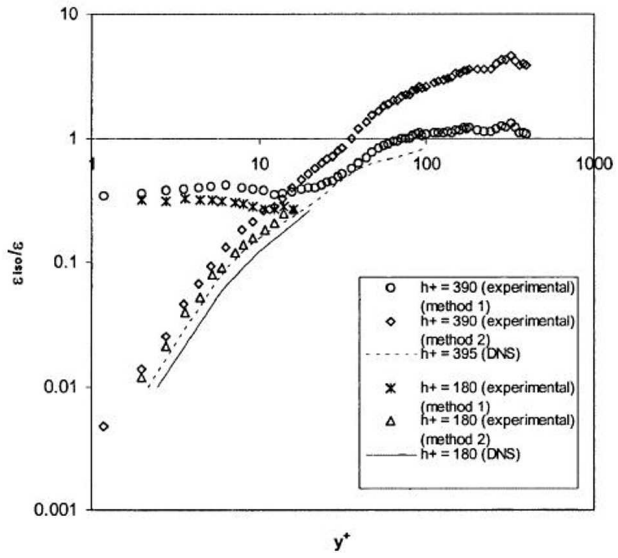

Figure 1.41: Distribution of $\varepsilon_{iso}/\varepsilon$ for a channel flow at different values of h^+, where $(\varepsilon_{iso})_1$, $(\varepsilon_{iso})_2$ and (ε_{iso}) are used to evaluate ε_{iso} for method 1, method 2 and DNS results, respectively.

Ligrani & Bradshaw was substantially higher at 0.55, thus lending support to the fact that Taylor's hypothesis (with $U_c = \overline{U}$) mitigates, to a certain extent, the underestimation of ε brought about solely by the assumption of local isotropy. Further away from the wall, for $y^+ \geqslant 100$, the value of $(\varepsilon^+_{iso})_{DNS}/\varepsilon^+$ approaches unity, thus substantiating the validity of local isotropy assumption for large values of y^+. Our experimental results show that the distribution for $(\varepsilon^+_{iso})_1/\varepsilon^+$ is close to 1 for $y^+ \geqslant 80$, which also reflects the validity of *both* the assumptions of local isotropy and Taylor's hypothesis with $U_c = \overline{U}$ for large values of y^+.

In addition, it should be noted that the value of the dissipation at the wall ε^+_w can be evaluated from the limiting value of the second derivative of the normalized turbulence kinetic energy k^+ with respect to y^+ as y^+ tends to zero. In fact, the expression

$$\varepsilon_w = \nu \left.\frac{\partial^2 k}{\partial y^2}\right|_{y=0}, \tag{1.50}$$

is often used as a boundary condition for ε in two-equation or second-order turbulence closures. The use of the correlation Eq.(1.43) obtained in Section 1.6.4 thus yields a value of 0.2162 for ε^+_w, which compares favorably to the value of 0.219 obtained by Antonia & Kim (1994) in their DNS of a channel flow at $h^+ = 395$. Based on the same methodology, Karlsson (1993) deduced a lower value of 0.192 for ε_w in a turbulent boundary layer ($\mathrm{Re}_\theta = 2400$) using LDV. The second derivative

of k^+ yields values of ε_w^+ which are more accurate. This can be attributed to the better accuracy of the measured distribution of k^+ and the fact that no assumptions of local isotropy and Taylor's hypothesis are made in evaluating ε_w^+. Next, one would like to investigate the slope of ε^+ at the wall, since the (usual) boundary condition imposed at the wall for two-equation and second-order turbulence closures can take the form of $(\partial\varepsilon^+/\partial y^+)|_{y^+=0} = 0$ (see Patel *et al.* (1985), for example). The present experimental results can be used to establish the validity of this wall boundary condition. It can further be shown that

$$\left.\frac{\partial\varepsilon^+}{\partial y^+}\right|_{y^+=0} = \frac{2}{3}\left.\frac{\partial^3(k^+)}{\partial(y^+)^3}\right|_{y^+=0} . \tag{1.51}$$

Based on correlation equation (1.43) ,$(\partial\varepsilon^+/\partial y^+)|_{y^+=0} = 4(-0.0059) = -0.0236$. This quantity is in reasonable agreement with the value of –0.0264 obtained by So *et al.* (1991). The latter quantity was estimated from available DNS results. One can observe that the slope of ε^+ at the wall is definitely not sufficiently small and certainly cannot be assumed to be negligible for application as a boundary condition for ε in turbulence studies, particularly for evaluation of turbulence closure models. The negative value of the slope of ε^+ at the wall indicates that ε increases as the wall is approached and possibly registers a maximum at the wall.

1.6.6 The convective velocity U_c

Experiments were performed to determine the convective velocities U_c of the streamwise velocity fluctuations in the boundary layer and channel flows under investigation. This was achieved by employing 2 hot wires separated by a streamwise distance of 9 mm and 10 mm for the boundary layer and channel flows, respectively. The near-wall hot-wire probe, with the active element placed 50 μm (corresponding to 2 wall units approximately) above the perspex wall substrate, is positioned upstream. The downstream wire consists of a DANTEC 55P15 single-wire probe located 0.35 mm above the wall (corresponding to approximately 13 wall units). The output voltages from the 2 wires are sampled simultaneously, and the two-point correlation for the streamwise velocity is determined from

$$R_{u1u2}(T) = \frac{\overline{u_1(t)u_2(t+T)}}{\overline{u_1^2(t)}} , \tag{1.52}$$

where u_1 and u_2 denote the instantaneous fluctuating streamwise velocities at the upstream and downstream locations, respectively. The time delay between the two velocities u_1 and u_2 is denoted by T. Results for the distribution of $R_{u1u2}(T)$ are plotted against T^+ ($\equiv Tu_\tau^2/\nu$) in Fig.(1.42) for the channel and boundary layer flows.

The time interval $(T^+)_{peak} = T_1^+$ corresponding to the peak value of $R_{u1u2}(T)$ signifies the time delay for the downstream instantaneous velocity to achieve a maximum correlation with the upstream instantaneous velocity. This value of T_1 and the streamwise separation of the 2 wires are used to evaluate the average

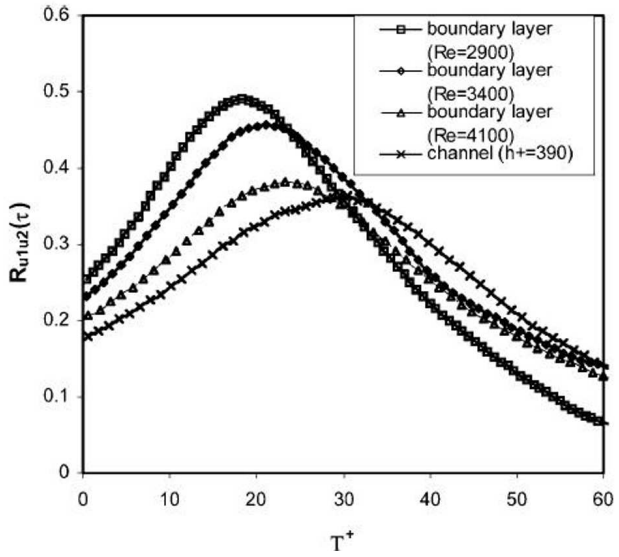

Figure 1.42: Distribution of two-point correlation with $T^+(Tu_\tau^2/\nu)$.

convective velocity U_c of the streamwise velocity fluctuations. This two-point correlation technique was also employed by Krogstad *et al.* (1998) to determine the convective velocities of ejections, sweeps and shear layers in a turbulent boundary layer at $Re_\theta = 1409$. At this point, it is worthy to highlight the relative advantage of hot-wire anemometry over LDV in determining spatial correlations very close to the wall. In addition to the costly requirement that two separate laser sources have to be employed, the extremely low particle count in the very near-wall region culminates in a low and variable data rate. It is thus not feasible to fix the time delay between the two LDV signals and the two point correlation as a function of the time delay $R_{u1u2}(T)$ cannot be determined in a straightforward fashion for the purpose of deducing the value of U_c.

The convective velocity U_c is found to be approximately $13u_\tau$ for the channel flow at $h^+ = 390$. For the boundary layer flow, U_c is observed to remain fairly constant at $15u_\tau$ for the range of Re_θ investigated. These values of U_c are perceptibly higher than those reported by other researchers in the literature. Johansson *et al.*'s (1991) VISA technique yielded a propagation velocity of $10.6u_\tau \pm 1.0u_\tau$ for near-wall shear layers of a channel flow at $h^+ = 180$, whereas Xu *et al.* (1996) deduced a coincidentally identical value of $10.6u_\tau \pm 0.8u_\tau$ for the propagation velocity of spikes in the very near-wall region based on DNS results of a channel flow at $h^+ = 172$. Using DNS results for a channel flow at $h^+ = 180$, Kim & Hussain (1993) found the propagation velocity for the streamwise velocity perturbations to be virtually constant at $9.6u_\tau$ in the viscous sublayer, which coincides with the convective velocity for the fluctuating streamwise wall shear stress reported by

Jeon *et al.* (1999) using the *same* DNS database. The experiments performed in a turbulent boundary layer flow at $Re_\theta = 1409$ by Krogstad *et al.* (1998) revealed a convective velocity ranging between $10.6u_\tau$ and $12.5u_\tau$ for the streamwise velocity fluctuations in the viscous sublayer at $y^+ = 5$. However, it should be noted that these reported values for U_c all pertain to low Reynolds number flows. Romano (1995) conducted two-point measurements of the streamwise velocity using LDV in a turbulent channel flow for values of h^+ ranging between 147 and 300. The convective velocity obtained at $y^+ = 20$ was found to exhibit an increasing trend with increasing Reynolds numbers. Unfortunately, Romano did not present any results for the convective velocity within the viscous sublayer for comparison to our own. Consistent with the findings of Romano, the marginally higher values of U_c we have obtained experimentally may be attributed to the higher Reynolds numbers for the boundary layer and channel flows in which we have performed our experiments.

Further experiments were performed to investigate the effect of the elevation of the upstream near-wall hot-wire on U_c. The elevation of the upstream near-wall hot-wire was varied between 25 and 100 μm (thus maintaining the upstream wire within the viscous sublayer), with the elevation of the downstream wire held fixed at 0.35 mm above the wall. Figure 1.43 shows results for U_c using the two-point correlation technique plotted against the elevation of the upstream near-wall hot-wire (expressed in wall units).

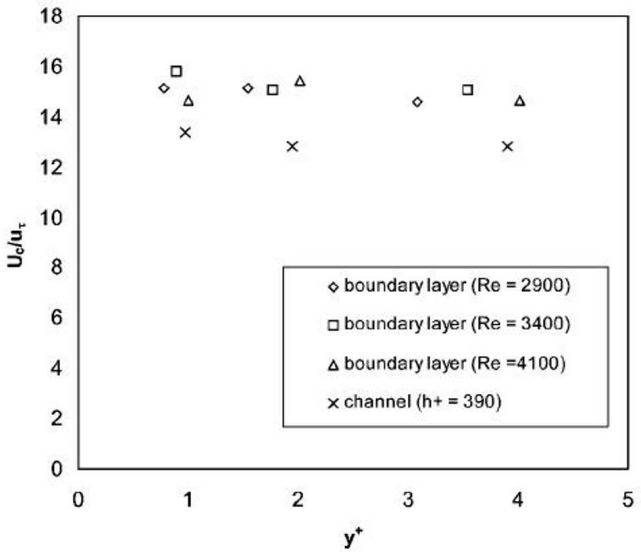

Figure 1.43: Convective velocity U_c for different values of y^+ in the viscous sublayer.

From Fig.(1.43), it can be clearly seen that under the same flow conditions, U_c remains fairly constant within the viscous sublayer and does not show any systematic dependence on y^+. Although the local mean velocity $\overline{U}$ increases linearly with elevation within the viscous sublayer and is zero at the wall, U_c assumes a constant value and bears a larger magnitude than $\overline{U}$ everywhere within the viscous sublayer. This may suggest that streamwise velocity perturbations propagate like waves in the very near-wall viscous sublayer region. A similar conclusion has been made by Kim & Hussain (1993), who obtained the streamwise component of the convective velocity U_c of velocity, vorticity and pressure fluctuations from the DNS results of a turbulent channel flow at $h^+ = 180$. It was found that U_c is approximately equal to the local mean velocity for most of the channel, with the exception of the near-wall region. For $y^+ < 15$, U_c was found to be virtually constant, thus signifying the wave propagating nature for perturbations of all flow variables very close to the wall. Krogstad *et al.* (1998) have also observed that U_c remains almost independent of y^+ for values of y^+ ranging between 5 and 40. As reported by Kim & Hussain, in the very near-wall region, streamwise vortices are temporally very persistent and do not lose their coherence for distances as long as $1000\nu/u_\tau$. The effective vertical mixing due to the presence of these vortices therefore suggests that the fluid particles very close to the wall are well correlated. The variation in U_c is thus expected to be negligible in the very near-wall viscous sublayer region.

It is of further interest to investigate whether the convective velocity U_c deduced using the two-point correlation technique is sensitive to the separation distance between the upstream and downstream probes. The experiments were further repeated for probe separation distances (s) of 6 and 12 mm. The upstream near-wall hot-wire was fixed at a distance of 50 μm from the wall, whilst the downstream hot-wire was placed 0.35 mm from the wall in both cases. The results of U_c for various probe separation distances s^+ (in wall units) are plotted in Fig.(1.44) for the boundary layer and channel flows.

It can be deduced from the figure that for identical flow conditions, U_c does not exhibit any systematic dependence on the probe separation for the range of separation distances investigated. The values of U_c derived for small probe separations are dominated by the small-scale motion and vice versa. The apparent invariance in U_c with probe separation thus suggests that very near the wall, events of different scales are probably convected at an almost constant velocity for the range of separation distances studied. In our experiments, distances larger than 12 mm were not used, as the peak value of two-point correlation $R_{u1u2}(T)$ defined in Eq.(1.52) becomes too small and the peak in the $R_{u1u2}(T)$ versus T^+ distribution becomes too ill-defined for the time delay T_1^+ and hence U_c to be determined accurately. On the other hand, separation distances smaller than 6 mm were not used, as the time delay T_1^+ becomes excessively small, thus culminating in considerable uncertainty in the determination of U_c. Furthermore, placing the two probes excessively close to each other may result in probe interference effects, especially for the downstream wire, which is likely to be influenced by the wake due to the prongs and the sensing element of the upstream probe.

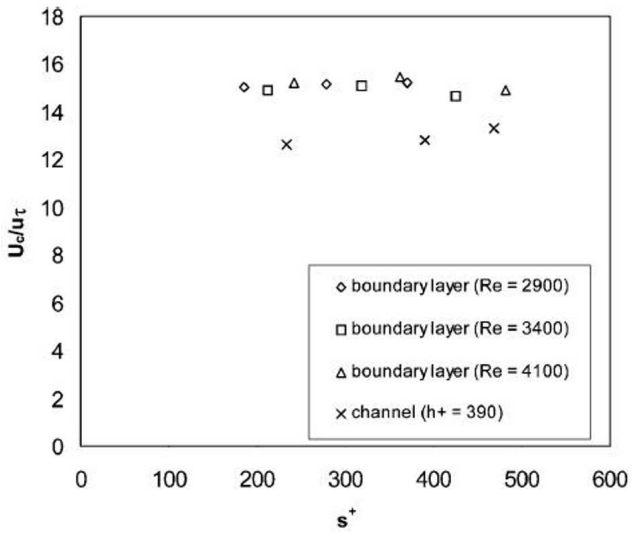

Figure 1.44: Convective velocity U_c for various probe separations s^+ (in wall units).

Krogstad (1998) reported that at $y^+ = 5$, U_c exhibits a very gradual increase with increasing probe separation, with U_c increasing by 11.5% when the probe separation distance was increased from 0.08δ to 1.54δ, thus suggesting that large-scale structures move at higher convective velocities than small-scale events. However, as mentioned above, when the two probes are placed excessively far apart (especially for 1.54δ, which corresponds to $930\nu/u_\tau$), it is expected that U_c can only be determined with increasingly large uncertainty, since the peak value of the two-point correlation becomes extremely small and the distribution of $R_{u1u2}(T)$ against T^+ becomes much flatter, with the consequence that the determination of the time delay T_1^+ for which the peak occurs becomes much more ambiguous. The gradual rise in U_c over such large separation distances in the midst of greater experimental uncertainty may have suggested the difference in trend observed for Krogstad and the present results (obtained for smaller range of separation distance) is not that significant or contradictory. Kim & Hussain (1993) performed bandpass filtering of DNS data for a turbulent channel flow at $h^+ = 180$ to investigate the scale-dependence of U_c.

In contrast to Krogstad, Kim & Hussain found that the large-scale events are convected at lower velocities than the small-scale events, although the variation turns out to be rather insignificant. However, this observation is inconsistent with results of Jeon *et al.* (1999), who obtained the convective velocity of wall shear stress fluctuations for a turbulent channel flow at the same h^+ of 180. Jeon *et al.* concluded that in general, large-scale fluctuations tended to have larger values of U_c as compared to small-scale fluctuations. However, when a overall

convective velocity for the streamwise wall shear stress fluctuations was used to convert the one-dimensional frequency power spectrum into the streamwise wave-number power spectrum for the purpose of testing Taylor's hypothesis, there was excellent agreement between the streamwise wave-number spectrum using Taylor's hypothesis and the actual spectrum.

In conclusion, different researchers have reported conflicting trends for the scale dependence of U_c corresponding to the streamwise velocity fluctuations in the very near-wall region. However, the general consensus is that this scale dependence on U_c is probably very marginal in the very near-wall region, which is reiterated from our experimental results, showing no systematic dependence of U_c on the probe separation distance. It is thus logical to assume a single representative or overall convective velocity for all scales in the very near-wall region. In adopting such an approach, substantial simplifications can be made in the practical implementation of Taylor's hypothesis and turbulence modeling.

1.6.7 The integral time scale

The longitudinal (streamwise) autocorrelation between the values of u(t) at times t and $t + \tau_1$ is defined as

$$R_u(\tau_1) = \lim_{T\to\infty} \frac{1}{T} \int_0^T u(t)\, u(t+\tau_1)\, dt \tag{1.53}$$

and the autocorrelation coefficient function can be subsequently obtained from the expression

$$\rho_u(\tau_1) = R_u(\tau_1) \,/\, \overline{u^2}\,. \tag{1.54}$$

The longitudinal (streamwise) integral time scale is then evaluated using

$$T_u = \int_0^\infty \rho_u(\tau_1)\, d\tau_1\,. \tag{1.55}$$

The dimensionless integral time-scale T_u^+ (normalized using inner variables) for the viscous sublayer of the channel and boundary layer flows is presented in Fig.(1.45).

It can be seen that for each h^+ for the channel flow and Re_θ for the boundary layer flow, T_u^+ is almost constant within the viscous sublayer. The channel flow seems to exhibit slightly lower values of T_u^+ than the boundary layer flow in the viscous sublayer. The channel flow yields T_u^+ values close to 15, while perceptibly higher values close to 18 are obtained for the boundary layer flow. Once again, it would be of interest to compare the experimental results to those of DNS and others. However, no such information is available directly in the literature to the best knowledge of the authors. Kim *et al.* (1987) presented two-point spatial correlations in the streamwise direction at $y^+ = 5.39$ for their channel flow DNS at $h^+ = 180$ and the longitudinal integral length scale at that location was estimated

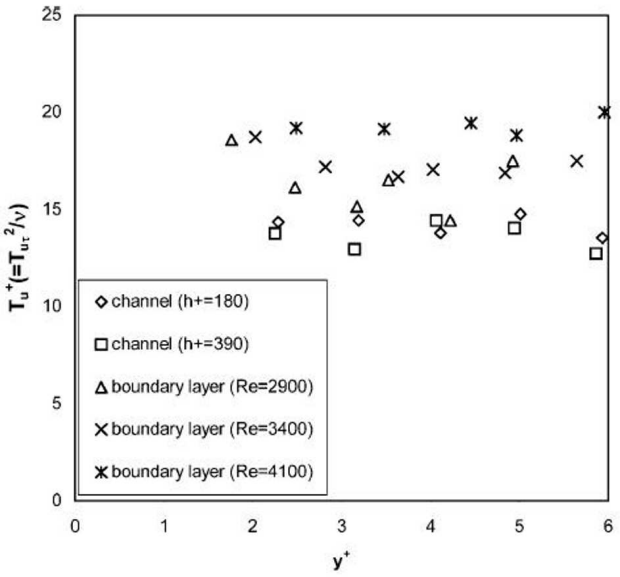

Figure 1.45: Longitudinal integral time scale (in wall units) in the viscous sublayer.

to be $190\nu/u_\tau$. According to Taylor's hypothesis, the integral length and time-scales at a particular point are simply related via the convective velocity U_c at that point. However, as discussed in Section 1.6.5, the conventional procedure of assuming the convective velocity U_c to be the mean velocity $\overline{U}$ at the point of measurement in Taylor's hypothesis only applies if the turbulence intensity does not exceed 10%, which is strictly not valid in the viscous sublayer. As mentioned in Section 1.6.6, Kim & Hussain (1993) used Kim *et al.*'s (1987) DNS results for a channel flow at $h^+ = 180$ and found the propagation velocity for the streamwise velocity perturbations to be virtually constant at $9.6u_\tau$ in the viscous sublayer. If an integral length-scale of $190\nu/u_\tau$ and a convective or propagation velocity of $9.6u_\tau$ is assumed in the viscous sublayer, the integral time-scale would work out to be approximately $20u_\tau^2/\nu$, which compares reasonably with the value of $15u_\tau^2/\nu$ obtained experimentally for the channel flow. Moreover, Spalart (1988) conducted a DNS of a turbulent boundary layer and commented that near the wall, a typical time-scale of turbulence is $15u_\tau^2/\nu$. This is in reasonable accord with our experimental findings of $T_u^+ \approx 18$ for boundary layer flows.

1.6.8 Concluding remarks for Section 1.6

Very near-wall velocity measurements were carried out using a specially constructed hot-wire probe in both a fully developed turbulent channel flow at $h^+ = 180$ and 390 and flat plate boundary layer flow at Re_θ of 2900, 3400 and 4100. The

near-wall hot-wire probe, having been calibrated in a specially constructed laminar flow calibration rig, was found to be capable of registering the mean velocity profile and distributions of streamwise and spanwise intensities of turbulence as well as turbulence kinetic energy k in the viscous sublayer; these distributions comparing favorably to available DNS results. Low Reynolds number effects were evident for the channel flow, as manifested by the monotonic increase in the streamwise and spanwise turbulence intensity as well as the turbulence kinetic energy k for the same value of y^+ when h^+ was more than doubled from 180 to 390.

By assuming the validity of Taylor's hypothesis, the dissipation rate ε_{iso} in the very near-wall viscous sublayer region and beyond was determined by assuming the dissipating range of eddy sizes to be statistically isotropic. If the convective velocity U_c in Taylor's hypothesis was assumed to be equal to the mean velocity $\overline{U}$ at the point of measurement, the value of $(\varepsilon^+_{iso})_1$ thus obtained was found to agree well with that of $(\varepsilon^+)_{DNS}$ for $y^+ \geqslant 80$, hence suggesting the validity of assuming $U_c = \overline{U}$ *and* local isotropy for large values of y^+. However, for $y^+ \leqslant 80$, $(\varepsilon^+_{iso})_1$ was found to underestimate $(\varepsilon^+)_{DNS}$, this discrepancy increasing as y^+ decreases. However, if U_c was assumed to be $10.6u_\tau$, the value of $(\varepsilon^+_{iso})_2$ thus obtained was found to compare reasonably well to the distribution of $(\varepsilon^+_{iso})_{DNS}$ for $y^+ \leqslant 15$, thus suggesting the reasonable assumption that $U_c = 10.6u_\tau$ in the viscous sublayer and inner part of the buffer region, where the local streamwise turbulence intensity grossly exceeds 10% and it is no longer valid to assume $U_c = \overline{U}$.

On the other hand, experiments performed to determine the convective velocity U_c of the streamwise velocity fluctuations in the viscous sublayer yielded values of $13u_\tau$ and $15u_\tau$ respectively for the channel flow at $h^+ = 390$ and the boundary layer flows under investigation. It was also found that the value of U_c remains fairly constant within the viscous sublayer and does not show any systematic dependence on y^+, thus suggesting that streamwise velocity perturbations propagate like waves in the very near-wall viscous sublayer region. U_c was also found to be relatively independent of the separation distance between the two hot-wire probes, thus implying that it is reasonable to assume a single representative or overall convective velocity for all scales in the very near-wall region, which leads to tremendous simplifications in the application of Taylor's hypothesis and turbulence modelling. Finally, the dimensionless integral time scale T^+_u for the viscous sublayer of the channel and boundary layer flows worked out to be 15 and 18, respectively; these values are in reasonable agreement with those deduced from DNS.

Further discourse on this Section 1.6 can be found in Khoo *et al.* (2000, 2001).

1.7 Overall concluding summary

Experiments using the electronic square-wave voltage perturbation test (Section 1.4.1) were systematically performed for the first time to evaluate the response frequency (f_S) of near-wall hot wires. In addition, two commercially available flush-mounted wall shear stress gauges were tested. At a fixed wire height above the wall substrate, an increase in the convective velocity leads to an increase in

f_S. For a hot-wire exposed to a constant convective velocity, f_S increases with decreasing heights from the wall substrate. This is also equivalent to a decreasing h^+ with increasing effect of wall influence, hence suggesting that f_S improves with greater wall effects. A hot-wire mounted at the same height h = 50 μm above a thermally more conducting Aluminium wall substrate exhibits a higher value of f_S compared to its counterpart above a Perspex wall substrate under similar operating conditions. These findings strongly suggest that f_S increases with increasing heat transfer from the wire, regardless of whether it is due to forced/natural convection or effects of wall influence.

For a flush-mounted hot-wire, an increase in the imposed wall shear stress yields a corresponding increase in f_S. The value of f_S (with and without "tail") for the DANTEC 55R45 wall shear stress gauge is consistently higher than that for the 55R46 gauge, hence indicating the better frequency response of the 55R45 gauge.

Results of the frequency response according to square-wave voltage perturbation tests (f_S) were then compared to those obtained using velocity perturbation tests (f_D) in Section 1.3.1 and Section 1.3.2. Although f_S and f_D show similar trends for the near-wall hot- wire and hot-film probes, f_S is consistently greater than f_D. The magnitudes of f_S and $f_D$are vastly different, being an order of magnitude for the marginally-elevated and flush-mounted hot wires. For the hot-film wall shear stress probes, this (ratio) difference is up to five orders of magnitude (without "tail") and three orders of magnitude (with "tail"). From a user's point of view, however, the dynamic frequency response (f_D) should serve as a more accurate indicator of the overall frequency response of the hot-wire/film system, since f_D signifies the onset of amplitude attenuation when the hot-wire/film is subjected to *direct* velocity or shear stress perturbations. The large differences in magnitude between f_S and f_D show that the square-wave voltage perturbation test may not be all-sufficient in establishing the response frequency of a near-wall hot-wire or flush-mounted hot-film shear stress probes.

Separately, the cutoff frequency of the anemometer yielded by the sine-wave test (f_{sine}) in Section 1.4.2 was found to be in fair agreement and to exhibit the same trends as results obtained using the traditional electronic square-wave voltage perturbation test (f_S). For the hot-film gauges, f_{sine} obtained for the DANTEC 55R45 gauge was consistently higher that those for its 55R46 counterpart under identical conditions of overheat ratio and wall shear stress (τ). For both gauges, an increase in overheat ratio resulted in a rise in f_{sine}, whereas variations in τ for the same overheat ratio did not seem to have cast any effect. For the marginally-elevated hot-wire probes, an increase in the convective velocity (V) leads to an increase in f_{sine} when the wire is either kept at a fixed physical distance or at the same y^+ above the wall substrate. When V is held constant, a decrease in y^+ signifying increased wall influence culminates in larger values of f_{sine}. These results suggest that f_{sine} increases with increasing heat transfer from the wire, regardless of whether it is due to forced convection or effects of wall influence. For the flush-mounted hot-wire wall shear stress sensor, an increase in the imposed τ results in a corresponding increase in f_{sine}.

Apart from yielding the cutoff frequency of the anemometer, the sine-wave test is also capable of indicating the flatness of the frequency response over a limited frequency range and detect the presence of any amplitude attenuation which arises as a result of the attenuation of heat waves to the surrounding wall substrate at high frequencies. A significant bulging effect appears in the sine-wave test response curves for the hot-film wall shear stress probes. A causality relationship $f_{bulge} \approx 20 f_D$ was observed for the hot-film gauges, where f_{bulge} and f_D denote the frequency characterizing the bulging effect and the dynamic frequency response respectively. Compared to f_S (and f_{sine}) which is five orders of magnitude greater than f_D, f_{bulge} provides a much better indicator or proxy for predicting f_D. It is to be realized that in the application of the hot-film wall shear stress gauges to measure fluctuating shear stress in a turbulent flow, it is the lower dynamic response frequency f_D which sets an upper limit to the overall responsiveness of the gauge. For the flush-mounted and marginally-elevated hot-wire sensors, a very slight bulging effect was also observed in the 0.8 to 4 kHz range, which corresponds much more closely to the values of f_D. This is contrasted to f_S, which is typically one order of magnitude larger than f_D. The frequencies f_{bulge} and f_D can be related by the causality relationship $f_{bulge} \sim f_D$ for the near-wall hot-wire probes. It must be noted that the lower magnitude f_D is the critical frequency ultimately determining the responsiveness of the near-wall hot-wire probe to fluctuating velocities expected in a turbulent flow. Therefore, it is suggested that instead of relying solely on the square-wave test, users of near-wall hot-wire or hot-film anemometers who do not have access to dynamic perturbation testing facilities should perform a sine-wave test to detect the presence of any amplitude attenuation for frequencies (f_{bulge}) below the cutoff frequency.

Very near-wall velocity measurements were carried out using a specially constructed hot-wire probe in both a fully developed turbulent channel flow at $h^+ = 180$ and 390 and flat plate boundary layer flow at Re_θ of 2900, 3400 and 4100. Further by assuming the validity of Taylor's hypothesis, the dissipation rate ε_{iso} in the very near-wall viscous sublayer region and beyond was determined by assuming the dissipating range of eddy sizes to be statistically isotropic. If the convective velocity U_c in Taylor's hypothesis was assumed to be equal to the mean velocity $\overline{U}$ at the point of measurement, the value of $(\varepsilon^+_{iso})_1$ thus obtained was found to agree well with that of $(\varepsilon^+)_{DNS}$ for $y^+ \geqslant 80$, hence suggesting the validity of assuming $U_c = \overline{U}$ *and* local isotropy for large values of y^+. However, for $y^+ \leqslant 80$, $(\varepsilon^+_{iso})_1$ was found to underestimate $(\varepsilon^+)_{DNS}$, this discrepancy increasing as y^+ decreases

Finally, experiments performed to determine the convective velocity U_c of the streamwise velocity fluctuations in the viscous sublayer yielded values of $13u_\tau$ and $15u_\tau$ respectively for the channel flow at $h^+ = 390$ and the boundary layer flows under investigation. It was also found that the value of U_c remains fairly constant within the viscous sublayer and does not show any systematic dependence on y^+, thus suggesting that streamwise velocity perturbations propagate like waves in the very near-wall viscous sublayer region. U_c was also found to be relatively independent of the separation distance between the two hot-wire probes, thus implying that it is reasonable to assume a single representative or overall convective

velocity for all scales in the very near-wall region, which leads to tremendous simplifications in the application of Taylor's hypothesis and turbulence modelling. The dimensionless integral time scale T_u^+ for the viscous sublayer of the channel and boundary layer flows worked out to be 15 and 18, respectively; these values are in reasonable agreement with those deduced from DNS.

Acknowledgments

The authors would like to put into record the contributions of our collaborators, namely G. L. Li, C. P. Lim and C. J. Teo to this series of works carried out at the National University of Singapore. A special word of thanks to Jeremy Chen who helped to prepare the notes.

One of us (BCK) gratefully acknowledges the financial sponsorship of the Brazilian Association of Mechanical Sciences and Engineering and Brazil's National Research Council to present at the Spring School on Transition and Turbulence 2006.

1.8 References

Alfredsson P., Johansson A., Haritonidis J. and Eckelmann H.; "The fluctuating wall-shear stress and the velocity field in the viscous sublayer," *Phys. Fluids* **31**, 1026-1033 (1988).

Antonia R. A., Teitel M., Kim J. and Browne L. W. B.; "Low-Reynolds-number effects in a fully developed turbulent channel flow," *J. Fluid Mech.* **236**, 579-605 (1992).

Antonia R. A. and Kim J. X.; "Low Reynolds number effects on near-wall turbulence," *J. Fluid Mech.* **276**, 61-80 (1992).

Azad R. S.; "Corrections to measurements by hot-wire anemometer in the proximity of a wall," *Report MET-7* Dept. Mech. Eng. Univ. of Manitoba, Winnipeg, Canada (1983).

Azad R. S. and Kassab S. Z.; "A new method of obtaining dissipation," *Exps. Fluids* **7**, 81-87 (1989).

Bellhouse B. J. and Schultz D. L.; "The determination of fluctuating velocity in air with heated thin film gauges," *J. Fluid Mech.* **29**, 289-295 (1967).

Bellhouse B. J. and Rasmussen, C. G.; "Low-frequency characteristics of hot film anemometers," DISA Information **6**, 3-10 (1968).

Berger E., Freymuth P. and Froebel E.; "Theorie and konstruktion von konstant-temperatur-hitzdrahtanemometern," *Konstruktion* **15**, 495-497 (1963).

Bradshaw P.; "'Inactive' motion and pressure fluctuations in turbulent boundary layers," *J. Fluid Mech.* **30**, 241-258 (1967).

Bremhorst K. and Gilmore D. B.; "Influence of end conduction on the sensitivity to stream temperature fluctuations of a hot-wire anemometer," *Int. J. Heat & Mass Transfer* **21**, 145-54 (1978).

Bhatia J. C., Durst F. and Johanovic J.; "Corrections of hot-wire anemometer measurements near walls," *J. Fluid Mech.* **122**, 411-431 (1982).

Brown G. L. and Davey R. F.; "The calibration of hot-films for skin friction measurement," *Rev. Sci. Instrum.* **42**, 1729-1731 (1971).

Bruun H. H.; "Hot-wire anemometry," Oxford University Press (1995).

Cendese A., Romano G. P. and Antonia R. A.; "A comment on the 'linear' law of the wall for fully developed turbulent channel flow" *Exps. Fluids* **25**, 165-170 (1998).

Chew Y. T., Khoo B. C. and Li G. L.; "A time-resolved hot-wire shear stress probe for turbulent flow: use of laminar flow calibration," *Exp. Fluids* **17**, 75-83 (1994).

Chew Y. T., Shi S. X. and Khoo B. C.; "On the numerical near-wall corrections of single hot-wire measurements," *Int. J. Heat & Fluid Flow* **16**, No. 6, 471-476 (1995).

Chew Y. T., Khoo B. C. and Li G. L.; "The investigation of the wall effects on hot-wire measurements using a bent sublayer probe," *Meas. Sci. Tech.* **9**, 67-85 (1998).

Chew Y. T., Khoo B. C. and Li G. L.; "Dynamic response of hot-wire anemometer. Part II: A flush-mounted hot element for wall shear stress measurements," *Meas. Sci. Tech.* **9**, 762-776 (1998).

Coles D. E.; "The turbulent boundary layer in a compressible fluid." Report R-403-PR, The Rand Corporation, Santa Monica, CA (1962).

Comte-Bellot G., Strohl A. and Alcarez E.; "On aerodynamic disturbances caused by a single hot-wire probe," *Trans. ASME J. Appl. Mech.* **93**, 767-774 (1971).

Comte-Bellot G.; "The physical background for hot film anemometry," *Proc. Symp. on Turbulence in Liquids*, University of Missouri, Rolla, 1-13 (1977).

Cook W. J.; "Response of hot-element wall shear stress gauges in unsteady turbulent flows," *A.I.A.A. Journal* **32**, 1464-1471 (1994).

Cook W. J. and Giddings T. A.; "Response of hot-element wall shear-stress gages in laminar oscillating flows," *AIAA J.* **26**, 706-713 (1988).

Davis M. R.; "The dynamic response of constant resistance anemometers," *J. Phys. E: Sci. Instrum.* **3**, 15-20 (1970).

Durst F., Jovanovic J. and Sender J.; "LDA measurements in the near-wall region of a turbulent pipe flow," *J. Fluid Mech.* **295**, 305-335 (1995).

Elsner J. W., Domagala P. and Elsner W.; "Effect of finite spatial resolution of hot-wire anemometry on measurements of turbulence energy dissipation," *Meas. Sci. Tech.* **4**, 517-523 (1993).

Fernholz H. H. and Finley P. J.; "The incompressible zero-pressure-gradient turbulent boundary layer: an assessment of the data," *Prog. Aerospace Sci.* **32**, 245-311 (1996).

Fernholz H. H. and Warnack D.; "The effects of a favourable pressure gradient and of the Reynolds number on an incompressible axisymmetric turbulent boundary layer. Part 1. The turbulent boundary layer," *J. Fluid Mech.* **359**, 329-356 (1998).

Finnicum D. S. and Hanratty T. J.; "Turbulent normal velocity fluctuations close to a wall," *Phys. Fluids* **28**, 1654-1658 (1985).

Fontaine A. A. and Deutsch S.; "Three-component, time-resolved velocity statistics in the wall region of a turbulent pipe flow," *Exps. Fluids* **18**, 168-173 (1995).

Freymuth P.; "Frequency response and electronic testing for constant-temperature hot-wire anemometers," *J. Phys. E: Sci. Instrum.* **10**, 705-710 (1977).

Freymuth P. and Fingerson L. M.; "Electronic testing of frequency response for thermal anemometers. *TSI Quart.* **III**, No. 4, 5-12 (1977).

Freymuth P.; "Theory of frequency optimisation for hot-film anemometers," *J. Phys. E: Sci. Instrum.* **11**, 177-179 (1978).

Freymuth P.; "Sine-wave testing of non-cylindrical hot-film anemometers according to the Bellhouse-Schultz model," *J. Phys. E: Sci. Instrum.* **13**, 98-102 (1980).

Freymuth P.; "Calculation of square-wave test for frequency optimised hot-film anemometers," *J. Phys. E: Sci. Instrum.* **14**, 238-240 (1981).

Gunther A., Papavassiliou D. V., Warholic M. D. and Hanratty T. J.; "Turbulent flow in a channel at a low Reynolds number," *Exps. Fluids* **25**, 503-511 (1998).

Guo Z. X. and Hyung J. S.; "Analysis of the Nusselt number in a pulsating pipe flow," *Int. J. Heat Mass Transfer* **40**, 2486-2489 (1997).

Hebbar K. S.; "Wall proximity corrections for hot-wire readings in turbulent flows," *DISA Information* **25**, 15-16.

Hinze J. O.; "Turbulence. An introduction to its mechanism and theory," McGraw-Hill, New York (1959).

Hinze J. O.; "Turbulence," 2^{nd} Ed., McGraw-Hill, New York, (1975).

Houdeville R., Juillen J. C. and Cousteix J.; "Skin friction measurements with hot-element gauges," *Recherche Aerospatial* **1**, 67-79 (1984).

Huang J. B., Ho C. M., Tung S., Liu C. and Yu C. T.; "Micro thermal shear stress sensor with and without cavity underneath," *IEEE IMTC (Instrumentation Measurement Technology Conf.)* Waltham, Massachusetts, 171-174 (1995).

Huang J. B., Tung S., Ho C. M., Liu C. and Tai Y. C.; "Improved micro thermal shear stress sensor," *IEEE Trans. Instrum. Meas.* **45**, 570-574 (1996).

Isomoto K. and Honami S.; "The effect of inlet turbulence intensity on the reattachment process over a backward-facing step," *Trans. ASME J. Fluids Eng.* **111**, 87-93 (1989).

Jeon S., Choi H., Jung H. H. and Moin P.; "Space-time characteristics of the wall shear-stress fluctuations in a low-Reynolds-number channel flow," *Phys. Fluids* **11**, 3084-3094 (1999).

Johansson A. V., Alfredsson P. H. and Eckelmann H.; "On the evolution of shear-layer structures in near-wall turbulence" in *Advances in turbulence,* Comte-Bellot G., and Mathieu J. (editors). Proc. First European Turbulence Conf., Lyon, July (1986).

Johansson A. V., Alfredsson P. H. and Kim J.; "Evolution and dynamics of shear-layer structures in near-wall turbulence," *J. Fluid Mech.* **224**, 579-599 (1991).

Karlsson R. I. and Johansson T. G.; "LDV measurements of higher order moments of velocity fluctuation in a boundary layer," *Third Int. Symp. on Application of Laser Anemometry to Fluid Mech.* Adrian, R. J. *et al.* (editors), 273-289. Lisbon, Portugal (1988).

Karlsson R. I.; "Near-wall measurements of turbulence structure in boundary layers and wall jets." *Near-Wall Turbulent Flows* So, R. M. C. *et al.* (editors). Amsterdam, Elsevier (1993). 423-432.

Khoo B. C., Chew Y. T. and Li G. L.; "A new method by which to determine the dynamic response of marginally hot-wire anemometer probes for near-wall velocity and wall shear stress measurements," *Meas. Sci. Tech.* **6**, 1399-1406 (1995).

Khoo B. C., Chew Y. T. and Li G. L.; "Time-resolved near-wall hot-wire measurements: use of laminar flow wall correction curve and near-wall calibration technique," *Meas. Sci. Tech.* **7**, 564-575 (1996).

Khoo B. C., Chew Y. T. & Li G. L. 1997: Effects of imperfect spatial resolution on turbulence measurements in the very near-wall viscous sublayer region. *Exp. Fluids* 22, 327-335.

Khoo B. C., Chew Y. T., Lim C. P. and Teo C. J.; "Dynamic response of hot-wire anemometer. Part I: A marginally-elevated hot-wire probe for near-wall velocity measurements," *Meas. Sci. Tech.* **9**, 749-761 (1998).

Khoo B. C., Chew Y. T. and Lim C. P.; "The flow between a rotating and a stationary disk: Application to near-wall hot-wire calibration," *Meas. Sci. Tech.* **9**, 650-658 (1998).

Khoo B. C., Chew Y. T., Teo C. J. and Lim C. P.; "The dynamic response of a hot-wire anemometer. Part III: Voltage perturbation versus velocity-perturbation testing for near-wall hot-wire/film probes," *Meas. Sci. Tech.* **10**, 152-169 (1999).

Khoo B. C., Chew Y. T., and Teo C. J.; "On near-wall hot-wire measurements," *Exp. Fluids* **29**, 448-460 (2000).

Khoo B. C., Chew Y. T., and Teo C. J.; "Near-wall hot-wire measurements. Part II: Turbulence time scale, convective velocity and spectra in the viscous sublayer," *Exp. Fluids* **31**, 494-505 (2001).

Kim J. and Hussain F.; "Propagation velocity of perturbations in turbulent channel flow," *Phys. Fluids.* **5**, 695-706 (1993).

Kim J., Moin P. and Moser R.; "Turbulence statistics in fully developed channel flow at low Reynolds number," *J. Fluid Mech.* **177**, 133-166 (1987).

Koskie J. E. and Tiederman W. G.; "Polymer drag reduction of zero and adverse pressure gradient boundary layers," *Near-Wall Turbulent Flows* So, R. M. C. *et al.* (editors). Elsevier, Amsterdam, 659-668 (1993).

Kreplin H. P. and Eckelmann H.; "Behaviour of the three fluctuating velocity components in the wall region of a turbulent channel flow," *Phys. Fluids* **22**, 1233-1239 (1979).

Krogstad P. A., Kaspersen J. H. and Rimestad S.; "Convection velocities in a turbulent boundary layer," *Phys. Fluids* **10**, 949-957 (1998).

Lange CF, Durst F and Breuer M.; "Wall effects on heat losses from hot wires," *Int. J. Heat & Fluid Flow* **20**, 34-47 (1999).

Launder B. E. and Spalding D. B.; "The numerical computation of turbulent flows," *Comput. Methods Appl. Mech. Engrg.* **3**, 269-289 (1974).

Lee T., Fisher M. and Schwarz W. H.; "Investigation of the stable interaction of a passive compliant surface with a turbulent boundary layer," *J. Fluid Mech.* **257**, 373-401 (1993).

Li W. Z., Khoo B. C. and Xu D.; "The thermal characteristics of a hot-wire in a near-wall flow," *Int. J. Heat Transf.* **49**, 905-918 (2006).

Ligrani P. M. and Bradshaw P.; "Subminiature hot-wire sensors: development and use." *J. Phys. E: Sci. Instrum.* **20**, 323-332 (1987).

Ligrani P. M. and Bradshaw P.; "Spatial resolution and measurement of turbulence in the viscous sublayer using subminiature hot-wire probes," *Exp. Fluids* **5**, 407-417 (1987).

Marusic I., Uddin A. K. M. and Perry A. E.; "Similarity law for the streamwise turbulence intensity in zero-pressure-gradient turbulent boundary layers," *Phys. Fluids* **9**, 3718-3726 (1997).

McAdams W. H., "Heat Transmission," 3^{rd} Edition, McGraw-Hill, New York (1954).

Mochizuki S. and Nieuwstadt F. T. M.; "Reynolds-number-dependence of the maximum in the streamwise velocity fluctuations in wall turbulence," *Exps. Fluids* **21**, 218-226 (1996).

Moen M. J. and Schneider S. P.; "The effect of sensor size and substrate properties on the performance of flush-mounted hot-film sensors," in *Thermal Anemometry.* Proceedings of the Third ASME International Symposium on Thermal Anemometry (1993).

Moen M. J. and Schneider S. P.; "The effect of sensor size on the performance of flush-mounted hot-film sensors," *J. Fluid Eng.* **116**, 273-277 (1994).

Mulhearn P. J.; "A simple device for dynamic testing of X-configuration hot-wire anemometer probes," *J. Phys. E. Sci. Instrum.* **11**, 678-681 (1978).

Niederschulte M. A., Adrian R. J. and Hanratty T. J.; "Measurements of turbulent flow in a channel at low Reynolds numbers," *Exps. Fluids* **9**, 222-230 (1990).

Ogata K.; "Modern Control Engineering," 2nd Ed. Prentice-Hall Inc (1990).

Patel V. C., Rodi W. and Scheuerer G.; "Turbulence models for near-wall and low Reynolds number flows," *AIAA J.* **23**, 1308-1319 (1985).

Perry A. E. and Morrison G. L.; "Static and dynamic calibrations of constant-temperature hot-wire systems," *J. Fluid Mech.* **47**, 765-777 (1971).

Polyakov A. F. and Shindin S. A.; "Peculiarities of hot-wire measurements of mean velocity and temperature in the wall vicinity," Lett. Heat Mass Transfer **5**, 53-58 (1978).

Polyakov A. F. and Shindin S. A.; "Hot-wire anemometer measurement of mean velocity very close to a wall," *Inshenerno-Fizicheskii Zurnal* **36**, 985-990 (1979).

Romano G. P.; "Analysis of two-point velocity measurements in near-wall flows," *Exps. Fluids* **20**, 68-83 (1995).

Saddoughi S. G. and Veeravalli S. S.; "Local isotropy in turbulent boundary layers at high Reynolds number," *J. Fluid Mech.* **268**, 333-372 (1994).

Savill A. M. and Mumford J. C.; "Manipulation of turbulent boundary layers by outer-layer devices skin friction and flow visualization results," *J. Fluid Mech.* **191**, 389-418 (1988).

Schewe G.; "On the structure and resolution of wall-pressure fluctuations associated with turbulent boundary-layer flow," *J. Fluid Mech.* **134**, 311-328 (1983).

Schlichting H.; "Boundary Layer Theory," 7^{th} ed., McGraw-Hill, New York (1979).

Shah D. A. and Antonia R. A., "Scaling of wall shear stress fluctuations in a turbulent duct flow," *AIAA J.* **25**, 22-29 (1987).

So R. M. C., Lai Y. G., Zhang H. S. and Hwang B. C.; "Second-order near-wall turbulence closures: a review," *AIAA J.* **29**, 1819-1835 (1991).

Spalart P. R.; "Direct simulation of a turbulent boundary layer up to $R_\theta = 1410$," *J. Fluid Mech.* **187**, 61-98 (1988).

Spalding D. B.; "A single formula for the law of the wall," *J. Appl. Mech.* **288**, 455-457 (1961).

Stewartson K.; "Flow between two rotating coaxial discs," *Proc. Camb. Phil. Soc.* **49**, 333-341 (1953).

Teo C. J., Khoo B. C. and Chew Y. T.; "The dynamic response of a hot-wire anemometer. IV. Sine-wave voltage testing for near-wall hot-wire/film probes and the presence of low-high frequency response characteristics," *Meas. Sci. Tech.* **12**, 37-51 (2001).

Townsend A. A.; "Equilibrium layers and wall turbulence," *J. Fluid Mech.* **11**, 97-120 (1961).

Walsh M. J.; "Turbulent boundary layer drag reduction using riblets," *AIAA Paper*, 82-0169 (1992).

Weidman P. D. and Browand F. K.; "Analysis of a simple circuit for constant temperature anemometry." *J. Phys. E: Sci. Instrum.* **8**, 553-560 (1975).

Xu C., Zhang Z., den Toonder J. M. J. and Nieuwstadt F. T. M.; "Origin of high kurtosis levels in the viscous sublayer. Direct numerical simulation and experiment," *Phys. Fluids* **8**, 1938-1944 (1996).

Zemskaya A. S., Levitskiy V. N., Repik Y. U. and Sosedko Y. P.; "Effects of the proximity of the wall on hot-wire readings in laminar and turbulent boundary layers," *Fluid Mech. - Soviet Res.* **8**, 133-141, (1979).

Chapter 2

Cross-correlation digital particle image velocimetry: a review

2.1 Introduction

The dream of experimental fluid dynamicists is to be able to measure complex, three-dimensional turbulent flow fields globally with very high spatial and temporal resolution. While we are still far from fully realizing this dream, significant progress has been made towards this goal during the last two decades. Early quantitative measurement methods using Pitot tubes, Venturi tubes and later measurement methods, such as Hot Wire Anemometry (HWA) and Laser-Doppler Anemometry (LDA), by their nature, were measurement methods that provided instantaneous velocity signals at single-points through time (see Figure 2.1). As can be seen from typical data such as those shown in Figure 2.1(a), early emphasis in turbulence research and its theoretical advancement necessitated a statistical description of turbulent flow fields, which relied heavily upon measurements provided by these single-point measurement techniques. Though useful, these statistical single point descriptions could not give us a clear instantaneous picture of what the fluid was doing globally, and how its instantaneous physics ultimately result in the fluid's statistical behavior.

Since the early seventies, the discovery of the existence of three-dimensional coherent structures within turbulent flows (Brown and Roshko, 1974) (see Figure 2.1(b)) using qualitative flow visualization methods (*i.e.* shadowgraphs, Schlieren systems, dye injection, etc) has been of significant interest for turbulence researchers. While flow visualization techniques have been around since the days of Prandtl, it is only recently that the advent of modern imaging, laser, and data acquisition technology has allowed for *qualitative* flow visualization to become *quantitative*. These advents have allowed for the development and advancement

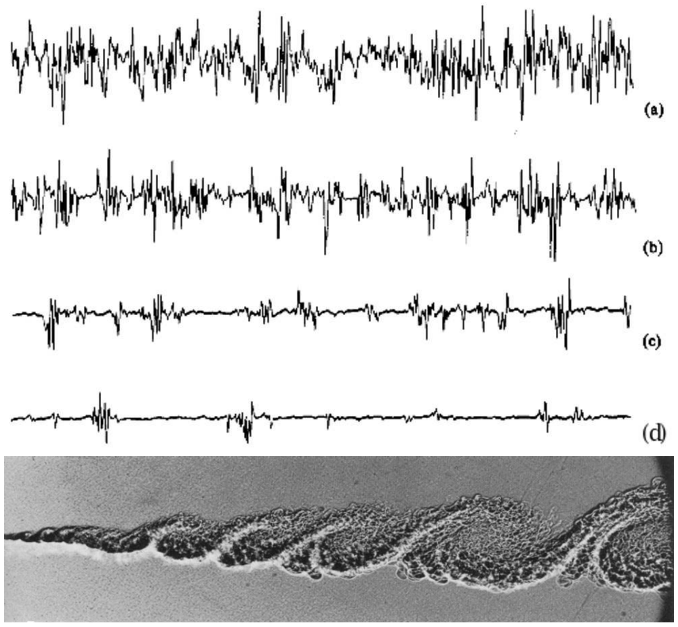

Figure 2.1: Above: Single-point measurements at various locations of a turbulent wake flow, Re=6500, x/d=28, y/d = a)0.87 b)2.25 c)3.4 d)4.2 (Tritton, 1988). Below: Shadowgraph of a turbulent shear layer revealing several levels of large coherent structures (Brown & Roshko, 1974).

of a relatively new measurement technique, Particle Image Velocimetry (PIV), specifically its digital implementation, which allows for the global measurements of two-component velocities within a two-dimensional domain through time. Because of its ability to provide global two-dimensional kinematic information as well as its ability to map the evolution of coherent structures through time, PIV has become a powerful tool in studying, understanding, and modeling fluid flow behavior. This chapter is therefore dedicated to reviewing digital PIV, specifically its most widely used implementation, the cross-correlation PIV. Section 2.3 presents a general description of 2D PIV, section 2.4 discusses the fundamentals of cross-correlation PIV, Section 2.5 discusses sources of errors within PIV measurements, Section 2.6 discusses calculations of differential and integral flow properties from PIV velocity data, Section 2.7 discusses outlier identification methods and Section 2.8 discusses advanced PIV methods. While PIV has become the dominant technique for flow field measurements, recent new methods have emerged that are allowing fluid mechanics experimentalists to interrogate and measure three-component velocities within a three-dimensional domain through time. One of these methods, the Three-Dimensional Defocusing Particle Image Velocimetry technique (3DDPIV) technique, will be presented in section 2.9.

2.2 Two-dimensional particle image velocimetry

Particle Tracking Velocimetry (PTV), Laser Speckle Velocimetry (LSV), and Particle Image Velocimetry (PIV) all measure instantaneous flow fields by recording images of suspended seed particles in flows at successive instants in time. An important difference among the three techniques comes from the typical seeding densities that can be dealt with by each technique. PTV is appropriate with "low" seeding density experiments, PIV with "medium" seeding density and LSV with "high" seeding density.

Historically, LSV and PIV techniques have evolved separately from the PTV technique. In LSV and PIV, fluid velocity information at an "interrogation region" is obtained from many tracer particles, and it is obtained as the most probable statistical value. In PIV, a typical interrogation region may contain images of 10-20 particles. In LSV, the particle densities are so large that individual particles are not distinguishable. Consequently, the scattered light interfere to form speckles, hence its name Laser Speckle Velocimetry. Correlation of either particle images or particle speckles can be done using identical techniques. Hence, LSV and PIV are essentially the same technique, used with different seeding density of particles.

In PTV, the acquired data is a time sequence of individual tracer particles in the flow. In order to be able to track individual particles from frame to frame, the seeding density needs to be small. Unlike PIV, PTV results in sparse velocity vectors distributions. Guezennec *et al.* (1994), for example, have developed an automated three-dimensional particle tracking velocimetry system that provides time-resolved measurements in a volume.

2.3 General description of 2D PIV

2.3.1 2D PIV setup

The principle layout schematic of a modern 2D PIV system is shown in Figure 2.2 (Raffel *et al.*, 1998). First, the flow facility must be seeded with particles that act as fluid tracers (section 2.3.2). A pulsed light source (most often a laser) and its necessary optics used to generate a thin light sheet is used to illuminate a cross-section of the seeded flow field (sections 2.3.3 and 2.3.4). A camera located perpendicular to the light sheet is used to acquire global and sequential images of the illuminated flow field (section 2.3.5). Electronic equipment is used to generate and synchronize the laser pulsing with the camera's frame rate timing sequence (not shown), such that each image is singly exposed (section 2.3.5). Lastly, a data acquisition system (not shown) is used to record sequential images from the camera.

Generally speaking, particle displacements are locally calculated from the acquired images using a cross-correlation algorithm (sections 2.4, 2.5, 2.6, 2.7, 2.8). These displacements are then converted from the image pixelated domain to the spatial domain via a calibration procedure. Finally, the particle displacements within the spatial domain are then divided by the time separation between the laser

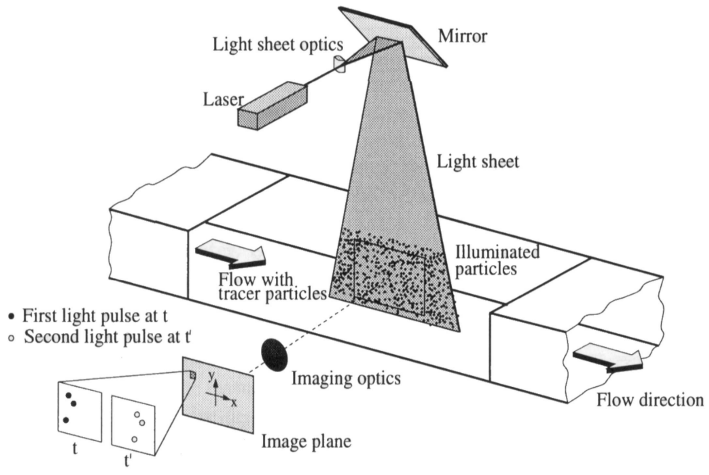

Figure 2.2: Principal layout of PIV system for typical wind or water tunnel applications (Raffel *et al.*, 1998).

pulses that singly exposed sequential images, *i.e.* velocity = displacement/Δt, to provide the velocity field.

2.3.2 Seeding particles

A PIV image is generated from the seeding particles in the flow field. Typically particles are added to the flow to have control over their size, distribution, and concentration. For ease of use, these particles should be non-toxic, non-corrosive, and chemically inert. They should also be small enough to be good flow tracers, yet large enough to scatter sufficient light for imaging. As a first estimate to particle motion in relation to fluid motion, it can be shown that the step response of the particle velocity, U_p, follows an exponential law (Merzkirch, 1974):

$$U_p(t) = U\left[1 - \exp\left(-\frac{t}{t_s}\right)\right], \tag{2.1}$$

where t_s is the relaxation time of the particle,

$$t_s = d_p^2 \frac{\rho_p}{18\mu}, \tag{2.2}$$

where ρ_p is the particle density, d_p is the particle diameter, and μ is the fluid dynamic viscosity. Therefore, the smallest time scales of the fluid must be greater than the particle's relaxation time, if the particle is to accurately represent the local fluid velocity.

In a detailed review paper, Melling (1997) presents a wide variety of tracer particles that have been used in liquid and gas PIV experiments, as well as methods of

generating seeding particles and introducing them into the flow. For gas flow applications, theatrical smoke, different kinds of atomized oils, glass micro-balloons, titanium dioxide (TiO_2), and aluminum oxide (Al_2O_3) have been used. Typical theatrical smoke generators are inexpensive, and they generate plenty of particles. Oil can be atomized using devices such as a Laskin nozzle, generating particles in the micron to submicron range, which are particularly useful for high-speed applications. Titanium dioxide (TiO_2), and aluminum oxide (Al_2O_3) are useful for high temperature applications such as combustion, and flame measurements. For liquid flow applications, silver-coated hollow glass spheres, polymers, titanium dioxide (TiO_2), aluminum oxide (Al_2O_3), conifer pollen, and hydrogen and oxygen bubbles are typically used. Most liquid applications of PIV are in recirculating flow set-ups, so when concentrated particles in suspension are added to the flow, homogeneous seeding is achieved in a short time. Many gas applications are also in recirculating flow set-ups. However, for single pass-through systems, the task of achieving homogeneous seeding at the test section is not trivial, and typically requires upstream injection systems that can provide adequate mixing of the tracer particles before they arrive into the area of interest.

2.3.3 Light sources

In the point measurement technique of LDA, the coherence property of lasers is utilized to generate a fringe pattern at the measurement volume. For PIV, however, the laser's coherence property is not a requirement for measurements; hence, the lasers are used only as a source of bright illumination. In addition, PIV image acquisition should be acquired using short light pulses to prevent particle image streaking. Hence, pulsed lasers become obvious choices for PIV work. The most commonly used laser in modern PIV systems is the Nd:YAG laser. Nd:YAG lasers emit infrared radiation at 1064 nm, where for PIV applications, the frequency is doubled to 532 nm, green, to allow for particle illumination and reflection in the visible spectrum. Presently, PIV Nd:YAG lasers can provide power from 12 mJ to 1000 mJ per pulse. Pulse durations for PIV Nd:YAG lasers are typically 5-10 nanoseconds, with pulse frequencies in the range of 1-1000 Hz, with power being inversely proportional to the pulse frequency. Pulse frequencies of 15 Hz and 30Hz are most commonly used in order to be able to properly synchronize with image acquisition cameras. As mentioned in section 2.3.1, cross-correlation PIV requires that each image be singly exposed. Therefore, to achieve a wide range of pulse separations, two separate laser cavities are used where the laser pulses can be adjusted with respect to each other using appropriate electronics equipment. These lasers, typically called dual lasers, are housed into a single unit, containing beam combining optics, frequency doubler, alignment optics, and an infrared beam dump. This setup allows the two laser pulses to be superimposed, and manipulated thereafter with the same optics (see Figure 2.3).

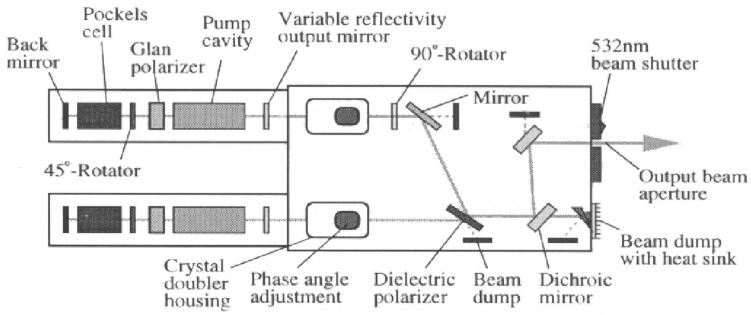

Figure 2.3: Dual-cavity Nd:YAG laser with resonators and beam combining optics (Raffel *et al.*, 1998).

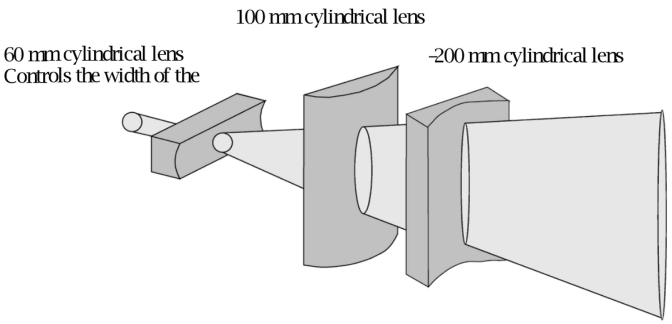

Figure 2.4: Example of a typical light sheet generating optical setup (Maheo, 1998).

2.3.4 Light sheet optics

Fiber optics are commonly used for delivering Argon-Ion beams conveniently and safely. Single-mode polarization preserving fibers can be used for delivering up to 1 Watt of input power, whereas multi-mode fibers can accept up to 10 Watts.

The short duration high power beams from pulsed Nd:YAG lasers can instantly damage optical fibers. Hence, the most standard methods generate a laser sheet by using laser optics. The variables to control in generating the light sheet in relation to the location of the laser with respect to the experimental setup are its spreading angle and its thickness, or its "beam waist". There are many ways to achieve proper control that include a variety of combinations of cylindrical and/or spherical lenses. A typical setup, for example as used by Maheo (1998) employing 3 cylindrical lenses, is shown in Figure 2.4. In this example, the first lens is a diverging cylindrical lens that is used to spread the beam into a sheet. The second and third lenses are used to control the location of the beam's waist. To do this,

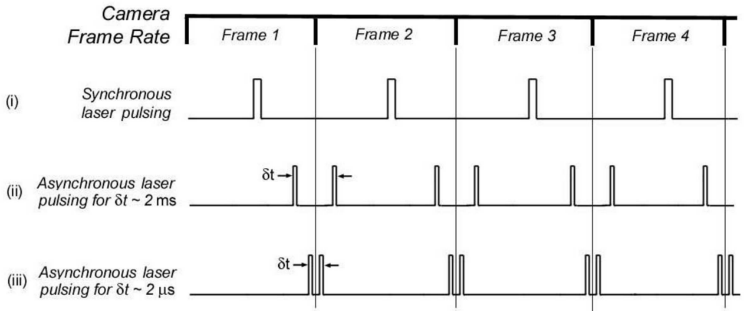

Figure 2.5: Timing diagram showing asynchronous laser pulsing in relation to the camera's frame rate (Gharib *et al.*, 2000).

second and third lenses, converging and diverging, respectively, and both rotated 90 degrees with respect to the first lens, are used. Then, varying the distance between the second and third lens will allow for the adjustment of the beam's waist's location.

2.3.5 Image acquisition CCDs

Cross-correlation cameras have become the preferred method of acquiring images. The cross-correlation cameras use high-performance progressive-scan frame interline CCD chips. Such chips include m x n light sensitive picture elements (pixels) and an equal number of storage cells (blind cells). The first laser pulse exposes the first frame, which is transferred from the light-sensitive cells to the storage cells immediately after the laser pulse (at the time of this publication, this transfer time can be as short as 200 ns). The second laser pulse is then fired to expose the second frame (see Figure 2.5). The storage cells now contain the first camera frame of the pair with information about the initial positions of seeding particles. The light-sensitive pixels contain the second camera frame, which has information on the final positions of the seeding particles. Using a framegrabber, these two image frames are then transferred sequentially from the camera onto the computer's RAM memory or its hard drive.

Cross-correlation CCD cameras are available with resolutions up to 2672 x 4008 pixels, and framing rates from 4.85 Hz to as high as 1KHz, with the framing rate being inversely proportional to the resolution. 8-Bit digitization has been shown to be sufficient for most purposes (Raffel *et al.*, 1998). Flow fields with velocities ranging from micrometers per second to supersonic speeds can be studied since inter-frame time separations down to few hundred nanoseconds can be obtained. One interesting option of these cameras is that they can be asynchronously reset. This is particularly useful in conjunction with the special triggering options for synchronizing measurements to external events, such as rotating machinery.

2.4 Fundamentals of cross-correlation particle image velocimetry

The historical development of PIV can be found in a series of papers archived in the SPIE Milestone Series Volume 99 (Grant, 1994), which include many foundational and fundamental works including Willert and Gharib (1991); Adrian (1991); Lourenco *et al.* (1989); Westerweel (1993). A fairly recent book, *Particle Image Velocimetry - A Practical Guide*, and paper by Westerweel, *Fundamentals of Digital Particle Image Velocimetry* (Westerweel, 1997), are also excellent sources of information on the fundamental aspects of PIV. Detailed derivations of the statistical description of cross-correlation PIV have been provided by Adrian (1984, 1988; Keane and Adrian, 1992), Westerweel (1993, 1997), and Raffel *et al.* (1998). Below, the main results of these works are presented.

2.4.1 A visual representation of the cross-correlation concept

Visually, the correlation concept can be shown using Figure 2.6 (Gharib *et al.*, 2000). Figure 2.6(a) and Figure 2.6(b) show instantaneous images taken from a particle field at two consecutives times, with a time separation of Δt. If the second particle field is translated horizontally, superposition of the translated image with the first (Figure 2.6(c)) allows for visual detection of horizontal particle motions. Likewise, if the second particle field is rotated, superposition of the rotated image with the first (Figure 2.6(d)) allows for visual detection of rotating motions.

To obtain a quantitative two-dimensional vector field from such images, particle images must be systematically interrogated. To do so, these recorded images are sampled using an interrogation window (see Figure 2.7, left), the dimensions of which determine the spatial resolution of the measurement. The interrogation regions can be adjacent to each other, or more commonly, have partial overlap with their neighbors that will allow for increased spatial resolution. The shape of the interrogation regions can deviate from square to accommodate flow gradients.

Historically, two PIV methods have been developed, first an autocorrelation method was developed, which was then followed by a cross-correlation method. The auto-correlation method required that the images be doubly exposed, while the cross-correlation required that the images be singly exposed. The displacement information is then obtained once the correlation peak is determined using either of these methods. The auto-correlation analysis technique was developed for photography-based PIV, since it was not possible to advance the film fast enough between the two exposures. The auto-correlation function of a doubly-exposed image has a dominant central peak, and two symmetric side peaks. This poses two problems: (1) although the particle displacement is known, there is an ambiguity in the flow direction, (2) for very small displacements, the side peaks can partially overlap with the central peak, limiting the measurable velocity range. In order to overcome the directional ambiguity problem, image shifting techniques using

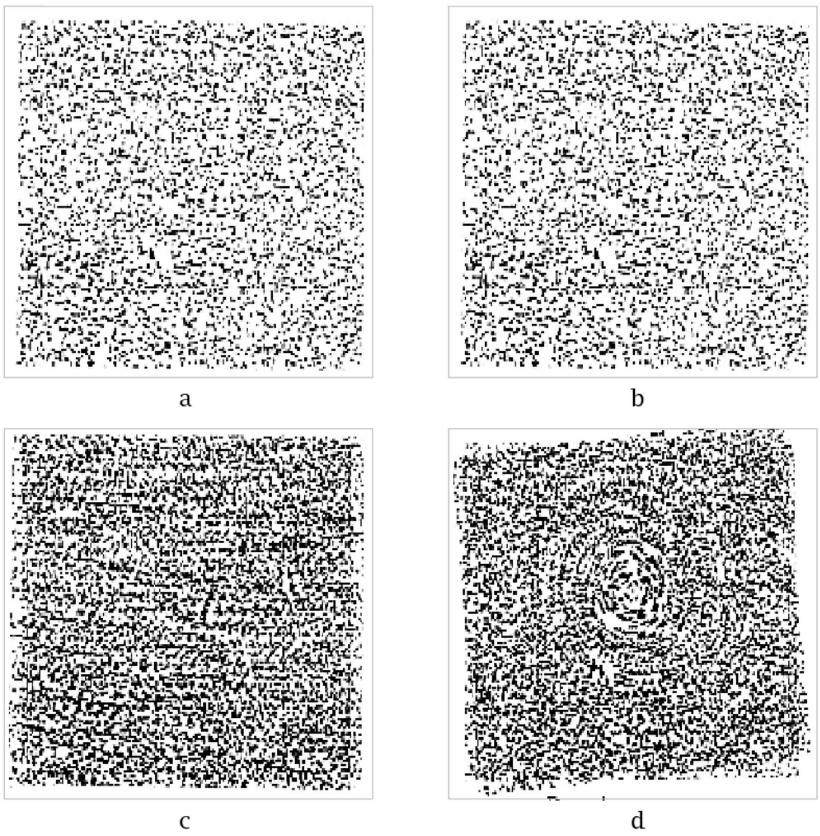

Figure 2.6: *a* and *b* are sample particle images. By translating *a* with respect to *b* and overlaying the two, a simulated translational shift is obtained and shown in *c*. By rotating *a* with respect to *b* and overlaying the two, a rotational shift is obtained and shown in *d* (Gharib *et al.*, 2000).

rotating mirrors (Landreth and Adrian, 1988; Landreth *et al.*, 1988) and electro-optical techniques (Landreth and Adrian, 1988; Landreth *et al.*, 1988; Lourenco, 1993) have been developed. To leave enough room for the added image shift, larger interrogation regions are used for auto-correlation analysis. By displacing the second image at least as much as the largest negative displacement, the directional ambiguity is removed. This is analogous to frequency shifting in LDA systems to make them directionally sensitive.

Due to these complications and to the fact that dual-cavity lasers have allowed for very small pulse separations (see section 2.3.3), the preferred method in PIV presently is to singly expose images, and perform cross-correlation analysis, such as that as shown in Figure 2.7. First, image subsamples, $f(i,j)$ and $g(i,j)$, are extracted at the same location within the images using an interrogation window (Figure 2.7(a)). Then, a cross-correlation procedure is performed on these two interrogated regions. Figure 2.7(b) shows an FFT cross-correlation algorithm, however, a direct cross-correlation procedure can also be used (see section 2.4.3). This procedure results in a cross-correlation distribution with the pixel domain within the interrogated regions with a dominant peak corresponding to the shift of the particles, (see Figure 2.7(c) and Figure 2.12) designated by (dx, dy). Lastly, the pixel shift (dx, dy) is converted into a velocity through calibration parameters (see Figure 2.7(d)). Details of these steps from a theoretical foundation to practical implementation are described in the following sections.

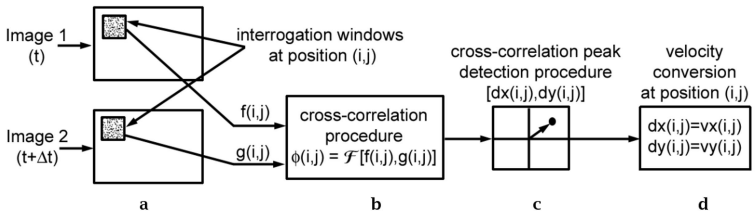

Figure 2.7: Cross-correlation data processing procedure using an FFT algorithm *a* an interrogation window subsamples the main sequential image pairs; *b* a cross-correlation procedure is performed, in this case, an FFT implementation is shown; *c* within the cross-correlation domain, the peak's location corresponding to the average shift of particles within the interrogation windows is identified; *d* this shift is converted to physical space, providing a velocity vector.

2.4.2 Statistical description of cross-correlation particle image velocimetry

Before discussing the presently used cross-correlation analyses methods, it is important that a theoretical foundation is established. First, the tracer particle ensemble cross-covariance in physical three-dimensional space is presented. As these

tracer particles are then imaged onto a two-dimensional domain, *i.e.* the CCD, the two-dimensional spatial ensemble cross-covariance of the projected tracer particles onto the two-dimensional domain is presented. Finally, several optimization considerations are discussed.

Tracer particle ensemble cross-covariance in physical space

The statistical description of fluid tracer particles is given by studying the ensemble of all possible tracer particle distributions, $G(\vec{X},t)$, for a given flow field, $u(\vec{X},t)$, where the tracer particle distribution within the physical spatial domain, $\vec{X}$, at time t is defined to be

$$G(\vec{X},t)=\sum_{i=1}^{N}\delta\left[\vec{X}-\vec{X}_i(t)\right], \tag{2.3}$$

where N is the total number of particles within the domain of interest, $\delta(\vec{X})$ is the Dirac delta function, and $\vec{X}_i(t)$ is the position vector of the i-th particle at time t, so that the integral of G over a volume yields the total number of particles within the volume. The particle distribution given in Equation (2.3) can also be represented in vector form as

$$\vec{\Gamma}=\begin{pmatrix}\vec{X}_1(t)\\ \vec{X}_2(t)\\ \vdots\\ \vec{X}_N(t)\end{pmatrix}. \tag{2.4}$$

In order to measure similarities between particle distributions at two different times, the ensemble cross-covariance is considered and defined as:

$$R_{G'G''}(\vec{X}',\vec{X}'')=\left\langle G'\left(\vec{X}'\right)G''\left(\vec{X}''\right)\right\rangle-\left\langle G'\left(\vec{X}'\right)\right\rangle\left\langle G''\left(\vec{X}''\right)\right\rangle, \tag{2.5}$$

where $\langle . \rangle$ symbolizes the ensemble average. The ensemble mean of $G\left(\vec{X},t\right)$ and $G'\left(\vec{X}',t\right)G''\left(\vec{X}'',t\right)$ are given by

$$\begin{aligned}\left\langle G\left(\vec{X},t\right)\right\rangle&=\int G\left(\vec{\Gamma}\right)\rho\left(\vec{\Gamma}\right)d\vec{\Gamma},\\ \left\langle G'\left(\vec{X}',t\right)G''\left(\vec{X}'',t\right)\right\rangle&=\iint G'\left(\vec{\Gamma}'\right)G''\left(\vec{\Gamma}''\right)\rho\left(\vec{\Gamma}'|\vec{\Gamma}''\right)d\vec{\Gamma}'d\vec{\Gamma}'',\end{aligned} \tag{2.6}$$

where $\rho\left(\vec{\Gamma}\right)$ is the probability density function for $\vec{\Gamma}$, and $\rho\left(\vec{\Gamma}'|\vec{\Gamma}''\right)$ is the conditional probability density function for $\vec{\Gamma}''$ given the initial state $\vec{\Gamma}'$. For a homogeneous tracer particle distribution, where the number density of the particles, C,

is constant,

$$\begin{aligned} \left\langle G'\left(\vec{X}',t\right)\right\rangle &= \left\langle G''\left(\vec{X}'',t\right)\right\rangle = C\,, \\ \left\langle G'\left(\vec{X}',t\right)G''\left(\vec{X}'',t\right)\right\rangle &= C\delta\left[\vec{X}''-\vec{X}'-\vec{D}\right]+C^2\,, \end{aligned} \tag{2.7}$$

where $\vec{D}\left(\vec{X};t',t''\right)$ is the displacement of the tracer particle during the time interval $[t',t'']$. The ensemble cross-covariance thus reduces to

$$R_{G'G''}(\vec{X}',\vec{X}'') = C\delta\left[\vec{X}''-\vec{X}'-\vec{D}\right]\,. \tag{2.8}$$

Spatial ensemble cross-covariance in projected 2D domain

It is important to realize that Equations (2.4)and (2.8) give the cross-covariance of particle distributions in the physical spatial domain, $\vec{X}$, thereby not making them directly applicable to images obtained from these particle distributions. Nevertheless, to develop a cross-covariance expression for PIV images, the imaging process must be first considered. As described in section 2.3.1, a laser sheet is generated, and used to illuminate a cross-section of the flow, which has been previously seeded with tracer particles. This light sheet will have a thickness, ΔZ_0, typically with a Gaussian intensity profile within the depth of the sheet (see Figure 2.8). The laser sheet is assumed to be uniform in its plane, and the image acquisition optics are assumed to be aberration-free circular lenses with a given numerical aperture $F\#$. The particles' images are assumed to be in focus, which is valid if the sheet thickness is less than the imaging depth of field (Adrian, 1991).

The imaging process projects the particles' reflected illumination onto the planar image domain, $\vec{x}=(x,y)$, *i.e.* the CCD, and is represented mathematically as

$$g\left(\vec{x},t\right) = \frac{1}{I_z}\int I_0\left(Z\right)G\left(\vec{X},t\right)dZ\,, \tag{2.9}$$

where x=MX, y=MY, M is the image magnification, and $I_0(Z)$ is the light sheet intensity profile with a maximum I_z, whereby it is assumed that tracer particle projections onto the image domain involves only an integration along the Z-coordinate. The tracer particles' image on the image domain can be represented by a point-spread function, *t(x,y)*, such that the image intensity *I(x,y)*, for particle tracer densities sufficiently low that do not allow particle overlap to occur, can be represented by

$$I\left(x,y\right) = I_z\iint t\left(s-x,t-y\right)g\left(s,t\right)ds\,dt\,. \tag{2.10}$$

Using the definition given in Equation (2.5), the image ensemble cross-covariance, *i.e.* $I\left(\vec{x},t'\right)$ and $I\left(\vec{x},t''\right)$, can be reduced to

$$R_{II}\left(\vec{s}\right) = F_0\left(\Delta Z\right)\cdot R_I\cdot\delta\left(\vec{s}-\vec{s}_D\right)\,, \tag{2.11}$$

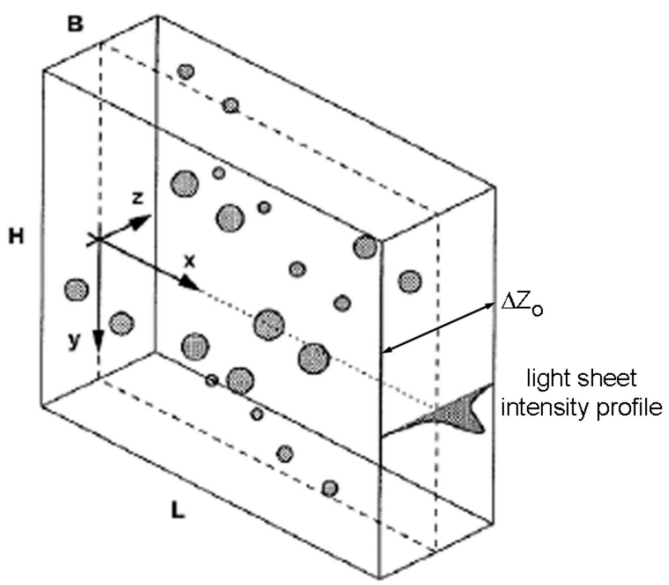

Figure 2.8: Three-dimensional volume representing the laser light sheet illumination and the particles illuminated within this light sheet (Westerweel, 1997).

where

$$\begin{aligned} R_I(\vec{s}) &= C\Delta Z_0 M^{-2} I_z^2 t_0^2 F_t(\vec{s}) \,, \\ t_0 &= \iint t(x,y)\,dx\,dy \\ F_t(x,y) &= \frac{1}{t_0^2}\iint t(u,v)\,t(u+x,u+y)\,du\,dv \,, \\ F_0(\Delta Z) &= \frac{\int I_0(Z)\,I_0(Z+\Delta Z)\,dZ}{\int I_0^2(Z)\,dZ} \,, \end{aligned} \tag{2.12}$$

$\vec{s} = (x, y)$ and $\vec{s}_D = M \cdot (\Delta X, \Delta Y)$ is the particle tracer displacement on the image domain (Adrian, 1988). $F_0(\Delta Z)$ represents the loss of correlation due to tracer particles' motion perpendicular to the light sheet, t_0^2 is the normalization to F_t, the self-correlation of each tracer particle image, and R_I is the image auto-correlation.

In implementation, ensemble averages of the flow field cannot be obtained unless the flow is steady or periodic. Therefore, if spatial averaging is ergodic with respect to ensemble averaging, the ensemble average can be replaced with spatial averaging defined as

$$C(\vec{s}) = \iint W'(\vec{x})\,I'(\vec{x})\,W''(\vec{x}+\vec{s})\,I''(\vec{x}+\vec{s})\,d\vec{s}. \tag{2.13}$$

If the tracer particle distribution is homogeneous, then ergodicity is satisfied, and the spatial averaging can be written as

$$C\left(\vec{s}\right) = \left\langle C\left(\vec{s}\right)\right\rangle + C'\left(\vec{s}\right) = C'\left(\vec{s}\right) + R_D\left(\vec{s}\right) + R_C\left(\vec{s}\right) + R_F\left(\vec{s}\right) \ , \tag{2.14}$$

where $\left\langle C\left(\vec{s}\right)\right\rangle$ is the ensemble mean, $C'\left(\vec{s}\right)$ is the fluctuating component with respect to the ensemble mean, $R_D\left(\vec{s}\right)$ is the displacement correlation peak, $R_C\left(\vec{s}\right)$ is the constant background correlation, and $R_F\left(\vec{s}\right)$ is the correlation between the mean and fluctuating image intensities. These last two terms can be eliminated by subtracting the mean image intensity from I' and I". The displacement correlation peak is given by

$$R_D\left(\vec{s}\right) = N_I\, F_I\, F_0\, I_Z\, t_0^2\, F_t * \delta\left(\vec{s} - \vec{s}_D\right) \ , \tag{2.15}$$

where * denotes a convolution operation, $N_I = C\Delta Z_0 D_I^2/M^2$ is the image density, D_I^2 is the area associated with the interrogation window, and

$$F_I\left(\vec{s}\right) = \frac{1}{D_I^2}\int W'\left(\vec{s}\right) W''\left(\vec{x}+\vec{s}\right) d\vec{s}. \tag{2.16}$$

It is important to realize that the spatial correlation resulting in Equation (2.15) correlates particles that are within two finite domains, W' and W". As such, due to the flow, tracer particles can leave and enter these interrogation domains such that not all particles within the first interrogation domain, W', will exist in the second interrogation domain, W". The portion of the area coincident to both interrogation domains that contain images of the same tracer particles is denoted by Equation (2.16), and is pictorially shown in Figure 2.9. This term therefore represents the loss of correlation in the spatial cross-correlation, Eq.(2.15), due to in-plane loss-of-pairs, and is the only difference between the ensemble correlation and the spatial correlation.

Figure 2.9: The number of particle-image pairs that can be contained in an interrogation region is reduced for increasing displacement (Westerweel, 1997).

Optimization considerations

The spatial cross-correlation derived above is best suited for capturing translational motion. For such motions, the resulting cross-correlation produces a near delta-function peak within the cross-correlation domain. However, any deviation from translational motion, *i.e.* rotation and/or shear, causes a broadening of the

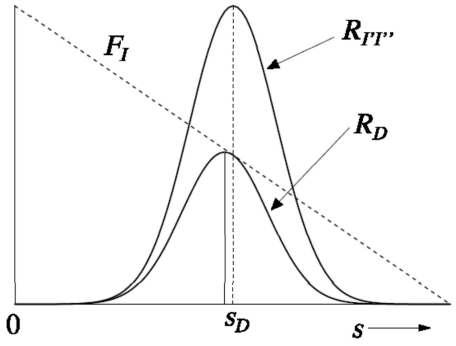

Figure 2.10: The displacement-correlation peak is skewed (Westerweel, 1997). $R_{I'I''}$ represents tracer particle ensemble cross-covariance.

peak distribution, as well as a reduction in its peak value. If the velocity differences (due to shear and/or rotation) within the interrogation volume are small with respect to the width of the interacting interrogation windows, then the displacement field will be sufficiently uniform.

While tracer particles' motion creates unpaired particle images within the two interrogation volumes that broaden the cross-correlation peak, it also shifts the peak value towards slightly lower displacement values (see Figure 2.10). This bias occurs for even the most basic motions, such as uniform flows, and is enhanced when flow gradients exist. Fortunately, there are three solutions that can eliminate this problem. The first is to divide the correlation by F_I (Westerweel, 1993). The second is to use different size interrogation windows such that F_I will be constant within its central portion, thus preventing any biasing (Keane and Adrian, 1992). This can be seen in the middle and bottom drawings of Figure 2.11. The third way is to shift one of the two interrogation windows an amount equal to the tracer particles' displacement, and in so doing, capture all tracer particle images common to both interrogation windows (Westerweel *et al.*, 1997). This can be seen in the top drawing of Figure 2.11, where the peak of F_I would coincide with the cross-correlation peak.

To further ensure displacement measurement accuracy, it is important that the correlation peak, R_D, be strong with respect to the fluctuating correlation, C', see Equation (2.14). In this respect, $N_I F_I F_O$, which represents the effective tracer particle image pair density within the interrogation region, should be maximized. Keane and Adrian (1992) suggest that for high intensity images

$$N_I F_I F_O > 7 \quad \text{and} \quad F_I = F_O = 1\,, \tag{2.17}$$

$$M\,|\Delta u|\,\Delta t/D_I < 0.03\,, \tag{2.18}$$

$$M\,|\Delta u|\,\Delta t/d_\tau < 1\,, \tag{2.19}$$

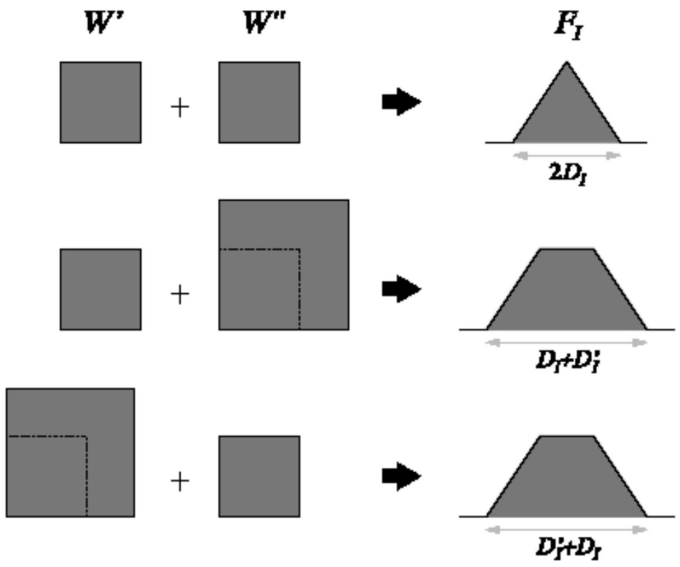

Figure 2.11: The effect of using differently sized interrogation windows on F_I (Westerweel, 1997).

where M is the image magnification, Δu is the velocity difference within the interrogation window, Δt is the time separation between image exposures, and d_τ is tracer particle image diameter. Following the procedures above, F_I can be easily maximized to unity. Furthermore, Equations (2.18), (2.19) provide constraints on the velocity gradients that can be tolerated within an interrogation window. Lastly, since F_O (Equation (2.12)) represents the loss of correlation due to tracer particles' motion perpendicular to the light sheet, it is important that out-of-plane tracer particles' displacements be less than one-quarter of ΔZ (Westerweel, 1997).

2.4.3 Digital implementation of cross correlation particle image velocimetry

Due to the nature of a CCD camera, once an image is acquired, it is pixilated and therefore discretized. The intensity value of each pixel is read through an analog-to-digital converter, and is therefore quantized; typically with an 8-bit converter for a total of 256 (2^8) quantized levels. The discretized cross-covariance can therefore be mathematically expressed within a discrete domain as (Westerweel, 1993, 1997)

$$C(r,s) = \frac{1}{M*N} \sum_{m=1}^{M} \sum_{n=1}^{N} \left[f(m,n) - \bar{f} \right] \left[g(m+r, n+s) - \bar{g} \right] , \qquad (2.20)$$

where $f(m,n)$ and $g(m,n)$ represent the first and second subsampled images, respectively, M and N represent the number of rows and columns within the images, $C(m,n)$ represents the discretized correlation function, (r,s) represents the location at which the correlation is calculated, and $\overline{f}$ and $\overline{g}$ represent the mean image intensity of the interrogation windows, f and g, respectively. Its corresponding in-plane loss-of-pair term is

$$F_I\left[r,s\right] = \left(1 - \frac{|r|}{M}\right)\left(1 - \frac{|s|}{N}\right) \qquad \text{(Westerweel, 1993,1997)}\,, \tag{2.21}$$

which, per section 2.4.2, can then be used to divide the cross-covariance (Equation (2.20)) in order to obtain an unbiased displacement measurement. Willert (Raffel *et al.*, 1998; Willert, 1996) also suggests using another discretized cross-covariance description that inherently accounts for the in-plane loss-of-pair term:

$$\begin{aligned}
C(r,s) &= \frac{C_{II}(r,s)}{\sqrt{\sigma_I(r,s)}\sqrt{\sigma_{II}(r,s)}}\,,\\
C_{II}(r,s) &= \sum_{m=1}^{M}\sum_{n=1}^{N}\left[f(m,n) - \bar{f}\,\right]\left[g(m+r,n+s) - \bar{g}(r,s)\right]\,,\\
\sigma_I(r,s) &= \sum_{m=1}^{M}\sum_{n=1}^{N}\left[f(m,n) - \bar{f}\,\right]^2\,,\\
\sigma_{II}(r,s) &= \sum_{m=1}^{M}\sum_{n=1}^{N}\left[g(m+r,n+s) - \bar{g}(r,s)\right]^2\,,
\end{aligned} \tag{2.22}$$

where $\overline{g}(r,s)$ is the average of g coincident with the interrogation window, f.

To relieve the heavy computation burden, Willert and Gharib (1991) have suggested using fast Fourier transforms (FFT) to significantly speed up the cross-correlation calculations, since doing so would reduce the number of computational operations for each interrogated region from N^4 to $N^2 \log_2 N$. This procedure is outlined in Figure 2.7. Furthermore, computational efficiency can be further increased by using the symmetry properties of real-valued images, which state that the real part of an FFT is symmetric, while its imaginary part is anti-symmetric. Once the cross-correlation peak is determined, the interrogation window systematically interrogates the rest of the image pair, thereby providing a two-dimensional vector field.

2.4.4 Classical sub-pixel peak finding methods

As the image domains are discretized, Equations (2.20) and (2.22) shows that the discretized cross-correlation domain will exist only at integer values (see Figure 2.12). This means that the peak value within the cross-correlation domain, corresponding to the particle shifts within the interrogated region, is at best measured to an integer value, with an uncertainty of $\pm 1/2$ pixel. While this may not seem

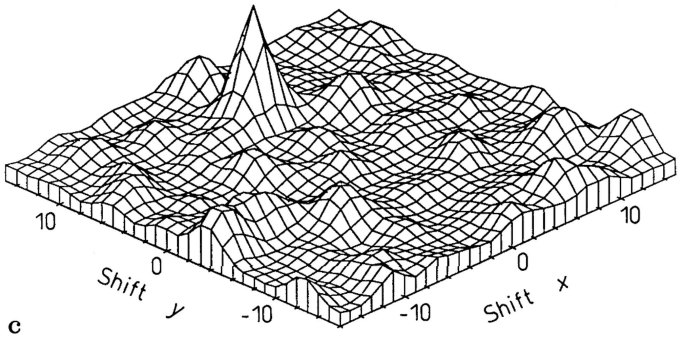

Figure 2.12: Sample cross-correlation peak showing single dominant peak corresponding to the magnitude and direction of particle shifts (Willert and Gharib, 1991).

significant, it is important to realize that, for example, for window sizes of 32 x 32, and maximum particle shifts of 1/3 of the window size, the uncertainty of a maximum particle shift of 10 pixels, is at best 5%. Given that vorticity and strain rates are differentiably calculated from the velocity (see section 2.5), their uncertainties will be about 10%, which is unacceptable. As such, methods were developed to obtain sub-pixel accuracy.

Initially, centroiding, defined as the ratio of the first order moment to the zeroth order moment, was used, which required the correlation domain to be thresholded in order to define the region containing the correlation peak (Alexander and Ng, 1991). Unfortunately, this method strongly biased the displacement measurements towards integer values, creating a severe peak-locking effect on processed data (see Figure 2.13) (Westerweel, 1997; Westerweel *et al.*, 1996). Fortunately, more robust approaches were also developed, which curve-fitted the maximum peak and its two side-peaks, separately in both the x- and y- directions, with a function, in order to obtain sub-pixel accuracy. Typically, these three-point estimating curve-fits have been either parabolic or Gaussian, with Gaussian being the more frequently used (see Table 2.1) function. Its frequent use has been justified, since the particle images, well approximated by Gaussian intensity distributions, when correlated also result in a Gaussian intensity distribution. Its estimation is therefore much better predicted using a Gaussian curve fit, rather than a parabolic curve fit, which has been also been shown through calibration experiments (Lourenco and Krothapalli, 1995). Furthermore, its peak-locking effect (see section 2.5) is dramatically reduced (see Figure 2.13).

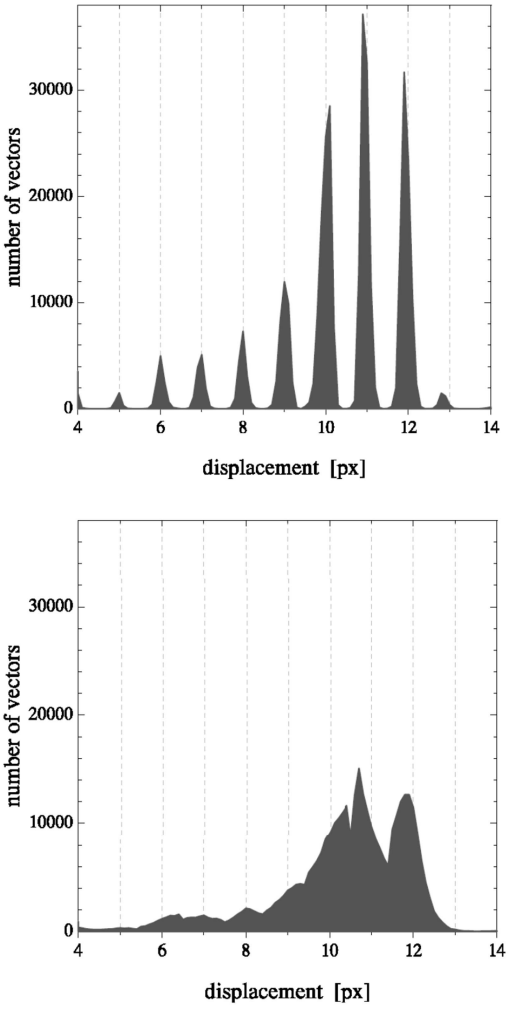

Figure 2.13: Histograms of the measured axial displacement (in pixels) in a turbulent pipe flow using the centroid and Gaussian peak fit for the sub-pixel interpolation (Raffel *et al.*, 1998; Westerweel, 1993).

Table 2.1: Three-point estimators used to achieve subpixel resolution. The indices (i, j) correspond to the spatial location of the maximum location of the correlation value within the correlation domain (Raffel *et al.*, 1998; Westerweel, 1993).

Curve-Fitting Function	Three-Point Estimators
Peak Centroid $f(x) = \frac{1^{st} order\ moment}{2^{nd} order\ moment}$	$x_0 = \frac{(i-1)R_{(i-1,j)}+iR_{(i,j)}+(i+1)R_{(i+1,j)}}{R_{(i-1,j)}+R_{(i,j)}+R_{(i+1,j)}}$ $y_0 = \frac{(j-1)R_{(i,j-1)}+jR_{(i,j)}+(j+1)R_{(i,j+1)}}{R_{(i,j-1)}+R_{(i,j)}+R_{(i,j+1)}}$
Parabolic $f(x) = A(x_0 - x)^2 + B(x_0 - x) + C$	$x_0 = \frac{R_{(i-1,j)}-R_{(i+1,j)}}{2R_{(i-1,j)}-4R_{(i,j)}+2R_{(i+1,j)}}$ $y_0 = \frac{R_{(i,j-1)}-R_{(i,j+1)}}{2R_{(i,j-1)}-4R_{(i,j)}+2R_{(i,j+1)}}$
Gaussian $f(x) = A \exp\left[\frac{-(x_0-x)^2}{B}\right]$	$x_0 = \frac{\ln R_{(i-1,j)}-\ln R_{(i+1,j)}}{2\ln R_{(i-1,j)}-4\ln R_{(i,j)}+2\ln R_{(i+1,j)}}$ $y_0 = \frac{\ln R_{(i,j-1)}-\ln R_{(i,j+1)}}{2\ln R_{(i,j-1)}-4\ln R_{(i,j)}+2\ln R_{(i,j+1)}}$

2.5 Sources of error

As with all experimental methods, PIV measurements are susceptible to error. There are many parameters that affect the accuracy of PIV measurements: sub-pixel peak fitting, tracer particle image diameter, tracer particle image intensity distribution, window interrogation size, tracer particle image shift, quantization effects, background noise, displacement gradients within an interrogation window, and out-of-plane tracer particle motion. It is therefore important to be able to understand how each of these variables affects the error, or uncertainty of PIV measurements.

2.5.1 Effect of sub-pixel peak finding methods

Error analysis shows that the total error within a measurement can be expressed as the sum of systematic or bias errors, ε_{biased}, and random errors, which are usually characterized as root-mean-square values, ε_{rms}:

$$\varepsilon_{total} = \varepsilon_{biased} + \varepsilon_{rms}\,. \tag{2.23}$$

Using a photographic auto-correlation PIV system, Prasad *et al.* (1992). Have shown that for fixed tracer particle image size, a bias error did exist, and was due to

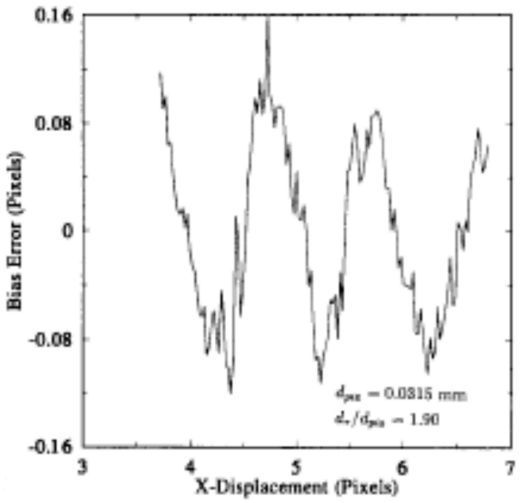

Figure 2.14: Bias error of horizontal displacements using 32 x 32 interrogation windows (Lourenco and Krothapalli, 1995).

the centroid sub-pixel peak finding method that was used (see Figure 2.14). Here, it can be clearly seen that the bias error is sinusoidal with respect to horizontal pixel shifts, where the bias error is zero at every integer and 1/2 integer pixel value.

In a detailed study of centroid, parabolic, Gaussian, and Whittaker (a truncated sinc kernel) interpolation peak finding methods, Lourenco and Krothapalli (1995) have shown that the Gaussian and Whittaker's interpolation peak finding methods were the most superior in performance (see Figure 2.15).

In a further study, Roesgen (2003) has suggested the use of the sinc function as a subpixel interpolation kernel, based on its spectral shape. The spectral shapes of various interpolation kernels are shown in Figure 2.16. In application to the data set that is periodic in the spectral domain, it can be seen that the nearest neighbor, linear, $M'4$ (a kernel used to resample irregularly gridded data onto a regular grid), and Whittaker kernels are either too wide, causing spectral leakage from the side lobes of the data spectrum, or are not constant over the desired section of the data spectrum, causing filtering of the data. The spectrum of the sinc interpolation kernel, however, shows that it is uniform over the desired section of the data spectrum, avoiding any data filtration, and zero thereafter, preventing any spectral leakage from any of the data's spectral side lobes. This strongly suggests that the sinc function would be a good choice for an interpolation kernel.

Upon application to synthetic PIV images provided by the Visualization Society of Japan (http://www.vsj.or.jp/piv/), the interpolation error was plotted as a function of the sub-pixel shift (see Figure 2.17). It can be seen clearly that the sinc

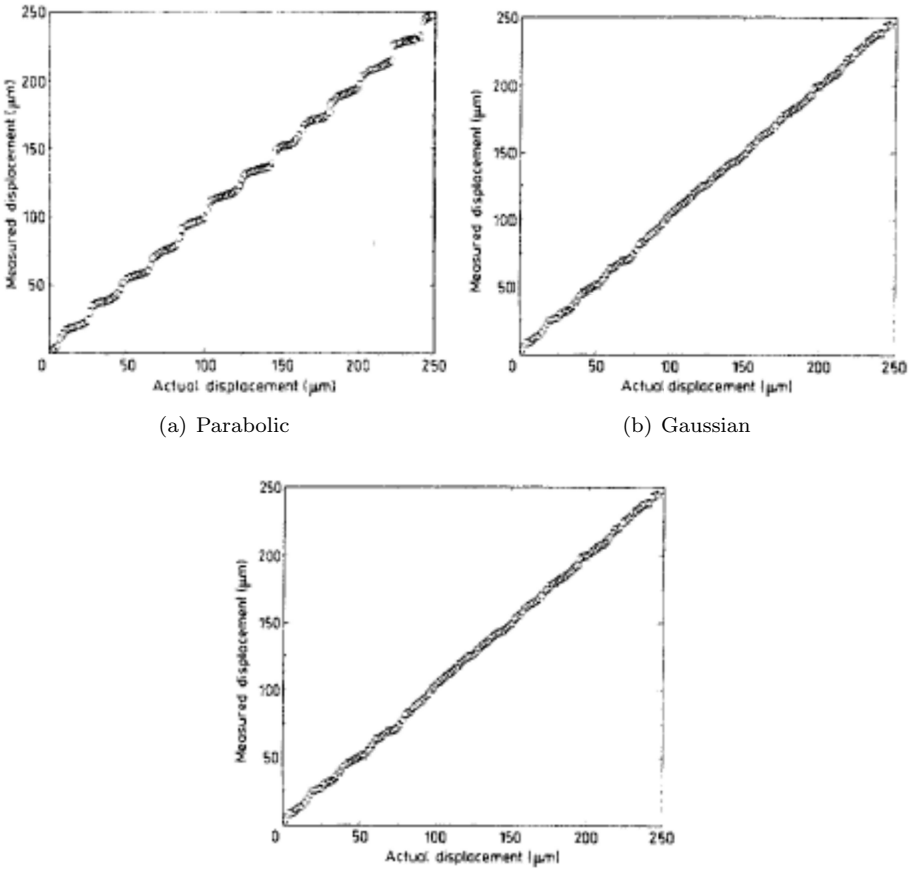

(a) Parabolic

(b) Gaussian

(c) Whittaker's interpolation peak finding algorithms

Figure 2.15: Actual vs. measured displacements (Lourenco and Krothapalli, 1995).

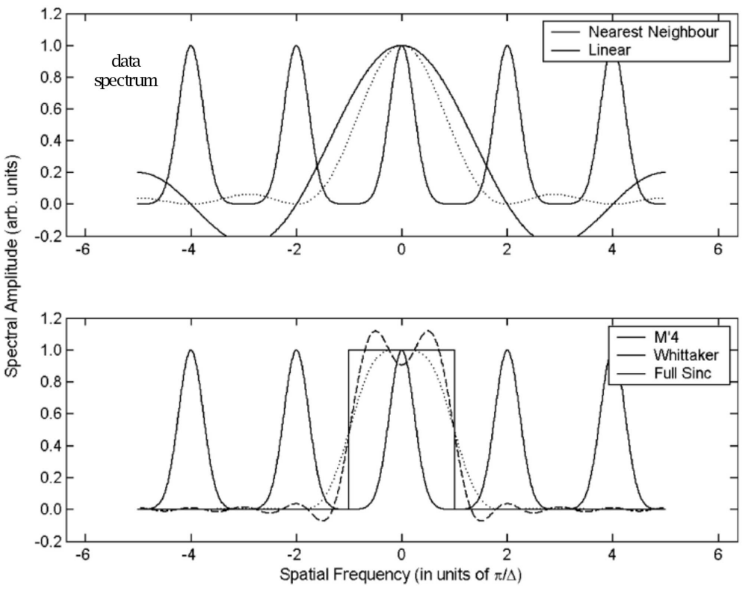

Figure 2.16: Spectral shape of different subpixel interpolation kernels (Roesgen, 2003).

interpolation kernel has almost non-existent interpolation errors, easily surpassing the performance of the widely used Gaussian interpolation kernel.

Most recently, Nobach and Honkanen (2005) have revisited subpixel interpolation kernels. Rather than implementing two one-dimensional interpolation kernels (one in the x-direction and one in the y-direction), they suggest using a two-dimensional 9-point Gaussian regression method (see Figure 2.18). Their results as applied to particle images with and without noise are shown in Figure 2.19. For the ideal case of images that are not noisy, the nine-point Gaussian regression and the two 3-point interpolators behave identically for particle image diameters larger than 4 pixels, since the particles are Gaussian shaped, and thus better approximated by the Gaussian one-dimensional and two-dimensional regression interpolators. For particle image diameters between 2-4 pixels, the extra particle image values used towards the two-dimensional regression are sufficiently different from a Gaussian regression that the introduced bias errors are non-negligible. Also discovered was that while the two-dimensional Gaussian regression worked perfectly for Gaussian shaped particle images or correlation peaks, if the particle shapes differed from the Gaussian shape, the regression did not work that well. To remedy this situation, the images were pre-processed with a low-pass Gaussian filter, which reduced the noise as well as deformed the particle shape towards a Gaussian profile. The results, also presented in Figure 2.19, show that for particle diameters just over 4 pixels, the bias error is reduced significantly to almost 10^{-4}

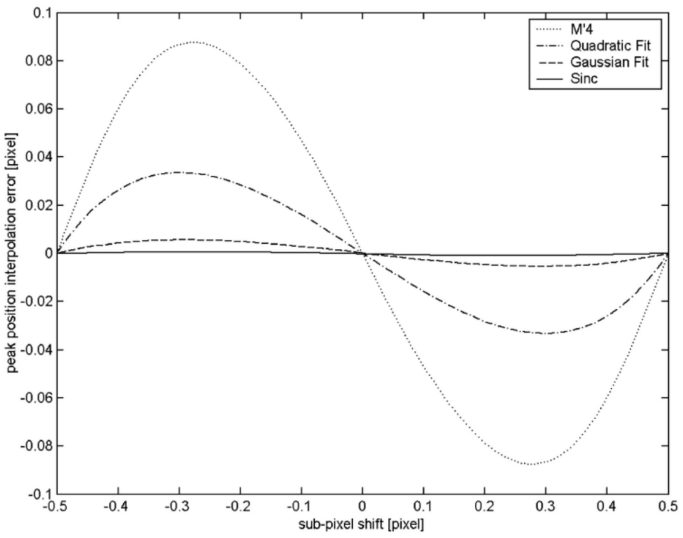

Figure 2.17: Subpixel interpolation error for different interpolation schemes (Roesgen, 2003).

pixels. Noisy images unfortunately reduce the performance of the filtered regression algorithm almost by an order of magnitude, though it still outperforms the two one-dimensional interpolation schemes for particle images larger than ~ 2.2 pixels (see Figure 2.19(b)).

2.5.2 Effect of tracer particle image diameter

Using Gaussian interpolation peak finding methods, Raffel *et al.* (1998) performed Monte Carlo simulations of translational tracer particle shifts using different particle diameters and interrogation window sizes, in order to determine their effects on the measurement uncertainty. (see Figure 2.20). As is shown, the optimum tracer particle image diameter that minimizes the measurement uncertainty is just above 2 pixels, depending on the interrogation window size. It is also seen that larger window sizes further reduce the measurement uncertainty, as more particles within the interrogation window contribute to the cross-correlation peak.

For particle image diameters smaller than the optimum diameter, the error increases, since the displacements become biased towards integer values (see Figure 2.21) that result in the "peak locking" effect introduced in the previous section. This indicates that the subpixel peak estimator, in this case the Gaussian peak finder, is not suitable for use with these tracer particle image diameters, since such particles are not Gaussian shaped. In fact, as can be seen from Figure 2.13, other peak finding methods, such as the centroid peak finder, can perform even worse.

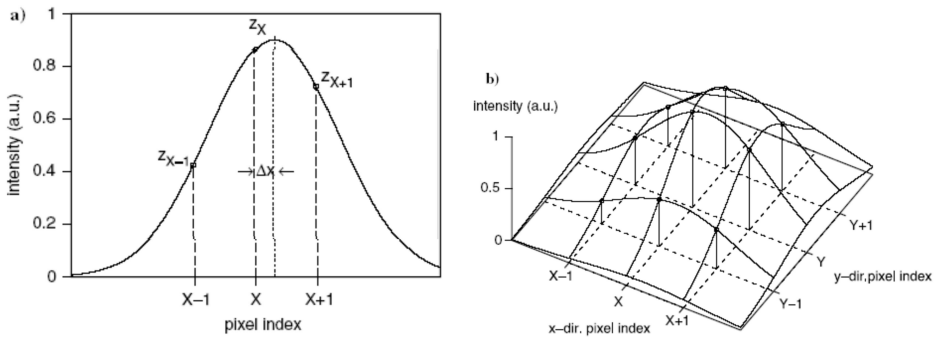

Figure 2.18: **a** One-dimensional three-point interpolation and **b** two-dimensional Gaussian regression (Nobach and Honkanen, 2005).

2.5.3 Effect of tracer particle image shift

In order to determine the effects of tracer particle image shifts, which had been predicted in section 2.4, Raffel *et al.* (1998) performed Monte Carlo simulations (see Figure 2.22) of translational tracer particle shifts showing that for particle image shifts larger than 0.5 pixels, the measurement uncertainty grows linearly. For the same tracer particle image diameter, it can be seen that larger windows will result in a shallower slope since the larger window size will still capture more particles in common to both interrogated windows that are cross-correlated. The effect of the tracer particle image diameter can also be seen in Figure 2.22. Note that the 2 pixel tracer particle image diameter results show a much lower uncertainty, as well as a much shallower slope for tracer particle image shifts greater than 0.5 pixels, confirming the results shown in Figure 2.20. Also interesting is that for particle shifts less than 0.5 pixels, the measurement uncertainty is linear, reducing to zero at zero shifts.

As predicted in section 2.4.2, the bias errors that result due to smaller portions of the interrogation windows containing the same tracer particle images can be corrected by dividing the correlation by F_I (Westerweel, 1993). This has also been tested by Raffel *et al.* (1998), the results of which are shown in Figure 2.23 (Raffel *et al.*, 1998). It can be seen that the corrected results have substantially lower bias errors than the non-corrected results, thus verifying the predictions made by theory.

2.5.4 Effect of tracer particle image density

As has been indicated previously, larger tracer particle densities will reduce the measurement uncertainty. This has also been specifically tested using Monte Carlo simulations of translational tracer particle shifts by Raffel *et al.* (1998), the results of which are shown in Figure 2.24 (Raffel *et al.*, 1998). It can be clearly seen here

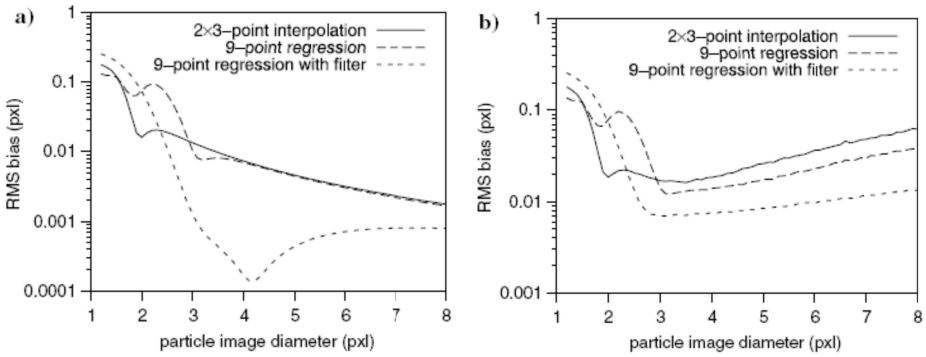

Figure 2.19: Root mean square (RMS) bias of the one-dimensional three-point interpolation and the two-dimensional Gaussian regression: a without noise and b with simulated photon noise (Nobach and Honkanen, 2005).

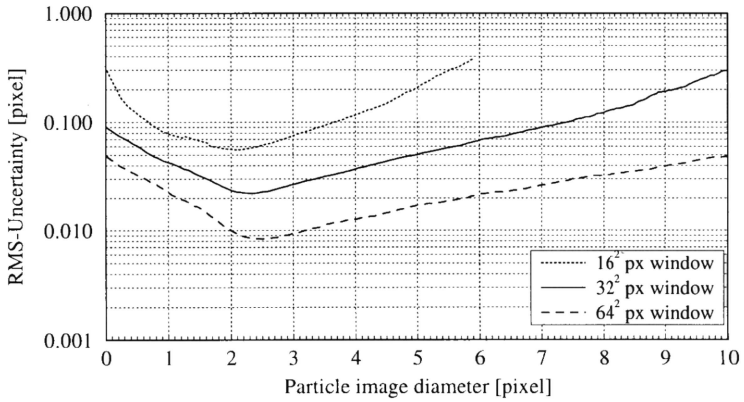

Figure 2.20: Measurement uncertainty (RMS random error) in digital cross-correlation PIV evaluation with respect to varying particle image diameter. (Simulation parameters: FFT-based correlations, quantization level = 8 bits/pixel, no noise, optimum exposure, top-hat light sheet profile, tracer particle image density=1/64 pixel^{-1}) (Raffel *et al.*, 1998).

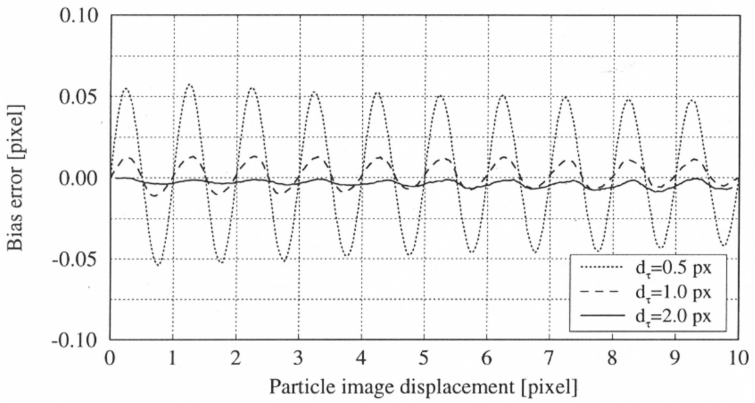

Figure 2.21: "Peak locking" is introduced when the particle image diameter is too small for the three-point estimator (simulation parameters identical to Figure 2.20.) (Raffel *et al.*, 1998)

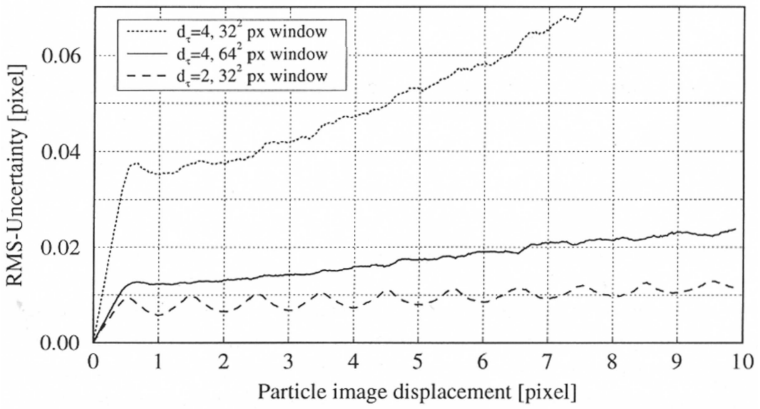

Figure 2.22: Monte Carlo simulation results using FFT-based correlations, for the measurement uncertainty in digital cross-correlation PIV evaluation as a function of particle image displacement (Raffel *et al.*, 1998).

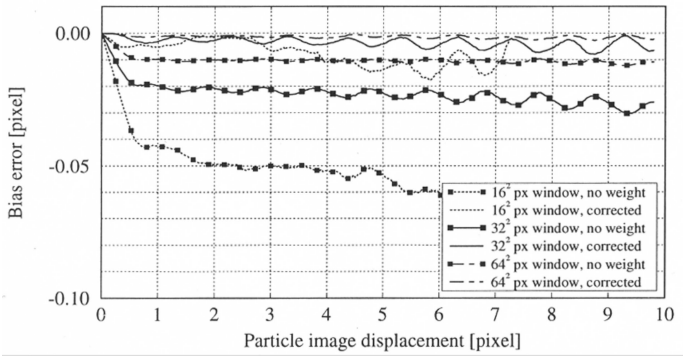

Figure 2.23: Simulation results showing the difference between actual and measured displacement as a function of the particle image displacement. Bias correction remove the displacement bias (simulation parameters: FFT-based correlations, $d_\tau = 2.0$, no noise, top-hat intensity profile, tracer particle image density=1/64 pixel^{-1}) (Raffel *et al.*, 1998).

that as the tracer particle image density increases from 5.2 to 32, the measurement uncertainty, for particle image shifts greater than 0.5, reduces by almost a factor of 3, from .04 to .015. As was also seen in Figure 2.22, for tracer particle image shifts less than 0.5 pixels, the measurement uncertainty is shown to be linear.

It should be noted, however, that the tracer particle density is not the only parameter that would determine a high probability of detecting a valid displacement. Other factors, such as the amount of in-plane displacement, F_I, and the amount of out-of-plane displacement, F_I,, also play a significant role, which has been expressed in Equation (2.17a). Towards this end, Raffel *et al.* have also performed Monte Carlo simulations showing what the percent valid detection probability is as a function of the effective particle image pair density, $N_I F_I F_0$, for a variety of tracer particle image densities, and interrogation window sizes (see Figure 2.25) (Raffel *et al.*, 1998). It is seen that for an effective particle image pair density greater than 7, the probability for detective valid displacements is greater than 95%. The theoretical Poisson distribution curves that describe the probability of detecting at least a given number of tracer particle image pairs, $P[n \geq i]$, is also shown. These theoretical curves show that detecting at least 3-4 particles matches the simulations, suggesting that in practice, the experimental setup and processing be optimized towards this end.

2.5.5 Effect of tracer image quantization levels

Monte Carlo simulations of translational tracer particle shifts have been performed by Raffel *et al.* to determine the effect of image quantization levels on the measurement uncertainty (see Figure 2.26) (Raffel *et al.*, 1998). These results show

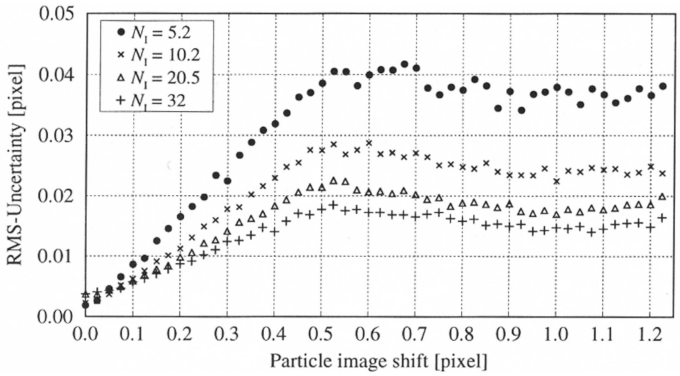

Figure 2.24: Measurement uncertainty for single exposure/double frame PIV as a function of particle image shift for various particle image densities N_I. (simulation parameters: FFT-based correlations, $d_\tau = 2.2$ pixels, quantization level = 8 bits/pixel, 32 x 32 pixel interrogation window size, no noise, optimum exposure, top-hat light sheet profile.) (Raffel *et al.*, 1998).

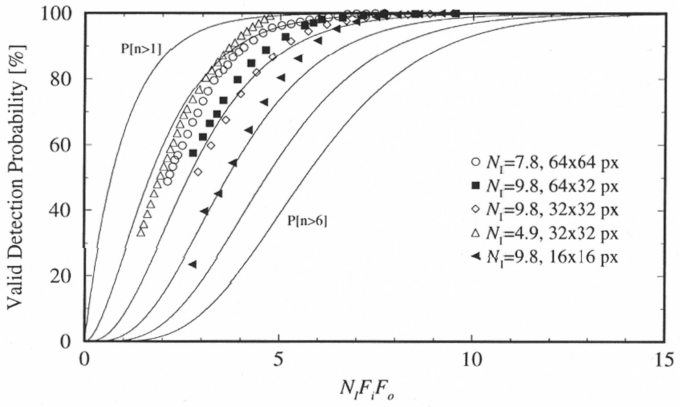

Figure 2.25: Vector detection probability as a function of the product of image density, N_I, in-plane loss of pairs, F_i, and out-of-plane loss of pairs, F_0. The solid line represents the probability for having at least a given number of particle images in the interrogation spot (Raffel *et al.*, 1998).

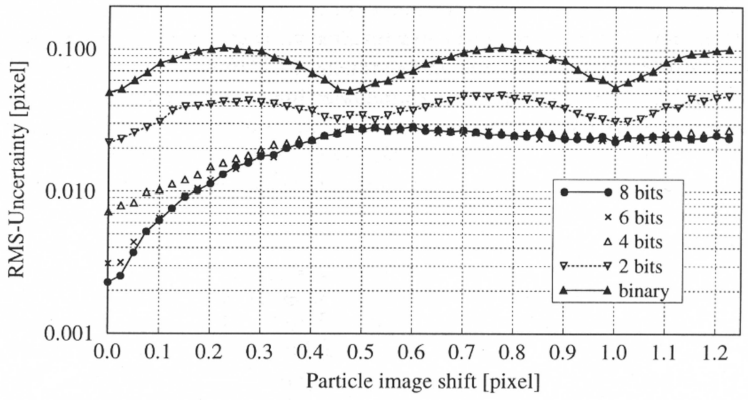

Figure 2.26: Measurement uncertainty for single exposure/double frame PIV as a function of displacement and image quantization (simulation parameters: FFT-based correlations, $d_\tau = 2.2$ pixels, $N_I = 10.2$, 32 x 32 pixel interrogation window size, no noise, optimum exposure, top-hat light sheet profile) (Raffel *et al.*, 1998).

that there is no difference in the measurement uncertainties for quantization levels of 4 bits/pixel and 8 bits/pixel for particle image shifts greater than 0.4 pixels. This implies that the noise due to the FFT-based correlation dominates. However, while it might be tempting to reduce image quantizations to 4 bits/pixel, it should be noted that the measurement uncertainty using 8-bit quantization drops by a factor of 3.5 as the particle image shift reduces to 0 pixels. As shown in section 2.5.3, by implementing the methods shown in section 2.4.2, it is possible to reduce the bias error to near zero values, suggesting that using 8-bit CCD will allow for further reduction of the measurement uncertainty. Any further reduction in quantization level below 4 bits/pixel is detrimental, as the measurement uncertainties increase by an order of magnitude.

2.5.6 Effect of background noise

Raffel *et al.* have also performed Monte Carlo simulations to determine the effect of background noise on the measurement uncertainty (see Figure 2.27) (Raffel *et al.*, 1998). The simulations used a white noise distribution added to each pixel, where the noise for each pixel was uncorrelated with its neighbors, or with its companion image at the same pixel location. These results show that for noise levels of up to 10%, the effect is negligible for particle image shifts greater than 0.4 pixels. However, there is noticeable change for particle shifts less than 0.4 pixels, thereby suggesting that low noise CCDs are desirable if the particle shifts can be reduced to less than 0.4 pixels (see sections 2.4.2 and 2.5.3).

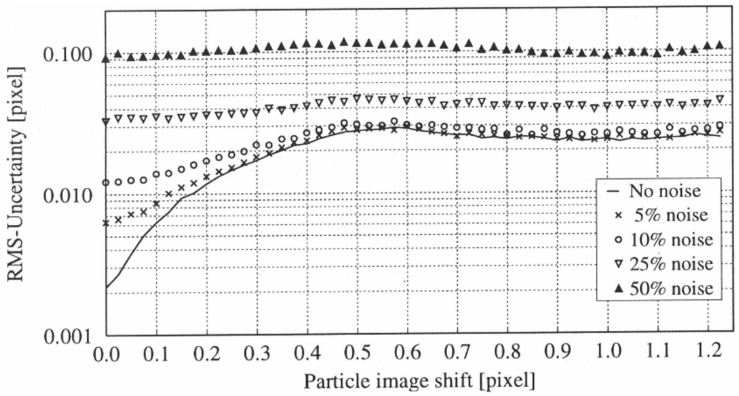

Figure 2.27: Measurement uncertainty as a function of displacement and various amounts of white background noise (simulation parameters: FFT-based correlations, $d_\tau = 2.2$ pixels, $N_I = 10.2$, 32 x 32 pixel interrogation window size, no noise, optimum exposure, top-hat light sheet profile) (Raffel *et al.*, 1998).

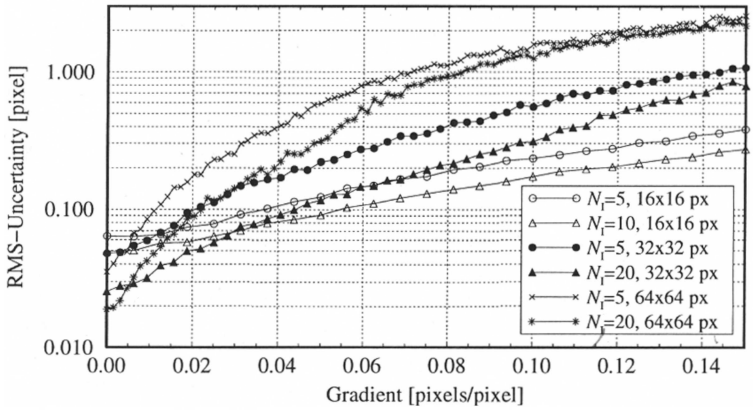

Figure 2.28: Measurement uncertainty as a function of displacement gradient for various particle image densities and interrogation window sizes (simulation parameters: FFT-based correlations, $d_\tau = 2.2$ pixels, quantization level = 8 bits/pixel, no noise, optimum exposure, top-hat light sheet profile). (Raffel *et al.*, 1998).

2.5.7 Effect of displacement gradients

Due to the fact that the pixels within most CCDs are either rectangular or square and therefore distributed in a Cartesian grid, the PIV methodology is best suited for measuring displacements that are uniform translations. However, since fluid flow, which PIV is designed to interrogate, is most often filled with velocity gradients, it is important to be able to characterize the behavior of PIV for tracer particles that contain gradients in their displacement fields. Raffel *et al.* have performed Monte Carlo simulations to determine the effect of displacement gradients on the measurement uncertainty, the results of which are shown in Figure 2.28 (Raffel *et al.*, 1998). Here, the particle image density and the interrogation window sizes were varied in order to ascertain their effects upon the measurement uncertainty for images with particle image shift gradients. Interestingly, it can be seen that the smaller interrogation windows and larger tracer particle image densities are able to tolerate larger displacement gradients. However, the window size seems to be the greater factor in reducing the measurement uncertainty since for the same interrogation window size, the measurement uncertainty reduction is relatively small compared to the its reduction when for the same particle image density, the window size is reduced.

2.6 Calculation of differential and integral flow properties from the velocity field

In the formulations developed in the previous section, PIV provides global velocity data within a two-dimensional domain and does not directly measure important differentiable quantities, such as vorticity and strain rates, or integral quantities such as circulation, streamlines, or potential lines. As such, they must be post-calculated from the velocity fields. The following two sections discuss how such calculations can be achieved.

2.6.1 Calculation of differential flow properties

The vorticity and strain rates fields are both a consequence of the deformation tensor, which is:

$$\frac{d\vec{U}}{d\vec{X}} = \begin{bmatrix} du/dx & d\nu/dx & dw/dx \\ du/dy & d\nu/dy & dw/dy \\ du/dz & d\nu/dz & dw/dz \end{bmatrix}. \tag{2.24}$$

When using the vorticity vector, $\vec{\omega}$, and the strain tensor, $\vec{\varepsilon}$, the deformation tensor can be expressed as:

$$\frac{d\vec{U}}{d\vec{X}} = \begin{bmatrix} \varepsilon_{xx} & \varepsilon_{xy}/2 & \varepsilon_{xz}/2 \\ \varepsilon_{yx}/2 & \varepsilon_{yy} & \varepsilon_{yz}/2 \\ \varepsilon_{zx}/2 & \varepsilon_{zy}/2 & \varepsilon_{zz} \end{bmatrix} + \begin{bmatrix} 0 & \omega_z/2 & -\omega_y/2 \\ -\omega_z/2 & 0 & \omega_x/2 \\ \omega_y/2 & -\omega_x/2 & 0 \end{bmatrix}, \tag{2.25}$$

where $\varepsilon_{ij} = 1/2\,(\partial u_i/\partial x_j + \partial u_j/\partial x_i)$, and $\omega_i = \varepsilon_{ijk}\partial u_j/\partial x_k$. As 2D PIV is a two-dimensional technique that can only provide two-components of the velocity, the measurable deformation matrix reduces to

$$\frac{d\vec{U}}{d\vec{X}} = \begin{bmatrix} \varepsilon_{xx} & \varepsilon_{xy}/2 \\ \varepsilon_{yx}/2 & \varepsilon_{yy} \end{bmatrix} + \begin{bmatrix} 0 & \omega_z/2 \\ -\omega_z/2 & 0 \end{bmatrix}, \tag{2.26}$$

since the third velocity component, and d/dz terms cannot be measured. Since the vorticity and strain rates fields cannot be directly measured, differentiation schemes must be used to derive these quantities. Such schemes, however, are susceptible to errors resulting from different grid spacing as well as noise within the velocity data. It is therefore important to be able to study and characterize various differentiation schemes in order to ascertain their performance.

In a study of several differentiation schemes, Raffel *et al.* (Raffel *et al.*, 1998) were able to document estimates for the first derivative, df/dx, of a function $f(x)$ at a discrete location, $f_i(x_i)$ (see Table 2.2). Here, ε_U is the velocity measurement uncertainty. The accuracy of each scheme is defined as the truncation error associated with each scheme, and the uncertainty of each scheme is dependent on the velocity measurement uncertainty within the velocity field. Table 2.2 suggests that the forward and backward differentiation schemes would perform poorly, as both their accuracies and uncertainties are the highest.

To test these predictions, these schemes were applied towards calculating the vorticity from the velocity field of a laminar vortex pair, where vorticity contours should be smooth (Raffel *et al.*, 1998; Willert, 1992). Figure 2.29 shows the vorticity fields of the laminar vortex pairs resulting from various differentiation schemes. It can be clearly seen that the least-squares approach produces the smoothest vorticity contours. Interestingly, the Richardson scheme, which is designed to minimize truncation errors, shows not-so-smooth vorticity contours, suggesting that schemes that can best minimize both accuracy and uncertainty are the most desirable. An interesting observation is that while Table 2.2 suggests that the center differencing scheme should produce the best results since it best maximizes the accuracy while minimizing the uncertainty, it in fact does not perform as well as the least-squares scheme.

Also of interest is the effect of the grid spacing. Table 2.2 suggests that reducing the size of the grid spacing should decrease the accuracy, while increasing the uncertainty. By increasing the interrogation window from 50% (Figure 2.29) to 75% (Figure 2.30), the effects of the grid spacing size is seen. Overall, the results show the undesirable effect of an increased vorticity noise level. However, the peak vorticity value at the vortices' center is significantly increased, closer to its true value. This suggests that the finer grid spacing gives better estimates for the vorticity (though noisier), since the area over which the vorticity is averaged is smaller.

An alternative to calculating vorticity is through the use of circulation:

$$\Gamma = \oint \vec{u} \cdot \vec{dl} = \int \vec{\omega} \times \vec{dS}\,, \tag{2.27}$$

Table 2.2: First order differential operators for data spaced at uniform ΔX intervals along the X-axis (Raffel *et al.*, 1998).

Scheme	**Implementation**	**Accuracy**	**Uncertainty**
Forward difference	$\left(\frac{df}{dx}\right)_{i+1/2} \approx \frac{f_{i+1}-f_i}{\Delta X}$	$0(\Delta X)$	$\approx 1.41\frac{\varepsilon_U}{\Delta X}$
Backward difference	$\left(\frac{df}{dx}\right)_{i-1/2} \approx \frac{f_i-f_{i-1}}{\Delta X}$	$0(\Delta X)$	$\approx 1.41\frac{\varepsilon_U}{\Delta X}$
Center difference	$\left(\frac{df}{dx}\right)_{i} \approx \frac{f_{i+1}-f_{i-1}}{2\Delta X}$	$0(\Delta X^2)$	$\approx 0.7\frac{\varepsilon_U}{\Delta X}$
Richardson extrapolation	$\left(\frac{df}{dx}\right)_{i} \approx \frac{f_{i-2}-8f_{i-1}+8f_{i+1}-f_{i-2}}{12\Delta X}$	$0(\Delta X^3)$	$\approx 0.95\frac{\varepsilon_U}{\Delta X}$
Least squares	$\left(\frac{df}{dx}\right)_{i} \approx \frac{2f_{i+2}+f_{i+1}-f_{i-1}-2f_{i-2}}{10\Delta X}$	$0(\Delta X^2)$	$\approx 1.0\frac{\varepsilon_U}{\Delta X}$

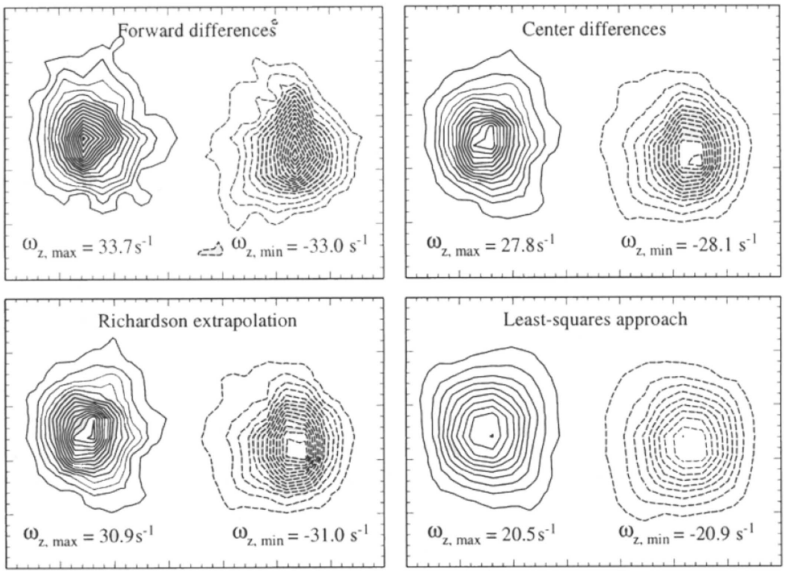

Figure 2.29: Vorticity field estimates obtained from twice oversampled PIV data, *e.g.* the interrogation window overlap is 50%. The vortex pair is known to be laminar and thus should have smooth vorticity countours (Raffel *et al.*, 1998).

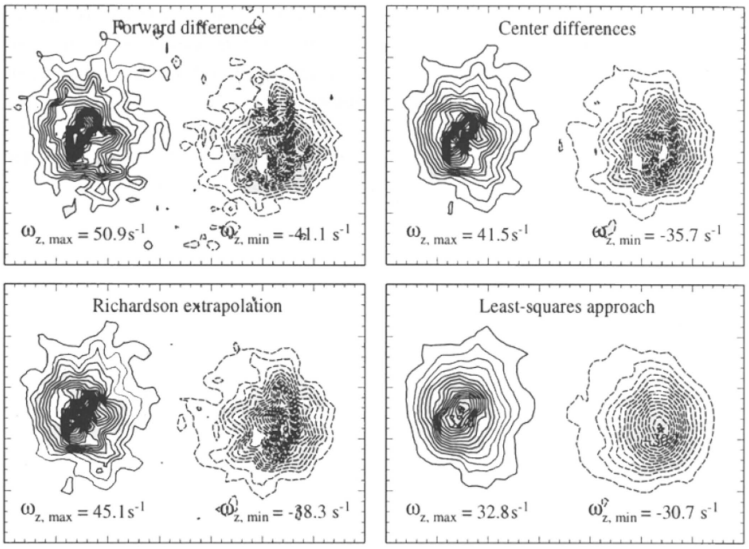

Figure 2.30: Vorticity field estimates obtained from four times oversampled PIV data, *e.g.* the interrogation window overlap is 75% (Raffel *et al.*, 1998).

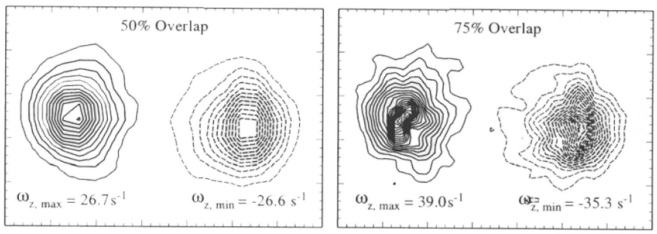

Figure 2.31: Vorticity field estimates obtained from PIV velocity fields by the circulation method: (left) the velocity field is twice oversampled, (right) four times oversampled. The contours of this laminar vortex pair are known to be smooth such that the nonuniformities are due to measurement noise (Raffel *et al.*, 1998).

where Γ is the circulation, and $\vec{\omega}$ is the vorticity vector. Given the above, for two-dimensional flows, the average z-component vorticity can be calculated as

$$\overline{\omega}_z = \Gamma / A \,, \tag{2.28}$$

where $\overline{\omega}_z$ is the average z-component vorticity, and A is the area over which the line and area integrals in Equation (2.27) are performed. This scheme is in fact identical to applying a 3 x 3 smoothing operator to the velocity field followed by a center differencing scheme (Westerweel, 1993). This approach reduces the uncertainty to $\approx 0.61\varepsilon_U/\Delta X$ (Raffel *et al.*, 1998). The application of this scheme to the laminar vortex pair is shown in Figure 2.31. The vorticity contours shown are comparable to those shown for the least-squares scheme. However, the advantage of this approach is its better estimation of the peak vorticity value. Again, it can be seen that smaller grid sizes better estimate the value of the vorticity peaks, since the area over which the vorticity is averaged is smaller.

In an effort to further reduce the total error due to velocity uncertainties and truncation errors, Lourenco and Krothapalli (1995) implemented an adaptive scheme based on the Richardson's extrapolation principle by combining the vorticity estimates at different grid sizes. Figure 2.32 shows a typical differentiation result using a central-difference scheme, while Figure 2.32(b) shows the improved result using the adaptive scheme. Further investigation showed that an improvement in accuracy could be achieved if each of the derivative estimates at the different grid sizes were computed using a least squares second order polynomial approximation (see Figure 2.32(c)).

Second order schemes have been further studied towards obtaining more accurate vorticity calculations. Fouras and Soria (1998), recognizing that the vorticity error was composed of both a bias error and a random error, investigated the transmission of the velocity uncertainties into the vorticity random error, and the effect of grid spacing on the vorticity bias error using various implementations of a second-order polynomial χ^2 fit, as described by Soria that used different grid patterns for calculating the vorticity (see Figure 2.33).

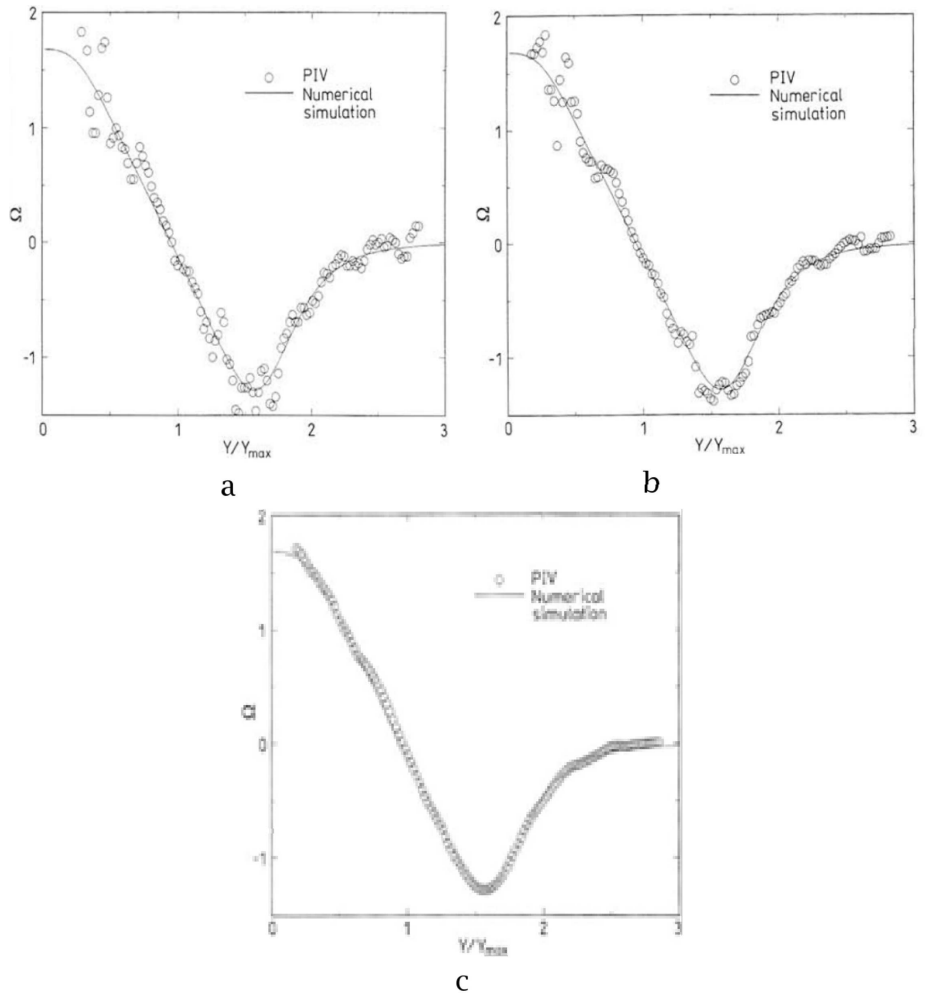

Figure 2.32: **a** Wall-jet vorticity distribution (central-difference scheme); **b** Wall-jet vorticity distribution (Adaptive Scheme) **c** jet vorticity distribution (adaptive scheme and least-squares) (Lourenco and Krothapalli, 1995).

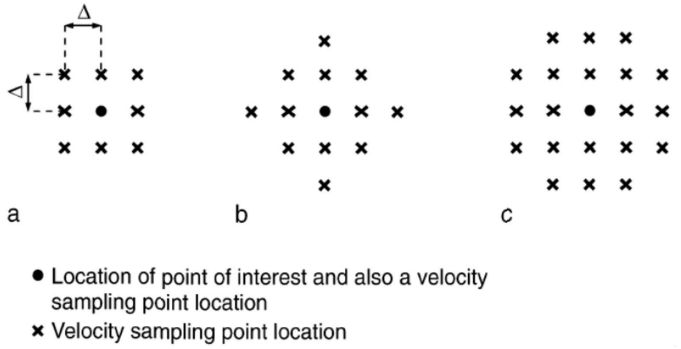

Figure 2.33: Rectangular grid patterns used for the calculation of ω_z using the χ^2 method. The locations of the velocity sampling points and the point of interest relative to the velocity sampling points are identified for. **a** The χ^2_9 method which uses 9 velocity sampling points; **b** the χ^2_{13} method which uses 13 velocity sampling points and **c** the χ^2_{21} method which uses 21 velocity sampling points (Fouras and Soria, 1998).

In addition, they developed a theoretical analysis of the random error for the χ^2 vorticity calculation method that estimates a priori the random vorticity error using χ^2_9 , χ^2_{13} , and χ^2_{21} vorticity calculation method to be σ_u/Δ, $.447\sigma_u/\Delta$, and $.328\sigma_u/\Delta$, respectively, where Δ is the grid spacing, and σ_u is the velocity uncertainty. The results, shown in Figure 2.34, show that their theory predicts the numerical simulations quite well. Furthermore, it is seen that the random error transmission errors for the χ^2_{21} method is lower than the χ^2_9 and χ^2_{13} methods by 67% and 26%, respectively.

The effects of grid spacing on the vorticity bias error were studied using numerical simulations of an Oseen vortex. The normalized vorticity bias errors as a function of normalized radial distance is shown in Figure 2.35. It can be seen that as the grid spacing gets smaller with respect to the characteristic length scale of the flow, the bias error reduces dramatically. While it is tempting to reduce this ratio to near zero values, it should be pointed out that in practice, this would require very highly resolved velocity measurements, which may be difficult to achieve with present technology. Also seen is that χ^2_9 has much lower bias error than χ^2_{13} or χ^2_{21}, which is due to the different spatial filtering characteristics of the vorticity calculation methods.

Recognizing that the spatial resolution is limited towards the large scales by the total image dimensions and towards the small scales by the interrogation window size, Foucaut and Stanislas (2002) performed an exhaustive investigation of conventional schemes by studying their transfer functions. The differentiation schemes studied where 2^{nd}, 4^{th}, 6^{th}, and 8^{th} order centered difference, compact difference and Richardson's extrapolation schemes; 2^{nd}, 4^{th}, and 6^{th} order noise minimized

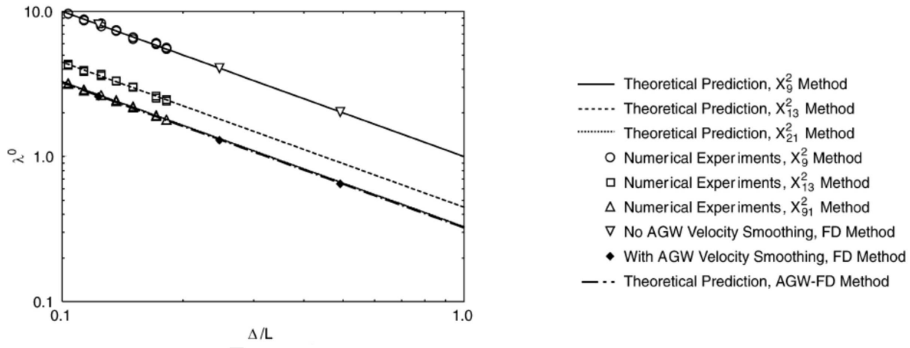

Figure 2.34: Ratio of normalized vorticity standard deviation to normalized velocity standard deviation, *i.e.* λ_0, as a function of Δ/L. The solid lines are the theoretically predicted variations for vorticity calculated using the χ^2 method. The symbols are the vorticity results calculated using the χ^2 method from numerical experiments using noisy velocity data for the Oseen vortex flow field. Some corresponding results for vorticity calculated using the finite difference method without and with prior smoothing of the velocity field are also shown for comparison (Fouras and Soria, 1998). $\lambda_0 = \sigma^*(\omega_z)/\sigma^*(u)$, where $\sigma^*(\omega_z) = \sigma(\omega_z)/(V_{ref}/L)$, $\sigma^*(u) = \sigma(u)/V_{ref}$, $\sigma(\omega)$ is the random vorticity error, $\sigma(u)$ is the random velocity error, L is a characteristic length scale of the flow, and V_{ref} is a characteristic velocity of the flow.

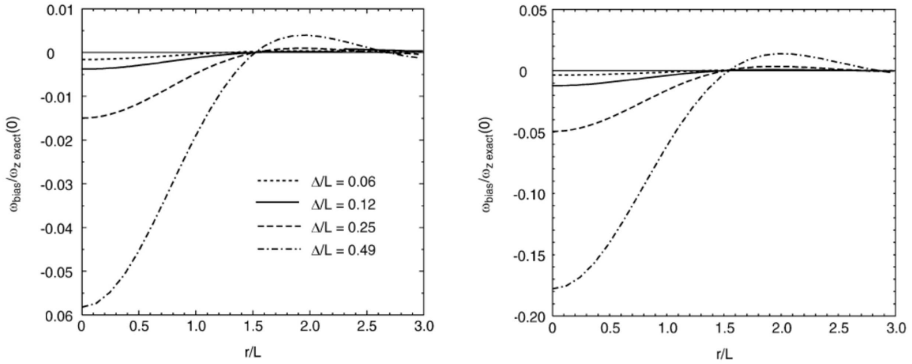

(a) χ^2 method using 9 velocity sampling points

(b) χ^2 method using 13 velocity sampling points

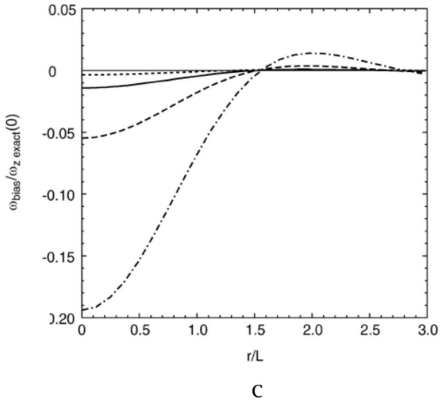

(c) χ^2 method using 21 velocity sampling points (Fouras and Soria, 1998).

Figure 2.35: Bias error in ω_z calculation using exact discretized velocity data of the Oseen vortex for different Δ/L sampling separations and using different vorticity calculation methods.

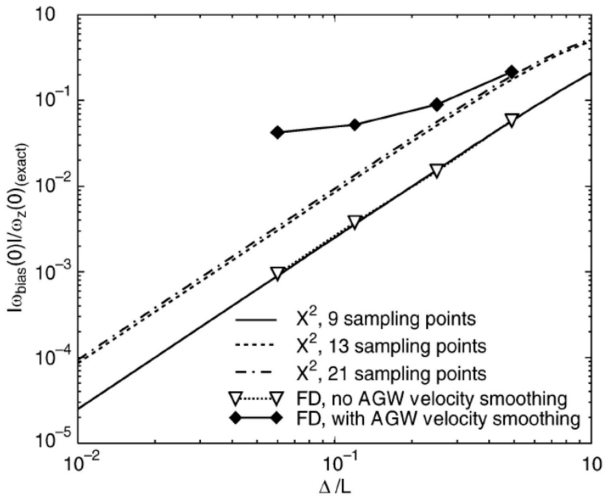

Figure 2.36: Bias error at the vortex centre, *i.e.* $|\omega_{bias}(0)|/\omega_z(0)_{exact}$ as a function of normalized velocity sampling distance Δ/L for the χ^2 vorticity calculation method when 9, 13 and 21 velocity sampling points are used in the interpolation process and for the FD and AGW-FD vorticity calculation methods (Fouras and Soria, 1998).

Richardson extrapolation schemes, a second-order noise minimized least squares scheme, and an eight-point circulation scheme. To characterize the PIV data, the PIV spectral response was first determined from experimentally obtained PIV results, and compared with results obtained with a hot wire anemometer (HWA).

Figure 2.36 shows the normalized vorticity bias errors as a function of the grid spacing with respect to the characteristic length scale of the flow, Δ/L. Comparison of this figure with Figure 2.34 shows that there is a conflict between simultaneously minimizing the random and bias errors: the larger the value of Δ/L, the lower the random vorticity error, but the higher the bias vorticity error, and visa versa. Overall, Fouras and Soria found that the χ^2_{21} vorticity calculation method resulted in the least overall error, thereby recommending it as the preferred differentiation scheme.

Also, a spectrum model,

$$E_{11PIV} = \left(E_{11HWA}^{1/2} + E_{noise}^{1/2}\right)^2 \left(\frac{\sin\left(kX/2\right)}{kX/2}\right)^2 , \tag{2.29}$$

where E_{noise} is the white noise level used to optimize the fit to the PIV spectrum (E_{noise} varies with the inverse of the window size), X is the interrogation window size, and k is the wave number, was used to best fit and model the PIV spectrum. Furthermore, the window size was optimized by setting the cutoff wave number of the PIV spectrum to be where the signal-to-noise ratio was equal to 1. This

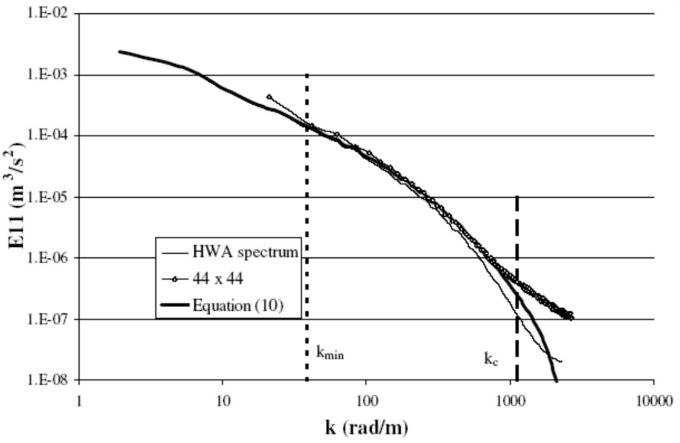

Figure 2.37: Power spectra of velocity along x, $44x44$ interrogation window, frequency optimization. Equation (2.10) in the figure refers to Equation (2.29) (Foucaut and Stanislas, 2002).

approach resulted in a noise level on the order of 1% of the velocity dynamic range, an interrogation window size of 44 x 44 pixels^2, and a cutoff wave number of 1200 rad/m (see Figure 2.35).

The transfer functions of the differentiation schemes are shown in Figure 2.38(a-c). Given that the cutoff wave number for the PIV data using 44 x 44 interrogation windows in these figures is 1.37, it can be seen that the differentiation scheme with the closest cutoff wave number is the second-order centered difference differentiation scheme, which has a cutoff wave number value of 1.39.

The power spectra of the differentiation schemes are shown in Figure 2.39. It can be seen that the best filter is the second-order centered difference scheme, since it has the same cutoff wave number as the PIV results. The 4^{th} order Richardson extrapolation and the least-square schemes are identical in behavior, showing a strong filtering effect. On the other hand, the 6^{th} and 10^{th} order compact difference schemes have higher cutoff wave numbers, thereby amplifying any noise that would exist in the PIV data.

In an effort to overcome the conflict of simultaneously minimizing the random and bias errors, first pointed out by Fouras and Soria, and confirmed by Foucaut and Stanislas, Etebari and Vlachos (2005) hypothesized that by combining the favorable bias-error reducing characteristics of the higher order implicit schemes with those of the noise-minimizing schemes, a new scheme could be developed that would reduce the overall errors and outperform the second order center differencing scheme recommended by both Fouras/Soria and Foucaut/Stanislas. Towards this end, they combined a 4^{th} order compact scheme, which has low bias error, with a noise-optimized Richardson extrapolation scheme, which has low noise am-

plification, which uses a summation procedure of various spatial samplings of the derivatives. Their results suggest that this hybrid compact-Richardson extrapolation scheme provides nearly 30% less noise amplification while simultaneously reducing the bias error with respect to the centered difference scheme. They also suggest that further improvements might be attainable if the cutoff wave number of this scheme is adjusted to meet the characteristics of the particular experimental PIV data set.

2.6.2 Calculation of integral flow properties

There are several parameters of interest that can be derived using integral methods. Circulation can be achieved using path integrals. Circulation is defined as

$$\Gamma = \oint \vec{u} \cdot \vec{dl}\,, \tag{2.30}$$

where $\vec{u}$ is the velocity vector, and $\vec{dl}$ is the differential path length of the total path defining the boundary C. The numerical integration of Equation (2.30) is straightforward using standard integration methods. Streamlines and potential lines can also be derived using integral methods. Assuming the flow is two-dimensional, the PIV results can be used to derive streamlines and potential lines using the following relations:

$$\Psi = \int_y u dy - \int_x \nu dx\,, \tag{2.31}$$

$$\Phi = \int_x u dx + \int_y \nu dy\,. \tag{2.32}$$

Performing the integration in Equation (2.31) to obtain S will not produce unique results, since different frames of reference will produce different streamlines. This is synonymous with reducing the Poisson equation

$$\Delta^2 \Psi = -\omega_z\,, \tag{2.33}$$

into the Laplace equation

$$\Delta^2 \Psi = 0\,. \tag{2.34}$$

However, since the vorticity field is an approximation, and since boundary conditions need to be specified, this integration becomes difficult. Figure 2.40, for example, shows the different resulting set of streamlines that occur due to different choices of the frame of reference.

2.7 Outlier detection methods

Regardless of how well PIV images are acquired, the post-processing cross correlation procedure can result in spurious vectors due to seeding inhomogeneities, effects of turbulence, varying intensity light sheet, etc. An example of spurious

vectors that would infect an otherwise perfect velocity field is shown in Figure 2.41. Such outliers are most often visibly detectable, and are necessary to identify in order to maintain the integrity of the data to allow for proper data interpretation and derivation of differential and integral quantities, such as vorticity, strain rates, circulation, and streamlines (see section 2.6).

Westerweel (1994) developed a statistical model for isotropic homogenous turbulent flow (in most cases flows that are not homogeneous or isotropic can be transformed to a domain where they are both) that characterizes outliers in PIV data. This model was then used to investigate three different outlier detection methods. For all these methods, a displacement residual vector was defined,

$$\vec{r}_{i,j} = \vec{V}'_{i,j} - \vec{V}_{i,j} \,, \tag{2.35}$$

such that its magnitude squared

$$r_{i,j}{}^2 = \left\| \vec{V}'_{i,j} - \vec{V}_{i,j} \right\|^2 \tag{2.36}$$

acts as the measure of the deviation of $\vec{V}'_{i,j}$, the vector in question, with respect to $\vec{V}_{i,j}$, the vector's true value. In practice, the true value of the vector is not known and is estimated using statistics, mean and variance, using the neighbors of the vector in question. The determination on whether the vector in question is spurious or not is then determined by statistical tests of the displacement residuals. In the first model, the global-mean test estimates the true value of the vector by using the mean velocity of the whole vector field. In the second model, the local-mean test estimates the true vector by using the mean velocity of a small neighborhood, typically a 3 x 3 eight-connected neighborhood (8 points), surrounding the vector in question. In the third model, the local-median test estimates the true vector components by using the median velocity components within a 3 x 3 neighborhood (9 points, including the vector of interest). Once an estimate of the true velocity is found, the displacement residuals are calculated, and tested against a user-selected threshold - if the displacement residual is larger than the threshold, the vector is labeled an outlier. Of the three methods, Westerweel found that the global-mean test performed the worst, the local-mean test better performed better, and the local-median performed the best. Specifically, the local-median test found 4 times fewer erroneous outlier vectors than the local-mean test. This procedure can be repeated until there is no change in the global vector field. While useful, this method is limited by the fact that the user must examine different threshold constants to determine the optimum value to use with a particular data set.

Raffel *et al.* (1998) suggest a different version of the local-mean test. Rather than applying the test to the velocity magnitude, the test is applied to each of the velocity components. Then the average velocity of the eight points surrounding the vector in question is calculated:

$$\langle u_{i,j} \rangle = \frac{1}{N} \sum_{n=1}^{N} u\,(n) \,, \tag{2.37}$$

where N is the 8 neighboring points, $u_i(n)$ is velocity component, and <> denotes an average. Then the standard deviation is calculated:

$$\sigma_{i,j} = \sqrt{\frac{1}{N}\sum_{n=1}^{N}\left(\langle u_{i,j}\rangle - u\left(n\right)\right)^2}\,. \tag{2.38}$$

The residual is then tested against a threshold,

$$|\langle u_{i,j}\rangle - u(n)| < \varepsilon_{thresh}\,, \tag{2.39}$$

where

$$\varepsilon_{thresh} = C_1 + C_2\sigma_{i,j} \tag{2.40}$$

and C_1 and C_2 are under-defined constants. This procedure can be repeated until there is no change in the global vector field. Similar to the local-median test, while useful, this method is also limited by the fact that the user must examine different constant values to determine the optimum values to use with a particular data set.

Nogueira *et al.* (1997) also describe a local validation method. First, the normalized velocity vector residual is calculated throughout the velocity domain,

$$\vec{r}_{i,j} = \frac{\sum_{n=1}^{N}\vec{V}_n - \vec{V}_0}{\sum_{n=1}^{N}\vec{V}_n}\,, \tag{2.41}$$

where N is the 8 neighboring points, $\vec{V}_n$ represents the 8 surrounding velocity vectors, and $\vec{V}_0$ is the velocity vector in question. The location within the velocity field where the residual is a minimum marks a zone where vectors achieve a degree of uniformity and hence a zone of "local coherence". Then, based on user-defined criteria, variations of vectors neighboring those labeled as coherent are examined and joined within the region of coherence. In this manner, regions of coherence grow and can merge. Then once an appreciable number of vectors are achieved within a zone, the vectors within this zone are validated. Figure 2.42(above) shows a PIV measurement field and Figure 2.42(below) shows the resulting validated vector field. Similar to the methods described above, this method is limited by the fact that the user must select two parameters, the tolerance of the prediction percentage, and the number of vectors a coherence zone should contain to be validated. The tolerance of the prediction percentage input, assumes a priori knowledge about the flow as to how much velocity differences can be tolerated. This value is typically set to 20%-35%. The number of vectors a coherence zone should contain for validation is around 10% of the total number of vectors for a correctly sampled flow.

Song *et al.* (1999) validate velocity vectors by verifying if the continuity equation is satisfied within Delaunay triangles. If all nodes within a triangle are good vectors, the total flux through all the sides of the triangle, $Q_1 + Q_2 + Q_3$, is very small. If a node within a triangle is an outlier, the total flux through the triangle

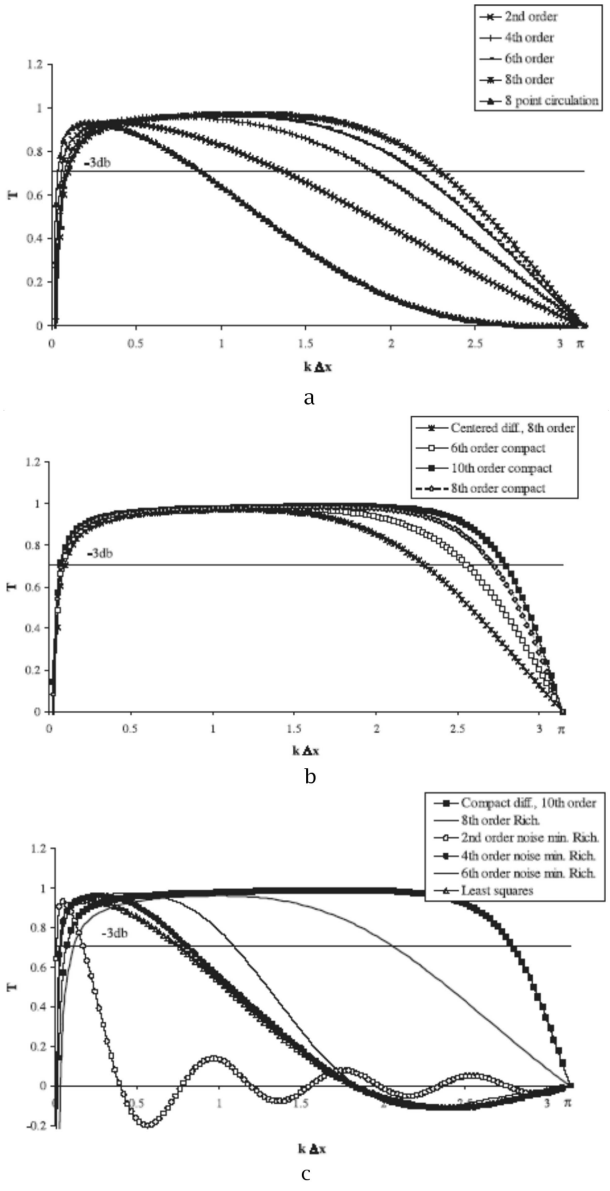

Figure 2.38: **a** Transfer functions of centered difference derivative filters. **b** Transfer functions of compact difference derivative filters. **c** Transfer functions of Richardson extrapolation derivative filters (Foucaut and Stanislas, 2002).

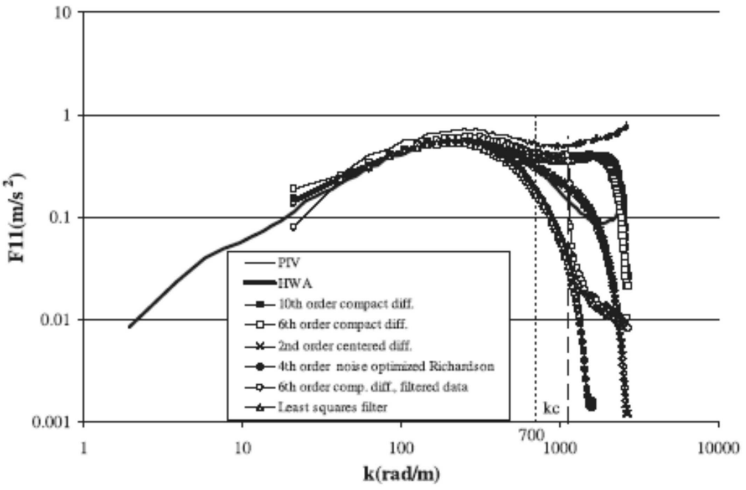

Figure 2.39: Power spectra of derivative of velocity along x, $44x44$ interrogation windows (Foucaut and Stanislas, 2002).

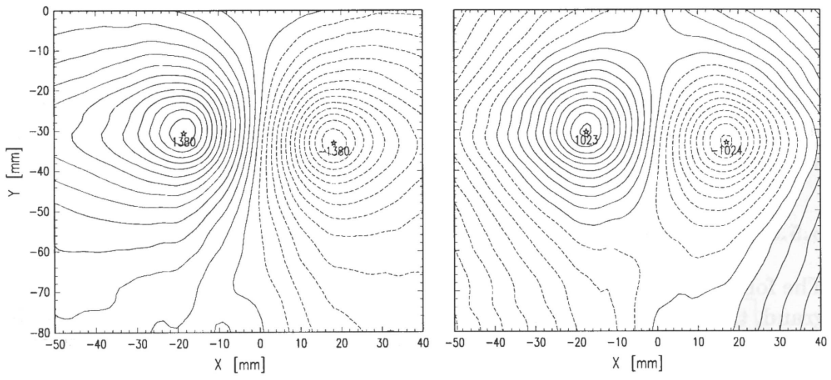

Figure 2.40: Two-dimensional stream function computed from vortex pair velocity data in a laboratory-fixed reference frame (left) and in a reference frame moving 20 mm/s upward with the vortex pair (right) (Raffel *et al.*, 1998).

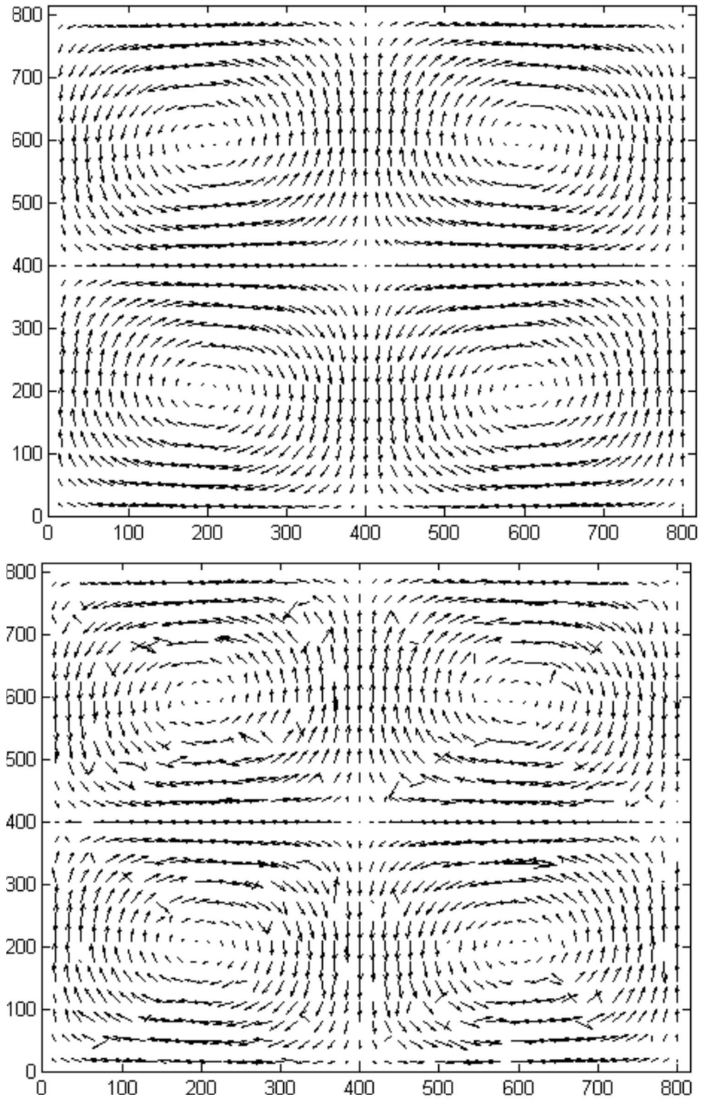

Figure 2.41: Example of a simulated vector field with outliers (above) shows the perfect simulated vector field; (below) shows the same field with outliers.

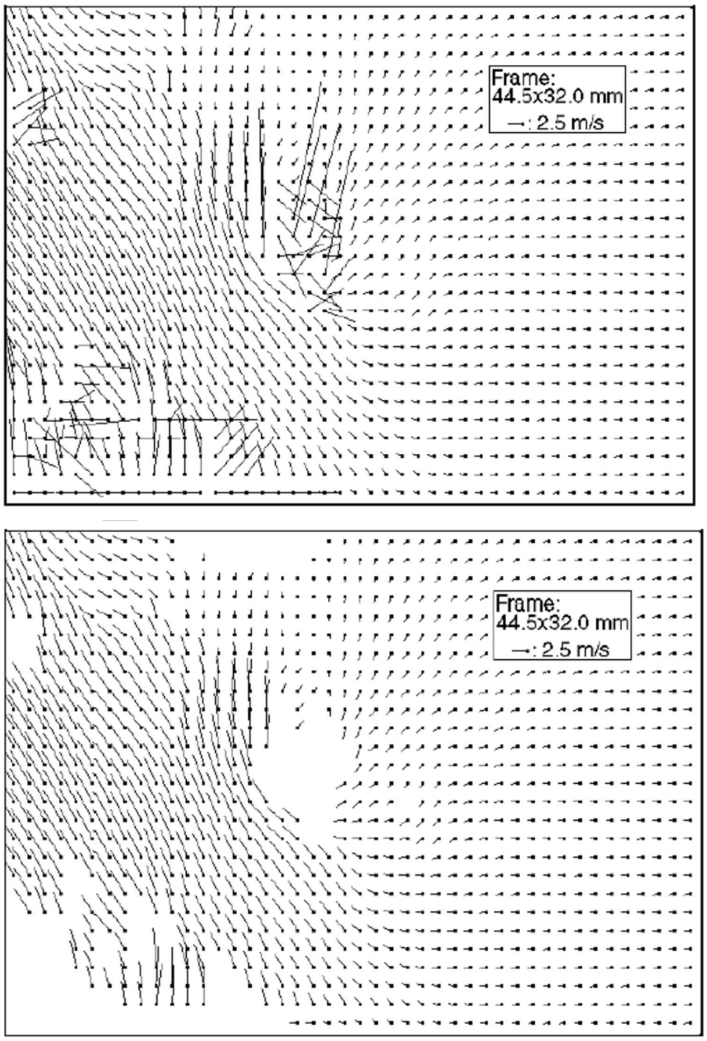

Figure 2.42: (above) Example of PIV measurement. Contains spurious vectors in an eddy, an undersampled mixing layer and a large random vector region due to light glimmer from the visualization window. (below) Validated data from left (Nogueira *et al.*, 1997).

is substantially larger. Hence, the normalized flux, which varies between 0 and 1 is defined as

$$E = \frac{Q_1 + Q_2 + Q_3}{\max\left(\left|Q^+\right|, \left|Q^-\right|\right)}\,, \tag{2.42}$$

where Q^+ and Q^- are the maximum positive and negative flux through the sides of the triangle, respectively. It is found that a threshold value of E=0.5 is sufficient to identify outliers. Figure 2.43(above) shows a simulated velocity field and Figure 2.43 (below) shows the resulting validated vector field. It should be pointed out that while this is a robust method for outlier detection, the Delaunay Tessellation method was originally developed as a new PIV algorithm, and therefore should the user want to only use the outlier detection scheme, they must go through the added steps of generating the Delaunay triangles.

Foucaut *et al.* (2000) describe an iterative procedure for outlier detection. First, during the PIV procedure, the three highest peaks from the correlation domain are recorded, their corresponding residuals are calculated, and the best candidate is selected through the use of a local-median filter. This is done iteratively until there is no change in the global vector field. Second, the surviving residuals are thresholded to identify spurious vectors. As noted by the authors, the difficulty is in identifying the proper choice of the threshold. For this determination, the authors suggest estimating the percentage of valid vectors by hand in a few vector fields, and calculating the cumulative histogram of the residual normalized by the velocity vector located at a particular location. Then by selecting an appropriate percentage limit, the appropriate residual, and hence threshold, can be identified and implemented for the rest of the data set. Similar to previous methods, while useful, this method is also limited by the fact that the user must determine the optimum threshold by manually examining the cumulative histograms for selected flow fields. Liang *et al.* (2003) suggest that spurious vector detection is a pattern recognition problem, and as such, proposed to use cellular neural networks (CNN), a local feedback network, to identify outliers. The weights of the neurons are defined as

$$W_{i,j} = T - r_{i,j}\,, \tag{2.43}$$

where $r_{i,j}$, the velocity residual, is defined as

$$r_{i,j} = \left|V_{x_i} - V_{x_j}\right| \qquad \text{or} \qquad r_{i,j} = \left|V_{y_i} - V_{y_j}\right|, \tag{2.44}$$

depending on which of the velocity component field is being investigated, and T is a threshold. The method was tested on several artificially generated stagnation flows scattered with spurious vectors, and which were also identified by the average velocity gradient defined as

$$G = \left\{\frac{1}{2}\left[\left(V_{x_{i+1,j}} - V_{x_{i,j}}\right)^2 + \left(V_{x_{i,j+1}} - V_{x_{i,j}}\right)^2 + \left(V_{y_{i,j+1}} - V_{y_{i,j}}\right)^2\right]\right\}^{1/2}. \tag{2.45}$$

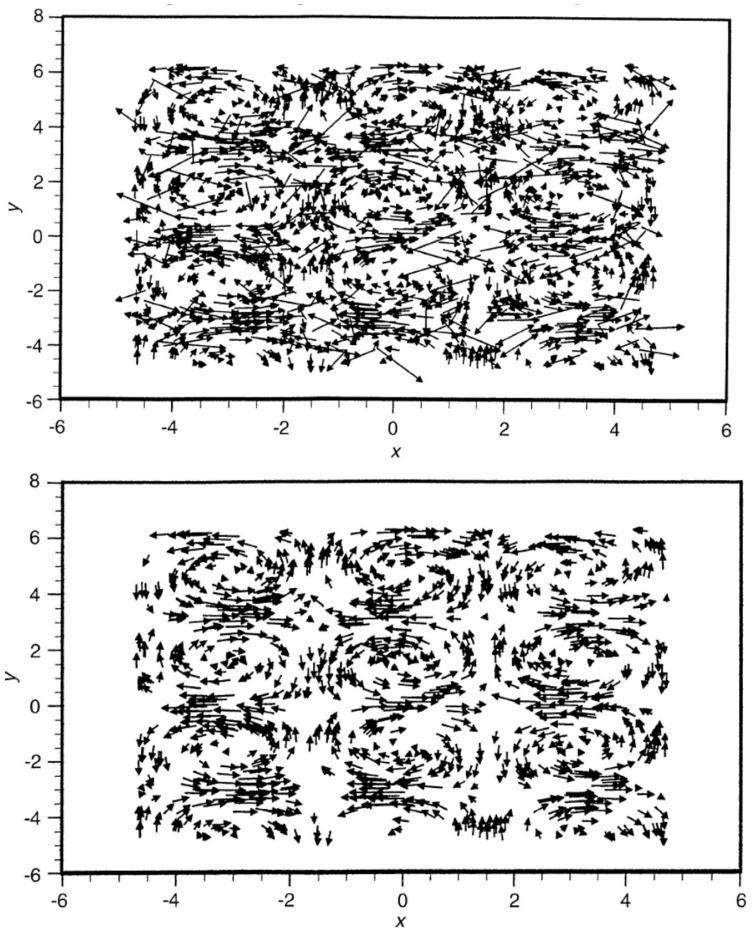

Figure 2.43: (above) Vector field by Delaunay Tessellation particle tracking Velocimetry method (DT-PTV) with 1505 particles (below) Vector field after removing the spurious vectors in the case of (above). Of the 1505 particles, DT-PTV found 1295 vectors. After removing the spurious vectors, 1077 vectors remained (Song *et al.*, 1999).

Also, two parameters were introduced to evaluate the effectiveness of the methods. The first is the undetected rate defined as the ratio of the number of spurious vectors that are not detected over the total number of spurious vectors; the second is the over-detected rate defined as the ratio of the number of valid vectors that are detected as errors over the total number of spurious vectors. For comparison, their scheme was tested against the local-median test. The results suggest that the CNN outperforms the local-median test. Figure 2.44(a) shows that for the stagnation flow with G = 0.2, the threshold value that minimizes both the undetected and over-detected rates for the CNN and local-median filter are ∼0.36 and ∼0.47, respectively. However, the CNN percentage rate, ∼0.08, is much lower than the local-median filter's percentage rate, ∼0.2. Similarly, Figure 2.44(b) shows that for the stagnation flow with G = 0.4, the threshold value that minimizes both the undetected and over-detected rates for the CNN and local-median filter are ∼0.6 and ∼1.05, respectively. Again, the CNN percentage rate, near 0.0, is much lower than the local-median filter's percentage rate, ∼0.53. Lastly, Figure 2.44(c) shows that for the stagnation flow with G = 0.64, the threshold value that minimizes both the undetected and over-detected rates for the CNN and local-median filter are ∼0.85 and ∼0.88, respectively. As in both previous cases, the CNN percentage rate, ∼0.1, is much lower than the local-median filter's percentage rate, ∼0.23. Also, similar to previous methods, while useful, this method is limited by the fact the user must select an appropriate threshold value. Nevertheless, as seen from the results, if the user picks thresholds slightly different than the optimum value, the increase in the undetected/over-detected percentages will be slight. For example, from Figure 2.44, it can be seen that if one uses the optimum threshold for G=0.2 (*i.e.* T=0.36 using the CNN method) on the G=0.4 and G=0.64 velocity fields, the over-detected percentage for both approaches infinity. Likewise, if one uses the optimum threshold for G=0.64 (*i.e.* T=0.88 using the CNN method) on the G=0.2 and G=0.4 velocity fields, the undetected percentage is 0.60% and 0.40%, respectively.

Shinneeb *et al.* (2004) , recognizing the importance of finding a threshold that is insensitive to flow gradients, suggested the use of a variable threshold procedure applied to both a local-median filter and the CNN procedure introduced by Liang *et al.* (2003). The procedure is as follows. First, an aggressive local-median filter is implemented to identify all outliers, even at the expense of falsely identifying good vectors as spurious vectors. The vectors are then replaced by a Gaussian-weighted average of their neighbors using Equation (2.46)

$$u_i = \frac{\sum_j \exp\left[-\frac{1}{2}\left(\left|\vec{x}_i - \vec{x}_j\right|/H\right)^2\right] u_j}{\sum_j \exp\left[-\frac{1}{2}\left(\left|\vec{x}_i - \vec{x}_j\right|/H\right)^2\right]}\,. \tag{2.46}$$

$H = 4\sqrt{2}$ pixels and is the width of the Gaussian filter, and the summation is performed over a 5 x 5 region surrounding *i*. Next, a threshold field is defined by the mean deviation in each velocity component calculated from this newly

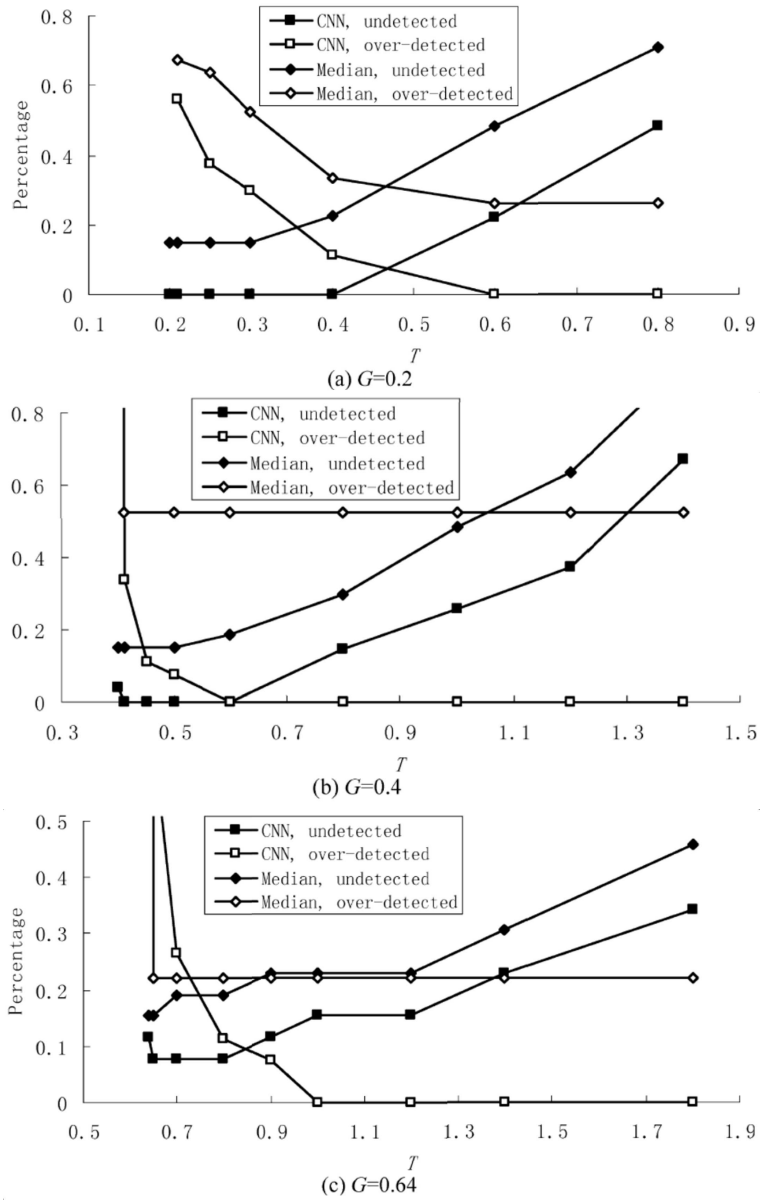

Figure 2.44: Influence of the threshold on the detecting method, Error=10%. **a** G=0.2, **b** G=0.4, **c** G=0.64 (Liang *et al.*, 2003).

generated velocity field

$$\tilde{T}_i^u = \frac{1}{N}\sum_{j=1}^{N} |u_i - u_j| + K\,, \tag{2.47}$$

where K is a constant and the summation is performed over the 8 neighboring points. This threshold field is then filtered by a Gaussian kernel (Equation (2.48))

$$T_i^u = \frac{\sum_j \exp\left[-\frac{1}{2}\left(|\vec{x}_i - \vec{x}_j|/H\right)^2\right]\tilde{T}_i^u}{\sum_j \exp\left[-\frac{1}{2}\left(|\vec{x}_i - \vec{x}_j|/H\right)^2\right]}\,, \tag{2.48}$$

$H = 4\sqrt{2}$ pixels and is the width of the Gaussian filter, and the summation is performed over a 9 x 9 region surrounding i.

To test these procedures, two different types of flow fields were generated. The first field was described by

$$u = Cx^2\,, \qquad u = Cxy \tag{2.49}$$

and the second was described by

$$\begin{aligned} u &= V_{max}\cos\left(\frac{xN_x\pi}{L_x} + \frac{\pi}{2}\right)\cos\left(\frac{yN_y\pi}{L_y}\right)\,, \\ v &= V_{max}\sin\left(\frac{xN_x\pi}{L_x} + \frac{\pi}{2}\right)\sin\left(\frac{yN_y\pi}{L_y}\right)\,, \end{aligned} \tag{2.50}$$

where C is a constant, N_x and N_y are the number of vortex cells in the x and y directions, respectively, L_x and L_y are the sizes of the particle images in the x and y directions, respectively, and V_{max} is the maximum velocity component. In addition, two different types of spurious vectors were used to populate these flow fields. The first type calculates a spurious vector in a random direction and magnitude distributed uniformly between zero and the maximum velocity within the velocity field. Such a spurious vector is designed to simulate the identification of a noise peak within the correlation domain far removed from the signal peak. The second type calculates a spurious vector whose magnitude deviates by a specified percent of the correct local velocity; its direction is randomly chosen. Furthermore, to simulate seeding imperfections, these outliers were positioned in randomly located clusters. To test the performance of this approach, the undetected and over-detected definitions introduced by Liang *et al.* (2003) were used. From the results shown in Figure 2.45 and Figure 2.46, it can be seen that both the median and CNN methods, using a variable threshold, outperform the constant threshold method. Also of interest was the variability of the optimum threshold with respect to flow fields having varying velocity gradients. The results, shown in Figure 2.47, show that these optimum variable thresholds are much more constant with respect to varying velocity gradients, indicated by C, than the optimum constant threshold. Results for Field 2 show similar results. Lastly, it should be

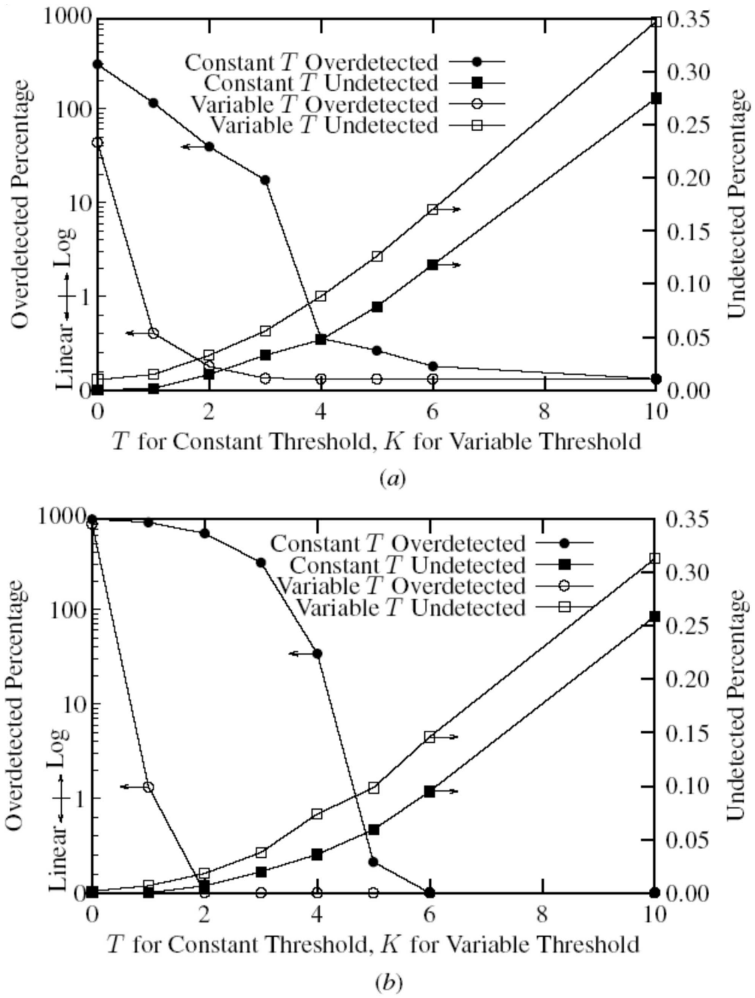

Figure 2.45: Performance of the **a** median and **b** CNN methods using uniform and variable thresholds for Field 1 ($C = 250x10^{-6}$) velocity field and 10% Type 1 spurious vectors (Shinneeb *et al.*, 2004).

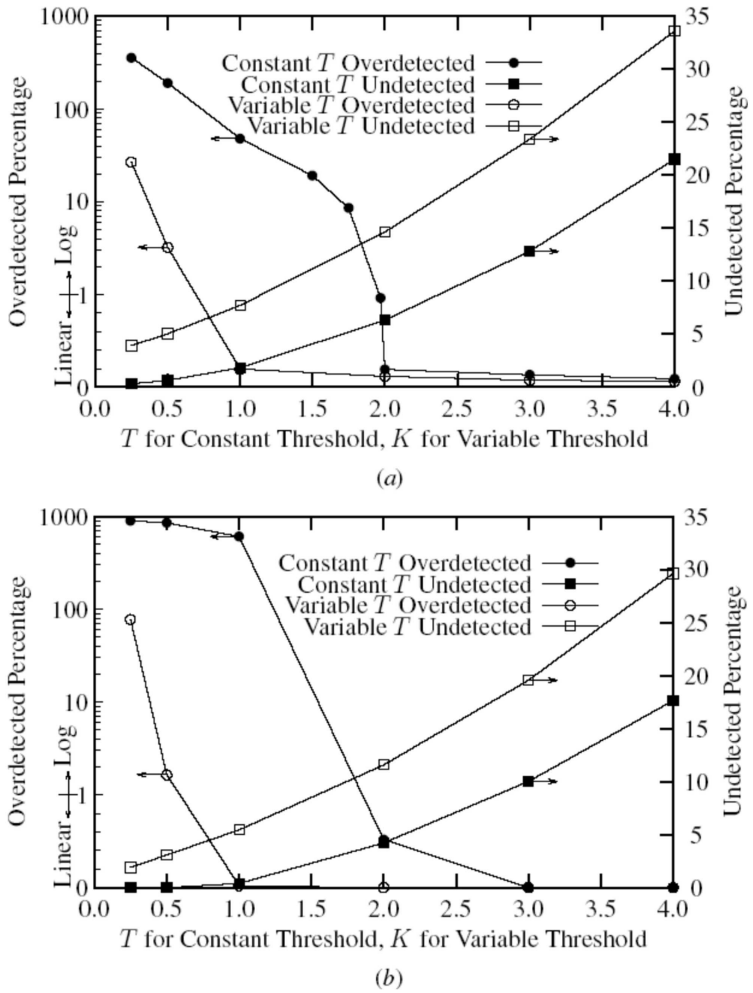

Figure 2.46: Performance of the **a** median and **b** CNN methods using uniform and variable thresholds for Field 2 velocity field ($N_x = N_y = 8, V_{max} = 10$) and 10% Type 1 spurious vectors (Shinneeb *et al.*, 2004).

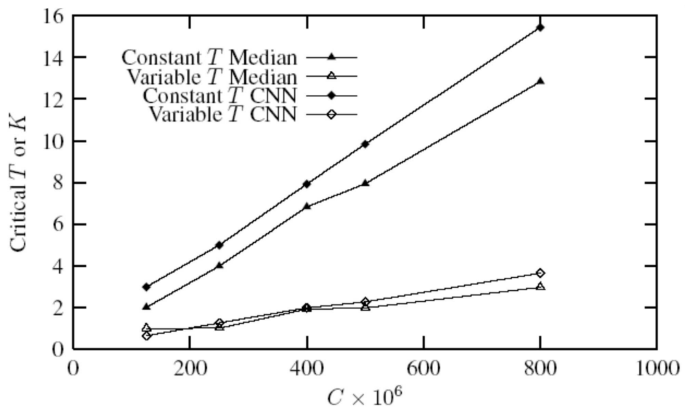

Figure 2.47: Critical value of T and K for constant and variable techniques. The critical value of T or K is determined as that value which yields 1% over-detected vectors. These results are for Field 1 velocity fields and 10% Type 1 spurious vectors (Shinneeb *et al.*, 2004).

pointed out that the smoothing filter parameter, H, has an impact on the percentage of over-detected vectors (see Figure 2.48). This is due to the fact that it is a function of the interrogation resolution and also the experimental conditions.

Lastly, Westerweel and Scarano (2005) studied probability density functions of various flows in order to identify a single universal threshold value to effectively detect spurious vectors. This was achieved by modifying the local-median filter test. Specifically, the original median residual field, defined and calculated as

$$r_i = |U_i - U_m| \tag{2.51}$$

was normalized by the median r_m of $\{r_1, r_2, \ldots r_8\}$

$$r_i^{'} = \frac{|U_i - U_m|}{r_m}\,, \tag{2.52}$$

where r_m are the medians of the points surrounding the vector in question. The normalized median residual was calculated for different grid turbulence data, where it was found that the corresponding histograms nearly collapsed onto a single curve (see Figure 2.49), suggesting that the existence of a universal probability density function. However, for regions where the turbulence levels are very low and the flow is laminar, it was found that the normalized median residual showed high values, since the normalization factor, $r_m^{'}$, approaches zero. This was compensated for by introducing a threshold, ε, into Equation (2.52), resulting in

$$r_i^{*} = \frac{|U_i - U_m|}{r_m + \varepsilon}\,. \tag{2.53}$$

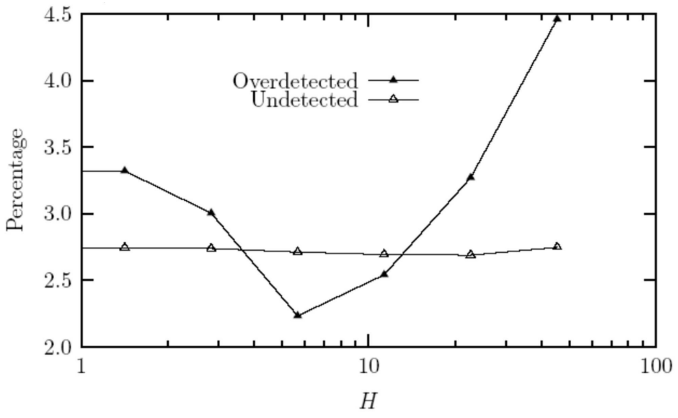

Figure 2.48: Effect of filter spread H for Field 1 ($C = 250x10^{-6}$) with 10% Type 2 ($\Delta V/V = 25\%$, number of clusters = 1) spurious vectors for the variable threshold CNN method (Shinneeb *et al.*, 2004).

Trial and error showed that the optimum value was $\varepsilon = 0.1$ pixel, which interestingly corresponds to typical rms noise levels within PIV data (Westerweel, 2000).

To test the universality of this approach, the histogram of the standard median residuals and normalized median residuals (Equation (2.53)) for various flow fields ranging in Reynolds number from 0.1 to 10^7 were calculated and plotted in Figure 2.50. It is clear from this figure that the probability density function does achieve a universal distribution. While the standard median test shows that the optimum residual threshold would be a function of the flow field, the normalized median test (Equation (2.53) shows that since the histograms almost collapse, the optimum normalized residual is independent of the flow field. Further tests show that for a single value of r'=2 applicable to all the tested flows, the largest 10% of the residuals and hence spurious vectors can be identified. This study, however, does not mention how many undetected and over-detected vector result from this procedure.

2.8 Advanced PIV methods

2.8.1 Window shifting methods

As discussed in section 2.4, PIV provides an estimate of the true velocity, which is different from the true velocity due to noise and in-plane loss-of-pairs due to particle motion. The variation of this bias error was shown in Figure 2.24. Upon observation, the question arises whether one can take advantage of the very small errors shown for particle shifts close to zero. In implementation, this can be done using an iterative adaptive approach. First, the image pairs are processed in a

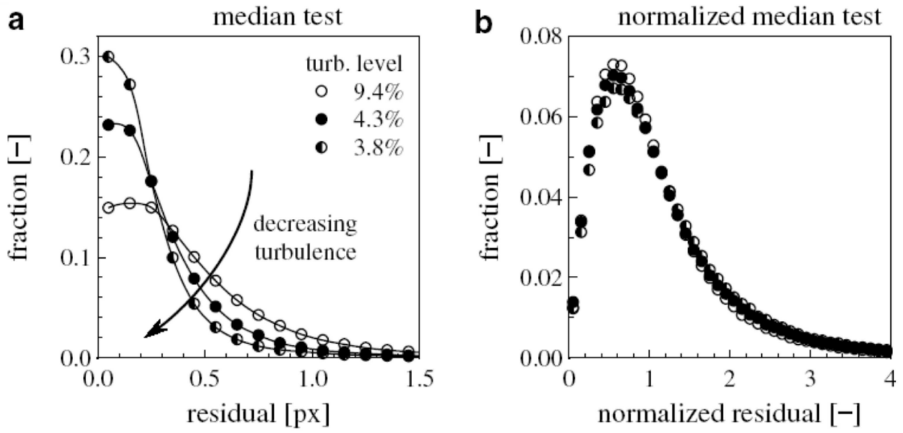

Figure 2.49: The histograms of the residual obtained with the conventional median test **a** and the normalized median test **b** for the grid turbulence data at decreasing turbulence levels. The histograms represent at least 99.7% of the vector data (Westerweel and Scarano, 2005).

Table 2.3: PIV data and corresponding references used in the data shown in Figure 2.50.

Description	Reference
Grid Turbulence	(Poelma, 2004)
Turbulent pipe flow	(Westerweel *et al.*, 1996)
Turbulent jet	(Fukushima *et al.*, 2002)
Microchannel flow	(Westerweel *et al.*, 2004)
Backward-facing step	(Scarano *et al.*, 1999)
Supersonic wake	(Scarano & van Oudheusden, 2003)
von Kàrmàn wake	(van Oudheusden *et al.*, 2005)

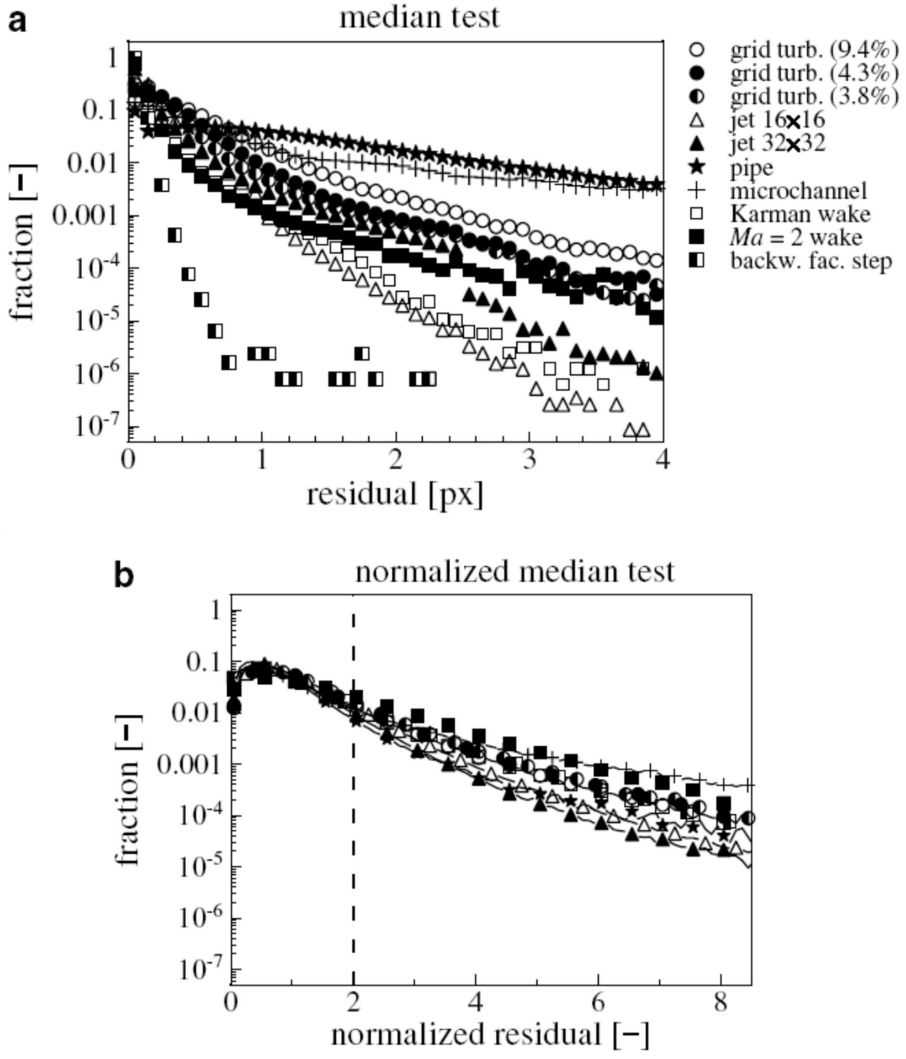

Figure 2.50: The histograms of the residuals using the conventional median **a** and the normalized median **b** for the experimental data listed in Table 2.3 (Westerweel and Scarano, 2005).

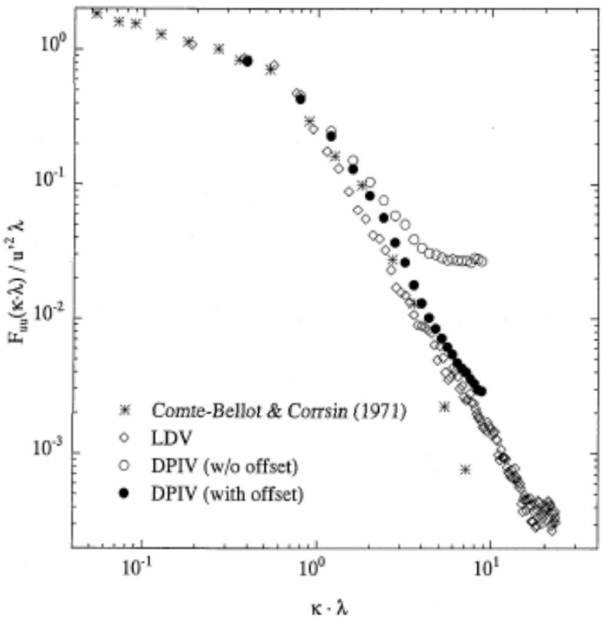

Figure 2.51: The normalized power spectrum of the fluctuating streamwise velocity of a turbulent flow behind a grid (at 40 grid-mesh lengths away from the grid). The open dots represent the result obtained with PIV without window offset; the closed dots the same image data but now with window offset. Also plotted are the result obtained with LDV (◊) in the same facility and at the same location as for the PIV, and the result obtained with hot-wire anemometry (x) by Comte-Bellot and Corrsin (1971).

conventional manner, and then reprocessed using the initial results as a guide to adaptively shift the second window for each interrogation region. This process is iteratively repeated until convergence is achieved. Keane and Adrian (1992) first proposed using a window offset equal to the particle displacement. They also recommended using a larger second interrogation window to avoid in-plane loss-of-pair. In this manner, F_I, the term representing the in-plane loss-of-pair (Equation (2.16)), is maximized, causing RD, the term representing the displacement correlation peak (Equation (2.15)) to be maximized as well (see Figure 2.11 center and bottom). Westerweel *et al.* (1997), using discrete offsetting of the same size windows, showed its effectiveness in reducing noise. Figure 2.51 best shows these results. With window shifting, the noise reduction in the PIV data is so great that its spectrum's noise level drops by an order of magnitude, agreeing quite nicely with the LDV data provided by Comte-Bellot and Corrsin (1971) .

Wereley and Meinhert (1999) recognized that by keeping the first window fixed and shifting the second window, one would be implementing a forward difference

interrogation (FDI) algorithm,

$$\left.\frac{d\vec{X}}{d\tau}\right|_{\tau=t} = \frac{d\vec{X}\left(t+\Delta t\right) - d\vec{X}\left(t\right)}{\Delta t} + \left.\frac{\Delta t}{2}\frac{d^2\vec{X}}{d\tau^2}\right|_{\tau=t} + \ldots, \tag{2.54}$$

where the images are recorded at times t and Δt. For better accuracy, they have suggested using a central difference interrogation (CDI) algorithm,

$$\left.\frac{d\vec{X}}{d\tau}\right|_{\tau=t} = \frac{d\vec{X}\left(t+\frac{\Delta t}{2}\right) - d\vec{X}\left(t-\frac{\Delta t}{2}\right)}{\Delta t} + \left.\frac{(\Delta t)^2}{24}\frac{d^3\vec{X}}{d\tau^3}\right|_{\tau=t} + \ldots, \tag{2.55}$$

where the images are recorded at times $t - \Delta t/2$ and $t + \Delta t/2$. For FDI, the velocity approximation is accurate to order Δt, while for the CDI, the velocity approximation is accurate to order Δt^2. In implementation, the first image's interrogation windows are shifted by an amount $-\vec{V}(\vec{x})\Delta t/2$, while the second image's interrogation windows are shifted by an amount $\vec{V}(\vec{x})\Delta t/2$. In practice, the amount of shift is first estimated by initially processing the images using conventional PIV, and using its results as guide for implementing the CDI routine. Wereley and Meinhert show that within 5 iterations, the solutions converge.

Gui and Wereley (2002) also recognized that even with discrete window shifting using the CDI method, a zero displacement (see Figure 2.24) within the correlation domain could never be achieved, since almost all shifts are never perfect integer values. Consequently, they developed a continuous window shifting routine using a bilinear interpolator to allow for fractional pixel shifts. Using synthetically generated images, they tested an FFT-accelerated non-shifting correlation-based algorithm (FCTR), a discrete window shifting correlation-based interrogation algorithm (CDWS), and the continuous window shifting correlation-based interrogation algorithm (CCWS). They then documented the influences of bias and random errors, images with and without random background noise, particle image size, and particle image number density. Figure 2.52 shows the bias and random errors for noiseless PIV images. Clearly, the CCWS algorithm outperforms the FCTR and the CDWS algorithms by almost a factor of 5, producing a maximum bias and random error of $\sim$.005 pixels and $\sim$.025 pixels, respectively. Figure 2.53 shows the bias and random errors for noisy PIV images. This figure also shows that the CCWS algorithm outperforms the FCTR and the CDWS algorithms by almost a factor of 5 for the bias errors, and a factor of 3 for the random error. Here, the noise has an effect on the random error, since for the CCDW algorithm the random error is $\sim$0.03, whereas for the noiseless image, it is near zero. Also seen is that for all three algorithms, the behavior of the bias error is near identical for both the noisy and noiseless images.

Figure 2.54 shows the influence of the particle image size on the peak-locking (Figure 2.54(a)) and the rms error (Figure 2.54(b)) for each of the algorithms. These figures show that for particle image diameters greater than 2, the peak-locking effect is minimized. For the effect on the rms errors, both the FCTR and the CDWS algorithms show a minimum effect for particle image diameters $\sim$1.5

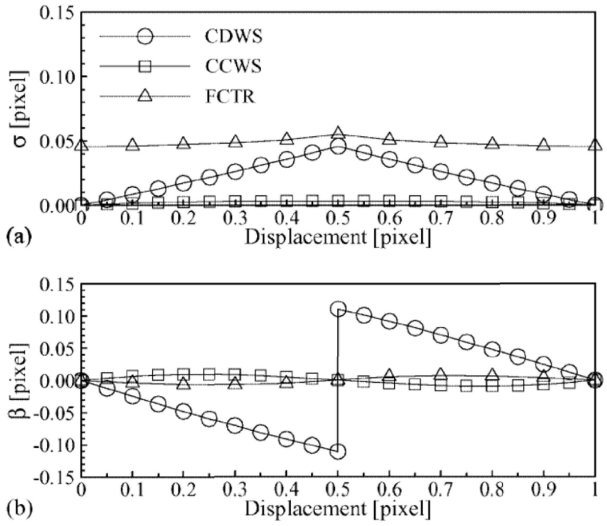

Figure 2.52: Random errors **a** and bias errors **b** of different algorithms for PIV images without background noise (Gui and Wereley, 2002).

pixels. However, for the CCWS algorithm, the rms error is nearly identical to the other algorithms for particle diameters less than 1.5 pixels, but continues to decrease for increasing particle diameters.

Figure 2.55(a) shows that the particle image number density has no effect on the peak-locking effect for each of the algorithms, but that its effect is the least for the CCWS algorithm. However, Figure 2.55(b) the rms errors decrease with increasing particle image number density for all algorithms, being the least for the CCWS algorithm. Figure 2.56(a) shows the effect of the interrogation window size on the peak-locking effect for each of the algorithms. The size of the interrogation window has the largest effect on peak-locking for the CDWS algorithm. The least effect is seen in the FCTR algorithm, and for the CCWS algorithm, the effect of the interrogation window is slight, with a slightly increasing effect with increasing window size. The effect of the interrogation window on the rms error, as shown in Figure 2.56(b), is seen to be the least with the CCWS algorithm, being almost constant for all interrogation window sizes tested. Gui and Wereley also tested their algorithms on a thermal convection flow, where they show the histogram of the resulting PIV vectors in Figure 2.57. In this figure, it can be clearly seen that the FDTR and the CDWS algorithms show a very strong peak-locking effect, while the CCWS algorithm does not show any evident peak-locking effects.

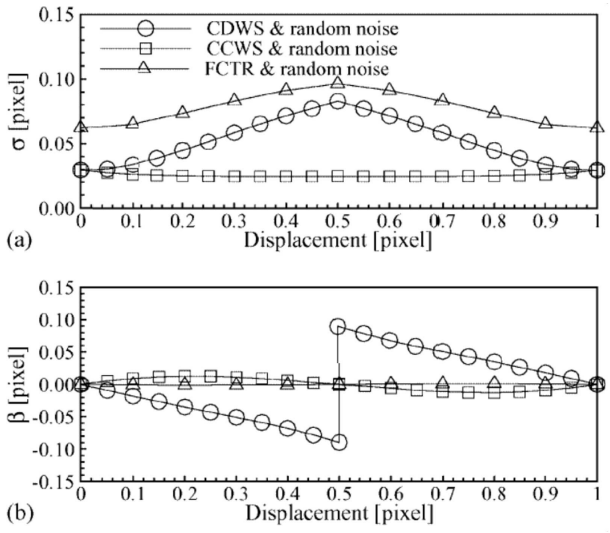

Figure 2.53: Random errors **a** and bias errors **b** of different algorithms (Gui and Wereley, 2002).

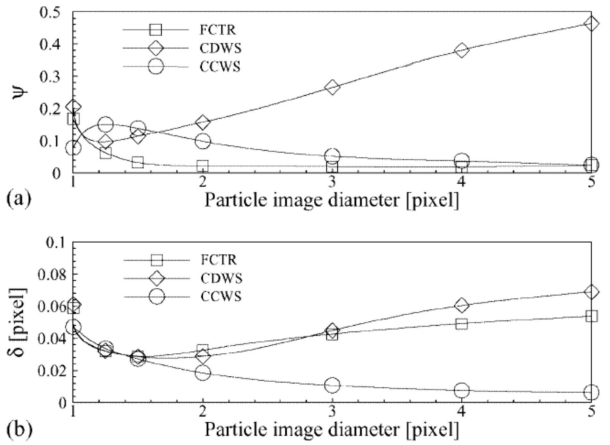

Figure 2.54: Influence of particle image size on: **a** peak-locking factor; **b** rms error (Gui and Wereley, 2002).

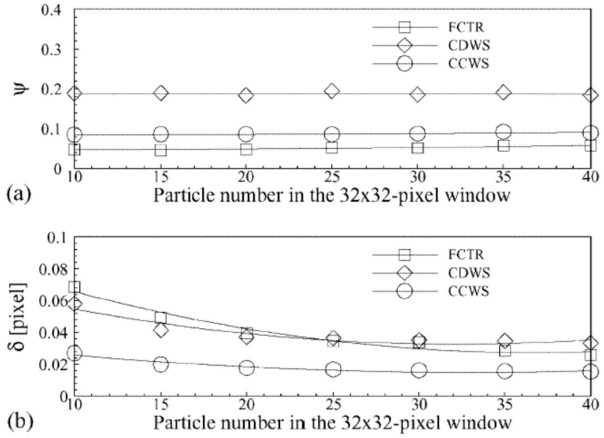

Figure 2.55: Influence of particle image number on: **a** peak-locking factor; **b** rms error (Gui and Wereley, 2002).

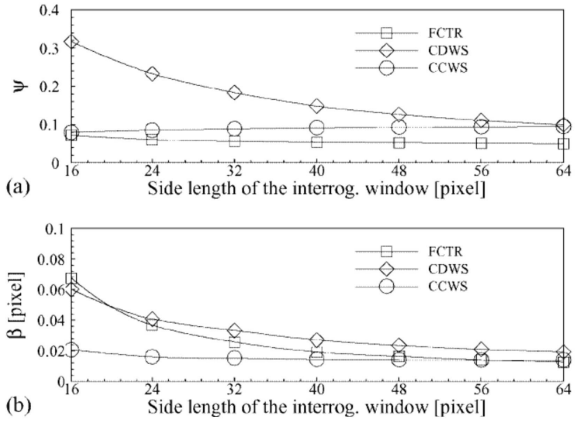

Figure 2.56: Influence of interrogation window size on: **a** peak-locking factor; **b** rms error (Gui and Wereley, 2002).

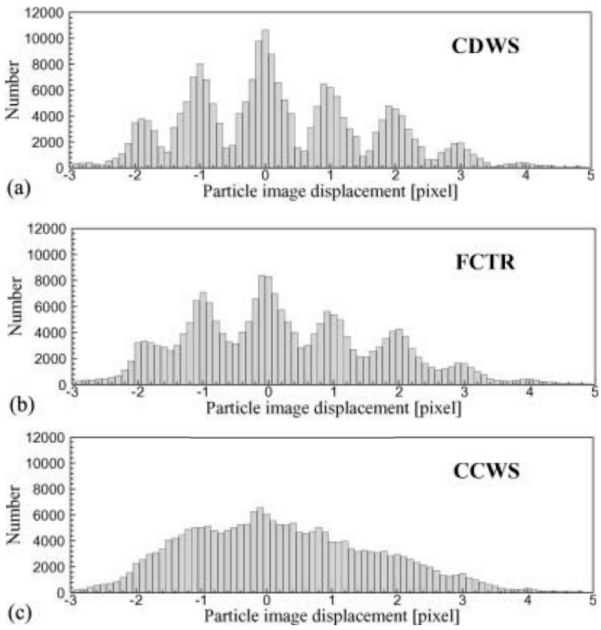

Figure 2.57: Histograms of particle image displacements for evaluating the PIV recording pair of the thermal convection flow with different algorithms: **a** CDWS; **b** FCTR; **c** CCWS (Gui and Wereley, 2002).

2.8.2 Image deformation methods

While the window shifting methods discussed in the previous section have been most helpful in reducing the uncertainty in PIV measurements, upon the inception of digital PIV (Willert and Gharib, 1991), Huang *et al.* (1993a, 1993b) recognized that motion can be decomposed into translation + rotation (a function of du/dy and $d\nu/dx$) + stretch (a function of du/dx and $d\nu/dy$). They consequently suggested a Particle Image Distortion (PID) technique, whereby through bilinear interpolation, the interrogation windows were distorted in the latter two terms in order to maximize on the correlation coefficient. Jambunathan *et al.* (1995) also recommended a similar procedure with the exception that the second image, rather than each of the interrogation windows, was rebuilt using a bilinear interpolator. While these results showed preliminary promising results, they were not pursued vigorously, perhaps due to the computational cost necessary for image deformation. Furthermore, Huang *et al.* and Jambunathan *et al.* both reported instabilities in the convergence of their software; Huang *et al.* fixed this by smoothing their results after each iteration, while Jambunathan *et al.* fixed this by setting a condition requiring that each iterated peak calculation be larger than the previous calculation.

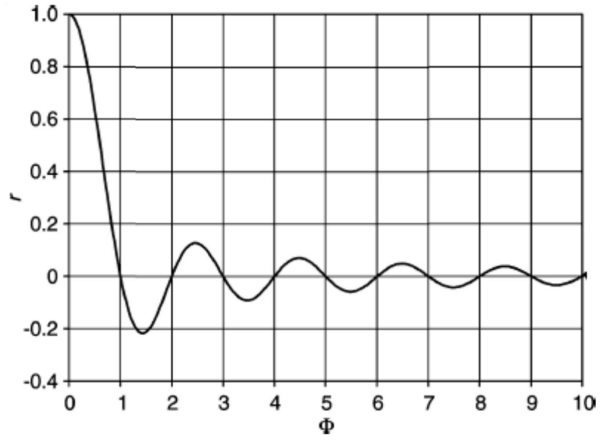

Figure 2.58: 1D view of the frequency response of the moving average window (Nogueira *et al.*, 1999).

Through the use of a proper weighting function, Nogueira *et al.* (1999, 2001, 2002, 2005a, 2005b; Lecuona *et al.* 1999) have been able to not only remedy the algorithm instability, but also produce a method whereby the results are more accurate and better spatially resolved. In their first work, they observed that the amplification response of a top hat window, r, of the wavelengths being measured showed a phase reversal such that the amplification factor became negative, and were able to show that the algorithm instabilities seen by Huang *et al.* and Jambunathan *et al.* were due to this phase reversal (see Figure 2.58).

They also show that for the nth iterative corrective step, the error will be

$$\varepsilon_n = A_i \left(1 - r\right)^n \,, \tag{2.56}$$

where A_i is the original displacement amplitude to be measured. To ensure that the error goes to zero, the condition $0 < r < 2$ must hold. To correct for this phase reversal, they suggest using a symmetric weighting function

$$W\left(\xi,\eta\right) = \sum_{i,j=0}^{\infty} \mu_{ij} \cos\left(\frac{2\pi i\xi}{F}\right) \cos\left(\frac{2\pi j\eta}{F}\right) \quad |\xi|\,,|\eta| \leq F/2\,, \tag{2.57}$$

which, under the restriction of $0 < r < 2$, becomes

$$W\left(\xi,\eta\right) = 9\left(4\left|\frac{\xi}{F}\right|^2 - 4\left|\frac{\xi}{F}\right| + 1\right)\left(4\left|\frac{\eta}{F}\right|^2 - 4\left|\frac{\eta}{F}\right| + 1\right)\,, \tag{2.58}$$

where F is the window size, and (ξ,η) denote the coordinates from the center of the window. Graphically, the weighting function and its frequency response is shown in Figure 2.59.

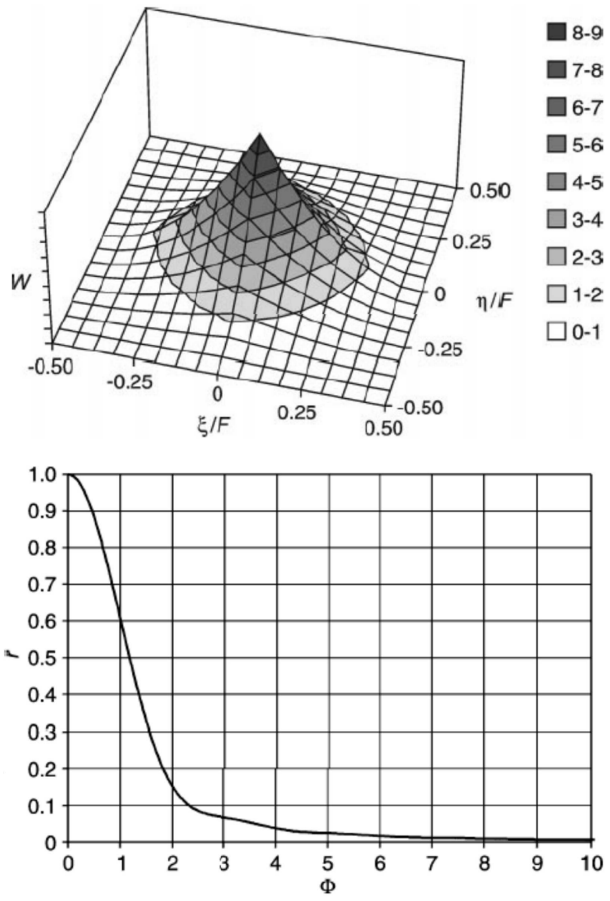

Figure 2.59: (above) Weighting function according to Equation (2.58); (below) 1D view of the frequency response of the moving average window, weighted with expression (2.58) (Nogueira *et al.*, 1999).

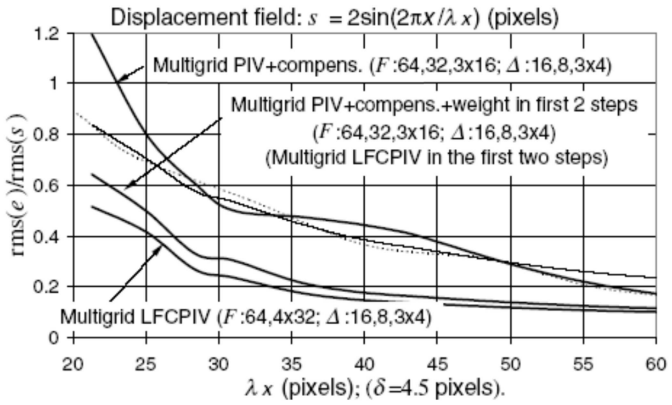

Figure 2.60: The performance of the five-iteration multigrid systems described in the text, together with those of the methods from Jambunathan *et al.* (1995) (thin full line) and Scarano and Riethmuller (2000) (thin broken line) (Nogueira *et al.*, 2001).

An unfortunate new source of error of using this function is that particle image centers are shifted towards the highest value of the weighting function (referred to as the slippage error), thus reducing the correlation peak from what it should otherwise be. To compensate for this, values of the maximum correlation coefficient are kept track of such that if they should decrease, they will not be further iterated. Using a forward differencing scheme and a biparabolic interpolator, the correlation function

$$C(l,m) = \frac{\sum_{\xi,\eta=-F/2}^{F/2} W(\xi,\eta)\, f(\xi,\eta)\, g(\xi+l,\eta+m)}{\sqrt{\sum_{\xi,\eta=-F/2}^{F/2} W(\xi,\eta)\, f^2(\xi,\eta)}\sqrt{\sum_{\xi,\eta=-F/2}^{F/2} W(\xi,\eta)\, g^2(\xi+l,\eta+m)}}, \tag{2.59}$$

is used iteratively. This method is referred to as Local Field Correction PIV (LFCPIV), and when implemented using a multigrid approach, it is referred to as a multigrid LFCPIV. Figure 2.60 shows various multigrid LFCPIV results for 5 iterations. Note that 2 of the 4 LFCPIV implementations produce better results than other deformation algorithms that do not apply weighting functions.

By using a central difference scheme instead of the forward difference scheme, keeping better track of the slippage error, and only using a single size window (64 by 64 pixels), Figure 2.61 shows that the uncertainties are even lower than those previously shown.

While the weighting function in Equation (2.58) helps significantly reduce errors, it is by no means the only weighting function that can be used. In this regard,

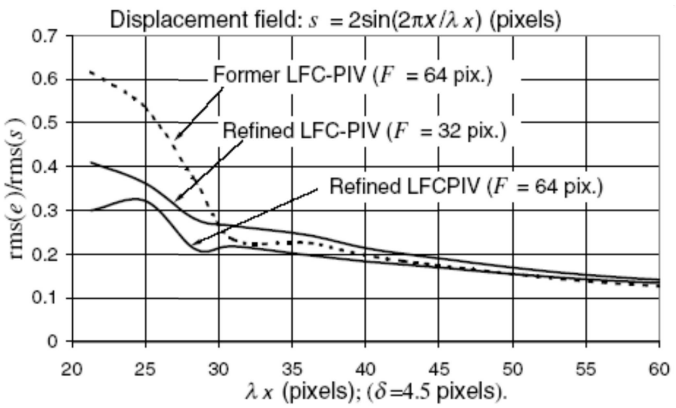

Figure 2.61: Performances of LFCPIV systems for the displacement fields indicated (Nogueira *et al.*, 2001).

Nogueira *et al.* (2005b) studied two other weighting functions:

$$W(\xi,\eta) = \frac{24}{\pi}\left(4\left|\frac{\sqrt{\xi^2+\eta^2}}{F}\right|^2 - 4\left|\frac{\sqrt{\xi^2+\eta^2}}{F}\right|\right), \quad \text{if} \quad \left|\frac{\sqrt{\xi^2+\eta^2}}{F}\right| < 0.5 \qquad W = 0\,, \tag{2.60}$$

and

$$\begin{aligned} W(\xi,\eta) = &\left[12\left|\frac{\xi}{F}\right|^2 - 12\left|\frac{\xi}{F}\right| + 3 + 0.15\cos(4\pi\frac{\xi}{F}) + 0.2\cos(6\pi\frac{\xi}{F})\right. \\ &\left. + 0.1\cos(8\pi\frac{\xi}{F}) + 0.05\cos(10\pi\frac{\xi}{F})\right] \\ &\times\left[12\left|\frac{\eta}{F}\right|^2 - 12\left|\frac{\eta}{F}\right| + 3 + 0.15\cos(4\pi\frac{\eta}{F}) + 0.2\cos(6\pi\frac{\eta}{F})\right. \\ &\left. + 0.1\cos(8\pi\frac{\eta}{F}) + 0.05\cos(10\pi\frac{\eta}{F})\right]. \end{aligned} \tag{2.61}$$

Equation (2.60) was chosen to test the asymmetric version of Equation (2.58), and Equation (2.61) was chosen to increase the frequency response for the wavelengths between $F/2$ and $F/5$. Their uncertainties as a function of iteration are shown in Figure 2.62, where Equation (2.61) is seen to have the best performance. In application to real images (see Figure 2.63), however, it can be seen that all three weighting functions perform satisfactorily, perhaps due to the equalizing effect of noise within the PIV images

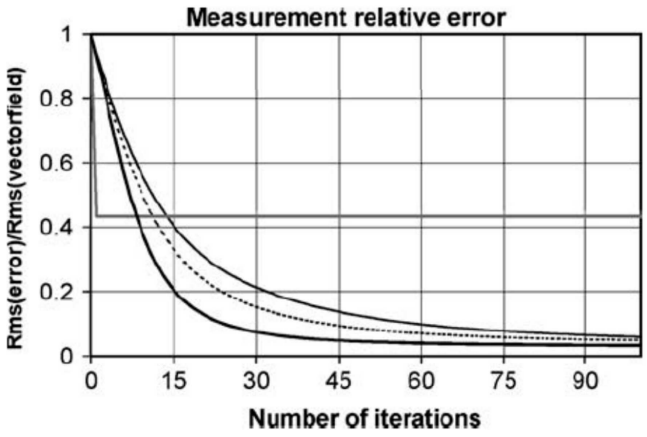

Figure 2.62: Comparison of algorithms. The thick horizontal line corresponds to a single-pass PIV with a 16x16-pixel non-weighted interrogation window. The smooth curves correspond to the iterative algorithms described in this section. The upper curve corresponds to Eq.(2.58), the middle curve to Eq.(2.60) and the lower curve to Eq.(2.61) (Nogueira *et al.*, 2005b).

Rather than use a bilinear interpolator, Scarano and Riethmuller (2000) , using a multigrid approach, incorporated a cardinal function interpolator

$$R\left(x,y\right)=\sum_{i,j=-F/2}^{F/2}f(i,j)\frac{\sin\left[\pi(i-x)\right]}{\pi(i-x)}\frac{\sin\left[\pi(j-y)\right]}{\pi(j-y)}\,, \tag{2.62}$$

where $R(x,y)$ is the image intensity at the sub-pixel location (x,y), in order to avoid or limit the loss of information in the re-sampling process (Hall, 1979). The results show a significant improvement over conventional PIV and window-shifting PIV methods, however, not quite as good as the LFCPIV methods (see Figure 2.60).

As indicated in this discussion so far, deforming the images is a key factor in deformation PIV methods. Towards this end, several researchers have studied the impact of various interpolation methods on the accuracy of the resulting PIV vectors, and the time necessary to calculate them. The first such study was performed by Astarita and Cardone (2005), where using synthetic noiseless images with translational shifts only, they studied the bias and random uncertainties of different interpolation schemes as well as the time necessary for measurement convergence. The interpolators studied were B-spline, FFT, Cardinal interpolator based on the sinc function, bilinear, bicubic, biquadratic, simplex, and discrete window offset (IDWOS) algorithms. For the B-spline, FFT, Cardinal interpolators, the grid sizes tested for interpolation ranged from 2x2 through 16x16, 3x3 through 16x16, 4x4 through 16x16, respectively. Their results are best summarized

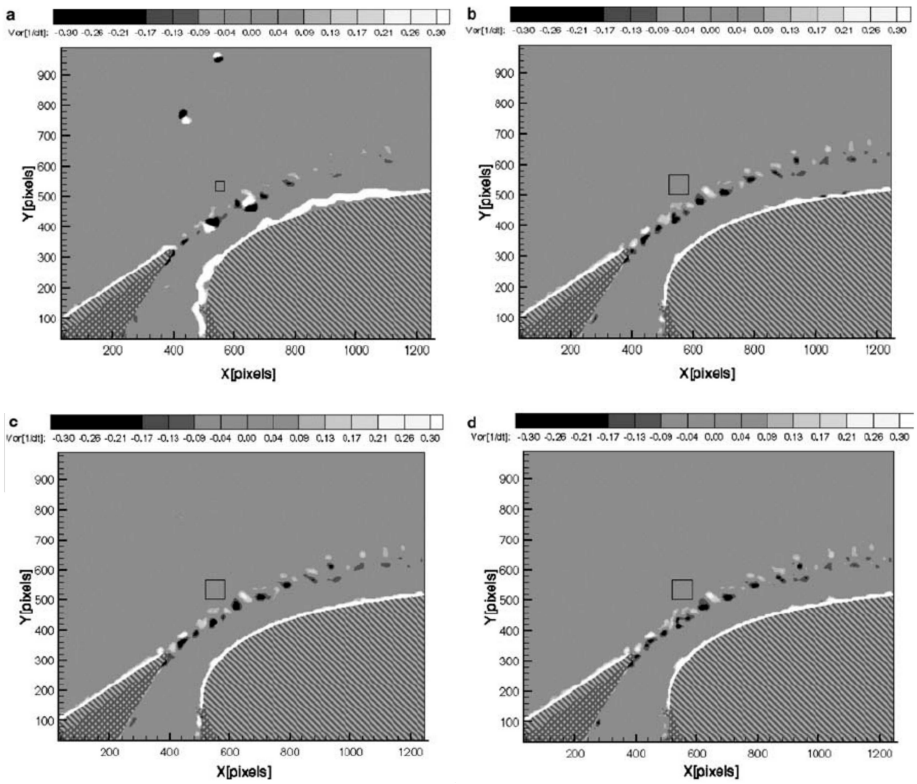

Figure 2.63: **a-d** Performance comparison on real images from an industrial facility. The hatched pattern indicates solid objects; the cross-hatched pattern indicates places where reflections and shadows suppress all data. **a** Vorticity plot obtained from conventional PIV data. The size of the interrogation window (32x32 pixels) is indicated by a dark box. **b** Vorticity plot obtained from LFC-PIV data with a 64x64-pixel interrogation window weighted by Eq.(2.58). **c** Same as **b**, but using Eq.(2.60). **d** Same as **b**, but using Eq.(2.61) (Nogueira *et al.*, 2005b).

in Figure 2.64, where the average bias error and total error are shown in Figure 2.64(a) and Figure 2.64(b), respectively. These averaged values were obtained by averaging the absolute value of the errors in the displacement interval from zero to 4 pixels. In general, it can be seen that the simpler and less computationally intensive schemes (IDWOS, bilinear, bicubic, simplex) produce results that are not as accurate as schemes that are more computationally intensive (B-spline, FFT, sinc with interpolation grid sizes 6x6 through 16x16). It is interesting to note that of the latter, the B-spline algorithms give the lowest total mean uncertainties in the shortest duration of time.

While useful, this study did not investigate the effects of these interpolation algorithms on non-translational motion. Towards this end, Kim and Sung (2006) further assessed various interpolation schemes by considering both uniform and sheared displacements. In this study, they investigated bilinear, biquadratic, B-spline, cubic, sinc, Lagrange and Gaussian interpolations using artificially generated noiseless images with different sized particle images. The best results for the uniform displacements are shown in Figure 2.65 through Figure 2.67. The top plot in each figure shows the bias error as a function of displacement, which for all cases shows a sinusoidal behavior, while the bottom plot in each figure shows the random error as a function of displacement. It is seen that the results show the least uncertainties for the largest particle image size studied (4.4 pixels). For this particle image diameter, it is seen that the cubic ($a = -0.61$), Lagrange ($N = 6$), sinc ($N = 10$), and Gaussian ($N = 6$) interpolation schemes have a maximum random error of .005 pixels. Of these interpolation schemes, however, the maximum bias error of the Gaussian scheme seems to be almost twice as large as the others.

The best results for the shear displacements are shown in Figure 2.68 through Figure 2.70. The top plot in each figure shows the bias error as a function of mean displacement, which for all cases shows a decaying sinusoidal behaviour, while the bottom plot in each figure shows the random error as a function of mean displacement. It is seen that the results show the least uncertainties for the largest particle image size studied (4.4 pixels). For this particle image diameter, it is seen that the cubic ($a = -0.61$), Lagrange ($N = 6$), sinc ($N = 10$), and Gaussian ($N = 6$) interpolation schemes have a maximum random error of .004 pixels. Of these interpolation schemes, however, the maximum bias error of the Gaussian scheme seems to be almost twice as large as the others, similar to the uniform displacement results.

Also instructive is the computational time required of the interpolation schemes. Table 2.4 shows the ratio of the computational time to the bilinear interpolation scheme. It can be seen that for the best performing schemes, the sinc ($N = 10$) and the Lagrange ($N = 6$), the computation times are 27.1 and 15.5 time larger than the bilinear scheme. While the increase in computational time due to the use of deformation methods (especially the more accurate schemes) may seem large and therefore a hindrance, it should be pointed out that the rapid increase of computer processing speeds over time and the need for generating more accurate results at higher grid resolutions easily justifies using such schemes.

Table 2.4: Ratio of computation time between each interpolation scheme to the bilinear interpolation scheme for a single iteration (Kim and Sung, 2006).

Interpolation		Time
Quadratic	$N = 3$	2.50
B-spline	$N = 3$	2.50
	$N = 4$	3.83
Lagrange	$N = 4$	6.08
	$N = 6$	15.5
	$N = 8$	31.6
	$N = 10$	57.2
	$N = 12$	94.1
sinc	$N = 4$	5.25
	$N = 6$	10.4
	$N = 8$	17.8
	$N = 10$	27.1
	$N = 12$	38.5
Gaussian		
4th	$N = 4$	20.9
	$N = 6$	46.0
6th	$N = 4$	31.4
	$N = 6$	77.0
	$N = 8$	122

2.9 3-D Volumetric measurements

While 2D PIV provides a valuable tool for studying fluid flow, it is still limited as they are confined to measurements within a plane. To study complex three-dimensional flows therefore requires methods that will allow measurements of three-component velocity vectors within a volume. Furthermore, if such studies are transient phenomena, then these methods must allow for sequential measurements through time. While several techniques have been developed that acquire three-dimensional data by scanning the light sheet through the desired volume (Brucker 1995,1997), to date, two techniques have stood out that are capable of true three-dimensional measurements. The first technique employs multiple cameras while the second employs holographic methods.

The hardware necessary for data acquisition is almost identical to those of PIV systems. The important items are bulleted below:

- The tracer particles used should be small enough to accurately follow the flow, yet large enough to provide sufficient light scattering. The particle response time as described by Equation (2.2) can be used to determine ap-

propriate sizes of particles.

- The illumination source should be pulsed in order to freeze the particle motions. Both lasers and strobe lights have been successfully used. The pulses should be synchronous with the camera for proper exposure and therefore correct data acquisition. The illumination should be such that there is homogeneous illumination throughout the interrogation volume. The illumination spectra should be within the CCD's detectable spectral range. The illumination source should be bright enough to provide a good signal, especially for small tracers.

- This is more important for volumetric methods than for planar methods when using lasers, since the laser beam must be spread into a volume for the volumetric methods, rather than a sheet for the planar methods.

- Digital high-resolution cameras (1K*1K or 2K*2K) are preferred in order to image higher number of particles, and also to allow for automated processing. While film provides higher resolution, its methods are extremely time-consuming for processing.

- Acquisition of digital images is done through the use of a framegrabber. Images can be stored onto RAM in real-time, but are limited to the maximum amount of RAM that can be put onto the host computer. Images can also be stored onto a real time disk. Typically disk arrays with special configurations using RAID controllers can be used to acquire massive amounts of data. If analog cameras are used, either laser disc recorders or VCRs are necessary for acquisition. For processing, however, these images must be digitized, most often not at as high a resolution or signal quality as CCDs provide, thereby degrading the quality of the digitized image.

  The limitation of holographic method is that this method can only provide a snap shot of the velocity field at only a single point in time, *i.e.* it cannot provide a sequence of data fields through time as do the multi-camera systems. In the following section one of the multi-camera systems, the Three-Dimensional Defocusing Particle Image Velocimetry (3DDPIV) method, is presented and discussed.

2.9.1 Three-dimensional defocusing PIV method

The most recent addition to the true 3D measurement methods is Defocusing Digital Particle Image Velocimetry. The concept was initially introduced by Willert and Gharib (1992) , and further developed and implemented by Pereira *et al.* (2000), Pereira and Gharib (2002) , and Kajitani and Dabiri (2005) . Unlike the previous method, which is based on triangulation, this method is based on imaging with a single lens within its defocused range. This system differs from 3D particle tracking methods in that the optics in this method share one optical axis, consistent with the original concept, thus eliminating the need for complex schemes

to identify particles through triangulation. Out-of-plane to in-plane error ratios using this methods are 4-6, with in-plane errors similar to those found in planar PIV techniques.

2.9.2 The defocusing principle

This method is best described by using a two-dimensional representation of the imaging system shown in Figure 2.71(a), which will demonstrate the defocusing concept used to acquire 3D information. Rays from point A focus onto point A' on the image plane. Rays from B (off the reference plane), while still traveling through the aperture, focus away from the image plane onto C, leaving a blurred image, B', on the image plane. Using the blurring, one can get information about a particle's position in space. In Figure 2.71(b), the aperture is replaced with another that has two apertures equally off-axis. This time, rays from A travel through both apertures, and are focused onto A'. Likewise, rays from B, focus off the image plane, onto B'''. Because the apertures are off-axis, as the rays converge onto point B''', they leave two blurred spots on the image plane, B' and B''. The separation between B' and B (denoted b) is a function of the distance B from the reference plane, thus providing depth information. If a particle located at B were to move farther from the reference plane to C, rays from this particle would focus off the CCD plane, onto C''', leaving two blurred spots on the CCD plane, C' and C'', separated by a distance b' that is larger than b. This geometry therefore shows that the particle image separation on the CCD plane gets larger as the particle moves farther away from the reference plane, thus providing a way to gauge the depth location.

2.9.3 The descriptive equations

Given this optical setup, a particle's position can be shown to be

$$\begin{aligned}
X &= \frac{1}{2L}\left(\frac{-2Zx_{TL}}{M} + \gamma(L-Z)\right) = \frac{1}{2L}\left(\frac{-2Zx_{TR}}{M} + \gamma(L-Z)\right) \\
&= \frac{1}{L}\left(\frac{-Zx_B}{M} + \gamma(L-Z)\right) = \frac{-Zx_0}{M}\,, \\
Y &= \frac{1}{2L}\left(\frac{-2Zy_{TL}}{M} + d(L-Z)\right) = \frac{1}{2L}\left(\frac{-2Zy_{TR}}{M} - d(L-Z)\right) = \frac{-Zy_B}{L} \\
&= \frac{-y_0 Z}{ML}\,, \\
Z &= \left(\frac{1}{L} + \frac{b}{MLd}\right)^{-1} = \left(\frac{1}{L} + \frac{\zeta}{M\gamma d}\right)^{-1}\,,
\end{aligned} \tag{2.63}$$

here

$$x_0 = \frac{x_B + x_{TL} + x_{TR}}{3},$$
$$y_0 = \frac{y_B + y_{TL} + y_{TR}}{3},$$

where M = geometrical magnification, d = distance between the centers of the apertures, and L = distance from the aperture plane to the reference plane, (X, Y, Z) = the coordinates of the point B in space, and (xTR, yTR), (xTL, yTL) and (xB, yB) = the blurred image coordinates for the top right, top left, and bottom coordinates, respectively, ζ= the distance from the center of this equilateral triangle to any of the particle's images that identify any vertex of the equilateral triangle (*i.e.* x_{TR},y_{TR}), and γ = the radial distance from the optical axis to each of the apertures.. The sensitivity of this system to detect changes in the depth location of particle is given by

$$\frac{\partial b}{\partial Z} = -\frac{1}{KZ^2}, \qquad K = \frac{1}{MLd}. \tag{2.64}$$

In practice, rather than using two pinholes, three pinholes positioned in the shape of an equilateral triangle are used. For images filled with thousands of particles, this allows more precise identification of particles. Also, for good system sensitivity, the aperture distance, d, must be large, which can be achieved by decreasing K, thereby increasing $\partial b/\partial Z$. Typically, experimental setup requirements necessitate system sensitivities such that aperture separations should be larger than the diameter of the lens. This poses a problem as obtaining custom-made large lenses can be quite costly. Furthermore, triply-exposing a CCD can cause it to overcrowd rapidly, thereby only allowing limited number of particle exposures. Therefore, rather than constructing the camera with one lens, it is possible to construct the camera with 3 separate imaging systems as shown in Figure 2.72. This solves the problem of over-saturating a single CCD with multiple images of many particles, while using off-the-shelf lenses for the camera design.

2.9.4 Application to flow around a propeller

In order to test the capability of the 3DDPIV system, the flow around a propeller was imaged and mapped. Instead of using reflective particles as is done in 2D PIV systems, small bubbles ($\sim 260\mu$m diameter) were used as flow tracers. A two-blade propeller (67 mm diameter) was rotated at 12 revolutions per second, achieving a tip velocity of 2.52 m/s within a $1m^3$ water tank. After phase averaging 50 velocity vectors, a three-dimensional velocity field was achieved (see Figure 2.73).

Once this velocity field was obtained and outliers were corrected for, massless particles were then numerically injected into this velocity field initially in a ring formation (Figure 2.74(a)) at one diameter upstream of the propeller, and the evolving pathlines were then observed Figure 2.74(b,c).

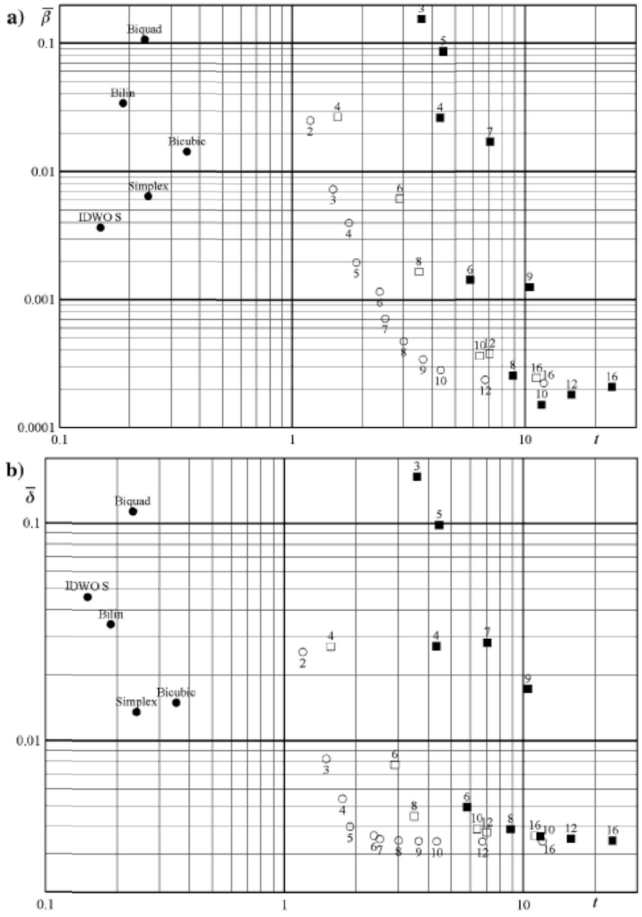

Figure 2.64: Bias **a** and total **b** mean errors as a function of time for various IS. Closed circles indicate high speed methods, open circles BSPL IS (the number indicates the spline order), closed squares and open squares FFT and SINC interpolation schemes (the number indicates the stencil linear dimension), respectively. The time scales are arbitrary (Astarita and Cardone, 2005).

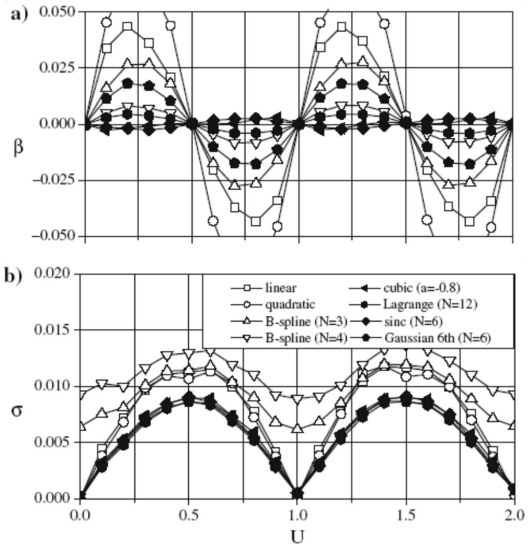

Figure 2.65: Comparison of the best performance for each interpolation for uniform flow (d_p = 2.2 pixel) (Kim and Sung, 2006).

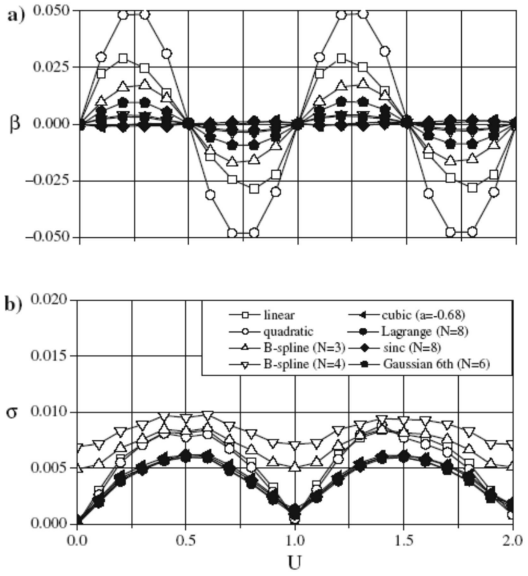

Figure 2.66: Comparison of the best performance for each interpolation for uniform flow (d_p = 3.3 pixel) (Kim and Sung, 2006).

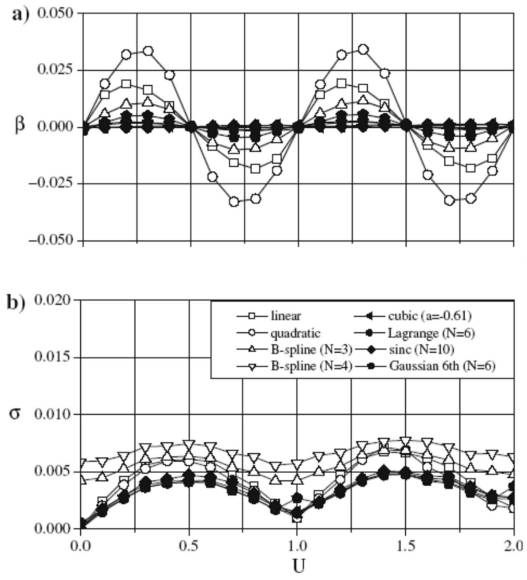

Figure 2.67: Comparison of the best performance for each interpolation for uniform flow ($d_p = 4.4$ pixel) (Kim and Sung, 2006).

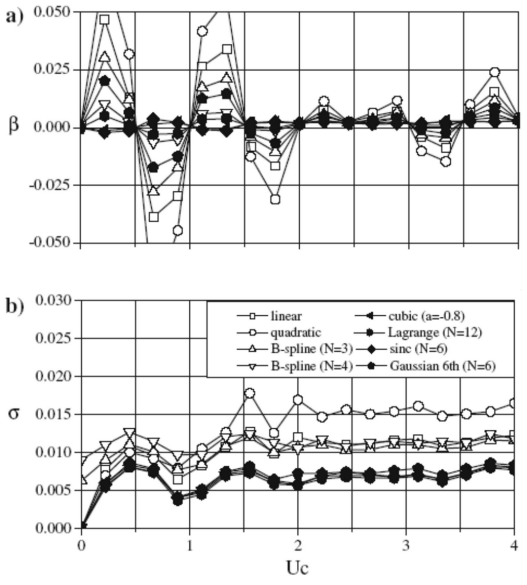

Figure 2.68: Comparison of the best performance for each interpolation for shear flow ($d_p = 2.2$ pixel) (Kim and Sung, 2006).

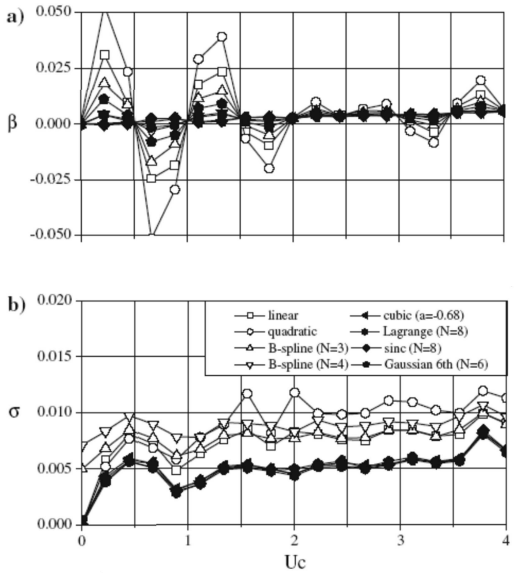

Figure 2.69: Comparison of the best performance for each interpolation for shear flow ($d_p = 3.3$ pixel) (Kim and Sung, 2006).

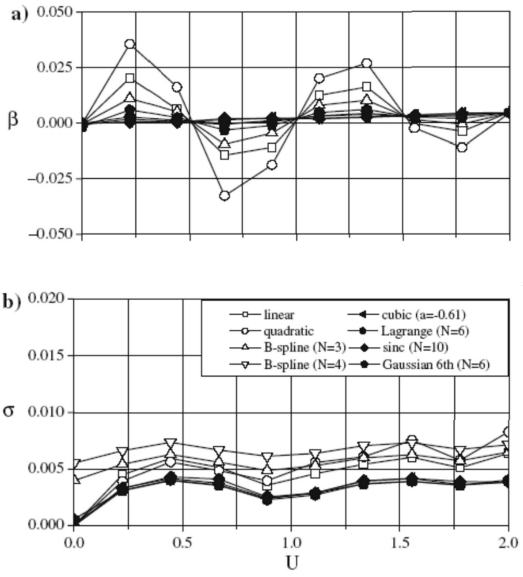

Figure 2.70: Comparison of the best performance for each interpolation for shear flow ($d_p = 4.4$ pixel) (Kim and Sung, 2006).

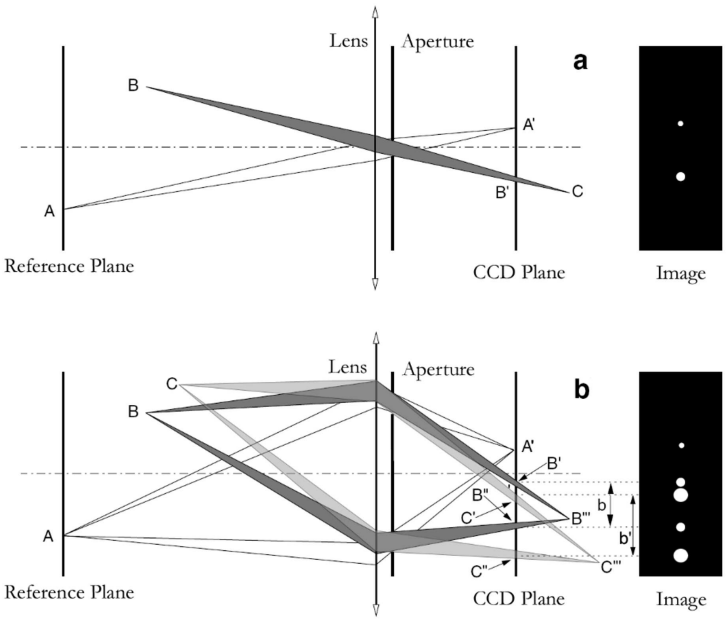

Figure 2.71: Diagram **a** Defocusing concept graphically demonstrated: a standard imaging set-up with aperture on-axis; **b** defocusing set-up with two off-axis apertures. Point A focuses from the reference plane onto A' on the CCD plane; point B focuses behind the CCD plane at point B"', leaving two slightly blurred images on the CCD plane (B' and B") at a distance b apart; point C focuses further behind the CCD plane at point C"', leaving two slightly larger blurred images on the CCD plane (C' and C") at a larger distance b' apart (adapted from Willert and Gharib, 1992; and Pereira and Gharib, 2002) (Kajitani and Dabiri, 2005).

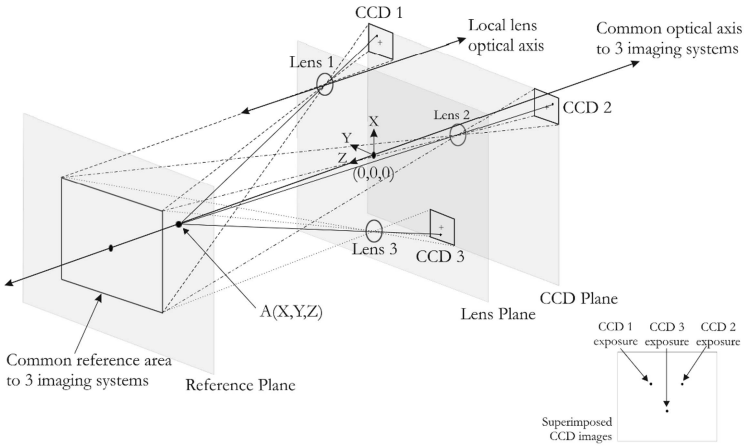

Figure 2.72: Implementation of 3D Defocusing PIV allowing for use of off-the-shelf hardware items (Kajitani and Dabiri, 2005).

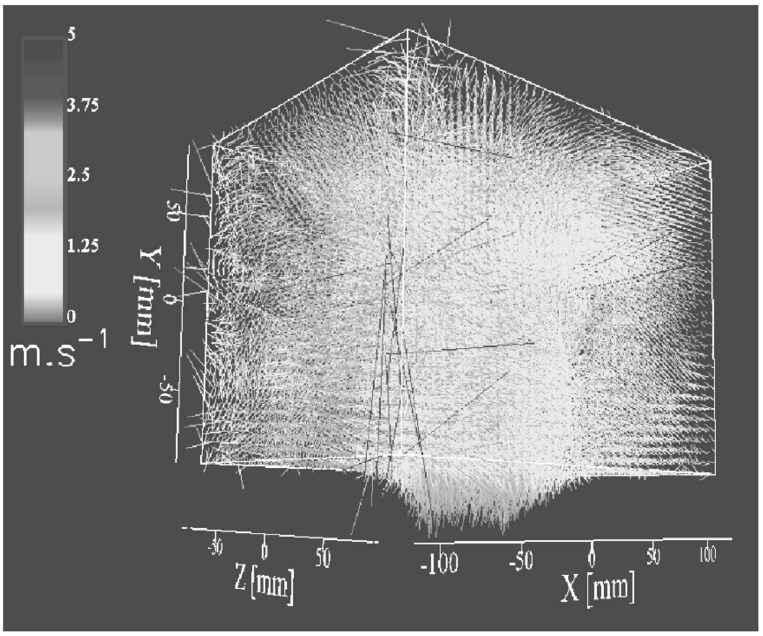

Figure 2.73: Three-dimensional velocity field around a rotating propeller. 3DDPIV images contain $1x10^4$-$2x10^4$ bubbles. The imaged volume is 200x200x400 mm^3 resulting in 72963 vectors (33*33*67 voxels) (Courtesy of Dr. Gharib, Graduate Aeronautics Laboratory, Caltech).

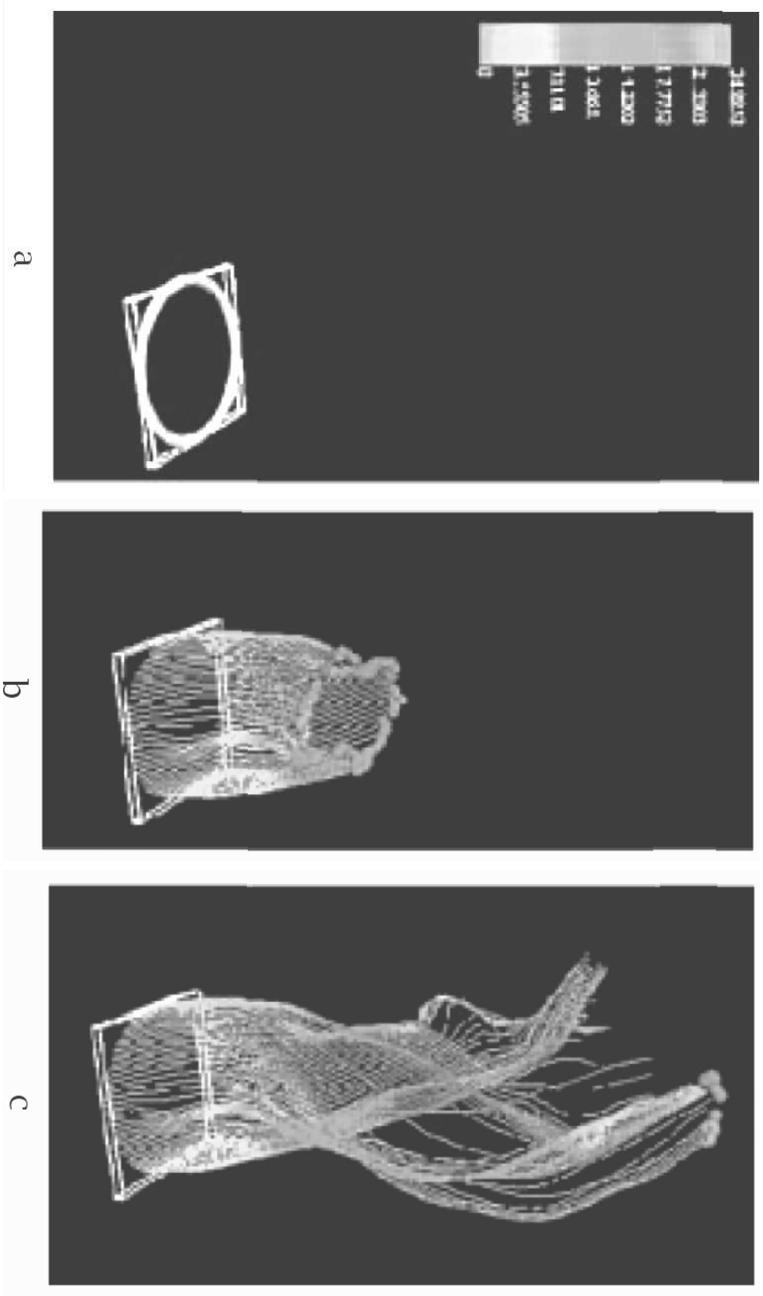

Figure 2.74: Pathlines of bubbles around the propeller (Pereira *et al.*, 2000).

2.10 Concluding remarks

While the fluid dynamicist's dream of being able to measure complex, three-dimensional turbulent flow fields globally with very high spatial and temporal resolution is still far from being fully realized, the rapid developments in the various hardware and algorithmic implementations of two-dimensional cross-correlation PIV have allowed for significant insights into fluid mechanics that would have otherwise been most difficult. Two-dimensional cross-correlation PIV methods have allowed for fluid flow measurements ranging from the micrometers per seconds in micro-scale flows to supersonic speeds, in academic research toindustrial applications. In addition, while single-point measurements only allowed inference to vorticity and strain rates, PIV, especially its implementation using image deformation, now allows the fluid dynamicist to directly measure these quantities globally and accurately. Most exciting is the emergence of three-dimensional methods that allow for volumetric studies of time-evolving flows, which will bring us yet a step closer to the fluid dynamicist's dream.

2.11 References

Adrian R. J.; "Scattering particle characteristics and their effect on pulsed laser measurements of fluid flow: speckle velocimetry vs particle image velocimetry," *Appl. Opt.* **23**, 1690 (1984).

Adrian R. J.; "Statistical properties of particle image velocimetry measurements in turbulent flow," in *Laser Anemometry in Fluid Mechanics*, 115-29. Adrian, R. J. *et al.* (editors) Instituto Superior Tecnico, Lisbon (1988).

Adrian R. J.; "Particle imaging techniques for experimental fluid mechanics," *Annual Review of Fluid Mechanics* **23**, 261-304 (1991).

Alexander B. F. and Ng, K. C.; "Elimination of systematic-error in subpixel accuracy centroid estimation," *Opt. Eng.* **30**, 1320-1331 (1991).

Astarita T. and Cardone G.; "Analysis of interpolation schemes for image deformation methods in PIV," *Exp. Fluids* **38**, 233-243 (2005).

Brown G. L., and Roshko A., "On density effects and large structure in turbulent mixing layers," *J. Fluid Mech.* **64**, 775-816 (1974).

Brucker C.; "3D scanning PIV applied to an air flow in a motored engine using digital high-speed video," *Meas. Sci. Technol.* **8**, 1480-1492 (1997).

Brucker C.; "Digital-particle-image-velocimetry (dpiv) in a scanning light-sheet - 3d starting flow around a short cylinder," *Exp. Fluids* **19**, 255-263 (1995).

Comte-Bellot G. and Corrsin S.; "Simple Eulerian time correlation of full and narrow-band velocity signal in grid-generated, 'isotropic' turbulence," *J. Fluid Mech.* **48**, 273-337 (1971).

Etebari A. and Vlachos P. P. "Improvements on the accuracy of derivative estimation from DPIV velocity measurements," *Exp. Fluids* **39**, 1040-1050 (2005).

Foucaut J. M., Carlier J., and Stanislas M.; "Post-processing of PIV records to allow derivative computation," *10th Int. Symp. On Appl. Of Laser Tech. To Fluid Mech.*, Lisbon (2000).

Foucaut J. M. and Stanislas M.; "Some considerations on the accuracy and frequency response of some derivative filters applied to particle image velocimetry vector fields," *Meas. Sci. Technol.* **13**, 1058-1071 (2002).

Fouras A. and Soria J.; "Accuracy of out-of-plane vorticity measurements derived from in-plane velocity field data," *Exp. Fluids* **25**, 409-430 (1998).

Gharib M. and Dabiri D.;. "Digital Particle Image Velocimetry," in *Flow Visualization, Techniques and Examples*, Smits A.J. and Lim T.T. (editors), Imperial College Press, Singapore (2000).

Grant I. (editor); "Selected Papers on Particle Image Velocimetry," *SPIE Milestone Series MS 99*, SPIE Optical Engineering Press, Bellingham, Washington (1994).

Guezennec Y. G., Brodkey R. S., Trigue N. T., and Kent J. C.; "Algorithms for fully automated three-dimensional particle tracking velocimetry," *Exp. Fluids* **17**, 209-219 (1994).

Gui L. and Wereley T.; "A correlation-based continuous window-shift technique to reduce the peak-locking effect in digital PIV image evaluation," *Exp. Fluids 32*, 506-517 (2002).

Hall E. L.; "Computer image processing and recognition," Academic Press, New York (1979).

Huang H. T., Feidler H. E. and Wang J. J.; "Limitation and improvement of PIV. Part I: Particle image distortion, a novel technique," *Exp. Fluids* **15**, 168-174 (1993).

Huang H. T., Feidler H. E. and Wang J. J.; "Limitation and improvement of PIV. Part II: Particle image distortion, a novel technique," *Exp. Fluids* **15**, 263-273 (1993).

Jambunathan K., Ju X. Y., Dobbins B. N. and Ashforth-Frost; "An improved cross correlation technique for particle image velocimetry," *Meas. Sci. Technol.* **6**, 507-514 (1995).

Kajitani L. and Dabiri D.; "A full three-dimensional characterization of defocusing digital particle image velocimetry," *Meas. Sci. Technol.* **16**, 790-804 (2005).

Keane R.D., and Adrian R.J.; "Theory of cross-correlation analysis of PIV images," *Applied Scientific Research* **49**, 191-215 (1992).

Kim B. J. and Sung H. J.; "A further assessment of interpolation schemes for window deformation in PIV," *Exp. Fluids* **41**, 499-511 (2006).

Landreth C. C. and Adrian R. J.; "Electro-optical image shifting for particle image velocimetry," *Applied Optics* **27**, 4216-4220 (1988).

Landreth C. C., Adrian R. J. and Yao C. S.; "Double-pulsed particle image velocimeter with directional resolution for complex flows," *Exp. Fluids* **6**, 119-128 (1988).

Lecuona A., Nogueira J., Rodriguez P. A., Ruiz-Rivas U., and Alfaro J.; "Local field correction PIV: a super-resolution technique," *3rd Int. Workshop on PIV*, Santa Barbara, CA, USA (1999).

Liang D. F., Jiang C. B. and Li Y. L.; "Cellular neural network to detect spurious vectors in PIV data," *Exp. Fluids 34*, 52-62 (2003).

Lourenco L. M.; "Velocity bias technique for particle image velocimetry measurements of high speed flows", *Applied Optics* **32**, 2159-2162 (1993).

Lourenco L. and Krothapalli A.; "On the accuracy of velocity and vorticity measurements with PIV," *Exp. Fluids* **18**, 421-428 (1995).

Lourenco L. M., Krothopalli A., and Smith C. A.; "Particle Image Velocimetry," in *Advances in Fluid Mechanics Measurements*, 127. Springer-Verlag, Berlin (1989).

Maheo P.; "Free-Surface Turbulent Shear Flows," Ph. D. Thesis, CalTech (1998).

Meinhart C. D., Wereley S. T. and Santiago J. G.; "PIV Measurements of a microchannel flow," *Exp. Fluids* **27**, 414-419 (1999).

Melling A.; "Tracer particles and seeding for particle image velocimetry," *Meas. Sci. Technol.*, **8**, 1406-1416 (1997).

Merzkirch W.; "Flow Visualization," Academic Press, New York (1974).

Nobach H. and Honkanen; "Two-dimensional gaussian regression for sub-pixel displacement estimation in particle image velocimetry or particle position estimation in particle tracking velocimetry," *Exp. Fluids* **38**, 511-515 (2005).

Nogueira J., Lecuona A. and Rodriguez P. A.; "Limits on the resolution of correlation PIV iterative methods. Fundamentals," *Exp. Fluids* **39**, 305-313 (2005).

Nogueira J., Lecuona A., Rodriguez P. A., Alfaro J. A. and Acosta A.; "Limits on the resolution of correlation PIV iterative methods. Practical implementation and design of weighting functions," *Exp. Fluids 39*, 314-321 (2005).

Nogueira J., Lecuona A., Ruiz-Rivas U. and Rodriguez P. A.; "Analysis and alternatives in two-dimensional multigrid particle image velocimetry methods: application of a dedicated weighting function and symmetric direct correlation," *Meas. Sci. Technol.* **13**, 963-974 (2002).

Nogueira J., Lecuona A. and Rodriguez P. A.; "Local field correction PIV, implemented by means of simple algorithms, and multigrid versions," *Meas. Sci. Technol.* **12**, 1911-1921 (2001).

Nogueira J., Lecuona A. and Rodriguez P. A.; "Local field correction PIV: on the increase of accuracy of digital PIV systems," *Exp. Fluids* **27**, 107-116 (1999).

Nogueira J., Lecuona A. and Rodriguez P. A.; "Data validation, false vectors correction and derived magnitudes calculation on PIV data," *Meas. Sci. Technol.* **8**, 1493-1501 (1997).

Pereira P. and Gharib M.; "Defocusing digital particle image Velocimetry and the three-dimensional characterization of two-phase flows," *Meas. Sci. Technol. 13*, 683-694 (2002).

Pereira F., Gharib M., Dabiri D. and Modarress D.; "Defocusing digital particle image Velocimetry: a 3-dimensional DPIV measurement technique. Application to bubbly flows," *Exp. Fluids* **29** S78-84 (2000).

Prasad A. K., Adrian R. J., Landreth C. C. and Offutt, P. W.; "Effect of resolution on the speed and accuracy of particle image velocimetry interrogation," *Exp. Fluids* **13**, 105-116 (1992).

Raffel M., Willert M. and Kompenhans J.; "Particle Image Velocimetry, A Practical Guide," Springer-Verlag Berlin, Heidelberg (1998).

Roesgen T. "Optimal subpixel interpolation in particle image velocimetry," *Exp. Fluids* **35**, 252-256 (2003).

Scarano F. and Riethmuller M. L.; "Advances in iterative multigrid PIV image processing," *Exp. Fluids*, S51-S60 (2000).

Shinneeb A-M., Bugg J. D. and Balachandar R.; "Variable threshold outlier identification in PIV data," *Meas. Sci. Technol.* **15**, 1722-1732 (2004).

Song X., Yamamoto F., Iguchi M. and Murai Y.; "A new tracking algorithm of PIV and removal of spurious vectors using Delaunay Tessellation," *Exp. Fluids* **26**, 371-380 (1999).

Soria J.; "An investigation of the near wake of a circular cylinder using a video-based digital cross-correlation particle image velocimetry technique," *Exp. Thermal Fluid Sci.* **12**, 221-233 (1996).

Tritton D.J.; "Physical Fluid Dynamics," Oxford Science Publications, Oxford (1988).

Westerweel J. and Scarano F.; "Universal outlier detection for PIV data," *Exp. Fluids* **39**, 1096-1100 (2005).

Westerweel J.; "Theoretical analysis of the measurement precision on particle image velocimetry," *Exp. Fluids* **29**, S3-S12 (2000).

Westerweel J.; "Fundamentals of digital particle image velocimetry," *Meas. Sci. Technol.* **8**, 1379-1392 (1997).

Westerweel J. Dabiri D. and Gharib M.; "The effect of a discrete window offset on the accuracy of cross-correlation analysis of digital PIV recordings," *Exp. Fluids* **23**, 20-28 (1997).

Westerweel J., Draad A. A., van der Hoeven, J. G. Th. and van Oord J.; "Measurement of fully-developed turbulent pipe flow with digital particle image velocimetry," *Exp. Fluids* **20**, 165-177 (1996).

Westerweel J.; "Efficient detection of spurious vectors in particle image velocimetry," *Exp. Fluids* **16**, 236-247 (1994).

Westerweel J.; "Digital Particle Image Velocimetry - Theory and Application," Ph.D. Thesis, Delft University Press (1993).

Willert C. E.; "The fully digital evaluation of photographic PIV recordings," *Applied Scientific Research* **56**, 79-102 (1996).

Willert C. E.; "The interaction of modulated vortex pairs with a free surface," Ph.D. dissertation, Department of Applied Mechanics and Engineering Sciences, University of California, San Diego (1992).
Willert C. E. and Gharib M.; "Three-dimensional particle imaging with a single camera," *Exp. Fluids* **12**, 353-358 (1992).

Willert C.E. and Gharib M.; "Digital Particle Image Velocimetry," *Exp. Fluids* **10**, 181-193 (1991).

Chapter 3

Elements of entrainment

3.1 Introduction

Turbulence has been called the most important unsolved problem in all of classical physics. From astrophysics to oceanography, aeronautics to combustion, turbulence is ubiquitous. Yet in spite of its central role in science and engineering, turbulence has defied solution for over a century.

The most important property of turbulence is entrainment. Both transport and mixing in turbulent flows are controlled by entrainment. Boundary layer heat transfer and skin friction are the transport of energy and momentum at a wall. The vertical transport of water and energy in the atmosphere and ocean are determined by stratified entrainment. In high Reynolds number flow, the mixing is entrainment-limited, so much so that the molecular diffusivity can change by three orders of magnitude while the molecular mixing rate changes by only a factor of two. Entrainment determines most of what we really want to know about a turbulent flow.

3.2 Entrainment hypothesis

Half a century ago, Morton, Taylor & Turner (1956) proposed the most successful hypothesis for entrainment. In order to model a thermal rising from the sudden release of buoyant fluid, they argued on dimensional grounds that the local entrainment velocity v_e into the thermal at any station must be proportional to the rise speed W of the thermal at that station. There is simply no other speed available on which to base the entrainment velocity (see figure 3.1). In this way, the thermal grows linearly with height, in accord with observation. Furthermore, their hypothesis is equally valid for a wide variety of other classical flows that might be termed "ordinary turbulence", correctly accounting for the entrainment rate in the plume, shear layer, jet, wake, etc.

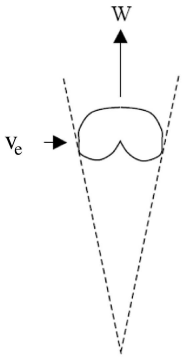

Figure 3.1: Entrainment velocity v_e is proportional to the thermal rise speed W according to the entrainment hypothesis (Morton *et al.*).

However, the entrainment hypothesis sometimes fails. For example, when the speed of sound becomes comparable to the velocity jump across a shear layer, the entrainment rate precipitously declines by a factor of five (Papamoschou & Roshko, 1989). This cannot be explained by the original entrainment hypothesis. The entrainment rate is also strongly affected when acceleration, confinement, rotation, or stratification become appreciable. This paper is an attempt to extend the entrainment hypothesis into a more general theory.

3.3 Entrainment process

Entrainment was thought to be a small-scale nibbling process at the edge of a turbulent region. Corrsin & Kistler (1955) proposed a "superlayer" there, across which fluid was thought to be entrained by small-scale nibbling. Shadowgraph images of the supersonic round wake of a projectile seemed to support this notion. However, shadowgraph images of the plane shear layer revealed the engulfment of large tongues of fluid by the largest vortices in the flow (Brown & Roshko 1974; Roshko, 1976). The two-dimensional geometry of their shear layer allowed a more clear view of the entrainment process. Instead of polite little nibbles, their images revealed that the turbulence really entrains like a hungry teenager taking big gulps of fluid. These large engulfed tongues of pure, unmixed fluid are transported by the large-scale vortices entirely across the layer (Konrad, 1976).

3.4 Entrainment rate

The entrainment rate ν_e is a velocity. From dimensional considerations, it must therefore always be expressible as the ratio of a relevant length scale to the rota-

tional period τ_λ of the eddy responsible for entrainment. If there is engulfment, then the relevant length scale must be the size λ of the entraining eddy.

$$\nu_e = \text{const.}\, \frac{\lambda}{\tau_\lambda}\,. \tag{3.1}$$

Of course, the dimensional argument cannot establish the value of the constant of proportionality. If there is no engulfment, such as at a solid wall or at a strongly stratified interface, the length scale must be a diffusive one, the square root of the product of the diffusivity and an eddy time.

For ordinary, incompressible, free shear flows, the entrainment rate must be proportional to the ratio of the size of the largest eddies to their rotation period. This is a direct consequence of Roshko's engulfment, whereby the first step of engulfment by the largest eddies is rate-limiting. The subsequent processing of the engulfed fluid by all smaller eddies is both proportional to and sufficiently fast compared to the largest eddies that only the largest eddies matter. Since the largest eddies control the rate, we do not need to know much about anything else. This happy circumstance vastly simplifies matters, such as modeling the mixing (Broadwell & Breidenthal, 1982). So for such flows equation (3.1) becomes

$$\nu_e = \text{const.}\, \frac{\delta}{\tau_\delta}\,, \tag{3.2}$$

where the subscript δ is the size of the largest eddies. Since the characteristic velocity of the turbulent flow is also proportional to δ/τ_δ , we recover the Morton *et al.* entrainment hypothesis for ordinary turbulence. As indicated above, equation (3.2) does not always work. Let us now consider the various violations of the entrainment hypothesis.

3.5 Acceleration

Like people, ordinary vortices slow down as they age. That means that the rotation period of the largest eddies τ_δ increases with time t. In self-similar turbulence, there is no other distinguished time scale, so the period must be proportional to the age of the vortex from its virtual origin.

$$\tau_\delta(t) = \text{const.}\, t\,. \tag{3.3}$$

For all ordinary turbulence, the constant of proportionality is positive, as is confirmed by examination of the observed growth laws of these flows. Their rotation period always increases with age. These flows are termed "unforced".

Note that the vortex rotation period in an unforced flow may not exactly follow equation (3.3) over a short time interval. For example, the large-scale vortices in the free shear layer obey equation (3.3) in the long term, but on time scales less than the pairing time, a vortex does not necessarily follow (3.3). We will ignore this subtlety here.

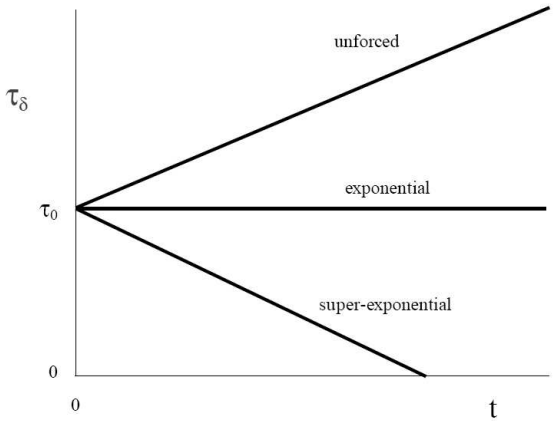

Figure 3.2: Temporal evolution of the vortex rotation period for self-similar flow.

3.5.1 Forced turbulence

However, it is possible to force the flow in such a way that the rotation period does not increase with age. Define an acceleration parameter α such that

$$\tau_\delta = \tau_0 - \alpha\, t\,, \tag{3.4}$$

where τ_0 is the large-eddy rotation period at the arbitrary time $t = 0$. For ordinary, unforced turbulence, $\alpha < 0$. If the flow is forced, α can be zero or even positive.

3.5.2 Temporal self-similarity

The vortices are temporarily self-similar if their next rotation period is proportional to their last one. Otherwise there would be a special, distinguished time scale, a contradiction of self-similarity. Figure 3.2 illustrates the evolution of the rotation period of temporally self-similar turbulence. The line must be straight and α must be a constant. For all ordinary, unforced turbulence, $\alpha < 0$ and slopes upward.

3.5.3 Exponential jet

The line is horizontal if the next rotation period is the same as the last ($\alpha = 0$). This can achieved in an exponential jet, where fluid is ejected from a nozzle with a speed $V_J(t)$ that increases exponentially in time,

$$V_J(t) = V_{J0}\, \exp\left(t/\tau_e\right)\,, \tag{3.5}$$

where V_{J0} is the nozzle speed at $t = 0$. Because of this forcing, every large-scale vortex in the exponential jet rotates with the same period, equal to the e-folding time τ_e imposed on the flow, no matter how old or how far from the nozzle. The vortices never age. It is a kind of perpetual youth.

Remarkably, acceleration reduces the normalized entrainment rate. A convenient way to measure entrainment at large Reynolds number is with a fast chemical reaction that destroys a visible chemical in the nozzle fluid when mixed with the ambient fluid. If the mixing is entrainment-limited, changes in the visible "flame length" reflect changes in the normalized entrainment rate. Compared to the ordinary jet, the exponential jet has about a 20% greater flame length (Kato *et al.*, 1987). In fact, such acceleration is the only known method for affecting the far-field entrainment rate of the incompressible jet, as noted by Zhang & Johari (1996). Their detailed images of jets with modulated nozzle speed demonstrate that acceleration only influences the entrainment rate when the imposed change in velocity during one vortex rotation is comparable to the initial velocity. In other words, the logarithmic derivative must be appreciable.

3.5.4 Super-exponential forcing

The third category is the line sloping downward in Figure 3.2 ($\alpha > 0$). In spite of getting older, the vortices spin ever faster. After a finite time, the spin rate becomes infinite and the rotation period vanishes.

One might anticipate that the entrainment rate would be further reduced as α increases. Using dimensional and heuristic arguments, one theory has been proposed (Breidenthal (2003) with different notation). The dimensions of the dissipation rate per unit mass are $(length)^2(time)^{-3}$. Every canonical turbulent flow has a conserved quantity Q. For example, in the shear layer, it is the velocity difference ΔU. If the dimensions of Q are in general $(length)^m(time)^{-n}$, the dissipation rate is proportional to $Q^{\frac{2}{m}}\tau_\nu^{-\left(3-\frac{2n}{m}\right)}$, where the vortex period is τ_ν. For super-exponential forcing,

$$Q = Q_0 \exp\left(\frac{t}{\tau_0 - \alpha t}\right) , \tag{3.6}$$

where Q_0 is the value of Q at $t = 0$. Define D to the dissipation rate normalized by that of the unforced flow. From heuristic grounds, we conjecture that the quantity is the natural scaling of effect of α on D. If so, then

$$\beta \equiv -\left(3 - \frac{2n}{m}\right)\frac{dD}{D} = \frac{d\alpha}{-\left(3 - \frac{2n}{m}\right)} , \tag{3.7}$$

$$D = \exp\left(-\frac{\alpha - \alpha^*}{\beta}\right) , \tag{3.8}$$

where α^* is the value of α for the unforced flow.

3.6 Compressibility

It has long been known that a compressible flow grows more slowly than an incompressible one. Papamoschou & Roshko (1989) found that the spreading angle of a turbulent shear layer dropped by a factor of about five as the Mach number increased. Linear stability theory may provide an indication of the entrainment behavior, since the underlying instabilities drive the basic flow. However, the indication can only be qualitative, in as much as the finite amplitude eddies are fully nonlinear.

Bogdanoff (1983) recognized that the important parameter for the instability is a "convective" Mach number, the Mach number of the outer flow with respect to the speed of the instability waves. A hint that this is the correct approach comes from the flow models of Brown (1974), Coles (1981) and Dimotakis (1986), discussed below.

One heuristic model that addresses the fully nonlinear flow supposes that nonsteadiness is essential to entrainment. This is a hint of this in the results of the Oster-Wygnanski (1982) experiment, where the vortices in a shear layer are forced to be equally spaced. For a certain time, these vortices are steady, resembling Kelvin's cat's eye pattern (Kelvin, 1880), with no vortex pairing. Remarkably, Oster & Wygnanski found that the Reynolds stresses vanish. There is no turbulent transport of momentum. Roberts (1985) found the mixing rate essentially vanishes, in spite of the fact that the vortices are continuing to rotate. If nonsteadiness is required for entrainment, it follows that the signaling speed of acoustic waves must control the physics, since the information about a nonsteady event can travel no faster than the speed of sound.

There is a subtle point to note here. Mach number plays two simultaneous and different roles in high speed flow (Roshko, private communication). On one hand, it indicates the signaling process above. It is also a measure of the energy content of the flow, i.e. thermal vs. kinetic. Indeed, most attempts to model compressibility have focused on energy and density considerations.

The second assumption is that the important time scale for an eddy to entrain is always about one vortex rotation. This is the behavior of the engulfment and mixing process in incompressible turbulence (Brown & Roshko, 1974). The immediate consequence of these two assumptions is that entrainment is controlled by a "sonic eddy" whose rotational Mach number is unity (Breidenthal, 1992). Such an eddy completes one rotation during the signaling time across its diameter. Any larger eddies that might exist would play no role in the entrainment process whatsoever.

The hypersonic wake provides a good opportunity for comparison with experiment. The model predicts that the initial wake growth rate should be zero, since the large-eddy rotational Mach number is greater than unity there. Only sonic eddies, much smaller than the total wake thickness, are capable of transporting momentum. The time scale for the sonic eddies to transport momentum across the entire wake is the square of the wake thickness divided by the product of the speed of sound and the sonic eddy size, this product being the effective turbulent

diffusivity. Note that the concept of turbulent diffusivity is rarely justified.

The initial wake should not grow at all until the rotational Mach number of the largest eddies has fallen to unity. Then the growth rate should transition to the incompressible value. The time for this transition is set by the transport of momentum by the sonic eddies across the width of the wake. Since they are small compared to the width of the wake, the process can be modeled by turbulent diffusion, with a diffusivity equal to the product of the speed of sound and the size of the sonic eddy. Note that for most flows, turbulent diffusion is not an appropriate model (Corrsin, 1974). Only in the rare circumstance of the entraining eddies being small compared with the distance in question is diffusion a reasonable model.

The transition is predicted to occur at a downstream station of $M^2 d$, where d is the effective body diameter. At $M = 20$, this would be 400 effective body diameters downstream, which is in accord with shadowgraph observations (Finson, 1973).

3.7 Confinement and mixing

When engineers mix chemicals together, they usually want to retain the mixture in a confined chamber. Examples include combustion and chemical processing. So we will generalize the term entrainment here to include the entire physics of transport and molecular mixing in a confined vessel.

Consider the probability density function (pdf) for the concentration of an inert scalar mixing with a second fluid in some general flow sketched in figure 3.3. Initially the pdf consists of two delta functions at the extrema, corresponding to the two pure fluids. As the turbulence mixes some of the two pure fluids together at intermediate concentrations, forming a central Gaussian in the pdf. For a self-similar free shear layer with two infinite supplies of pure fluid, the pdf would reach a steady state (Konrad, 1976; Broadwell & Breidenthal, 1982). However, if only one fluid supply is infinite, such a finite jet injected into an infinite reservoir, then eventually there is only one delta function in the pdf. If both fluid supplies are finite, then the two delta functions both disappear, and the pdf consists of a central Gaussian, the width of which is the rms concentration fluctuation. As the turbulence further mixes the fluid, the Gaussian progressively narrows and the fluctuations decline.

Here the simplest two assumptions are that both the flow and the mixing are self-similar (Breidenthal *et al.*, 1990). The former requires that the vortex rotation period is proportional to its age, as we have seen above. The latter implies that the concentration fluctuations decline by a factor of e at each rotation. The simple result is that the concentration fluctuations should be proportional to a characteristic time scale τ divided by time.

$$\frac{c'}{\overline{c}} = \text{const.}\, \frac{\tau}{t}\,, \tag{3.9}$$

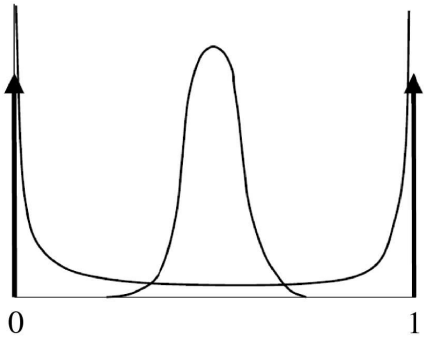

Figure 3.3: Probability density function of the concentration field of a passive scalar is composed of contributions from the pure fluid, Taylor layers, and the vortex cores (Broadwell).

The characteristic time scale is determined by dimensional considerations of the problem. For example, if one fluid is initially in a spherical chamber and a second fluid is momentarily injected into the chamber, τ depends on the jet impulse and the chamber diameter. The characteristic time τ must also equal the vortex rotation period at the moment $t = \tau$ when all pure fluid has disappeared and the large-scale vortices have filled the chamber. Measurements of concentration fluctuations are consistent with (3.9), in spite of the fact that the actual vorticity field appears to decay exponentially instead of as inverse time (Aarnio, 1994).

3.8 Density ratio

The coherence of large-scale structure in turbulence was discovered by accident. Brown & Roshko (1974) were attempting to find out about the compressibility effects on entrainment. It was known that supersonic jets exhibited an anomalously low spreading angle. It was not clear if this was due to Mach number or to the density ratio of the supersonic experiments. Since density ratio was easier to control, they elected to measure its effect on spreading angle in incompressible flow by taking shadowgraph pictures. While the most important result of their experiment was the coherent structure revealed by their pictures, they also determined that density ratio has a remarkably weak effect on entrainment rate. The density ratio must vary by a factor of 49 to achieve a factor of two change in spreading angle. This proved that the main influence on jet spreading angle was Mach number.

A simple picture readily accounts for the effect of density ratio on entrainment into a shear layer. Coles (1981) drew the shear layer in the Lagrangian frame of the vortices (see figure 3.4). Fluid enters a vortex from each stream due to the

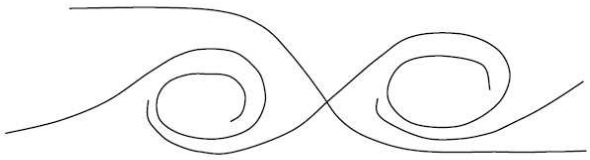

Figure 3.4: Sketch of the flow in the shear layer for an observer moving with the vortices (Brown, Coles and Dimotakis).

relative speed of the stream with respect to the vortex. Brown (1974) showed that the relative speed ratio comes from consideration of the stagnation streamlines. Assuming quasi-steady inviscid flow, the total pressure on both streamlines must be constant and equal. Furthermore, the streamlines far from the stagnation point are quasi-parallel, so that their static pressures must be equal. The result is the dynamic pressures of the relative flows far from the stagnation point are equal. So the speed ratio in this frame is just the inverse square root of the density ratio. Dimotakis (1986) neatly summarizes the effects of both density and velocity ratio on both the spreading angle and the entrainment ratio from the two sides of the layer.

3.9 Rotation

Bradshaw (1969) noted that when a fluid rotates, the higher speed fluid tends to want to move to the outside of the turn. This corresponds to a state of lower kinetic energy for the same angular momentum. The difference in kinetic energy between the two states can dissipated into thermal energy in accord with the second law. On the other hand, if the higher speed fluid is already on the outside of the turn, a rotating flow acts as if it is stratified. This occurs even when the fluid has uniform density. This effective stratification inhibits entrainment.

Cotel (2002) used Bradshaw's analogy to explain the remarkable behavior of aircraft trailing vortices. Even many kilometers behind a large aircraft, the wingtip vortices are compact, laminar cores of only about a meter in diameter, in spite of the large Reynolds number. The radial transport of momentum is strongly inhibited by the effective stratification due to the rotation.

3.10 Stationarity

When a vortex is near a surface, the motion of the vortex with respect to the surface becomes important. The entrainment rate across the surface depends on

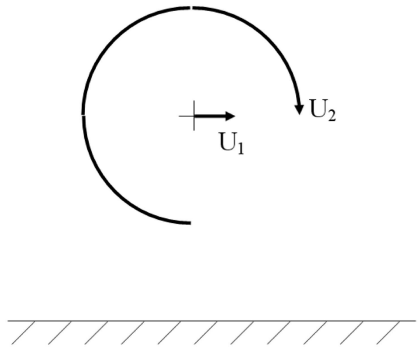

Figure 3.5: The intrinsic velocity ratio of a vortex near a surface - vortex persistence $T = U_2/U_1$ (Cotel).

the amount of stationarity of the vortex. Even a small amount of vortex movement completely changes the physics.

Cotel & Breidenthal (1997, 1999) first identified this effect at a stratified interface. The entrainment rate across a stratified interface was much different for an impinging vertical jet compared to other turbulent flows, such as from an oscillating grid. The impinging vertical jet entrained fluid across the interface with stationary, lateral vortices, in contrast to the moving vortices from an oscillating grid or horizontal jet.

In order to quantify the stationarity, Cotel defined a new parameter. The persistence parameter T is essentially the ratio of the rotational to the translational speed of the vortex with respect to the surface (figure 3.5). When T is much less than one, the flow is in the nonpersistent limit. When T is much greater than one, the flow is said to be persistent. For a vortex near a surface, there is no more important parameter than this.

Cotel asserted that the surface may be of any type: a stratified interface, a solid wall, or even an iso-vorticity contour of a neighboring vortex. Thus her theory is applicable to a wide class of flows.

When a piston suddenly begins to push fluid out of a tube at constant velocity, a starting vortex is formed. The subsequent jet never catches up with this vortex ring (Johari *et al.*, 1997). If the piston advances sufficiently far, the starting vortex cannot accept all the injected vorticity. Gharib *et al.* (1998) defined a "formation number" to be the ratio of the stroke length to piston diameter. The formation number is essentially identical to the persistence parameter, as noted by Gharib (private communication, 1995). There is a transition in vortex behavior at a critical value of the formation number at about four, when the starting vortex ring can no longer accept all the injected vorticity. This transition is important in heart flow.

Another example of persistence is the boundary layer. When the surface is a solid wall, the wall fluxes can be drastically modified by persistence. In order to achieve the persistent limit, strong stationary vortices must be introduced. This is difficult, since a linear vortex near a flat wall is unstable to both short wavelength Widnall (Widnall *et al.*, 1974) and long wavelength Crow (1970) instabilities, which would promptly render the vortex nonsteady. Balle (Balle & Breidenthal, 2002) suggested that vortices could be stabilized by a wavy wall, substituting for the dividing streamline in a von Karman wake. The wake vortices are known to be at least quasi-stable. Balle found the wall flux measured at the bottom of a trough to be laminar, as predicted by Cotel's theory. Using flow visualization, Dawson (2005) subsequently confirmed that an otherwise turbulent boundary layer was indeed made laminar by the addition of persistent vortices. However, she found that a small segment of the wavy wall did not achieve laminar flow, due to an adverse pressure gradient in the spanwise direction. It is still an open question if a wall shape can be found that will achieve laminar flow everywhere under persistent vortices. Reducing the heat flux to a laminar value would be useful for turbine blades and hypersonic flow.

Surprisingly, Dawson found that the flow pattern did not correspond to the von Karman wake. Instead, it resembled Kelvin's cat's eye flow. As mentioned above, this flow pattern always seems to be associated with laminar fluxes.

These discoveries raise interesting questions about the stabilizing effect of stationary vortices on the flow. It seems reasonable that a stationary vortex would not directly hand off energy into smaller scale eddies, since that presumably requires some kind of nonsteadiness in that vortex. However, the persistent vortex seems to inhibit instabilities even in neighboring vorticity, such as that in the boundary layer below the streamwise vortices. Recent results by Fransson *et al.* (2005) indicate that streamwise vortices can stabilize Tollmein-Schlichting waves.

3.11 Stratification

Based on the persistence parameter, Cotel (Cotel & Breidenthal, 1997) proposed a new model for stratified entrainment. It consists of different entrainment regimes, determined by the Richardson, Reynolds, Schmidt, Prandtl, and persistence parameters. For simplicity, we will only consider the limit of a thin stratified interface.

The Richardson number Ri (of the largest eddies) is defined as the ratio of the potential to the kinetic energy of the largest eddies at the stratified interface. One can also define the *eddy* Richardson number Ri_λ of a smaller eddy of size λ . For a Kolmogorov spectrum, the eddy Richardson number increases with eddy size.

If $\mathrm{Ri} << 1$, the potential energy is dominated by the kinetic energy and stratification is not important for any eddy. If $\mathrm{Ri} > 1$, there are at least two possibilities. Depending on the Reynolds number, the smallest eddies at the Kolmogorov microscale λ_0 may have an eddy Richardson number Ri_{λ_0} greater than one. If so, then they and therefore all eddies have insufficient kinetic energy to engulf a tongue

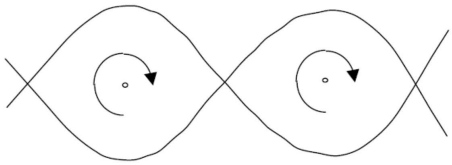

Figure 3.6: Cat's eye flow (Kelvin).

of fluid across the interface. Consequently, in this limit of strong stratification the interface must be essentially flat. All fluxes are purely diffusive. From dimensional considerations, we can define a corresponding effective entrainment velocity to be the square root of the ratio of the diffusivity divided by some eddy rotation period. The diffusivity corresponds to the flux in question, i.e. mass, momentum, or energy.

There are many choices for the eddy rotation period, ranging from that of the largest to the smallest eddy. Clearly, eddies in the middle cannot be rate limiting, since there is no basis to select one over another. So only the largest or the smallest eddy could be correct. Cotel proposed that in the persistent limit, the correct choice is that of the largest eddy. Remarkably, the fluxes would then be completely independent of any fine-scale turbulence.

While this prediction may not yet have been tested in stratified flow, it does seem to work in the corresponding wall flow discussed above. The heat flux is laminar because the persistent vortices make the flow laminar.

In the non-persistent limit, the fluxes would be controlled by the smallest-scale eddies, corresponding to ordinary turbulent flow. This is in accord with many observations at stratified interfaces and the boundary layer.

If the smallest scale vortices have an eddy Richardson number less than unity, then the interface is not flat. The eddy whose Richardson number is equal to about unity can engulf fluid across the interface. It determines the entrainment rate.

Dramatic evidence of the importance of persistence on stratified entrainment was measured by Cotel *et al.* (1997). Following a suggestion by L. Redekopp (private communication, 1995), they tilted an impinging jet and precessed it. The entrainment rate was reduced by orders of magnitude compared to that of the vertical jet. The effect is not only large, but counter-intuitive.

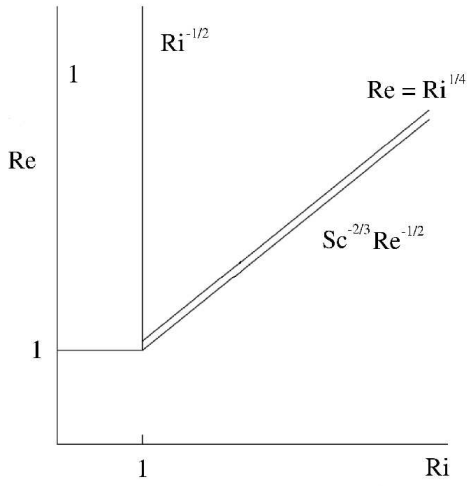

Figure 3.7: Stratified entrainment diagram in the persistent limit (Cotel).

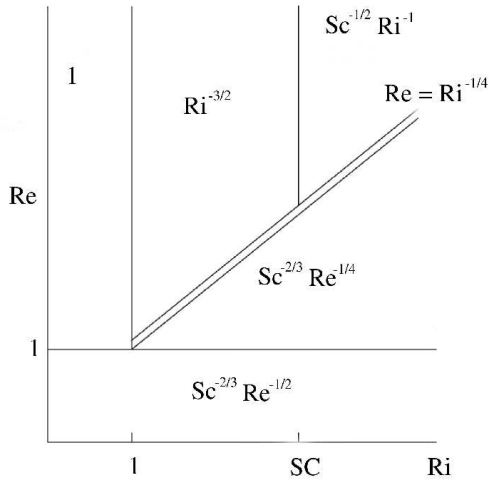

Figure 3.8: Stratified entrainment diagram in the nonpersistent limit (Cotel).

3.12 Conclusions

The entrainment rate of a turbulent flow can always be expressed as the ratio of a length to a time scale corresponding to the entraining eddy. This is a generalization of the entrainment hypothesis of Morton, Taylor & Turner that accounts for a variety of effects, such as acceleration, compressibility, confinement, stratification, and stationarity.

3.13 Acknowledgements

The author would like to acknowledge the contributions of his instructors, colleagues, and students.

3.14 References

Aarnio M.J.; "Mixing by turbulent streamwise vortices confined in a duct," Ph.D. thesis, University of Washington (1994).

Balle G. J. and Breidenthal R.E.; "Stationary vortices and persistent turbulence in Karman grooves," *J. Turbulence* **3**, 33-51 (2002).

Bergantz G. W. and Breidenthal R. E.; "Non-stationary entrainment and tunneling eruptions: A dynamic template for eruption processes and magma mixing," *Geophys. Res. Letters* **28** 3075-3078.

Bhat G. S. and Narasimha R.; "A volumetrically heated jet: Large-eddy structure and entrainment characteristics," *J. Fluid Mech.* **325** 303-330 (1996).

Bogdanoff D.; "Compressibility effects in turbulent shear layers, *AIAA J.* **21** 926-927 (1983).

Bradshaw P.; "The analogy between streamline curvature and buoyancy in turbulent shear flow," *J. Fluid Mech.* **36** 177-191 (1969).

Breidenthal R. E., Buonadonna V. R. and Weisbach M. F.; "Mixing of jets in confined volumes," *J. Fluid Mech.* **219** 531-544 (1990).

Breidenthal R. E.; "Sonic eddy - A model for compressible turbulence," *AIAA J.* **30**(1) 101-104 (1992).

Breidenthal R. E.; "Turbulent stratified entrainment and a new parameter for surface fluxes," in *Recent Research Developments in Geophysical Research*, Pandalai S.G. (editor). Research Signpost, Trivandrum, India, (1999).

Breidenthal R. E.; "The vortex as a clock," in *Advances in Fluid Mechanics*, Alam M., Govindarajan R., Ramesh O. N., and Sreenivas K. R. (editors). Jawaharlal Nehru Centre for Advanced Scientific Research, Bangalore, India (2003).

Broadwell J. E. and Breidenthal R. E.; "A simple model of mixing and chemical reaction in a turbulent shear layer," *J. Fluid Mech.* **125** 397-410 (1982).

Brown G. L.; "The entrainment and large structure in turbulent mixing layers," in *5th Australian Conference on Hydraulics and Fluid Mechanics*, 352-359 (1974).

Brown G. L. and Roshko A.; "On density effects and large scale structure in turbulent mixing layers," *J. Fluid Mech.* **64** 775-816 (1974).

Coles D.; "Prospects for useful research on coherent structure in turbulent shear flow," in *Proc. Indian Acad. Sci. (Engng. Sci.)* **4** 111 (1981).

Corrsin S.; "Limitations of gradient transport models in random walks and in turbulence," *Adv. Geophys.* **18** A, 25 (1974).

Corrsin S. and Kistler A. L.; "Free-stream boundaries of turbulent flows," *NACA TR 1244*, Washington D.C. (1955).

Cotel A. J.; "Turbulence inside a Vortex - Take Two," *Phys. Fluids* **14** (8) 2933 (2002).

Cotel A. J. and Breidenthal R. E.; "Persistence effects in stratified entrainment," *Applied Scientific Research* **57** 349-366 (1997).

Cotel A. J. and Breidenthal R. E.; "Vortex persistence - A recent model for stratified entrainment and its application to geophysical flows," *Geophysical Flows*, Klewer (1999).

Cotel A. J., Gjestvang J. A., Ramkhelawan N. N. and Breidenthal R. E.; "Laboratory experiments of a jet impinging on a stratified interface," *Exp. Fluids* **23** 155-160 (1997).

Crow S. C.; "Stability theory for a pair of trailing vortices," *AIAA J.* **8** 2172-2179 (1970).

Dimotakis P. E.; "Two-dimensional shear-layer entrainment," *AIAA J.* **21** 1791. "l shear-layer entrainment", *AIAA J.* **21** 1791 (1986).

Dimotakis P. E.; "Turbulent mixing," *Annual Reviews of Fluid Mechanics* **37** 329-356 (2005).

Dawson O. R.; "The effect of persistent vortices on boundary layer behavior in flow along a wavy wall," M.S. thesis, University of Washington (2005).

Finson M. L.; "Hypersonic wake aerodynamics at high Reynolds numbers," *AIAA J.* **11**(8), 1137-1145 (1973).

Fransson J. H. M., Brandt L., Talamelli A. and Cossu C.; "Experimental study of the stabilization of Tollmein-Schlicting waves by finite amplitude streaks," *Phys. Fluids* **17**(054110) (2005).

Gharib M., Rambod E. and Shariff K.; "A universal time scale for vortex ring formation," *J. Fluid Mech.*, **360** 121-140 (1998).

Johari H., Zhang Q., Rose M. and Bourque S.; "Impulsively started turbulent jets," *AIAA J.* **35**(4) 657-662 (1997).

Kato S. M., Groenewegen B. C. and Breidenthal R. E.; "On turbulent mixing in nonsteady jets," *AIAA J.*, **25**(1) 165-168 (1987).

Kelvin Lord (Thomson, William T.); "On a disturbing infinity in Lord Rayleigh's solution for waves in a plane vortex stratum," *Nature* **23**, 45-46 (1880).

Konrad J. H.; "An experimental investigation of mixing in two-dimensional turbulent shear flows with applications to diffusion-controlled chemical reactions," Ph.D. thesis, California Institute of Technology (1976); and *Project SQUID Tech. Rep.* CIT-8-PU.

Morton B. R., Taylor G. I. and Turner J. S.; "Turbulent gravitational convection from maintained and instantaneous sources," *Proc. Roy. Soc. A* **234** 1-23 (1956).

Oster D. and Wygnanski I.; "The forced mixing layer between parallel streams," *J. Fluid Mech.* **123** 91-130 (1982).

Papamoschou D. and Roshko A.; "The compressible turbulent shear layer: An experimental study," *J. Fluid Mech.* **197** 453 (1989).

Roberts F. A.; "Effects of a periodic disturbance on structure and mixing in turbulent shear layers and wakes," Ph.D. thesis, California institute of Technology (1985).

Roshko A.; "Structure of turbulent shear flows: A new look," *AIAA J.* **14**(10) 1349-1353 (1976).

Widnall S. E., Blis D. B. and Tsai C-Y; "The instability of short waves on a vortex ring," *J. Fluid Mech.* **66** 35-47 (1974).

Zhang Q. and Johari H.; "Effects of acceleration on turbulent jets," *Phys. Fluids*, **8**(8) 2185-2195 (1996).

Chapter 4

New results on turbulent entrainment in stratified flows

4.1 Introduction

Transport across a stratified interface is an essential aspect of many geophysical processes. Consider a catastrophic volcanic eruption close to a large city, for example, Mount Rainier in Washington State next to the Seattle-Tacoma urban area. The winds are light and the ashes are approaching the city. How much time is available to evacuate the city? How high will the ashes rise? Will they reach the stratosphere? How will the weather be affected? These questions regarding the transport of ashes will be essential for the survival of a large number of people.

Imagine now another scenario: a large city in a valley where atmospheric conditions have created an unprecedented strong inversion above the city. The pollution levels are dramatically high, people are suffering from a variety of respiratory problems. The katabatic winds are not strong enough to penetrate through the inversion and dilute the polluted air above the city. A cost-effective way to destroy the interface has to be designed.

Similar problems not only exist in atmospheric environments, but also in oceanic and freshwater surroundings. It is important for large coastal cities to take into account tides, stratification and winds in the design of their sewage outfalls. For example, the newly redesigned Boston sewage outfall takes advantage of summer stratification to trap effluents below the water surface. To start solving these issues, one must begin with a profound understanding of the entrainment process and the vortex dynamics at the interface. Once one can quantify these physical processes at the interface, more accurate transport models can be developed. Other possible applications of transport across stratified interfaces can include the contribution of hydrothermal plumes on the global ocean energy budget, turbidity

currents on the ocean floor, the design of lake de-stratification systems, modeling gas leaks from storage reservoirs, weather forecasting, and global climate.

Cotel and Breidenthal (1997) proposed a theoretical model to predict the turbulent entrainment rate across a stratified interface over a wide range of parameters. A new parameter was proposed in addition to the conventional Reynolds, Richardson and Schmidt numbers (Section 4.2). This parameter called persistence is the ratio of a rotational to a translational velocity pertaining to the trajectories of vortices in the vicinity of a stratified interface. To further test the validity of persistence, laboratory experiments are performed for a tilted jet with and without precession (Section 4.4) and compared to experiments with a vertical jet impinging on a stratified interface (Cotel, 1995). Furthermore, the effect of a solid boundary is examined by investigating a sloping gravity current impinging on a stratified interface (Section 4.5). The importance of the forcing mechanism, *i.e.* momentum versus buoyancy, is examined by studying thermals in a stratified environment (Section 4.6). The experimental techniques are described in Section 4.3.

4.2 Entrainment theory

Entrainment is defined as engulfment of tongues of fluid (Roshko, 1976). Entrainment is different from mixing, as fluid can be entrained but not mixed at the molecular level. This might happen for lower Reynolds numbers for example. With no or weak stratification in a stagnant environment, it is assumed that the entrainment velocity is proportional to the centerline velocity or some other characteristic velocity of the flow (Morton, Taylor and Turner, 1956). For example, the entrainment of surrounding fluid into a jet is directly proportional to the centerline velocity of the jet. When stratification or compressibility effects become important, other time and length scales enter the problem, the entrainment no longer follows the hypothesis of Morton *et al.* (1956). In the presence of a stratified interface, experiments have shown that in general the entrainment rate declines with increasing stratification. It is observed that the relationship between the entrainment rate and the Richardson number obeys a power law (Turner, 1973) when the Richardson number is between one and a few hundreds. The relationship is often defined as:

$$\frac{w_e}{w_1} = c\ \mathrm{Ri}^{\alpha}\,, \tag{4.1}$$

where w_e is the entrainment velocity across the interface, w_1 the characteristic velocity of the impinging turbulent flow, c and α are dimensionless constants. The Richardson number, Ri (the ratio of potential energy to kinetic energy), is defined in terms of the impinging turbulence quantities:

$$\mathrm{Ri} = \frac{g'\delta}{w_1^2}\,, \tag{4.2}$$

$$g' = \frac{\Delta\rho}{\rho} g\,, \tag{4.3}$$

with g' is the buoyancy acceleration due to the density difference $\Delta\rho$. The acceleration of gravity is g. $\Delta\rho$ is the density difference across the interface. The density of the surrounding fluid is ρ. δ is the length scale of the incident turbulence at the interface and w_1, its characteristic velocity. For Ri < 1, the kinetic energy of the largest eddies is greater than the potential energy investment in engulfing a tongue of fluid, so there is little or no effect of stratification on entrainment. When the Richardson number is very large, the interface becomes flat, and potential energy can no longer affect the entrainment. Therefore, the entrainment rate becomes independent of Ri (Cotel and Breidenthal, 1997). Diffusion becomes the only available entrainment mechanism.

The entrainment velocity, w_e, represents the rate at which the interface is rising due to entrainment of upper layer fluid into the turbulent flow emerging from the lower layer. The dimensionless entrainment rate is defined as the ratio of the entrainment velocity w_e to the characteristic velocity w_1. In the literature, the value of the entrainment exponent α has been found to be -1/2 (Cotel *et al.*, 1997; Price, 1979), -1 (Turner, 1968; Buch, 1980), -3/2 (Baines, 1975; Schneider, 1980) or in one case -2 (Jones and Mulhearn, 1983). Linden (1973) concluded from theoretical arguments that α should be -3/2 for a vortex ring. Kumagai (1984) measured α for a plume, finding it close to -3/2. For a jet impinging on a stratified interface (Cotel *et al.*, 1997); α was measured to be -1/2. Turner (1973) also found that the value of α seemed to depend on the Schmidt or the Prandtl number from his stirring grid experiments with heat and salt. The Schmidt number, Sc, is defined to be

$$\mathrm{Sc} = \frac{\nu}{D_m}\,, \tag{4.4}$$

where D_m is the molecular diffusivity and ν is the kinematic viscosity. The Prandtl number, Pr, is

$$\mathrm{Pr} = \frac{\nu}{D_t}\,, \tag{4.5}$$

where D_t is the thermal diffusivity. When the Richardson number is less than seven, the value of α equals -3/2. If Ri > 7, the value of α remains -3/2 for salt stratification, but becomes -1 for heat stratification (Turner, 1973). The Reynolds number is defined by where δ and w_1 represent the characteristic length scale and velocity scale of the flow respectively, and ν is

$$\mathrm{Re} = \frac{w_1\delta}{\nu}\,, \tag{4.6}$$

the kinematic viscosity.

A model was recently proposed by Cotel and Breidenthal (1997) to extend the Morton, Taylor, and Turner's (1956) entrainment hypothesis to stratified flows. It distinguishes between flows on the basis of a new parameter, T, the vortex persistence. The model postulates the existence of a vortex (or eddy) that is responsible for the entrainment. The persistence is defined to be the number of rotations this vortex completes during the time interval it moves a distance equal to its own diameter at the interface. It is a measure of the stationarity of the vortex.

T is proportional to the ratio of the rotational, w_r, the translational speed, w_t, of the entraining eddy. The translational speed is the speed at which the eddy is moving with respect to the interface. T is independent of Ri, Re or Sc), since they all can be varied separately while T is held constant. In combination with the conventional parameters of Richardson (Ri), Reynolds (Re) and Schmidt (Sc) numbers, the persistence T defines the entrainment regime (Cotel, 1995; Cotel and Breidenthal, 1997).

4.3 Experimental techniques

Laser-Induced Fluorescence: The beam of an ion-argon laser is transformed into a thin sheet via a cylindrical lens. The sheet is directed towards the tank using mirrors and is located along the centerline of the tank, providing a 2-D image of the three-dimensional flow. The entrainment rate and the location of the mixed fluid are measured directly from the images recorded on a CCD camera. The entrainment velocity w_e is measured by the rate of advance of the upper interface of the mixed layer, after subtracting the displacement due to the volume flow of the jet, thermal or gravity current entering the tank. This entrainment velocity is normalized by the flow centerline speed w_1 at the interface in order to obtain the entrainment rate. The entrainment velocity is measured shortly after the beginning of a run, while the mixed layer thickness is still small compared to the flow width (Cotel, 1995).

Particle Image Velocimetry provides non-intrusive and planar flow measurements. A thin laser sheet of green light (532 nm) is positioned in the flow seeded with Titanium Oxide particles. The laser (120 mJ New Wave Research, Inc.) is pulsed at an interval of 50 ms. Simultaneously, a frame is recorded on a CCD camera. The digitized images are analyzed with a PIV processing software (Pixelflow) from General Pixels. The software determines the velocity at points on a equally spaced grid covering the region of interest. The grid spacing used is 16 pixels. Cross correlation techniques applied to an interrogation window of 32x32 pixels are used to determine the particle displacement. The average velocity of the particles is deduced from their displacement; vorticity and streamlines are calculated from that information. The disturbances on the flow are not significant, since the particles are very small. The error in the measured velocity is estimated to be ± 0.2 cm/sec. The index of refraction needs not to be matched in these experiments as the density difference between the fluids is small, on the order of a few percents.

4.4 Turbulent jet impinging on a stratified interface

4.4.1 Background

A vertical round jet is formed when fluid issues from an axisymmetric nozzle into a quiescent environment. In the near field, the jet structure consists of a curved shear layer, which separates the potential core from the ambient fluid. As the shear layer grows, the potential core is completely consumed, typically at five diameters for a density ratio of unity. Then there is a transition zone from the initial shear layer to the asymptotic jet. Eventually, the statistical properties of the turbulence approach a far-field, asymptotic level.

The far-field jet structure may be most readily revealed by the concentration field of an inert scalar. Gibson *et al.* (1977) and Dahm & Dimotakis (1987) found that the jet consists of large regions of approximately uniform fluid with arrowhead or boomerang cross sections. Presumably these regions reflect the underlying structure. Work of Mungal & O'Neil (1989) suggests that the far-field structure jumps back and forth between two modes, an axisymmetric and a helical one.

The literature on jets is extensive and only a very brief review is given above since the focus of this particular project is on tilted and tilted/precessing jets. Zhang (1999) studied the vortical structure of an inclined jet (45° angle) within a boundary layer. Schneider *et al.* (1997) obtained LDA velocity measurements and looked at the turbulent structure associated with a precessing jet in a uniform environment.

4.4.2 Experiment set-up and procedure

A water tank, 28 cm x 28 cm x 60 cm high, is divided by a horizontal sliding splitter plate into two regions, as sketched in Figure 4.1. The experimental procedure is the following. The reservoir containing the jet solution is first filled with a saline solution mixed with fluorescein dye. The conduit between the reservoir and the tank is also filled to avoid trapping air. If air were present upon opening the valve, the stratified interface would be destroyed. A saline solution equal in density to the jet solution is then poured in the lower section of the tank. Once the lower section is filled, the horizontal splitter plate is pushed in. The upper layer is filled with a lower density saline solution, whose density varies depending on the experiments. Once the fluids have settled, *i.e.* turbulence from the filling process has dissipated, the splitter plate is slowly withdrawn, leaving a thin, stratified interface between the two fluids of thickness equal to 0.3 cm. The valve located in the vicinity of the jet nozzle is opened to start the experiment.

Different nozzles have been constructed to provide a range of different tilt angles. The nozzle is attached to a disc that can be rotated at different speeds using a standard DC motor.

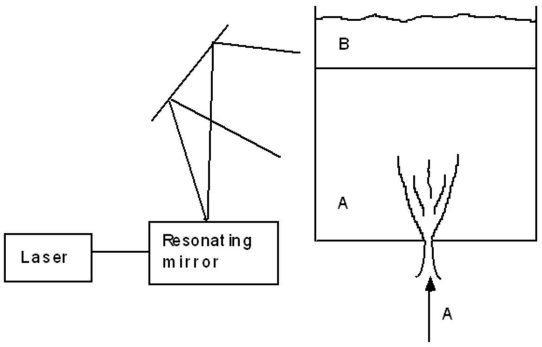

Figure 4.1: Experimental set-up for the jet experiments.

4.4.3 Results

LIF and PIV measurements are performed for a tilted jet at two different angles: 5°, 10° and compared with previous data for 15° (Cotel *et al.*, 1997). For a tilt angle of 5°, the range of Richardson was from 0.2 to 20.8 and the range of Reynolds number was from 7520 to 11700. For a tilt angle of 10°, the range of Richardson was narrowed to the region of interest, between 1.2 and 8.6. Previous work (Cotel, 1995) has shown a transition around Ri = 10, where the entrainment process changes from an engulfment-driven mechanism to a diffusion-dominated process. The entrainment measurements are performed soon after the impingement.

The internal waves produced at the interface during impingement do not interfere with the dynamics of the flow since no breaking of the internal waves was observed. Furthermore, the interface between the jet and surrounding fluid is sharp, diffusion does not play a significant role in the entrainment process for the range of Ri investigated.

Tilt only - No precession

The entrainment rate was measured for a jet at different tilt angles. The Richardson number is defined on the jet quantities and the initial density difference across the interface as stated above. Figure 4.2 shows the measured entrainment rates (and error bars) as a function of Ri for different jet tilt angles. The error in the entrainment law fit ranges from 0.1% (15° case) to 24% (10° case). For angles up to 10°, the entrainment rate follows the same power law, $\mathrm{Ri}^{-1/2}$ whereas for the 15° case, the entrainment rate is now proportional to $\mathrm{Ri}^{-3/2}$. There is no significant difference in the data for the 5° and 10° cases. There appears to be a significant change in the jet dynamics between the angles of 10° and 15°. One proposed explanation is that the half-angle of expansion, which lies between 12° and 15° for a vertical turbulent jet (Dahm and Dimotakis, 1987), is important in determining this particular transition.

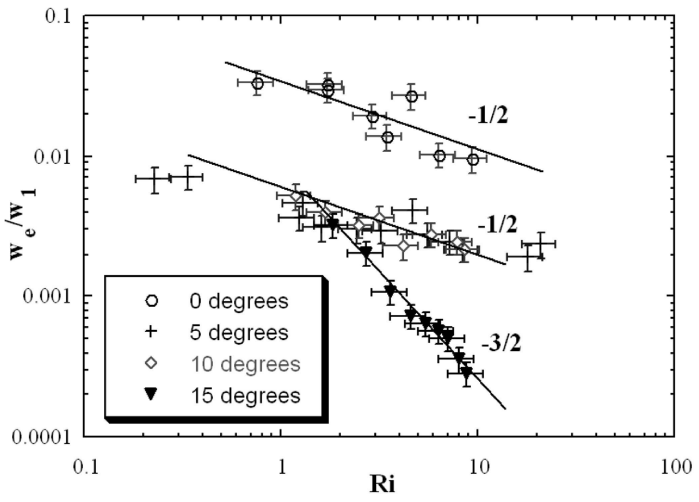

Figure 4.2: Entrainment rate versus Richardson number for different tilt angles.

Laser-Induced Fluorescence is used to visualize the internal structure of the jet at the time of impingement and to reveal any difference in baroclinic vorticity near the interface (Figure 4.3). It was demonstrated previously (Cotel *et al.*, 1997) that baroclinic vortices are responsible for the entrainment in a vertical jet impinging on a stratified interface. It seems reasonable to assume that a similar process would occur in the case of a tilted jet, in particular for small angles of tilt. The baroclinic vorticity generated by the impingement process can be clearly seen in Figure 4.3. Each photograph is taken at approximately 30 s after the valve is opened and the jet has exited the nozzle located at the bottom of the tank. The bright fluid represents a mixture of upper layer and jet fluids. The tank walls do not affect the entrainment measurements as they are taken in the first few seconds after impingement to ensure no wall or internal wave effects are present.

A vertical jet impinging on a stratified interface exhibits the following structure: on each side of the dome, a strong baroclinic vortex is formed, and that vortex is responsible for entraining and mixing surrounding fluid (Cotel, 1995). For a tilt angle of 15°, this vortical structure is not fully formed, only one baroclinic vortex completely rolls up and is strong enough to entrain fluid, while the opposite side shows much weaker baroclinic vorticity. Figure 4.4(a) shows the vorticity contours for Ri = 8.7 and for a tilt angle of 10° before impingement. The jet vortices are clearly shown in red and blue representing the two signs of vorticity within the jet structure. In Figure 4.4(b), which represents the after-impingement situation, there is a baroclinic vortex on the left side located just above the jet vortex, rotating in opposite direction to the jet vortex. However on the right side of the image, there is no distinct baroclinic vortex above the jet vortex. Even at that

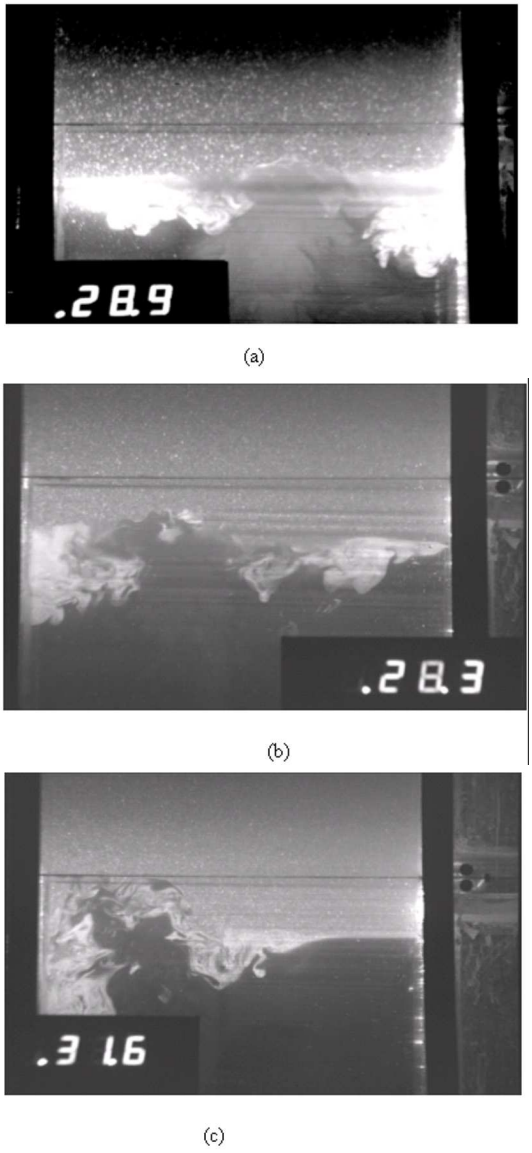

Figure 4.3: LIF photographs of tilted jet at various angles for Ri = 2.5. The numbers in the images represent the time elapsed after the valve to the jet reservoir has been opened. (a) 5° (b) 10° (c) 15°

angle, the baroclinic vorticity starts changing its dynamics and is not able to roll-up completely around the impingement dome. Figure 4.4(b) is an average of 5 image pairs, representing an average over 0.1 s given our PIV data acquisition conditions.

Furthermore, the circulation of baroclinic vorticity around the impingement dome is quantified. From PIV data averaged over 2 seconds, the area of the vortex (or vortices) and the corresponding average vorticity are determined in order to calculate circulation. Circulation, defined as the surface integral of vorticity, provides a measure of the strength of a vortex. Figure 4.5 shows a decrease of in the circulation of baroclinic vorticity as a function of tilt angle for a given Richardson number, in this case, $\mathrm{Ri} = 8.7$. The error bars are on the order of 20% as there is some error in precisely characterizing the edge of a vortex.

As the tilt angle increases, less and less baroclinic vorticity is able to fully roll-up in the area surrounding the impingement dome. The lack of baroclinic vorticity roll-up and the decrease in the strength of the baroclinic vorticity are reflected into the decreased capacity of the jet to entrain surrounding fluid. This change of the vortical structure of the jet translates into a different entrainment regime. Both the power law exponent and the magnitude of the entrainment rate change with tilt angle. The entrainment rate of a tilted jet is at least one order of magnitude lower than that of a vertical jet.

Effect of precession

A DC motor is installed in order to provide means to rotate the jet nozzle at various angular velocities. The goal of this set of experiments is to determine the transition between entrainment regimes by only changing the vortex persistence parameter, *i.e.* the precessing speed.

Figure 4.6 compares the entrainment rate as a function of Richardson numbers for different values of the vortex persistence parameter. The precessing speed is varied to determine the transition from persistent to non-persistent for the 10° case. With no precession, a 10° tilted jet follows a $\mathrm{Ri}^{-1/2}$ power law. For low values of the precessing speed, no clear pattern is observed, a significant amount of scatter is present. The entrainment is in-between persistent and non-persistent regimes. However, for a persistence parameter equal to 1/2, we found that the entrainment rate is consistently in the non-persistent regime, proportional to $\mathrm{Ri}^{-3/2}$. It is possible to physically force a persistent regime into a non-persistent regime by imposing a large enough precessing speed. Precession is a valuable tool when a low entrainment rate is desirable in a particular situation; by manipulating the persistence parameter, a reduction of two orders of magnitude in entrainment rate can be achieved.

4.4.4 Discussion

There is a direct relationship between entrainment rate for a tilted jet impinging on a stratified interface and the vortical structure surrounding the impingement

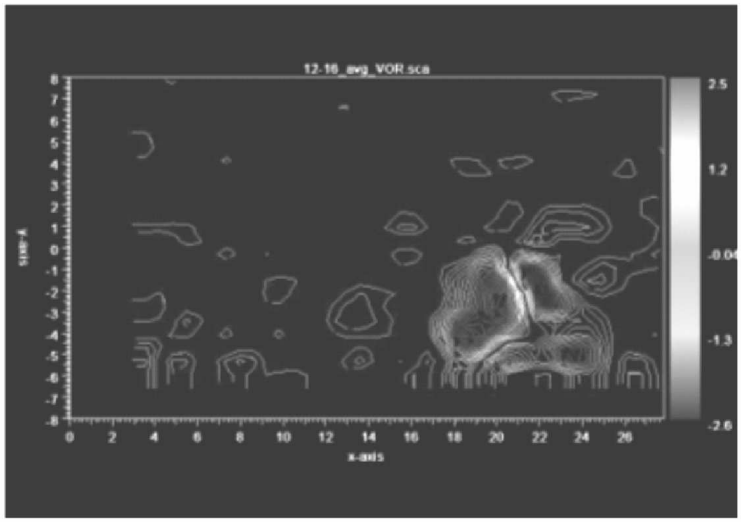

(a)

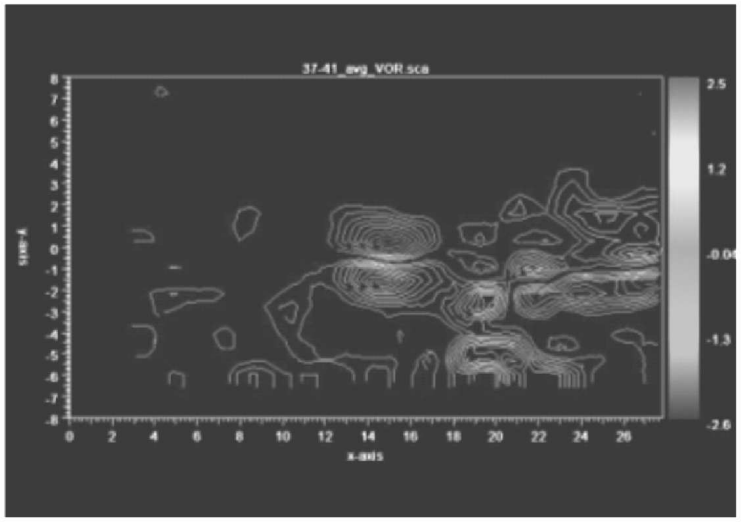

(b)

Figure 4.4: Vorticity contours (in 1/sec) from PIV data for a 10° tilted jet at Ri = 8.7. The x and y axes represent the horizontal and vertical axes of the apparatus (in cm). (a) Before impingement (b) After impingement, note the formation of baroclinic vortices, counter-rotating to the jet vortices only on one side.

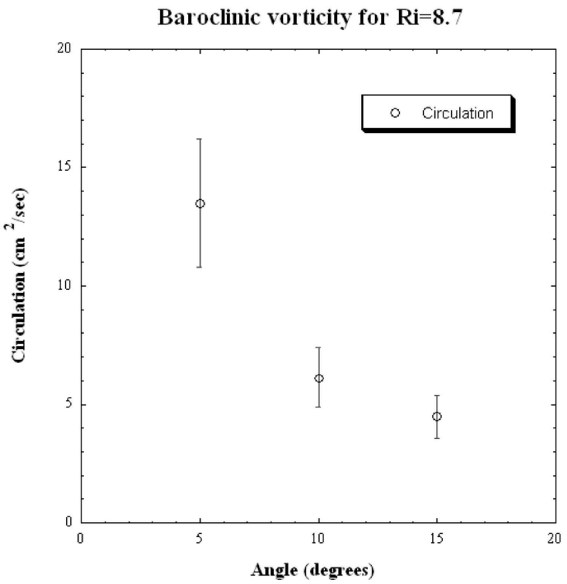

Figure 4.5: Circulation (in cm^2/sec) of baroclinic vorticity as a function of tilt angle of the jet (in degrees) for Ri = 8.7.

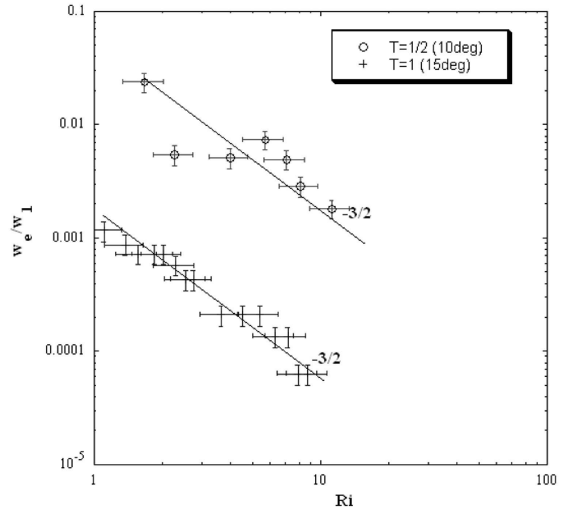

Figure 4.6: Effect of the persistence parameter on entrainment rate for a tilt angle of 10°, compared to 15° tilt.

dome. When the baroclinic vortices are stationary, the entrainment rate follows an entrainment law (proportional to $\mathrm{Ri}^{-1/2}$) characteristic of a persistent regime, as defined by Cotel and Breidenthal (1997). The transition between persistent and non-persistent regimes occurs at an angle between 10° and 15°, which is equivalent to the half-angle of the jet. When the tilt angle is greater than the critical half-angle of the jet, the entrainment rate always exhibits a non-persistent behavior. In other words, the baroclinic vortices created at impingement are either weak or non-existent. However, when the tilt angle is smaller than the half-angle of expansion, most of the baroclinic vortices around the impingement dome complete a full rotation and greatly contribute to the entrainment. The combination of PIV and LIF measurements reveals the correlation between the presence (Figures 4.3 and 4.4) and strength of baroclinic vorticity (Figure 4.5), jet angle and entrainment rate.

At low tilt angles, it is possible to reduce the entrainment rate by imposing a large enough precessing speed. A naturally persistent regime is then forced into a non-persistent entrainment regime, therefore providing a much lower entrainment for the same values of Richardson number.

4.5 Sloping gravity currents impinging on a stratified interface

4.5.1 Background on gravity currents

Benjamin (1968) did some of the early work on gravity currents. His theoretical approach based on inviscid fluid theory provided solutions for depth and velocity of a gravity current. Previous experiments were performed in a homogeneous environment along the bottom of a tank. Measurements included growth rate, hydrodynamic instabilities, structure, such as Simpson (1982), Hallworth *et al.* (1996) Simpson (1982) described the gravity current as a succession of clefts and lobes, due to gravitational instability of the less dense fluid overrun by the nose of the current. Kelvin-Helmholtz instabilities are present in the region of the current behind the head, which is a region of intense mixing. Hot wire measurements were taken to quantify the fluxes in and out of the head of a gravity current (Winant and Bratkovich, 1977). They found that the mass flux of heavy fluid into the head is 0.15 times the flux of the current itself.

Laser-Doppler Anemometry (LDA) measurements were performed recently to map out the velocity profile and Reynolds stresses on the bottom surface (Kneller *et al.*, 1999). It was found that the dominant length scale was of the order of the thickness of the dense underflow. Fleischmann and McGrattan (1999) studied the same type of flow in the context of fire backdrafts, which behave as gravity currents. Entrainment measurements have been performed for 2-D and axisymmetric currents along a flat surface in a uniform environment, *i.e.* no horizontal stratification. The entrainment was found to be independent of g' and therefore of the Richardson number. The entrainment coefficient was different between 2-D

and 3-D currents, and varies with the surface of propagation, a smooth surface yielded a different entrainment constant than a rough surface (Hallworth *et al.*, 1996). The entrainment in the head of gravity current was found to only depend on the initial volume of the current and the distance from the release point.

This represents a sample of the literature on horizontal gravity currents and intrusions. The literature on this subject is extensive, however, the present experiments use a slightly different configuration, *i.e.* the propagation of a gravity current along an inclined slope. For gravity currents down a slope in a homogeneous environment, *i.e.* no density stratification, Turner (1973) found that

$$E = \mathrm{Ri}_0 \tan\theta\,, \tag{4.7}$$

where E is the entrainment, Ri_0 the overall Richardson number and θ the slope angle. The dynamics of a gravity current flowing downslope is changed dramatically (Hopfinger and Tochon-Danguy, 1977). The entrainment into the head increases with increasing slope (Britter and Linden, 1980). Whitehead and Chapman (1986), and Mitsudera and Baines (1992) studied the behavior of a gravity current on a sloping bottom in a linearly stratified environment. Detrained layers at different levels above the tank bottom were observed as well as shelf waves in one of the experiments. Monaghan *et al.* (1999) studied the case of gravity currents descending a ramp in a two-layer stratified tank. Different ramp angles of 20, 45 and 90 degrees were set-up. A numerical model was compared to the experiments to explain the behavior of large amplitude waves.

Hacker *et al.* (1996) performed experiments of finite volume gravity currents on a horizontal surface. They found that substantial mixing occurs in the early stages of the propagation of the current. The location of the gate separating the gravity current fluid from the ambient (uniform) environment was varied, producing different aspect ratios of total water depth to the length of the lock holding the gravity current fluid. They investigated the effect of this aspect ratio on the evolution of the flow and concluded that it has an effect on the structure of the head, but other factors such as changes in Reynolds number and the disturbance caused by the withdrawal of the gate may have also played a role. Similarly, Huq (1996) investigated experimentally the role of the initial aspect ratio (height/radius) on the dilution and entrainment rates of instantaneous releases of a dense, finite volume gravity current into a larger, sector-shaped volume of less dense fluid. The effect of increasing the aspect ratio is to increase the dilution.

The case of gravity currents in a two-layer stratified environment has been studied by others. Lowe *et al.* (2002) performed laboratory experiments in which an intrusive gravity current was observed using shadowgraph and particle tracking methods. The intrusion was generated in a two-layer fluid with a sharp interface, with the gravity current propagating along the interface. Their purpose was to determine the structure of the velocity field inside the intrusion and they concluded that the structure of the flow inside the intrusion can be divided into three regions: the head region in which the fluid velocity is nearly uniform with speed equal to the front speed, a dissipative wake region and behind that a tail region in which there is very little mixing. Monaghan *et al.* (1999) was interested on the creation

of internal waves along the stratified interface. They used different ramp angles of 20°, 45° and 90°. The results of a numerical model, using the Lagrangian particle method, were compared to the experiments to explain the behavior of large amplitude waves. Sutherland *et al.* (2004) and Flynn and Sutherland (2004) used a two-layer stratified environment for their studies. In both cases, the gravity current was propagating along the interface. Sutherland et al. (2004) compared the prediction from an analytical solution for the speed and the vertical extent of the gravity current head with experimental results. They found an excellent agreement when the density of the gravity current is the average of the upper and lower-layer densities. Flynn and Sutherland (2004) studied the vertical flux of horizontal momentum due to the generation of internal waves along the interface and related it to properties of the fluid intrusion.

4.5.2 Gravity current experiment set-up and procedure

The experiments are carried out in a 5 m long horizontal flume. The flume, made of Plexiglas, is 30 cm wide by 50 cm deep (Figure 4.7). The sloping bottom where the current is propagating is made of a thin Plexiglas sheet caulked to the sides of the flume and the slope is set at $\alpha = 6°$. The x-axis is considered to be along the sloping bottom, with $x = 0$ being at the origin that is represented by the location of the gate. The location of the stratified interface is at $x = 1.0$ m and the end of the slope (where it becomes horizontal) is at $x = 2.0$ m. The height of the ramp at the origin (where $x = 0$), from the bottom of the flume is 21 cm.

Saline solutions are used to achieve the density differences necessary to reach a given range of Richardson numbers. The saline solutions are prepared with the following procedure: A 55 gal tank is completely filled with fresh water and a fine sieve is placed on top of the tank, so that it is partially under the water surface. The salt is poured on the sieve and left to dissolve. As the salt dissolves the water on the surface of the tank becomes heavier and a circular motion starts in the tank, with the fresher water at the bottom replacing the heavier at the surface of the tank. With this procedure, the density of the fluid is uniform throughout the tank. The saline solution is used for the experiments in 24 to 36 hours after the salt has dissolved, to ensure that all impurities are settled at the bottom of the tank. A portion of this dense fluid is diluted with the appropriate quantity of fresh water in two different tanks, to achieve the required density of the two different dense fluids that are necessary for an experiment (gravity current fluid and bottom layer fluid). Then depending on the experiment to be performed, different chemicals are added to these two fluids. The range of density of the gravity current fluid is between 1,012 to 1,100 kg/m^3, while the range density of the bottom layer is between 1,008 to 1,022 kg/m^3. Fresh water is used for the top layer. Initially the flume is filled with the fresh layer to a height of 35 cm. The lower denser layer is set in place using a diffuser, connected to a tank of heavy, salty water.

The diffuser is made of a thin Plexiglas plate glued to a short PVC pipe into which the salty water is supplied very slowly with a pump (around 5x10^{-5} m^3/sec). This procedure prevents mixing between the two layers and creates a thin stable

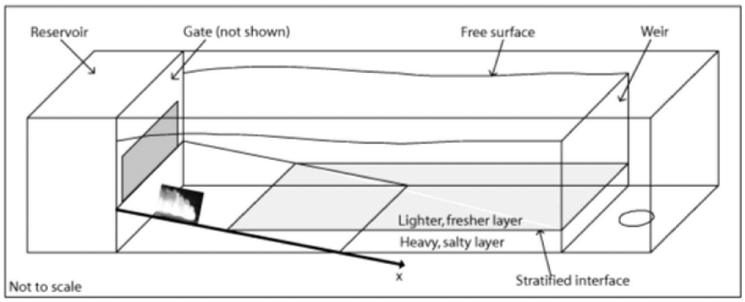

Figure 4.7: Schematic of the experimental apparatus for the gravity current experiments.

stratified interface with a thickness of approximately 0.5 cm. In order to have a constant depth in all experiments, an overflow weir is placed at the downstream end of the flume (Figure 4.7). The total height of fluid in the flume is 46 cm before the release of the gravity current fluid. The reservoir is filled with the dense gravity current fluid by a pump and a lock release mechanism is used to generate two-dimensional gravity currents in the laboratory.

During the filling process of the flume and the gravity current reservoir, a gate is locked in place to separate the gravity current fluid in the reservoir from the flume containing the stratified environment; therefore no initial mixing takes place between the gravity current and the stratified environment. Once the reservoir is full with the gravity current fluid, the gate is lifted to initiate an experiment.

To quantify the mixing and entrainment processes at the region of impingement, Planar Laser-Induced Fluorescence (PLIF) experiments are performed. Disodium fluorescein, whose fluorescence is pH sensitive, is used in these experiments. It is added to the gravity current fluid with a concentration of $7.5\text{x}10^{-4}$ grams per liter of dense fluid, together with sulfuric acid (H_2SO_4) with a concentration of 4 mlit per liter of dense fluid. The pH of the solution is lowered to around 3. When sodium hydroxide (NaOH) is added to the bottom layer (1 mlit per liter of fluid), mixing between the different fluids is visualized with an ion-argon laser. No chemicals are added to the top layer fluid and the pH is at 7. The beam of the laser is transformed into a thin sheet through a pair of cylindrical lens with focal length f = -12.7 mm.

4.5.3 Parameters

It is necessary to define the parameters that govern the propagation of a gravity current on a slope at an angle α to the horizontal (Figure 4.8). The Reynolds number is in the range of 4,000 to 15,000 and is defined as:

$$\mathrm{Re} = \frac{U_f d}{\nu}\,, \tag{4.8}$$

where U_f and d are the characteristic velocity and height of the head of the gravity current before the impingement and ν is the kinematic viscosity of water.

Accordingly the Richardson number is defined by the characteristics of the head before the impingement:

$$\mathrm{Ri} = g\frac{\Delta\rho}{\rho}\frac{d}{U_f^2}\cos\alpha\,, \tag{4.9}$$

where g is the acceleration of gravity and $\Delta\rho$ is a density difference. There are three different ways for the Richardson number to be defined, depending on the choice of $\Delta\rho$ (Samothrakis and Cotel, 2006). When $\Delta\rho$ is defined by the density difference between the current and top layer fluids, $\mathrm{Ri}_{(C-T)}$ determines the velocity and height of the head of the gravity current before the impingement. The balance between the initial buoyancy and the characteristics (velocity and height of the head) of the gravity current is represented by $\mathrm{Ri}_{(C-T)}$. The second one, $\mathrm{Ri}_{(B-C)}$, is defined by the density difference between the current and bottom layer fluids. After the impingement, the gravity current encounters the bottom layer fluid and their density difference is taken into account through $\mathrm{Ri}_{(B-C)}$. This definition of Ri number governs the rate by which bottom-layer fluid is entrained into the gravity current. Finally the third one, $\mathrm{Ri}_{(B-T)}$, is defined by the density difference between the bottom and top layer fluids. This definition of Ri number represents the relative strength of the interface with respect to the energy of the gravity current acquired before the impingement and the easiness by which the gravity current penetrates the interface.

The range of the $\mathrm{Ri}_{(B-C)}$ and $\mathrm{Ri}_{(B-T)}$ numbers is highly affected by the velocity of the gravity current (which is squared in the definition). When a large density difference between the gravity current fluid and the ambient layers is used, the velocity is high, producing small Ri numbers. With a small density difference between the gravity current fluid and the ambient layers, the velocity is small and the resulting Ri number is high.

As our interest is on penetrating gravity currents, there is a limit in the density difference that can be used and therefore the upper limit of the range of Ri is dictated by the physical constraints of the experimental set-up.

4.5.4 Results

The following procedure was used: before a series of experiments, a ruler is placed at the location of the laser sheet and the magnification is calculated (in terms of pixels/cm). The number of pixels that correspond to a certain dimension on the picture (like the height d of the head, or the location x of the head) is obtained through image processing. Based on the size of the images (776x484 pixels), the uncertainty is estimated to be ± 0.60 pixels or (with a typical magnification of 15 px/cm) $\pm 0.4mm$.

Constant flux: The typical lobes and clefts structures (Simpson, 1997) are observed along the upper surface of the gravity current head. As a result fluctuations are seen in this area. When the flow is visualized with dye or shadowgraph, it is

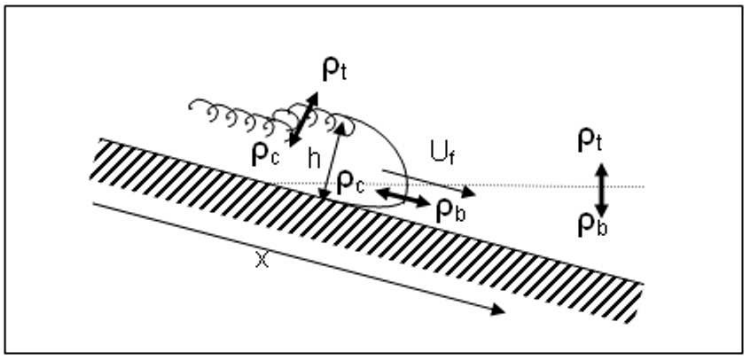

Figure 4.8: Sketch of a gravity current on a slope, with an initial head followed by a steady layer flow. Various variables are defined.

more difficult to define the height and location of the head. But for the measurements based on the PLIF images, where a slice of the flow is visualized, the height/location of the head is easily determined through image processing. The velocity of the gravity current, U_f and the height d of its head were measured for all the experiments, before the impingement, when the nose of the gravity current head is just touching the interface at $x = 1.0$ m. The velocity of the gravity current, U_f , compares very well with previous studies (Britter and Linden, 1980). This shows that the gravity current is well developed when it hits the interface and the effect of friction is negligible in our experiments.

Figure 4.9 shows a photographic sequence of the gravity current, visualized by the PLIF technique. It can be seen from the images that there are two mechanisms responsible for mixing. The first one is the over-riding and engulfment of ambient fluid beneath the nose of the head. There is no mixing at the front of the current. Similarly Johari (1992) for the case of a thermal observed that the volume of entrained fluid by the small-scale eddies on the front of the thermal is small compared to the entrainment by the large-scale eddies in the perimeter of the thermal. Furthermore, these large eddies are responsible for entraining surrounding fluid and bringing it to the center of the thermal where it is ultimately mixed. This is similar to the process of overriding and engulfment in the case of the gravity current. The second mixing mechanism is due to the Kelvin-Helmholtz instabilities along the upper surface of the head (Britter & Simpson, 1978). This confirms that the Kelvin-Helmholtz vortices, formed on the upper surface of the head, represent the dominant mixing mechanism. Similar observations have been reported in other turbulent flows by Brown and Roshko (1974), Dahm and Dimotakis (1987) and Papantoniou and List (1989). In Figures 4.9(c) and 4.9(d) we can see more details of the flow, *e.g.* two large structures following one another.

Hallworth *et al.* (1996) measured the entrainment for a two-dimensional,

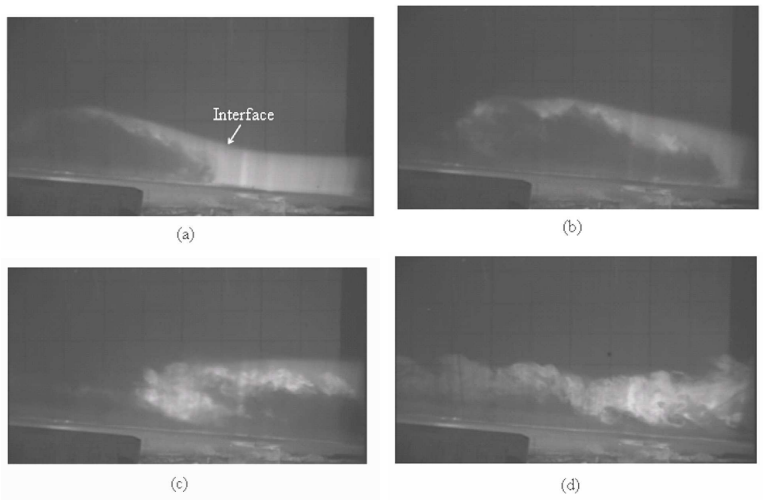

Figure 4.9: Sequence of PLIF images for a constant flux gravity current (Re = 10,500 and $\mathrm{Ri}_{(B-C)} = 1.8$).

constant-volume gravity current, as the ratio of the volume of ambient fluid to the initial volume of the gravity current in the head. For the case of a constant-flux gravity current, Britter and Linden (1980) defined the entrainment as the rate of change of the head height. The rate of growth of the head dh/dx was measured using Planar Laser Induced Fluorescence, with h being the height of the head and x the downstream distance along the slope. This ratio was measured at two different locations to ensure that the effect of the interface on the entrainment of the gravity current is considered. The first one is at a distance 10 to 30 cm after the interface and the second one at a distance 60 to 80 cm after the. The rate of growth of the head at the two locations is found to be proportional to $\mathrm{Ri}_{(B-C)}^{-1\pm.1}$ (Figure 4.10). As the gravity current is propagating through the bottom layer, the density difference of the two fluids controls the entrainment rate between them.

Also, both the velocity and height of the gravity current before the impingement affect the entrainment rate. These parameters are implicitly included in $\mathrm{Ri}_{(B-C)}$. The relevant Ri is based on the difference between the current and the bottom layer. The entrainment we are interested in quantifying is the entrainment of lower or bottom layer fluid into the gravity current. Implicitly, the density of the top layer is important as it defines the gravity current velocity and size before impingement. Therefore, the relevant Ri combines the density of the gravity current, its size and velocity; and the density of the bottom layer. Finally, it should be noted that the range of variation of the Ri number is close to a decade. The range is limited due to constraints linked to the experimental apparatus.

Finite volume: A photographic sequence of the gravity current taken from the

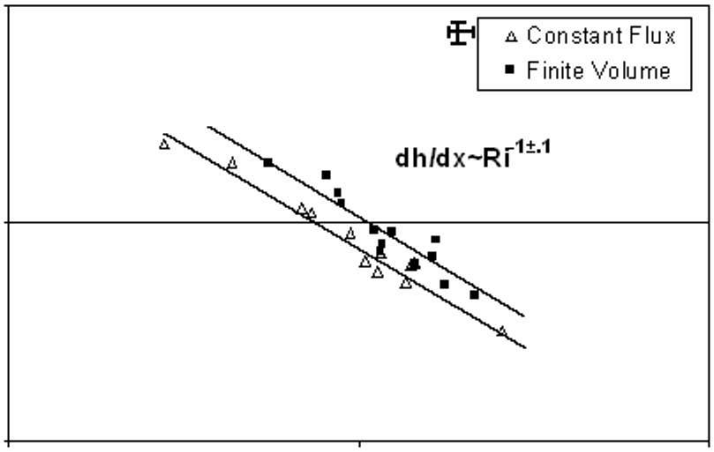

Figure 4.10: Comparison of head growth rate for constant flux and finite volume gravity currents.

Planar Laser Induced Fluorescence experiments is shown in Figure 4.11. In Figure 4.11(a) the location of the interface is marked and the gravity current can be seen entering the image from the left. The color of the gravity current fluid is grey, as it has not yet mixed with the bottom layer fluid. When the mixing between these two fluids occurs (Figures 4.11(b), 4.11(c) and 4.11(d)), the dye in the gravity current fluid fluoresces abruptly. In Figure 4.11(b) the two mechanisms responsible for mixing are observed for the case of a finite volume gravity current. The first mixing mechanism is the overriding of ambient fluid by the gravity current head (marked as location 1 in Figure 4.11(b). The second one is the Kelvin-Helmholtz instabilities (Britter and Simpson, 1978) that appear on the upper surface of the head (marked as location 2 in Figure 4.11(b)). The Kelvin-Helmholtz vortices represent the dominant entrainment and mixing mechanism, responsible for the bulk of the mixing.

Figure 4.12 provides a more detailed view of the mixing occurring during impingement. The top image in Figure 4.12(b) is a magnified picture of the area in the black rectangle of Figure 4.12(a), where an eddy is being formed. The rest of the images in column (b) are 0.2 sec apart and provide a magnified picture of the same eddy as it propagates downstream. We can clearly see in the top image of column (b), the process of bottom layer fluid being entrained in the gravity current head. Then the fluid is brought to the core of the vortex and finally, in the last image of the sequence of Figure 4.12(b), being mixed.

Each pixel of the PLIF images (Figure 4.11) has a corresponding light intensity with a range from 0 (black) to 255 (white). With image processing, the range of light intensity that corresponds to the mixed fluid can be determined. In each image, the number of pixels that lie in this range of mixed fluid is measured and

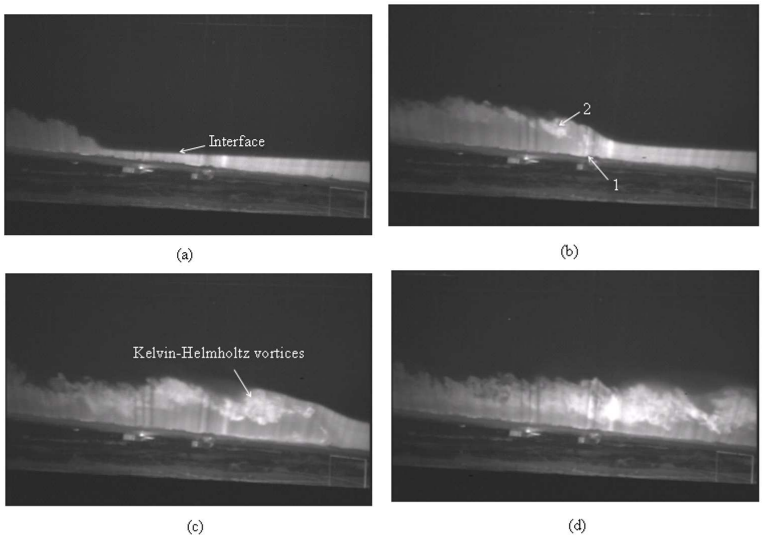

Figure 4.11: Sequence of PLIF images, 2 seconds apart for a finite volume gravity current (Re = 10,000 and $\mathrm{Ri}_{(B-C)} = 0.7$)

with the given magnification (in terms of pixels/cm), the area of mixed fluid in each picture is evaluated and the volume per unit width of mixed fluid, V_{mix}, in each picture is then deduced. The ratio of the volume of mixed fluid, V_{mix}, to the initial volume of the gravity current, Vo, is plotted versus the Richardson number in Figure 4.13 at four different locations of the tip of the gravity current head. These four locations are 105, 115, 125 and 135 cm downstream of the origin (defined as the beginning of the ramp) or 5, 15, 25 and 35 cm downstream of the location of impingement. For all four locations, the ratio of mixed fluid to the initial volume of gravity current fluid, V_{mix}/Vo is found to be proportional to $\mathrm{Ri}_{(B-C)}^{-1\pm.15}$ (Figure 4.13). The difference in the measured values is due to the fact that as the gravity current fluid is propagating deeper into the bottom layer, the volume of mixed fluid is increasing (*i.e.* more bottom fluid is entrained into the gravity current head). Error estimates are provided in the upper right corner of the graph.

The entrainment measurements were taken at a distance 10 to 30 cm after the interface. In Figure 4.10, the rate of growth of the head of a finite volume gravity current is plotted versus Richardson number and is found to be proportional to $\mathrm{Ri}_{(B-C)}^{-1\pm.1}$. Error estimates are provided in the upper right corner of the graph.

Both the ratio of mixed fluid to the initial volume of gravity current fluid V_{mix}/Vo (*i.e.* the mixing rate) and the rate of growth of the head dh/dx (*i.e.* the entrainment rate), are found to be proportional to $\mathrm{Ri}_{(B-C)}^{-1}$. The Ri number governing the entrainment and mixing rate is based on the difference between the

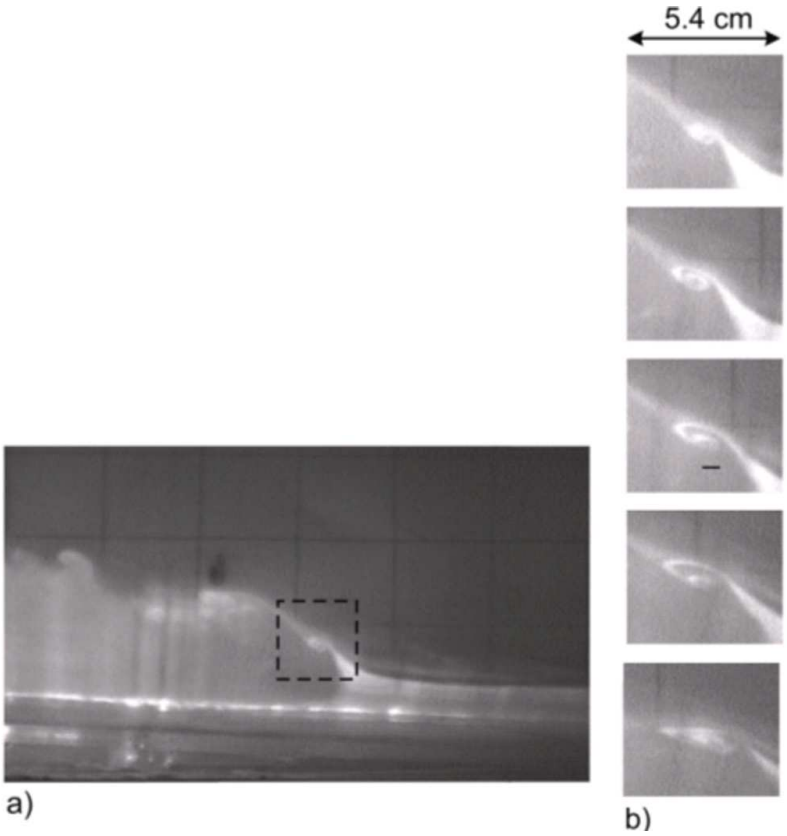

Figure 4.12: Details of the mixing process from PLIF images. The images in column b) are 0.2 seconds part (Re = 6,000 and $\mathrm{Ri}_{(B-C)} = 0.4$)

current and the bottom layer, since we are interested in quantifying the entrainment/mixing of lower or bottom layer fluid into the gravity current.

4.5.5 Discussion

For both cases of a constant flux gravity current and a finite volume gravity current impinging on a stratified interface, we observed that the Kelvin-Helmholtz vortices, formed on the upper surface of the head of the gravity current, represent the main mixing mechanism. In terms of the mixing and entrainment rates, we found that both are proportional to $\mathrm{Ri}^{-1}_{(B-C)}$ which corresponds to a shear-dominated regime (Figures 4.10 and 4.13). Finally, as the Reynolds number for all the experiments was above the mixing transition, the entrainment and mixing are proportional to each other (Breidenthal and Baker, 1985; Cotel et al, 1997). In Figure 4.13

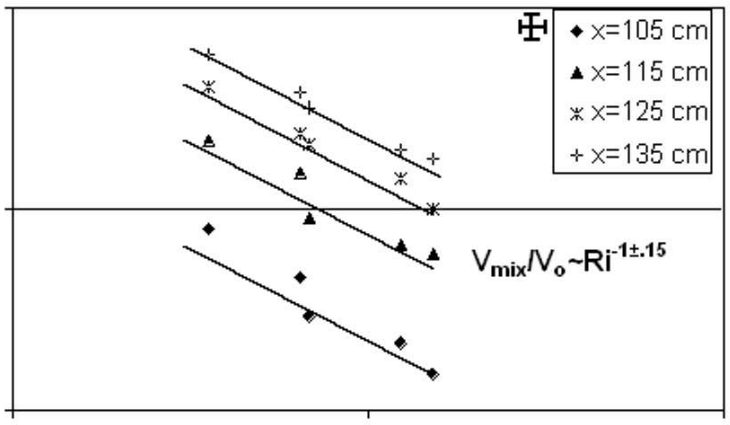

Figure 4.13: Ratio of mixed fluid to initial volume of gravity current fluid versus Richardson number at 4 different locations. The location of impingement is at x = 100 cm.

a comparison of the rate of growth of the head between the cases of constant flux and finite volume gravity currents, is presented. Details of the measurements for the constant flux case can be in found in Samothrakis and Cotel (2006) and Samothrakis (2005). The measured values for the case of the finite volume gravity current are slightly higher, but the difference is close to our estimated error. Part of the difference can be attributed to the fact that in general the velocity of a finite volume gravity current is smaller compared to a constant flux one. Therefore, as it penetrates the interface with a smaller velocity and encounters the denser bottom layer fluid, it spreads more (slightly higher values of dh/dx) than a constant flux gravity current. The initial volume used in our experiments is within the range of volumes used by previous researchers for finite volume gravity current experiments (Huppert & Simpson, 1980; Beghin *et al.*, 1981; Hallworth *et al.*, 1996; Monaghan, 1996; Monaghan *et al.*, 1999; Hacker, *et al.*, 1996; Huq, 1996; Lowe *et al.*, 2002; Maxworthy *et al.*, 2002; Sutherland *et al.*, 2004). Therefore, the volume used in our experiments (14,000 cm^3) represents a finite volume gravity current based on previous work.

4.6 Thermal/plume impinging on a stratified interface

4.6.1 Background on thermals

The term "thermal" is used to denote a parcel of isolated buoyant fluid suddenly released from rest, which subsequently moves under the action of buoyancy forces

alone. An isolated thermal represents a purely convective flow in the atmosphere, with absolutely no momentum, circulation, or kinetic energy initially present in the flow (Woodward, 1959). From the motion of cumulus clouds, it appears that convection, which is produced by buoyancy forces, consists largely of more or less isolated masses of buoyant air rising into and mixing with their surroundings (Scorer, 1957). Characterized by its total buoyancy force, a thermal acquires circulation, kinetic energy, and momentum as it accelerates in the near field. The circulation is generated entirely by buoyancy after the thermal is released. In laboratory experiments, buoyancy force is conveniently induced by salinity differences. Scorer (1957), Woodward (1959), and Turner (1963) performed tank experiments involving heavy brine parcels sinking through a uniform environment of fresh water. They observed that the diameter increases linearly with vertical distance from the source. Their results seemed to confirm the applicability of self-similar entrainment. In an un-stratified environment, a thermal first accelerates to a maximum speed near the source, and decelerates as mixing is accomplished with loss of buoyancy force. The advancing front of a thermal has traditionally been used for measurements since it is a relatively distinctive point (Johari, 1989). A self-similar thermal in the far-field has a width of about half the distance the front traveled (Johari, 1992) while a thermal starting from rest initially exhibits much less entrainment than a self-similar thermal. Grabowski and Clark (1991, 1993) used two and three-dimensional numerical experiments to simulate thermals in a stratified environment and considered cloud-environment interface instability a primary entrainment mechanism.

Linden (1973) proposed a theoretical model based on the impingement of a vortex ring on a stratified interface to explain entrainment results from stirring grid experiments (Turner, 1973). Baines (1975) performed laboratory experiments for the case of an impinging plume. All three studies report an entrainment law proportional to $\mathrm{Ri}^{-3/2}$. No observations of interface dynamics are reported by Linden (1973).

Dahm *et al.* (1989) studied the interface dynamics resulting from the impingement of a vortex pair and a vortex ring on a stratified interface. Saunders (1962) and Richards (1962) independently conducted experiments related to a penetrating thermal into a stably two-layer stratified environment. The penetration height was measured as a function of time (Saunders, 1962) and as a function of the density difference across the interface (Richards, 1962), but neither studied the relationship between penetration height and Richardson number. In both sets of experiments, the density of the thermal and the density difference across the interface were varied simultaneously.

4.6.2 Thermal experiment set-up

An ideal mechanism for releasing thermals would simulate the atmospheric release process as closely as possible. The experimental apparatus described below allows us to create repeatable thermals without imposing initial circulation. The dimensions of the tank used in these experiments are 30 x 30 cm^2 in cross section and

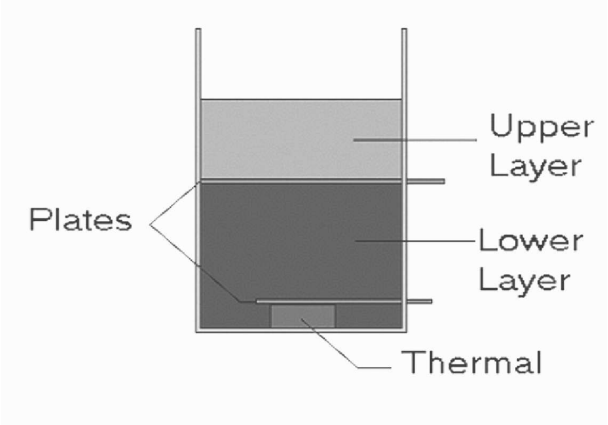

Figure 4.14: Schematic of the experimental set-up for the thermal experiments.

65 cm in height. A vertical cylinder, 2.5 cm inside diameter and 2.9 cm high, is located at the bottom of the tank, in the center, and covered by a thin, horizontal sliding stainless steel lid. For the purpose of generating a thin stratified interface, the tank is separated into two chambers by another thin, horizontal sliding stainless steel plate (Figure 4.14).

The interface is located 15 diameters downstream of the initial thermal diameter, therefore we assume that far field conditions are reached at the interface location. Bond (2001) studied the near field of buoyancy driven vortex rings. The near field was defined as any distance less than 5 nozzle diameters.

The tank walls are made of chemically resistant lucite to give an unobstructed view of the flow. The top and bottom fluid layers consist of aqueous solutions of different salt concentrations. The density of the lower layer fluid is greater than that of the upper layer fluid, which in turn is greater than the thermal fluid density.

The experimental procedure is the following: the cylinder at the bottom of the tank is filled with freshwater and covered with the sliding lid. Then, the lower section of the tank is filled and the sliding plate is pushed in. Finally fluid is poured into the upper section. The sliding plate and the lid are used to minimize mixing between the different fluids before a run. This allows us to obtain a thin stratified interface, on the order of 4 to 5 millimeters. In addition, no initial circulation is imposed on the thermal before release.

4.6.3 Results

Preliminary experiments of a thermal impinging on a stratified interface have been performed and produced counterintuitive results. Instead of behaving similarly to a vortex ring (Linden, 1973), *i.e.* rebounding away from the interface, two vortices are created by baroclinic torque from the tilted interface, then these vortices merge

with the original thermal vortices to form a vortex pair moving horizontally in the vicinity of the interface (Figures 4.15 and 4.16). No significant vertical transport was observed, as would be expected from the rebound argument.

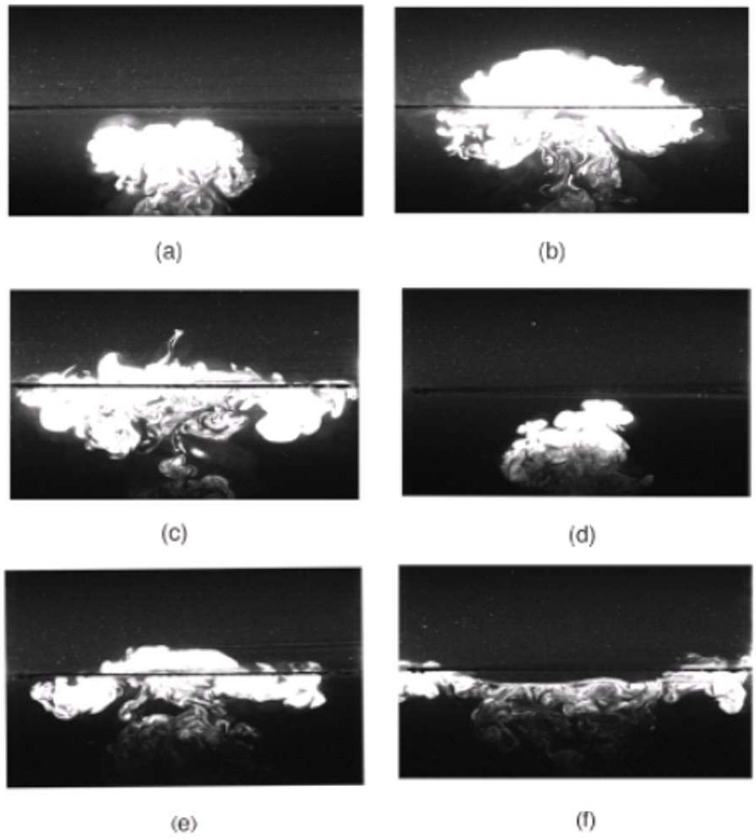

Figure 4.15: Time series of LIF photographs for lower Richardson numbers a) Ri = 1.9, t = 5 s b) Ri = 1.9, t = 45 s c) Ri = 1.9, t = 80 s d) Ri = 4.2, t = 5 s e) Ri = 4.2, t = 45 s f) Ri = 4.2, t = 80 s

Zhang and Cotel (2000) measured the entrainment rate of a single thermal impinging on a stratified interface and found it proportional to $\mathrm{Ri}^{-3/2}$ as predicted by Cotel and Breidenthal's (1997) persistence theory.

4.7 Conclusions

The new results presented above confirm the wide application of the persistence theory. The entrainment rate across a stratified interface for a thermal; precessing,

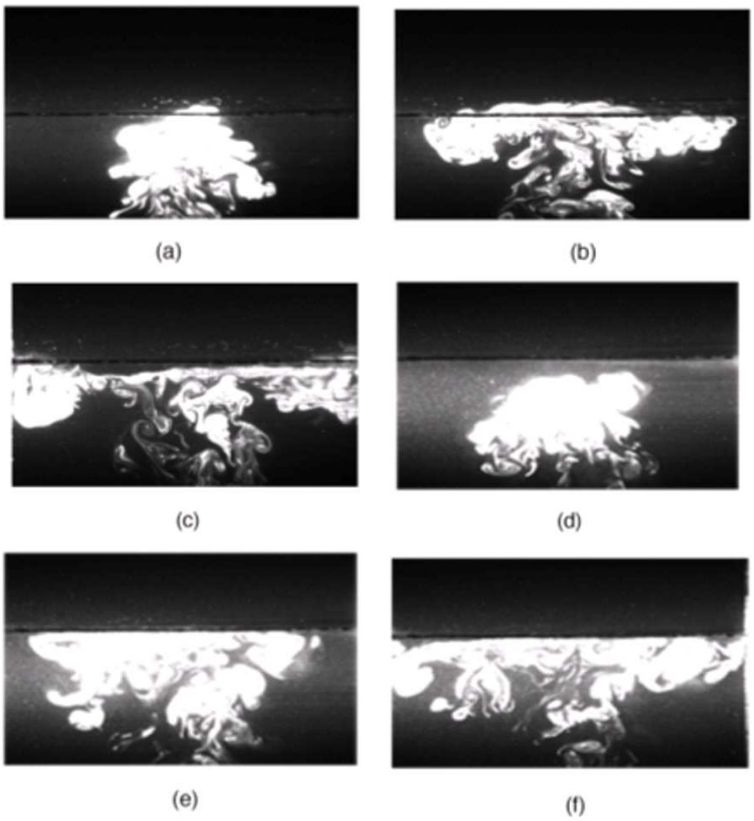

Figure 4.16: Time series of LIF photographs for higher Richardson numbers a)Ri = 8.8, t = 5 s b)Ri = 8.8, t = 45 s c) Ri = 8.8, t = 80 s d) Ri = 16, t= 5 s e) Ri = 16, t = 45 s f) Ri = 16, t = 80 s

tilted jet and a sloping gravity current is predicted by the persistence theory.

In the case of the sloping gravity current, shear, through the action of Kelvin-Helmholtz vortices, dominates the entrainment process and therefore a Ri^{-1} power law is observed.

In the case of buoyancy driven flow such as the thermal, the persistence theory applies directly, no stationary eddies are created along the impingement dome, the rebound eddies control the entrainment which is then proportional to $\mathrm{Ri}^{-3/2}$.

The forcing mechanism, *i.e.* buoyancy or momentum has no effect on the entrainment rate; the vortical structure resulting from the impingement is responsible for the type of entrainment that takes place.

The ultimate test for the persistence theory is provided by the precessing and tilted jet experiments. It is found that the entrainment rate is strongly dependent

on the strength of the baroclinic vorticity near the interface. The vortical structure of the jet is deeply affected by the tilt angle of the jet. A transition between persistent and non-persistent regimes is observed for a tilt angle between 10° and 15°. A naturally occurring persistent regime can be forced into a non-persistent regime by imposing a sufficiently large precessing speed, which corresponds to a critical value of the persistence parameter for the jet. As a result the entrainment rate of the jet is reduced by at least one order of magnitude.

4.8 References

Baines W. D.; "Entrainment by a plume or jet at a density interface," *J. Fluid Mech.* **68**, 309-320 (1975).

Beghin P., Hopfinger E. J., Britter R. E.; "Gravitational convection from instantaneous sources on inclined boundaries," *J. Fluid Mech.* **107**, 407-422 (1981).

Benjamin T. B.; "Gravity currents and related phenomena," *J. Fluid Mech.* **31**, 209-248 (1968).

Bond D.; "Near field development of buoyancy driven flows," Master's Thesis, Mechanical Engineering, Worcester Polytechnic Institute (2001).

Britter R .E., Simpson J. E.; "Experiments on the dynamics of a gravity current head," *J. Fluid Mech.* **88**, 223-240 (1978).

Britter R. E., Linden P. F.; "The motion of the front of a gravity current traveling down an incline," *J. Fluid Mech.* **99**, 531-543 (1980).

Brown G. L. and Roshko A.; "On density effects and large structure turbulence," *J. Fluid Mech.* **64**, 775-816 (1974).

Buch E.; "On entrainment and vertical mixing in stably stratified fjord," in *Proc. Int. Symp. Strat. Flows*, Trondheim (1980).

Cotel A. J.; "Entrainment and detrainment of a jet impinging on a stratified interface," Ph.D. Thesis, University of Washington, Seattle (1995).

Cotel A. J. and Breidenthal R. E.; "A model of stratified entrainment using vortex persistence," *Applied Scientific Research*, **57**, 349-366 (1997).

Cotel A. J., Gjestvang J. A., Ramkhelawan N. N. and Breidenthal R. E.; "Laboratory experiments of a jet impinging on a stratified interface," *Experiments in Fluids*, **23**, 155-160 (1997).

Dahm W. J. A. and Dimotakis P. E.; "Measurement of entrainment and mixing in turbulent jets," *AIAA J.* **25**, 1216-1223 (1987).

Dahm W. J. A., Scheil C. M., Tryggvason G.; "Dynamics of vortex interaction with a density interface," *J. Fluid Mech.* **205**, 1-43 (1989).

Fleischmann C. M. and McGrattan K. B.; "Numerical and experimental gravity currents related to backdrafts," *Fire Safety Journal* **33**, 21-34 (1999).

Flynn M. R., Sutherland B. R.; "Intrusive gravity currents and internal gravity wave generation in stratified fluid. *J. Fluid Mech.* **514**, 355-383 (2004).

Gibson C. H., Friehe C. A. and McConnell S. O.; "Structure of sheared turbulent fields," *Phys. Fluids* **20(10)**, S157-S167 (1977).

Grabowski W. W. and Clark T. L.; "Cloud-environment interface instability: Rising thermal calculations in two spatial dimensions," *Journal of the Atmospheric Sciences*, **48**, 527-546 (1991).

Grabowski W. W. and Clark T. L.; "Cloud-environment interface instability. Part II: Extension to three spatial dimensions," *Journal of the Atmospheric Sciences*, **50**, 555-573 (1993).

Hacker J., Linden P. F. , Dalziel S. B.; "Mixing in lock-release gravity currents," *Dynam Atmos Ocean* **24**, 183-195 (1996).

Hallworth M. A., Huppert H. E., Phillips J. C., Sparks S. J.; "Entrainment into two dimensional and axisymmetric turbulent gravity currents," *J Fluid Mech* **308**, 289-311 (1996).

Hopfinger E. J. and Tochon-Danguy J. C.; "A model study of powder-snow avalanches," *Glaciology*, **19**, 343-356 (1977).

Huppert H. E. and Simpson J. E.; "The slumping of gravity currents," *J Fluid Mech* **99**, 785-799 (1980).

Huq P,; "The role of aspect ratio on entrainment rates of instantaneous, axisymmetric finite volume releases of dense fluid," *J Hazard Mater* **49**, 89-101 (1996).

Johari H.; "An experimental investigation of mixing in buoyant flows," Ph.D. thesis, University of Washington, Seattle (1989).

Johari H.; "Mixing in thermals with and without buoyancy reversal," *Journal of the Atmospheric Sciences* **49(16)**, 1412-1426 (1992).

Jones I. S. and Mulhearn P. J.; "The influence of external turbulence on sheared interfaces," *Geophys. Astrophys. Fluid Dynamics* **24**, 49-62 (1983).

Kneller B. C., Bennett S. J. and McGaffrey W. D.; "Velocity structure, turbulence and fluid stresses in experimental gravity currents," *J. of Geophysical Research-Oceans* **104(C3)**, 5381-5391 (1999).

Kumagai M.; "Turbulent buoyant convection from a source in a confined two-layer region," *J. Fluid Mech.* **147**, 105-131 (1984).

Linden P. F.; "The interaction of a vortex ring with a sharp density interface," *J. Fluid Mech.* **60**, 467-480 (1973).

Lowe R. J., Linden P. F., Rottman J. W.; "A laboratory study of the velocity structure in an intrusive gravity current," *J. Fluid Mech.* **456**, 33-48 (2002).

Maxworthy T., Leilich J., Simpson J. E., Meiburg E. H.; "The propagation of a gravity current into linearly stratified fluid," *J. Fluid Mech.* **453**, 371-394 (2002).

Mitsudera H. and Baines P. G.; "Downslope gravity currents in a continuously stratified environment: a model of the Bass Strait outflow," *11th Australasian Fluid Mechanics Conference*, (1992).

Monaghan J. J.; "Gravity currents and solitary waves," *Physica D* **98**, 523-533 (1996).

Monaghan J. J., Cas R. A. F., Kos A. M., Hallworth M.; "Gravity currents descending a ramp in a stratified tank," *J. Fluid Mech.* **379**, 39-69 (1999).

Morton B. R., Taylor G. I. and Turner J. S.; "Turbulent gravitational convection from maintained and instantaneous sources," *Proc. Roy. Soc. A* **234**, 1-23 (1956).

Mungal M. G. and O'Neil J. M.; "Visual observations of a turbulent-diffusion flame," *Combustion and flame* **78(3-4)**, 377-389 (1989).

Papantoniou D. and List E. J.; "Large scale structure in the far field of buoyant jets," *J. Fluid Mech.* **209**, 151-190 (1989).

Price J. F.; "On the scaling of stress-driven entrainment experiments," *J. Fluid Mech.* **90**, 509-529 (1979).

Richards J. M.; "Experiments on the penetration of an interface by buoyant thermals," *J. Fluid Mech.* **11**, 369-384 (1962).

Roshko A.; "Turbulent shear flow: A new look," *AIAA J.* **14**, 1349-1357 (1976).

Samothrakis P.; "An experimental investigation of the dynamics of a sloping gravity current impinging on a stratified interface," Ph.D. thesis, The University of Michigan, Ann Arbor (2005).

Samothrakis P., Cotel A. J.; "The propagation of a gravity current in a two-layer stratified environment," *J. Geophys. Res.* **111**, C01012 (2006).

Saunders P. M.; "Penetrative convection in stably stratified fluids," *Tellus* **14**, 177-194 (1962).

Schneider G. M., Froud D., Syred N., Nathan G. J. and Luxton R. E.; "Velocity measurements in a precessing flow using a 3-D LDA system," *Experiments in Fluids* **23**, 89-98 (1997).

Schneider H. H.; "Laboratory experiments to simulate the jet-induced erosion of pycnoclines in lakes," *Proc. Int. Start. Flows*, Trondheim (1980).

Scorer R. S.; "Experiments on convection of isolated masses of buoyant fluid," *J. Fluid Mech.* **2**, 583-594 (1957).

Simpson J. E.; "Gravity currents in the laboratory, atmosphere, and ocean," *Ann. Rev. Fluid Mech.* **14**, 213-234 (1982).

Simpson J. E.; "Gravity currents in the environment and the laboratory," 2nd edn. Cambridge University Press (1997).

Sutherland B. R., Kyba P. J., Flynn M. R.; "Intrusive gravity currents in two-layer fluids," *J. Fluid Mech.* **514**, 327-353 (2004).

Turner J. S. and Yang I. K.; "Turbulent mixing at the top of stratocumulus clouds," *J. Fluid Mech.* **17**, 212-224 (1963).

Turner J. S.; "The influence of molecular diffusivity on turbulent entrainment across a density interface," *J. of Fluid Mech.* **33**, 639-656 (1968).

Turner J. S.; "Buoyancy Effects in Fluids," Cambridge University Press (1973).

Whitehead J. A. and Chapman D. C.; "Laboratory observations of a gravity current on a sloping bottom: the generation of shelf waves," *J. Fluid Mech.* **172**, 373-399 (1986).

Winant C. D. and Bratkovich A.; "Structure and mixing with the frontal region of a density current," *Sixth Aust. Hydraul. and Fluid Mech. Conf.*, Adelaide (1977).

Woodward B.; "The motion in and around isolated thermals," *Quarterly Journal of the Meteorological Society* **85**, 144-151 (1959).

Zhang Q. and Cotel A. J.; "Entrainment due to a thermal impinging on a stratified interface with and without buoyancy reversal," *J. Geophys. Research* **105(D12)**, 15,457 - 15,467 (2000).

Zhang X.; "Counter-rotating vortices embedded in a turbulent boundary layer with inclined jets," *AIAA J.* **37(10)**, 1277-1284 (1999).